Coordination Polymer: Synthesis, Characterization and Structure-Property Correlation for Sensing and Electrical Conductivity

THESIS SUBMITTED FOR THE DEGREE OF

DOCTOR OF PHILOSOPHY (SCIENCE)

JADAVPUR UNIVERSITY

By
Suprava Bhunia

Index No. 26/19/chem./26

Registration No.: SCHEM1102619

DEPARTMENT OF CHEMISTRY

JADAVPUR UNIVERSITY

KOLKATA-700032

2023

Dr. Chittaranjan Sinha, Ph.D.
Professor & Former Head
Department of Chemistry

JADAVPUR UNIVERSITY
KOLKATA – 7 0 0 0 3 2, I N D I A
Telephone: 91+033-2414-6223 (O),
Mobile: +91-7044231277
e-mail: crsjuchem@gmail.com

Certificate from the Supervisor

This is to certify that the thesis entitled "*Coordination Polymer: Synthesis, Characterization and Structure-Property Correlation for Sensing and Electrical Conductivity*", submitted by Sri. Suprava Bhunia, who got his name registered on 14/08/2019 and Index No. 26/19/chem./26, for the award of Ph. D. (Science) degree of Jadavpur University, is absolutely based upon his own work under the supervision of Prof. Chittaranjan Sinha and that neither this thesis nor any part of it has been submitted for either any degree/diploma or any other academic award anywhere before.

Professor of Chemistry
Department of Chemistry
Jadavpur University
Kolkata-700 032

(CHITTARANJAN SINHA)

(Signature of the Supervisor, date with official seal)

i

Declaration of the Scholar

I declare that this written submission suggests my creative approaches in my own words and where other's ideas have been included; I have properly cited with suitable reference from the authentic sources. I also declare that I have adhered to all origins of academic principle and honesty and have not misled or fabricated or falsified any approach/ data/ origin in my submission. I understand such violation of the above will cause for disciplinary action by University and can evoke penal action from the sources which have thus not been properly cited or from whom proper permission has not been taken when needed.

Suprava Bhunia
16/02/2023

Suprava Bhunia

Dedicated to

My Maa and Baba

Acknowledgement

Suprava Bhunia
16/02/2023

Suprava Bhunia

No. 0213

Jadavpur University

Registration Certificate

Shri/Sm _Suprava Bhunia_

has been registered as a student of **Ph.D. programme of this**

university

His/her Registration Number is SCHEMI102619

Date of Registration 14.08.2019   **Registrar** 02.12.22

vi

JADAVPUR UNIVERSITY

KOLKATA-700 032

MARK SHEET

NO.: CW/16052/ 000732

(For Ph.D/M. Phil. Course Work)

Results of the	PH.D. COURSE WORK EXAMINATION, 2020
In CHEMISTRY	held in DECEMBER,2019 - JANUARY, 2020
Name SUPRAVA BHUNIA	Class Roll No. 201920104014
Examination Roll No. PHDCHEM20115	Registration No. of

Subject Code / Name	Credit Hr.(c_i)	Marks
COMPULSORY UNITS:: EX/CHEM/PHD/A & B RESEARCH METHODOLOGY & REVIEW OF RESEARCH WORK	4	88
ELECTIVE UNITS ::	4	84
EX/CHEM/PHD/I-1 :: APPLICATION OF SPECTROSCOPIC STUDIES IN CHEMICAL RESEARCH EX/CHEM/PHD/I-2 :: MATERIALS, CATELYSES & ELECTROCHEMICAL STUDIES EX/CHEM/PHD/I-3 :: METALS IN LIFE & REACTION DYNAMICS EX/CHEM/PHD/I-4 :: SINGLE CRYSTAL X-RAY STR. SUPRAMOLECULAR CHEM.& DFT COMPUTN.		

Total Marks : 172 (out of 200)

Remarks: P

Prepared by :

Checked by :

Date of issue : 15 / 09 / 2020

Controller of Examinations

vii

CONTENTS

Abstract

Title: Coordination Polymer: Synthesis, Characterization and Structure-Property Correlation for Sensing and Electrical Conductivity

Coordination Polymers (CPs) or Metal-Organic Frameworks (MOF) have extensive role in the field of sensing, electrical conductivity, gas absorption, magnetism, water splitting, environmental management, drug delivery and other biological applications. Structural diversity plays important role to exhibit different property with diverse applications. The coordination polymers are synthesized using the different metal nodes with the combination of bridging ligands. Transition metal CPs with N-heterocyclic bridgers and/or aromatic or aliphatic carboxylate (linker) serve as efficient magnetic materials. Many methods (like, slow evaporation, hydrothermal etc.) are followed to synthesize the CPs and characterised by using different spectroscopic methods (SXRD, TGA, PXRD, IR etc.). Coordination polymers are assembled via C-Cl$\cdots\pi$, $\pi\cdots\pi$, C-H$\cdots\pi$ and H-bonding. The CPs are also used for the selective detection of environmentally important metal ions, anions and small molecules. Extended π-conjugation, structural flexibility, $\pi\cdots\pi$ interaction and metal nodes are the reason for electrical conductivity in the dark/light condition and these materials are used to fabricate the Schottky diode. The CPs are also used in the field of biology to derive microbiologically potential drugs. A short review and motivation of this research is delineated in the **Chapter 1**.

In **Chapter 2** the design, synthesis and structural characterization of two Zn(II) based 1D coordination polymers, [Zn(adc)(4-Cltpy)(H$_2$O)] (CP**1**) and [Zn(*trans*-muca)(4-Cltpy)] (CP**2**) (4-Cltpy = 4′-Chloro-2,2′:6′,2″-terpyridine, H$_2$adc = Acetylene-dicarboxylic acid, *trans*-H$_2$muca = *trans*, *trans*-muconic acid) are described. Both CPs have selectively detected Cu^{2+} in aqueous medium with limit of detection 0.14 μM (CP**1**) and 0.06 μM (CP**2**). Also these CPs have shown internalization within HepG2 cells and subsequent microscopic cell images are collected.

In **Chapter 3** Zn(II) based 1D coordination polymer, {[Zn(2,6-NDC)(4-Cltpy)](H$_2$O)$_4$} (4-Cltpy = 4′-chloro-[2,2′;6′,2″]terpyridine and 2,6-NDC = 2,6-Naphthalene dicarboxylic acid) is spectroscopically characterized and has been confirmed by the Single Crystal X-Ray diffraction measurements. Here, 1D chains are assembled via Cl$\cdots\pi$, $\pi\cdots\pi$ and H-bonding and

have formed 3D geometry. This CP was used to detect the $Fe^{2+/3+}$ by Absorption spectroscopic studies. Zn(II) coordinated metal centre was substituted by Fe and color of CP was changed from colorless to pink in aqueous medium. Limit of detection (LOD) are 0.11 μM (Fe^{2+}) and 0.15 μM (Fe^{3+}). The Zn-CP also exhibits microscopic cell imaging using MDA-MB 231 cells.

In **Chapter 4** the design and synthesis of Cd(II) based 2D coordination polymer, $\{[Cd(HAIPA)(tppz)(OH)].3H_2O\}_n$ (2,3,5,6-Tetrakis(2-pyridyl)pyrazine (tppz), and 5-Aminoisophthalic acid (H_2AIPA)) is reported. Single crystal X-ray diffraction data had helped to evaluate the structure. In presence of different secondary interaction, a 2D network was assembled. The 2D-CP uses selectively and specifically to detect Pd^{2+} in aqueous medium with a limit of detection is 0.08 μM even in presence of large number of cations. The CP shows exhibited electrical conductivity in light and dark condition and upon incorporation of Pd^{2+} in the CP the electrical conductivity is increased.

The **Chapter 5** reports three Cd(II) based 3D coordination polymers, [Cd(tppz)(adc)(MeOH)] (**1**), [Cd(tppz)(trep)] (**2**) and [Cd(tppz)(2,6-ndc)] (**3**) (tppz = 2,3,5,6-Tetrakis(2-pyridyl)pyrazine, acetylene dicarboxylic acid (H_2adc), terephthalic acid (H_2trep) and 2,6 naphthalene dicarboxylic acid (2,6 H_2ndc)). Different spectral techniques have helped to characterise these CPs. The CPs **1** and **2** form 2D network and compound **3** forms 1D chain. DFT computational study of CPs helped to evaluate the band gap that supported the electrical conductivity results.

In **Chapter 6** one coordination complex, [CdI_2(4-nvp)$_2$] (**1**) (CdI_2 = Cadmium iodide and 4-nvp = 4-(1-naphthylvinyl)pyridine)) has been reported. Single crystal X-ray diffraction study confirms the formation of complex (**1**). Different secondary interactions help to assemble the complex. This complex is very much selective and sensitive towards the detection of TNP (trinitrophenol) in acetonitrile. DFT computational study helps to determine the band gap and mechanistic aspect of sensing.

Chapter 1

Introduction

Chapter 1

Abstract

Diversity in Coordination chemistry enters into the strange fields of polymers to explore astounding prodigious wonderful area of CPs (Coordination Polymers)/ MOFs (Metal-Organic Frameworks). These are beyond the conventional solid-state materials and open an arena of potential applications of exceptional scope, extending from gas storage and separation, sensing, drug delivery, outstanding magnetic activity, to electronic applications. The development of electrically conductive CPs/MOFs is a research objective of Sustainable Development Goal (SDG) which provides avenues to novel technologies including electrical energy storage materials, photovoltaics, electrocatalysis etc. In the construction of CPs/MOFs in addition to general covalent and ionic interaction, the role of different secondary interactions to assemble the monomeric motif/s is very crucial. The physical significance of this secondary interaction and application of the CPs/MOFs in the different fields such as, physics, environment, biology, engineering, pharmaceuticals and drugs, etc. are important. The introductory chapter (**Chapter I**) focuses briefly outline - the type of synthesis, principles of characterization, the area of applications in consultation with updated research literature, in general to the particular fields explored in this Thesis. It is expected that literature survey will be helpful to justify the results and discussion that have been exemplified in the successive chapters.

1.1 Introduction: coordination polymers

Coordination polymers (CPs) are the polymeric forms of the coordination compounds. Highly ordered crystalline coordination polymers are formed with combination of organic linkers and inorganic metal ions/clusters as knot. Solid crystalline compounds have greater chemical, thermal, mechanical and optical stability.[1-5]

The definition of coordination polymers (according to Wikipedia)[6] is "*A coordination polymer is an inorganic or organometallic polymer structure containing metal cation centers linked by ligands. More formally a coordination polymer is a coordination compound with repeating coordination entities extending in 1, 2, or 3 dimensions*". Depending upon the structural diversity, dimensionality and availability of permanent cavity in the CPs are recognizing as MOFs (metal-organic frameworks)[4] or MOCNs (metal-organic coordination networks). The repeating coordination entities are extended through 1D (one dimensional), 2D (two dimensional) and 3D (three dimensional) way (**Figure 1.1**).
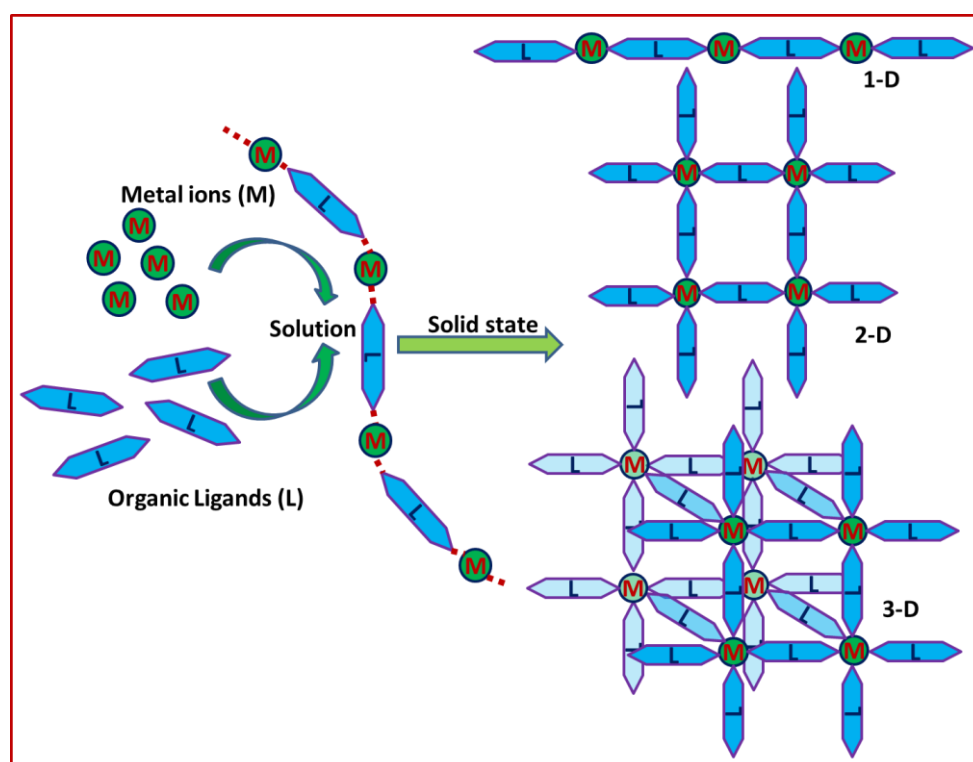
Figure 1.1 Design of **1**, **2** and **3** dimensionally CPs.

The CPs associated with the internal porosity are known as the MOF (Metal-Organic Framework) or PCPs (Porous Coordination Polymers). From the last few decades, research in hybrid material is increased extensively due to their various application fields. In 1995 Prof.

O. Yaghi et al. first observed and investigated the sorption of guest molecule and recently, this is coming from different other research groups.

In this aspect, The CP is different from the organic polymers[3]. Organic polymers are containing high molecular weight and known as macromolecules consisting of only C, H, N, O, S and/or P while CPs contain any element from the Periodic Table. However, in the last three decades exploration of CPs includes s, p, d (3d/4d) block elements and very recently f-block elements are using to develop this field. In the coordination polymers the repeated structural unit is growing via coordination bonds (**Figure 1.2**) along with the noncovalent weak interactions such as C–H···π, π···π and H-bonding etc. Coordination bond forms when ligand is coordinated with the metal ion centres and corresponding interaction is directional than the weak secondary interaction. But both the interactions are important for the assemblage of CPs.
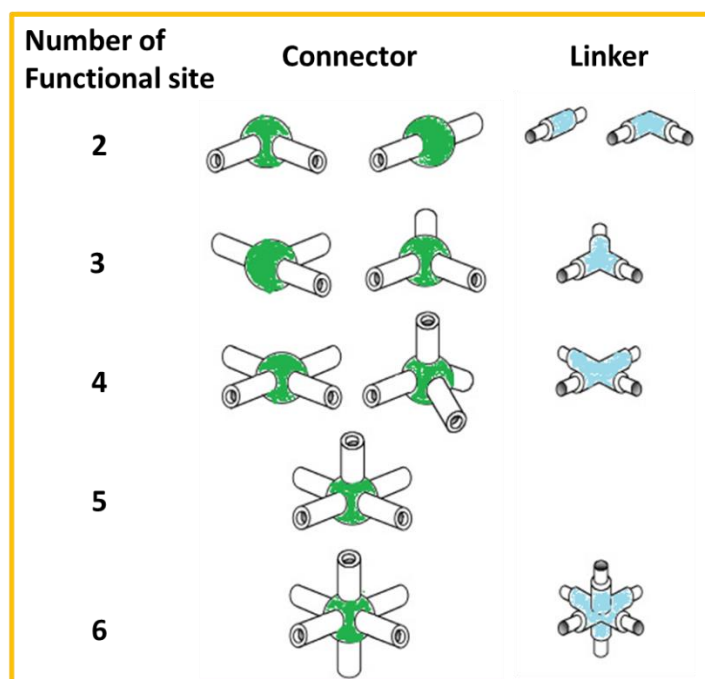
Figure 1.2 Components of coordination polymers (metal centres).[12]

In early 1890s, Alfred Warner first used the word "coordination compound" and he awarded the Noble Prize in 1913 to explore the field of the coordination chemistry. Research area in this topic has grown gradually and the structure-property relationship was noted. J. C. Bailar first introduced the word "coordination polymer" in 1964 and developed the structural concept, diversity and comparative discussion of organic polymer with the inorganic polymer.[7] Based on this concept, he established a guideline for the formation of building block, structural unit and essential property for the construction of new species containing the metal node and

ligands. Organic linker and metal ion as knot have designed the structural diversity of the CPs those have explored outstanding application in the field of sensing, gas storage, biology, magnetism, conductivity, energy storage and conversion, environmental monitoring etc.[5,8-11]

Coordination geometry, around the metal centre has diversity and it could be the linear, planar, tetrahedral, trigonal bipyramidal, octahedral etc. The interesting fact about the metal-organic polymers are organised in the infinite number of possibilities using the metallic system (centre or knot) and organic ligand as a linker. Most popular bridging ligand (linker) is carboxylate moiety. Because of versatile binding mode of the poly-carboxylates with the metal ions/clusters along with bridging capacity make thermally and chemical stabile materials those are finding wide application.

The synthetic routes of the coordination polymers are valuable for their fine structure, chemical, physical, magnetic, electronic and optical propertis in an organized way by the choice of metallic system and ligands. New realm of research in the material chemistry arises due to the design and synthesis of the desirable coordination polymers. Porous coordination polymers (PCPs) have been designed and synthesized by Prof. Yaghi and his group members using the polycarboxylic acid for the diversity of CPs and have applied in gas storage.[13,14] They also proposed the "reticular chemistry"[15] for the careful synthesis of the framework. Prof. Kitagawa et al. has established a method of synthesis of flexible, porous CPs with different functionalized groups using robust and flexible molecular framework.[16]

The stability of the CPs is increased if the auxiliary ligand is added in the carboxylate polymer. For the synthesis of multidimensional coordination polymer, mostly used functional groups carboxylate and pyridine moiety. To fabricate the pillar like coordination polymer, nitrogen donor pyridyl ligand has been used.

In 1998, Kitagawa et al. classified the PCPs (**Figure 1.3**).[16] According to the classification, first generation material framework is collapsed irreversibly during the exclusion of the guest molecule. The second-generation material is stable, robust framework and after exclusion of guest molecules they attained the stable framework. These are used for the studies on the adsorbent materials (like zeolites). Third generation materials exhibit the flexibility and pores are dynamic in nature. In presence of external stimuli, they give reversible response and induce excellent deliverable properties.
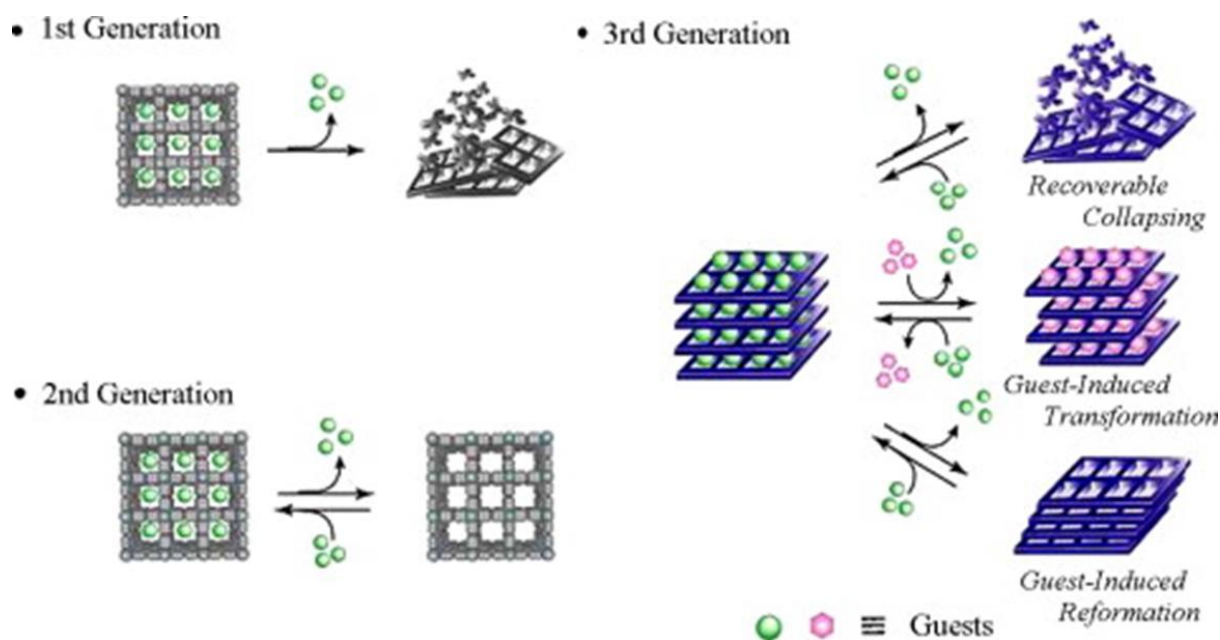
Figure 1.3 Classifications of PCPs by Kitagawa et al

The flexible structure of third generation PCPs materials exhibits many exclusive properties. On the basis of structural transformation ability, PCPs materials are classifying mainly two types (i) rigid or robust and (ii) flexible. In presence of the external stimuli like, heat, guest molecule, magnetic field, electric field, light irradiation the robust PCPs are not stable and they do not show structural transformation whereas flexible PCPs exhibit the structural conversion in presence of external stimuli. The formation of such flexible materials and their application in the various field is helpful to explore the research extensively.

1.2 Crystal Engineering

For the last three decades the field of coordination polymer is expanding exponentially to design, synthesize, characterization and exploration of different fields of application. The single crystal X-ray diffraction (SXRD) structure analyses have explored the crystal engineering that has discussed growth through the self-assembly via supramolecular interaction. Dr. Schmidt was used the word crystal engineering in 1971 and synthesized dimerization product of cinnamic acid[18] in sloid state in presence of light. According to Prof. G. R. Desiraju, the definition of the crystal engineering is "*the understanding of intermolecular interactions in the context of crystal packing and the utilization of suchunderstanding in the design of new solids with desired physical and chemical properties.*"[19] This field is developed

and broadened tremendously and interlinked the crystal field with the chemistry.[20] Crystallography is related with the crystal, extended crystal and assemblies form of crystal whereas chemistry is related to the molecules.

Initially, this field is only in the organic based system. The last three decades this field has witnessed tremendous expansion and exploration of metal-organic framework and organic-inorganic hybrid materials with different interesting structural architecture, topology and unthinkable arena of application towards the achievement of SDG.

The information of the crystal engineering field is more important towards the area of materials science, biology and pharmaceutical science.[21] In the presence of different noncovalent interactions and self-assembly the union of molecules and ions form solid materials. This is the center of the crystal engineering. The weak interaction forces like H-bonding, X-H--π, π---π interaction etc those are associated with the organic chemistry crystal engineering make Covalent Organic Framework (COF) and in coordination with metal ions/metal clusters prepare the Metal-Organic Framework (MOF) or Metal-Organic Coordination Network (MOCN). Investigation of halogen-halogen, S---S interaction are important part in MOF or Organic-Inorganic hybrids to assemble the molecular unit supramolecularly. Design and synthesis of the 3D structure is an indefinite aim but recently developed this area and synthesized some functional 3D network.[19,22]

Crystal engineering is a growing research field and published international journals with a very good impact factor. These include the *Inorganic Chemistry*, *ACS Applied Materials & Interfaces*, *Crystal Growth Design* from the American Chemical Society; *Journal of Materials Chemistry*, *New Journal of Chemistry*, *CrystEngChem* from the Royal Society of Chemistry; *Journal of Molecular Structure*, *Polyhedron*, *Inorg. Chim. Acta*. etc, from Elsevier; *Crystals* of MDPI (Multidisciplinary Digital Publishing Institute) and IUCrJ publishes on the crystal engineering, *Acta Crystallographica Section D*, *Journal of Applied Crystallography* and an open access *Journal International Union of Crystallography*.

1.3 Supramolecular Chemistry

Latin word 'Supra' means beyond and above, that indicates the chemistry beyond the molecules. Previously, this term was used for the understanding of interaction between different macromolecules, membrane system and arrangements of enzyme. However, Jean-Marie Lehn first applied the concept in the modern science in 1978 and defined as '*chemistry of the intermolecular bond, covering the structure and functions of the entities formed by the association of two or more chemical species'.*[23] Donald J. Cram, Jean-Marie Lehn and Charles J. Pedersen explored the importence of the supramolecular chemistry and awarded the Nobel Prize in 1987 for their work in this area.[24]

This chemistry discussed in the Supramolecular Chemistry that is beyond the chemistry of simple discrete molecules and their importance towards the assembled of chemical system through distinct number of components and subunits.[23] However, conventional molecular chemistry commonly inflections on the covalent bond whereas far weaker and noncovalent interaction[25] ($\pi\ldots\pi$ interactions, H-bonding, metal coordination and van der Waals forces etc.) was explored in the supramolecular chemistry.

The supramolecular chemistry explores multidisciplinary topic which have discussed the different other discipline, such as area of physical, organic and inorganic chemistry, synthetic strategy of precursor, to recognize the properties of supramolecular units and composite behavior of the system even by the computational modeling. Molecular self-assembly, host-guest chemistry, molecular recognition and mechanically-interlocked molecular constructions such type of important concepts are core in the supramolecular chemistry.[26]

1.3.1 Molecular self-assembly

 It is the very important term in the supramolecular chemistry. Relatively, small molecule was aggregated spontaneously and formed the large, stable and structurally well-defined material under equilibrium condition. The driving force operates in the molecular assembly is generally noncovalent.[27] Careful designed of molecular building blocks that can occur naturally through the stepwise interaction and lead to form assemblies which is most important feature of the molecular self-assembly. Stable structural framework is formed through ionic bonds, C–H⋯π, π⋯π and H-bonding interactions. Even this type of interaction is relatively weak but the collectively these interactions form the high stability of supramolecular assemble body. Self-assembly is mainly two types: intramolecular and intermolecular self-assembly. Formation of

the supramolecules was included in the intermolecular self-assembly whereas intramolecular self-assemble was responsible for the construction of the macromolecules like membranes, micelles, liquid crystals, vesicles and this topic has more important in the crystal engineering field.[28]

1.3.2 Molecular recognition

A well discussed terminology in the supramolecular chemistry is molecular recognition. This topic has discussed about the specific binding through the different noncovalent interaction between the two or more molecules. Here, noncovalent interaction is $\pi\cdots\pi$ interactions, hydrogen bonding, halogen$\cdots$halogen interactions, metal coordination and van der Waals interaction etc.[29] This type of force can be electrostatic or electromagnetic[30] in nature. Additionally, molecular recognition in the solution,[31] solvent plays the important role. Noncovalent interaction is helpful in the identifying of different types of molecules. The area is applicable in molecular sensor and catalysis[32]. Organic and organic-inorganic type[33] functional materials were designed and synthesized following the route of molecular recognition along with the self-assembly of molecular building blocks.

1.3.3 Host-guest chemistry

In the supramolecular chemistry, most significant branch is the host-guest chemistry. Herein, host molecules form a chemical compound with the interaction with the guest molecule or ions. Weak type of chemical forces present in this chemistry and this force is the weaker than the covalent interaction. Self-assembly and molecular recognition type noncovalent interaction are included in the host-guest chemistry. As a definition of the host and guest which compound is included in the guest and which one is host - it is arbitrary. According to Donald Cram, "*The host component is defined as an organic molecule or ion whose binding sites converge in the complex… The guest component is any molecule or ion whose binding sites diverge in the complex*".[34]

During the host-guest interaction, host molecule occupied the appropriate binding site for the binding of guest molecule. For an example, if the guest molecules possess the greater number of hydrogen bond acceptor site (like carboxylates) then host molecule hold the same number of hydrogen bond donating site (like secondary, primary amine). To get the maximum stability they are oriented in such a manner where the greater number of interactions is present in between the host and guest molecules. Lewis acid base interaction is included in the host-guest

interaction where host acts as a Lewis acid center and gust possess the Lewis base center. After discovery of the crown ethers[35,36] in 1967, host-guest chemistry field was improved more sharply.
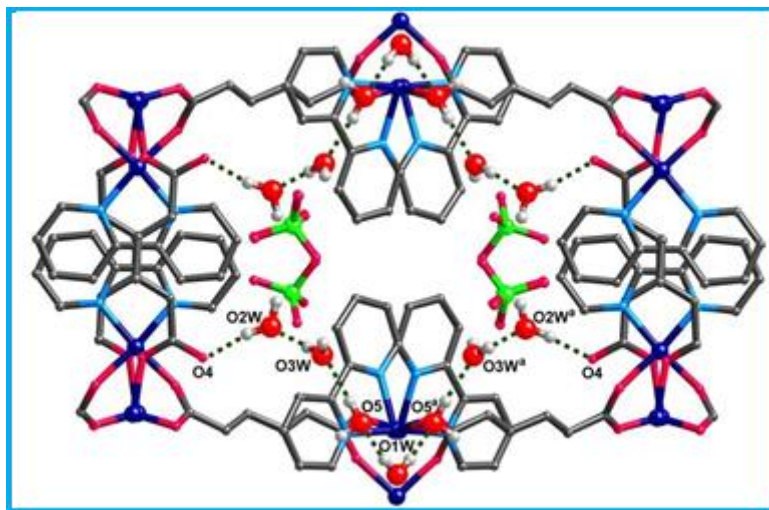
Figure 1.4 Host-Guest Interactions with the water helicate inside the channel of the coordination polymer $[Cu_3(bpy)_3(muco)_2(H_2O)_2](ClO_4)_2 \cdot 5.5H_2O$.[37]

To find the relationship between the supramolecular chemistry and coordination chemistry, we have to go back in 1960,[35,36] at that time broad research area on macrocyclic and macro-polycyclic and their association with the different metals in solution is linked between the supramolecular chemistry and coordination chemistry.

Initially progress of the supramolecular chemistry was very slow but it is exposed in 1990 to onwards. In the present time major journals come from the metal-ligands coordination entities (**Figure 1.4**) and this chemistry is included in the supramolecular chemistry.

1.4 Supramolecular interactions

Important part of the chemistry is supramolecular interaction or intermolecular interaction. Supramolecular interactions are responsible for the periodic arrangement of molecular crystal. This interaction is also responsible for the stability of chemical and biological macromolecules, organic molecules and different structural motif of coordination polymers.[38a,38b] It is also evaluated the orientation of the molecular species in crystal lattice. From the crystal engineering view this is the most important part and corresponding force is called the noncovalent interaction.

More disperse electromagnetic force of attraction is related with the noncovalent interaction but electron pair sharing is not involving in this interaction. The role of the noncovalent interaction in the synthesized molecular crystal structure and 3D structure in the large molecule is very important. The chemistry of the noncovalent interaction is the dynamic research area with valuable application in the field of chemistry, physics, biology and engineering field.[39]

The weak interactions have some common properties which are important in the crystal engineering field.

(i) The strength of the acting force is weak, moderate and strong. The attractive force for an interaction has the fixed energy value and the corresponding value is ~0.6 kcal mol^{-1}.

(ii) Direction of this interaction is important for the design and synthesis of desirable supramolecular crystal with valuable application.

(iii) The nucleation and crystallization process are dependent in the distance which is an important factor.

A strong noncovalent force is the classical H-bonding which is studied from the many years ago and used in the field of crystal engineering as an important tool.[38,40] Recently, non-classical H-bonding[41] is included in the weak noncovalent interaction. The $\pi\cdots\pi$, C-H$\cdots\pi$ and halogen$\cdots$halogen interactions (**Table 1.1**; **Figure 1.5**) are included in the formation and orientation of the 3D structure and this type of the interactions have been investigated.
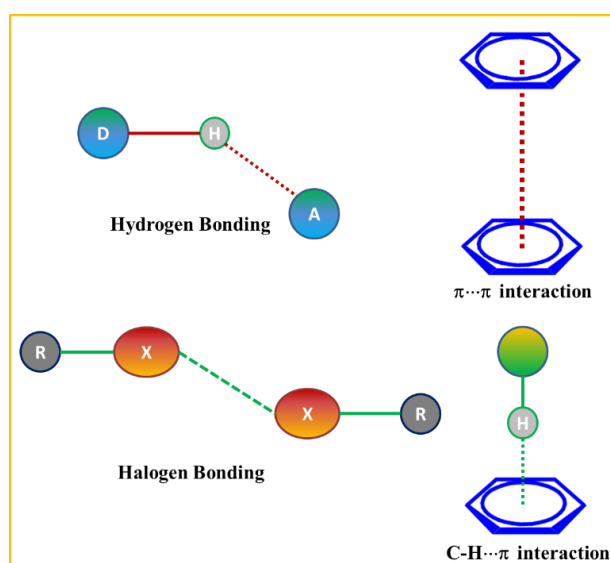
Figure 1.5 Various types of supramolecular interactions.

Table 1.1. Different types of supramolecular interactions

Types of interactions	Strength (kJ/mol)
Ion---Ion	100-350
Ion---dipole	50-200
Dipole---dipole	5-50
H-bonding	4-162
Halogen---Halogen Interaction	5-180
π---π	1-50
C–H---π Interactions	6-13
van der Waals	< 5.0

1.4.1 Hydrogen bonding

Hydrogen bond is weak natured electrostatic interaction. This bonding is weaker than the ionic or covalent bond but it is stronger than the van der Waals force. According to the definition, hydrogen bonding is the interaction between the pair of atoms where H atom situated in it.[42] This electropositive hydrogen is interacted with the electronegative N, O, F atoms when hydrogen atom bonded to this atom and it is binding with another atom through H-bonding within the same molecule or other molecule. It is not like that true bond; it is a weak interaction. This type of interaction plays a vital role in the field of crystal engineering and increases the stability of molecular arrangement in the crystal structure.

The classical hydrogen bonding may describe as X–H···Y–Z. H-bonding is denoted by the three dotted line. Here, Y is bonded with the Z and acceptor is Y atom or anions, or may be the molecular part of Y-Z. In the many cases X and Y are same and distance of X-H is same with the Y-H and forms symmetric hydrogen bonds. Here, acceptor is electron rich atoms and may be the lone pair of Y atom or electron pair of π-bond in the Y-Z.

According to definition, H-bonding is (a) weak electrostatic nature, (b) electronegativity of the X atom is greater than the electronegativity of H, and (c) the bond formation has been evidenced by spectroscopy; and has been supported energetically, functionally and geometrically. It is not a simple type interaction, it has cooperative effect in the component interaction, polarization, electrostatic and van der Waals interaction with small amount of

covalency. Contribution of this interaction to the H-bonding is discussed in the broad range.[43] In this type, the hydrogen bonds (X–H⋯Y– Z) have some important criteria which are discussed in the *Pure Appl. Chem.*[42] by E. Arunan et al.

(i)   H-bonding involves electrostatic force, dispersion or charge transfer.

(ii)   If the electronegativity of the X atom increases, bond strength is increased.

(iii)   For the greater stability X–H⋯Y angel should be 180º or nearly 180 º.

(iv)   During H-bond formation the X-H length is increased as a result red shift of the IR stretching frequency occurs.

(v)   In the ^{1}H NMR spectrum H goes to the more deshielding zone that indicates the formation of the H-bonding.

(vi)   Gibbs energy corresponding to the formation of H-bonding is greater than the thermal energy of system.

From the energy calculation it is revealed that the H-bond exhibits the low energy range (1-2 kJ/mol) to high energy range (161.5 kJ/mol in the ion HF_2^{2-})[44,45]. Here, all type of H-bonding discussed but more focused to the O-H⋯O bonds.[46]

Hydrogen bonding is the electrostatic interaction that is first established by the Pauling in 1939 and he assumed the X and Y are two electronegative atoms like N, O and F. Under certain condition H atom is attracted by the other ion or same ion and formed hydrogen bonds.[47] It is exhibit that the electrostatic interaction is predominate in the N–H⋯O, O–H⋯O, and O–H⋯F types of H-bonds. C–H⋯O, C–H⋯N, C–H⋯π this type of weak force is excluded from the H-bonding interaction. From the recent definition this type weak interaction is included in the subject of evidence of *bond formation*. Hirshfeld surface analysis is a useful tool for visualizing weak interactions like H-bonding interactions in molecular crystals. When donor and acceptor centres are very powerful and they form strong hydrogen bond (energy range 80-160 kJ/mol), in this situation the covalent character[48,49] of H-bond is included. Weak van der Waals force is included when the weak hydrogen bond is formed.

Types of hydrogen bonding

Various types[39a] of H-bonding are present in the compound which is based on the geometry of the H-bonds. Generally, simple type is the D–H⋯A and angel is ~180° and is shown in the **Figure 1.6**. Here, donor denoted by the D and acceptor is A. H-bonding shows the liner interaction and it is very rarely observed in the crystal structure. Bent structure type b was

observed with angel ~165°. In type c of the hydrogen bonds one H atom is bonded with the two acceptor atoms. This H-bonding is called the bifurcated H-bonding and formed a center with three atoms. Trifurcated H-bonding is observed in the hydrogen bonding type e. Here one hydrogen atom is interacted with the three acceptor atoms. In the organic crystal multifurcated hydrogen bonds is also observed. In the carbohydrate molecules hydrogen bonding is multifurcated and this is over 25% and this value is higher for the amino acids.[46a]
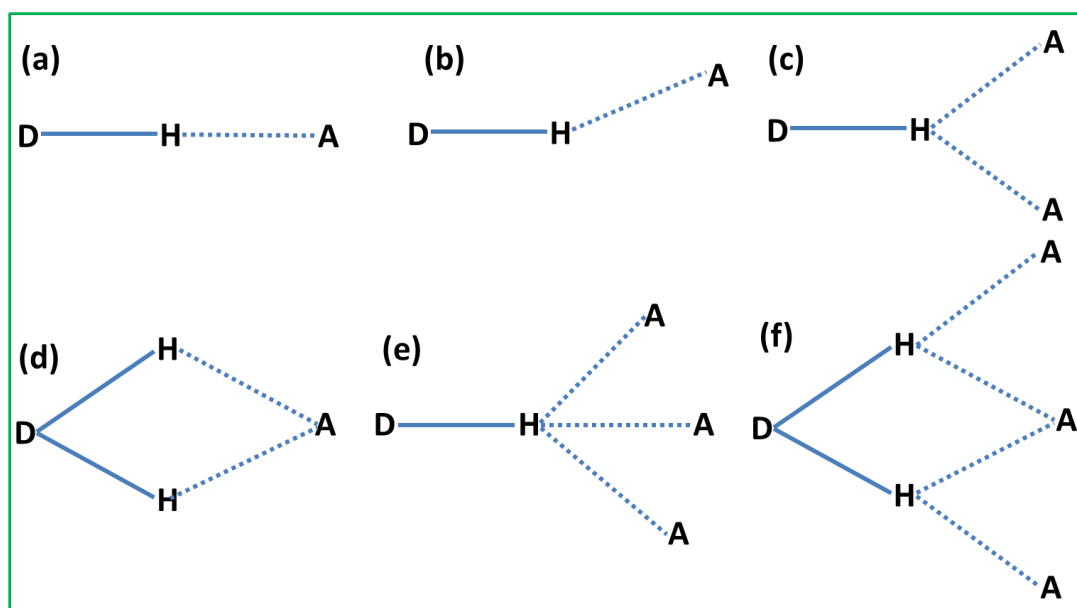
Figure 1.6 Different types of hydrogen bonding geometries: (a) Linear; (b) Bent; (c) Donating bifurcated; (d) Accepting bifurcated; (e) Accepting Trifurcated; (f) Three-centred bifurcated.[39a]

Graph sets

The connectivity of the H-bonded array and recognition of the morphology are the reasons for the graph set. For a particular pattern, the H-bonds have assigned the specific graph set. On the basis of the donor and acceptor nature of the H-bonding, distinguish the different types of hydrogen bonds are distinguished. Margaret Etter,[50] was proposed the nomenclature of the different pattern of this type of the hydrogen bonds. In simplest way, one type of hydrogen bond is repeated to generate the complex system; more than one type of of H-bonds repeat to generate complex form of structures. For the intermolecular hydrogen bonding, designators are ring (R), chain (C) and dimer or finite set (D). Intramolecular hydrogen bonding is denoted by the 'S'. Motif subscript (d) and superscript (a) are denoted the number of donors and acceptors, respectively. Total number of atoms was present in the motif is indicated in parentheses. Herein, benzoic acid dimer is a motif with graphic set $R_2^2(6)$ (**Figure 1.7**).
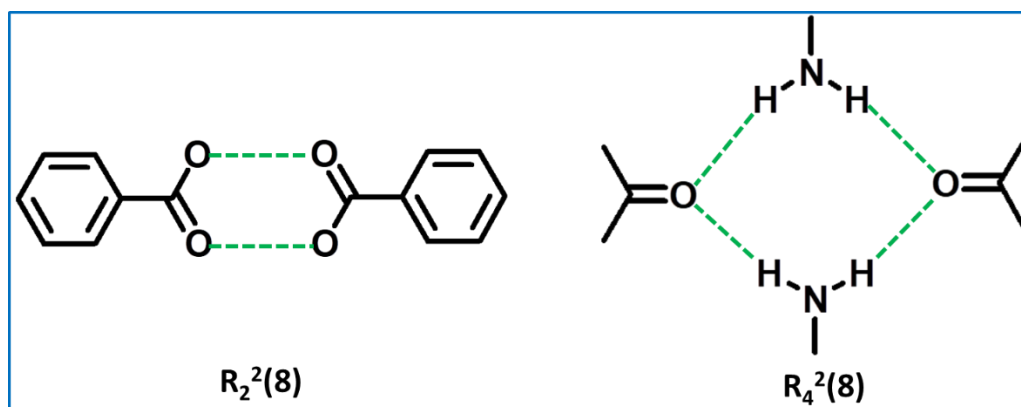
Figure 1.7 Graph set nomenclature of hydrogen bonding (Hs are omitted for clarity).

1.4.2 Halogen⋯Halogen Interaction

Halogen⋯Halogen interaction is the weak interaction involved amongst the halogen atoms. This type of weak noncovalent interaction was used by Desiraju and his groups for the design of crystal engineering of the organic crystals.[51] Interhalogen distance (r_i) should be less than the sum of van der Waals radii (r_{vdw}) of halogen atoms then halogen⋯halogen (R^1–X_1⋯X_2–R^1) interaction is considerable (**Figure 1.8**). Recently, the nature of this interaction is explained by the polarization effect but it is unknown in the past. When carbon atom is covalently bonded to the halogen atom then a positively polarized region is formed in the shortest distance of the halogen atom which is along the C-X axis and equatorial region is negative charge and maintain the overall charge is zero of the atom. In this aspect, negative polarize end is interacted with the positive polarize end of another same or different halogen atom. In the presence of this halogen⋯halogen interaction molecules (**Figure 1.9**) are aggregated supramolcularly and form the 3D network.
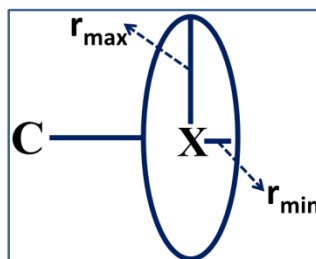
Figure 1.8 Polar flattening effect.[52]
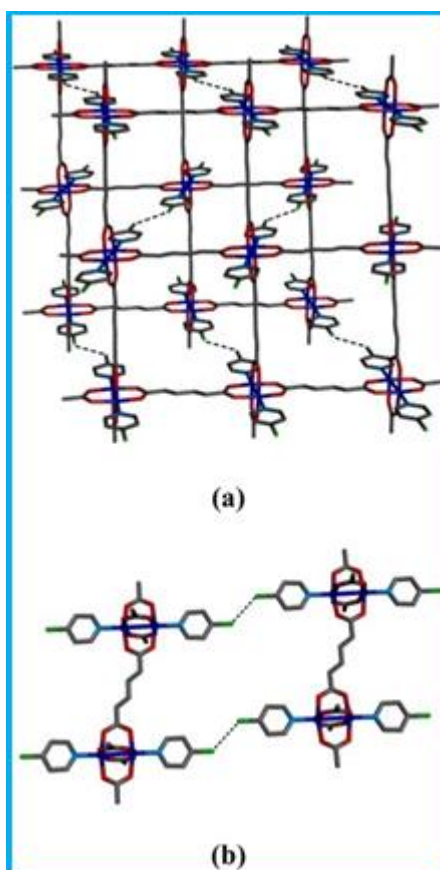
Figure 1.9 (a) View of 3D supramolecular aggregate by Cl⋯Cl interactions and (b) View of Cl⋯Cl interactions.[53]

1.4.3 π⋯π Interaction

This type of noncovalent interaction was observed in the aromatic 'π' system and this is similar to the H-bonding. In the self-assembly[54] to molecular recognition process, π⋯π stacking and arene⋯arene interaction plays the important role and it is very crucial in biology[55,56] as well as in chemical system. For the last three decades, research progress is in a great volume and is oriented in the π⋯π interaction in aromatic ring to find out the physical and geometrical convenience in the π-involving stabilizing system.[57] π⋯π interaction is an important factor for the molecular self-assembly and with the help of this interaction design the desired crystal structure is designated and has been used in the field of crystal engineering. Average energy calculated for this interaction is 1.5-2.0 kJ/ mol.[58] Prof. Christoph Janiak et al. discussed this area in the various aspect of its interaction in their article.[59] If the two arene moieties are parallel with inter-planer distance 3.3-3.8 Å, then they attain supramolecular assemble through π⋯π stacking.

There are two types of π···π stacking: (i) Face-to-face and (ii) edge-to-face present in aromatic ring. Edge-to-face arrangement has created the T-shaped through C-H···π interaction. Face-to-face arrangement is not perfect rather a displaced or offset arrangement and this phenomenon is observed in the major cases.

To understand the nature of π···π stacking performed various type of theoretical as well as experimental study have been conducted and have concluded the importance of the nature of this interaction. Hunter and Sanders[56] proposed the model to discuss the π···π interaction (**Figure 1.10**).

Hunter-Sanders suggested a rule for the non-polarize π-system to understand the π···π interaction.[56c] These are as follows:

• **Rule 1:** In the face-to-face π-stacked geometry, the π–π repulsion predominates.

• **Rule 2:** T-shaped geometry or in an edge dominates π–σ attraction.

• **Rule 3:** In the offset π-stacked geometry, the π–σ attraction predominates.

• **Rule 4:** Charge–charge interaction dominates due to the interaction between highly charged atoms.

• **Rule 5:** For pronounced face-to-face interaction of neutral or weakly polarized site, it needs a π polarization in the aromatic ring (π-deficient atom).

• **Rule 6:** The face-to-face interaction of neutral or weakly polarized site needs a σ polarization in the aromatic ring (positively charged atom).
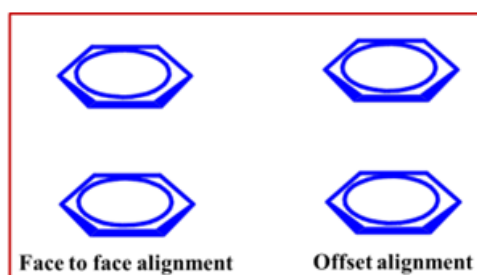
Figure 1.10 Principal orientations of π···π stacking interactions.

Houk and Wheeler provided the computational evidence of the $\pi\cdots\pi$ stacking.[60] As a result, it may be evaluated the dispersion, electrostatic interaction and direct interaction by $\pi\cdots\pi$ stacking. Weak nature of $\pi\cdots\pi$ stacking plays a very important role in molecular packing, self-assembling, folding[61] and thermal stability of proteins.[62] It can play important role to design and synthesis of metal-organic framework or metal-ligand coordination polymers just like hydrogen bonding.

1.4.4 C–H$\cdots\pi$ Interaction

This is one type of weaker non-classical H-bonding interaction.[41] Herein, soft acidic C-H interacted with the soft or borderline basic π- system. This interaction plays an important role for crystal packing,[63] self-assembly[64] and molecular recognition.[65] In supramolecular system this type of interaction was first shown by Andreetti and his co-workers and that was discovered on the crystallographic data in the various calix[4]arene with toluene system.[66] The conventional hydrogen bonds have attractive nature and it is strong directional whereas the C–H$\cdots\pi$ interaction (**Figure 1.11**) is weaker and originated from the charge transfer from the π to σ^* or may be due to delocalization of electron and dispersion. Herein, direction is not important in this force. This interaction is nonpolar and is also observed in the aqueous medium that has indicated the important role in the biological system[67]. The average energy value is 6-13 kJ mol^{-1} for this typical C–H$\cdots\pi$ interaction.
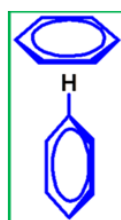
Figure 1.11 Orientation in case of C-H$\cdots\pi$ interactions.

Atom in molecules (AIM) studies[68] was helped to evaluate the nature of H-bonding interaction and this study is comparative with the MOs of intermolecular system.[69] Electrostatic energy[70] follows the order sp^3-CH$\cdots\pi$ < sp^2-CH$\cdots\pi$ < sp-CH$\cdots\pi$. This type of interaction for the aromatic C-Hs is more efficient than the aliphatic ones. C–H$\cdots\pi$ interaction (**Figure 1.11**) forms a T-shaped dimer of benzene ring. Main origin of this interaction is dispersion force. The electron donating ability of the π donor moiety plays vital role. Toluene has more π donating (C-H acceptor) ability than the benzene and toluene forms the stronger CH$\cdots\pi$ bonds.

An inclusive review in the C–H⋯π interaction field is presented by Prof. Motohiro Nishio[72] and gives more information about it. Novel single-chain magnets (SCMs)[73] is designed with the help of theoretical study of C–H⋯π interaction between the monomeric units. This interaction is very significant in the field of crystal engineering but it is less explored. For the design and synthesis of the coordination polymer in the presence of this type of weak interaction has needed the strong motivation and toolkit in the construction of supramolecular layer structure.

1.5 Electrical Conductivity Related Terms

Diode is an electronic device which flow the current in one direction and it consists of two terminal electronic components. There is low resistance in one side but other side has higher resistance which opposes the current flow. A Schottky diode is known as hot carrier semiconducting diode. In the combination of a metal and semiconductor generally form a Schottky diode which is created the barrier. Here, metal acts as anode and semiconductor acts as cathode in the n-type diode.

1.5.1   Schottky Barrier

The energy difference between the fermi energy level of metal and conduction (or valence) band of semiconductor edge is known as Schottky barrier. Rectifying property is belonging to the Schottky diode and the barrier develops due to the difference of work function between the semiconductor and metal. In case of n-type, electron flows from the semiconductor to metal due to surpasses of work function of metal (ϕ_m) into the work function of semiconductor (ϕ_s) and attains equilibrium with the fermi level and forms a depletion region. This charge transfer process attains the thermal equilibrium.

Diffusion potential (V_{do}) is writing as

$$V_{do} = \phi_m - \phi_s \qquad\qquad (1)$$

If the value of $\phi_m > \phi_s$, then V_{do} is positive, for the n-type semiconductor the band is rising upward and electron transfer from the semiconductor to the metal occurs (**Figure 1.12a**). In this process, electron overcomes the barrier and transfer into metal. It occurs mainly due to the rectifying property. For the p-type semiconductor no obstruction of the hole motion is observed due to the band-bending. In the 'ohmic' contact rectification does not occur   (**Figure 1.12b**).

The band is going to the downward direction if the $\phi_m < \phi_s$. The rectifying contact is formed for the p-type (**Figure 1.12c**) and ohmic contact is formed for the n-type in shown in **Figure 1.12d**.
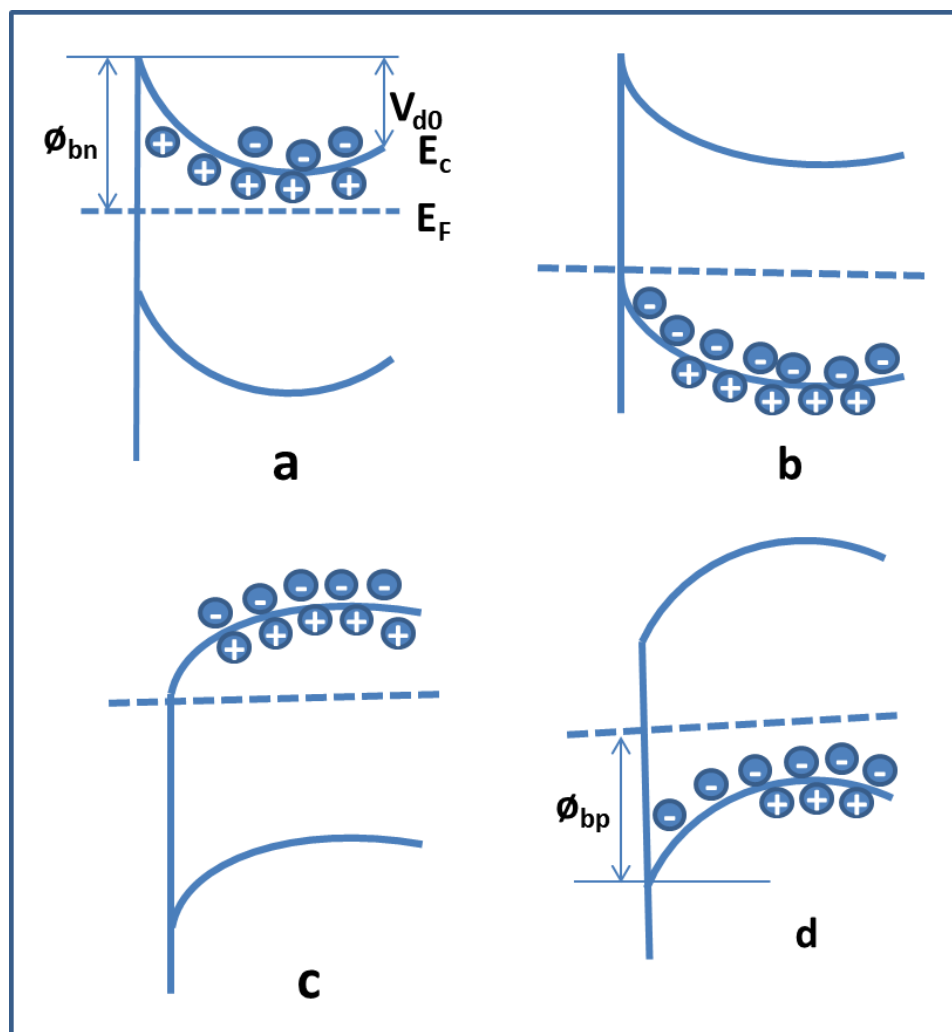
Figure 1.12 Schottky barriers for semiconductors of different types and work function. The n-type semiconductor: (a) the electron transfers from the semiconductor to the metal, (b) electron transfers from the metal to the semiconductor, ohmic contact (c) the p-type ohmic contact, (d) the n-type ohmic contact.

Advantages of Schottky Diode

Low turn on voltage: Turn on voltage in between the 0.2 to 0.45 volts is good for Schottky diode.

Fast recovery time: A small amount of stored charge is used for the high speed switching application due to the fast recovery time.

Low junction capacitance: Capacitance level is very low if the contact area is very small.

Applications

Schottky diode is used in the application of radio frequency and radio detector due to their low capacitance, high switching speed and high frequency capability. Most powerful application appears in the rectifiers. Because of low forward voltage drop and high current density. So, low power was used in the Schottky diode than the general p-n junction. Schottky barrier acts as circuits in the two power supplies.

Solar cell applications: In the solar cell low voltage drop Schottky diode is used, because voltage drop in the scholar cell is not expected. Ability of the solar cell is reduced due to this voltage drops.

Clamp diode: Actually, clamp diode is a Schottky diode and it is used in the transistor circuit to controlling the speed of the process during the switching process.

1.5.2 Diode Parameters

Ideality Factor: Ideal behavior of the Schottky diode is measured by ideality factor. Current in the low voltage region is measured by this factor and it is directly proportional to the d*V*/dln*I*.

Series Resistance: Total amount of resistance value in a series of Schottky diode is known as series resistance and current flows through the all resistors.

Barrier Height: One of the most important parameter is Schottky barrier height (SBH) in metal semiconductor (MS) interface. Schottky barrier height is signifying the rectifying barrier of electrical conduction through the MS. For the metal/n-type semiconductor, Schottky barrier height is the difference between the metal fermi level and conduction band minimum of the semiconductor. The Schottky barrier height is the difference between the metal fermi level and valance band maximum of the semiconductor in case of p-type.

1.5.3 Charge transport parameter

Mobility: Mobility is defined as the how fast carriers transfer charge through the metal or semiconductor. Mobility of the semiconductor depends on the electron, hole concentration, impurity concentration (like, donor and acceptor concentration), electric field and temperature.

Transit time: Time required for a carrier to travel from the cathode to anode or vice versa is called the transit time. This time related to the total time of free carries as well as time required for the trapped carrier in the traps.

Diffusion Length: The current flow through the metal semiconductor junction is dependent on the majority carriers. Among the exciting mechanism, diffusion of the carriers from the semiconductor to metal is an important mechanism. According to the diffusion theory, diffusion length is a length of depletion layer where driving force is distributed.

1.5.4 Photosensing Parameter

Responsivity: When unit power of photocurrent is generated in the effective area of the device is called the responsivity.

Specific Detectivity: Device performance, as detector is characterizing using the specific directivity and it is denoted the D^*. This is the reciprocal of the noise-equivalent power (NEP).

Photosensitivity: A fixed amount of energy is absorbed by the targeted materials/substance during the irradiation process is known as photosensitivity.

Photoconductivity Sensitivity: At a certain voltage conductivity is increased due to the irradiation on materials at a certain input power. This phenomenon is known as photoconductivity sensitivity.

1.6 Sensor Application

In the growth of civilization as well as the origin of life, its growth and reproduction of all living systems are regulated by the cations and anions. Metal ions are non-biodegradable and play an active role in the food chain, ecological system and causes very high level of pollution. Therefore, all the metals have the certain limit of safe zone. Maximum contaminate level of different metals in the various type of drinking water is examined by the different organizations like, Environmental Protection Agency (EPA), World Health Organisation (WHO) from all over the world. WHO and EPA are recommended the standard guideline for the heavy metals (**Table 1.2).** [74-78]

Table 1.2. Threshold limit of biologically important/toxic metals in human body

Metal	WHO ppm	EPA ppm	Metal	WHO ppm	EPA ppm	Metal	WHO ppm	EPA ppm
Mn	0.4	-	Pd	4×10^{-7}	-	Hg	0.001	0.002
Zn	3	5	As	0.010	0.010	Al	0.9	-
Cr	0.05	-	Fe	1.0	-	Cu	2	1.3
Ni	0.07	0.04	Pb	0.010	0.015	Cd	0.003	-

1.6.1 Advantages of Fluorescence Technique in Quantitative Analysis

Different analytical methods like volumetric, spectrophotometric, gravimetric and electrochemical techniques are used for quantitative analysis of ions and elements in the analytical field. Traditionally elemental analysis proceeds using the different technique like, voltammetry,[79] ICPMS (inductively coupled plasma mass spectrometry),[83] ICP-AES (inductively coupled plasma-atomic emission spectrometry),[81,82] AAS (flame or graphite furnace atomic absorption spectroscopy),[80] thin chitosan films,[85] flame atomic absorption spectroscopy (FAAS),[84] and several functionalized metal nanoparticles[86,87] etc. In addition to this, fluorescence and UV-Visible spectroscopy are used to recognize the important analytes environmentally as well as physically. Importance of this method is cell imaging of analyte in biological system and low level detection limit. Fluorescence technique is important for researcher in the biochemical and chemical field due to their sensitivity, selective detection, quick response, operational simplicity, cost-effectiveness, and high temporal resolution and easy to signal detection.

1.6.2 Chemical sensor

Sensor is a device that measures the physical quantity and transforms it to a signal and this signal is read by the instrument or observer. Mercury thermometer is an example of the sensor. Here, thermometer measures temperature by liquid expansion or contraction and that shows the reading in glass tube. A chemosensor is a combination of three units (signaling subunit, spacer and binding subunit) (**Figure 1.13**). Chemical receptor accepts the guest unit with a high selectivity and this binding mode is converted by the signaling subunit and measurable physical changes occur.

Different group of the receptors has been used in different types of approaches. Mainly, three types of approaches are used (i) Chemodosimeter, (ii) Binding site-signaling approach and (iii) Displacement approach[88,89] which differs in the method the last two are arranged with respect to each other. A specific ion-induced chemical reaction is occurring in the chemodosimeter as a result the optical signal appears. In the binding site-signaling approach, covalent bond[90] is the connector of the two parts. When analyte contacts to the binding site, it helps to change the electronic properties of signaling subunit and hence the sensing of the targeted analyte. Molecular assemble occurs between the binding site and signaling subunit in the displacement approaches.[91] Here, coordination of the binding site to the certain ion/s occurs then release signal subunit in the solution or optical properties changed.[92]
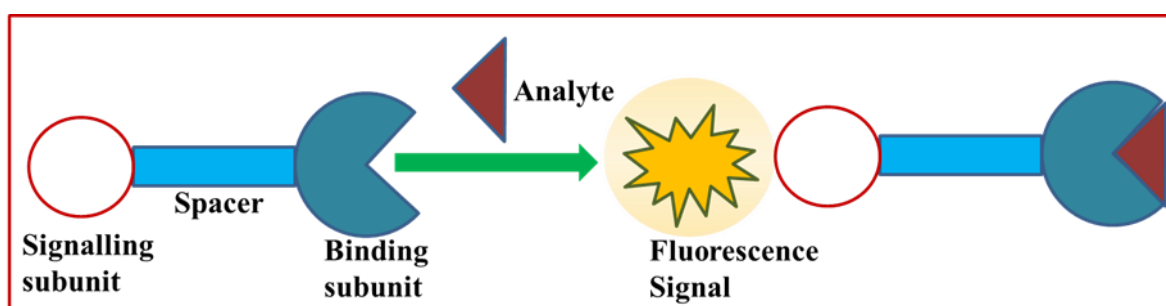
Figure 1.13 Schematic diagram of an analyte (guest) by a chemosensor (host).

1.6.3 Fluorescence sensing mechanism

Three basic requirements are receptor, transducer and signal processing unit for the ideal fluorescence sensing device; (i) receptor has strong binding affinity towards the target analytes and bind to the analytes selctively, (ii) environment interference is neglected by the fluorescence signal and (iii) under this experimental process sample should be stable. Generally, 'Turn on' and 'Turn off' type fluorescence is observed. 'Turn on' process is mainly three types : (a) wavelength shift, (b) normal turn on and (c) ratiometric turn on.

(i) Paramagnetic fluorescence quenching

Paramagnetic metal ions added to the fluorophore materials which assist forbidden inter-system crossing (ISC) very fast and it is defining as paramagnetic quenching. Upon excitation of the fluorophore goes to the S_1 state and presence of the paramagnetic metal ions moves from S_1 to T_1 through the ISC and subsequently deactivated by non-radiative process (**Figure 1.14**).[93]
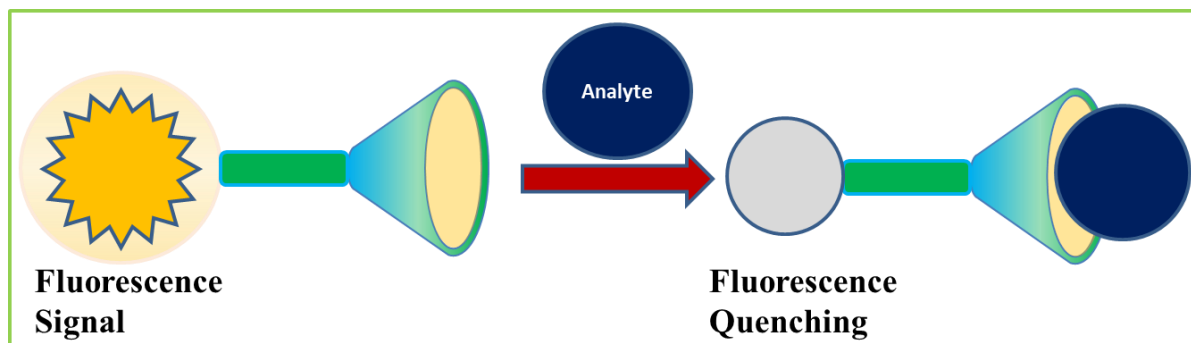
Figure 1.14 Schematic diagram shows binding of a paramagnetic ion (eg. Cu^{2+}) with fluorophore.

(ii) Photo-induced electron transfer (PET)

Electron donation from the donor centers of N, O, S and P to the HOMO of excited fluorophore generally happen the PET. The PET process is inhibited when the metal ions are
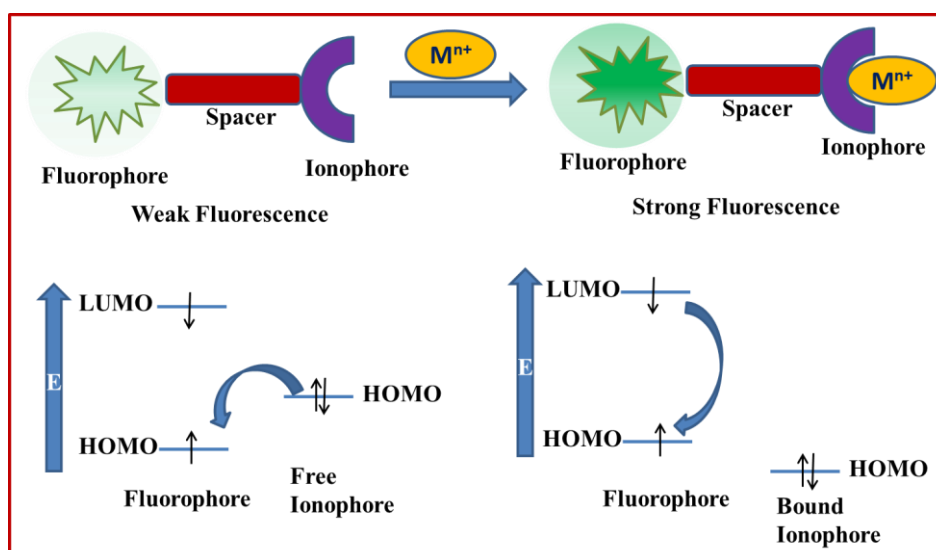
Figure 1.15 Schematic diagram for PET mechanisms.

interacted with the donor atoms and fluorescence turn on happens. In addition to this the PET process depends on the solvent polarity. Electron transfer is easier in the polar solvent. Fluorescence sensor occurs through the photo-induced electron transfer (PET) inhibition mechanism and addition of the metal ions inhibit PET and switch on emission (**Figure 1.15**).[94]

(iii) Intra and intermolecular charge transfer (ICT)

Intra and intermolecular charge transfer from the electron donor centre to the acceptor is increased in the presence of the light excitation and fluorophore is directly linked with acceptor without any spacer forming π-electron conjugated electron rich system and electron deficient terminals (**Figure 1.16**).[95]
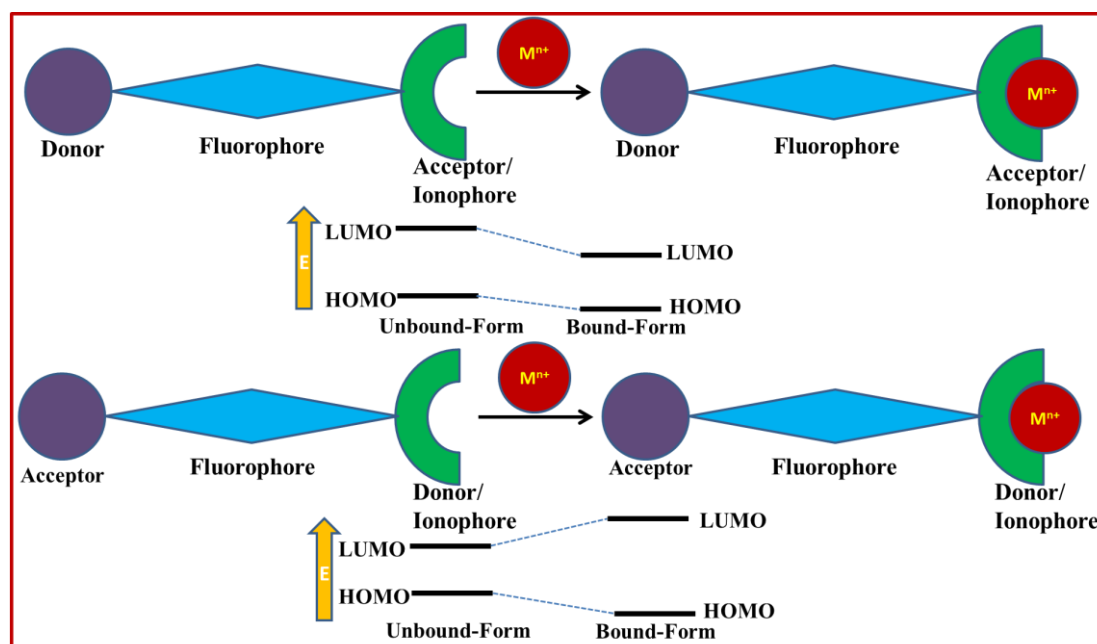
Figure 1.16 Schematic diagram of ICTmechanism.

(iv) Chelation enhanced fluorescence (CHEF) and Chelation enhanced quenching (CHEQ)

A metal ion binds with the receptor in a fluorescent probe, emission intensity is enhanced or quenched. Chelation enhanced fluorescence (CHEF) exhibits the red shift of emission band and blue shift was shown due to the chelation enhanced quenching (CHEQ). Forbidden intersystem crossing (ISC) was faster upon addition of the paramagnetic metal ions in the fluorophore and quenching process occurs. Upon excitation, the fluorophore moves from S_1 state and presence of the paramagnetic metal ions goes S_1 to T_1 through the ISC and subsequently deactivated by non-radiative process (**Figure 1.17**).[96]
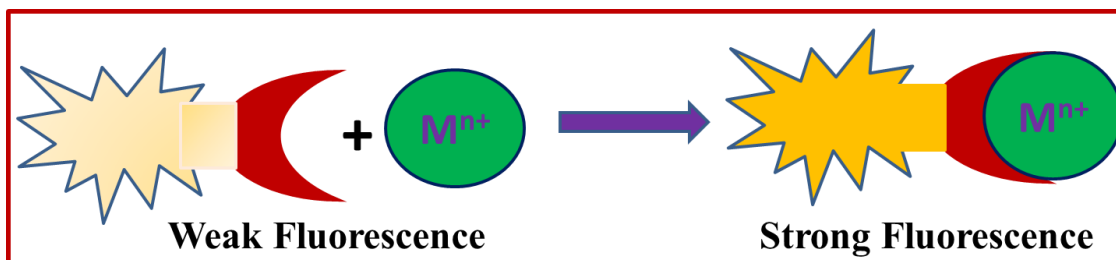
Figure 1.17 Schematic diagram of CHEF processes.

(v) Fluorescence resonance energy transfer (FRET)

Distance dependent FRET process is the interaction between the excited fluorophore with another fluorophore. In this process the excitation energy was transferred from the donor unit without any emission of the photon and the emission of another fluorophore is identified upon excitation of a fluorophore. For the FRET process some necessary condition was to required : (i) distance between the donor and acceptor unit is 10 to 100 Å, (ii) emission spectra of the donor and absorption spectra of the acceptor must overlap, (iii) transition dipole orientation of the donor and acceptor should be parallel (**Figure 1.18**).[97]
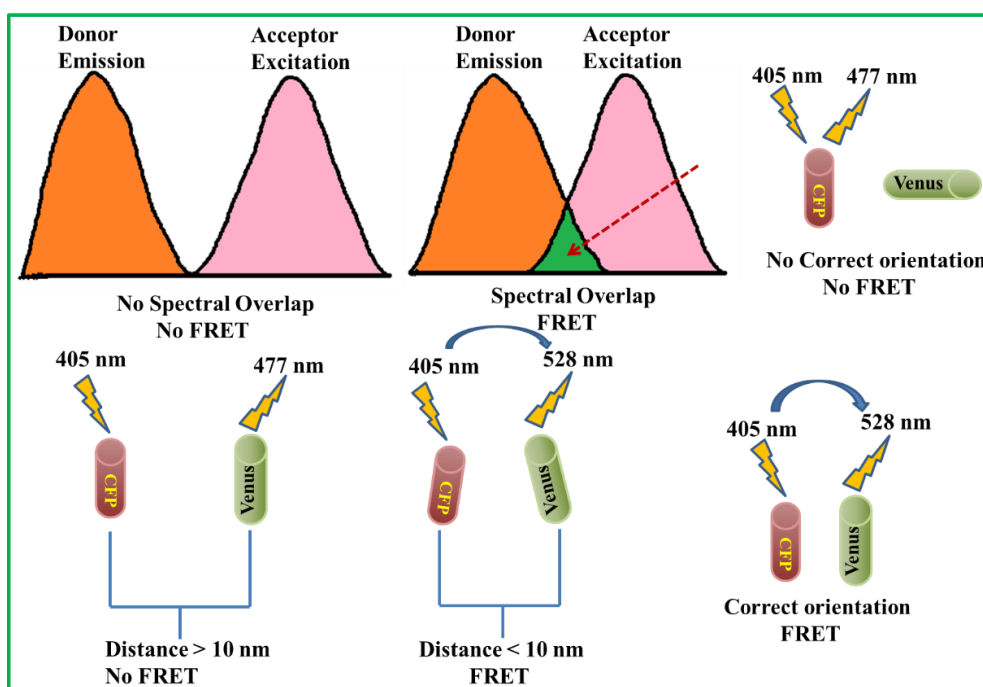
Figure 1.18 Schematic diagram of FRET processes.

(vi) Excited-state intramolecular proton transfer (ESIPT)

ESIPT process is the process where the excited molecules relax their energy through the proton transfer in the excited state. Hydroxyl/amino group acts as a proton donor and acceptor group is containing nitrogen or oxygen atoms who are engaged by the intramolecular H-bonding mainly. During ESIPT process the excited molecule has less probability of the photochemical reaction and increase the photo stability of the molecule with a large specious stokes shift (**Figure 1.19**).[98]
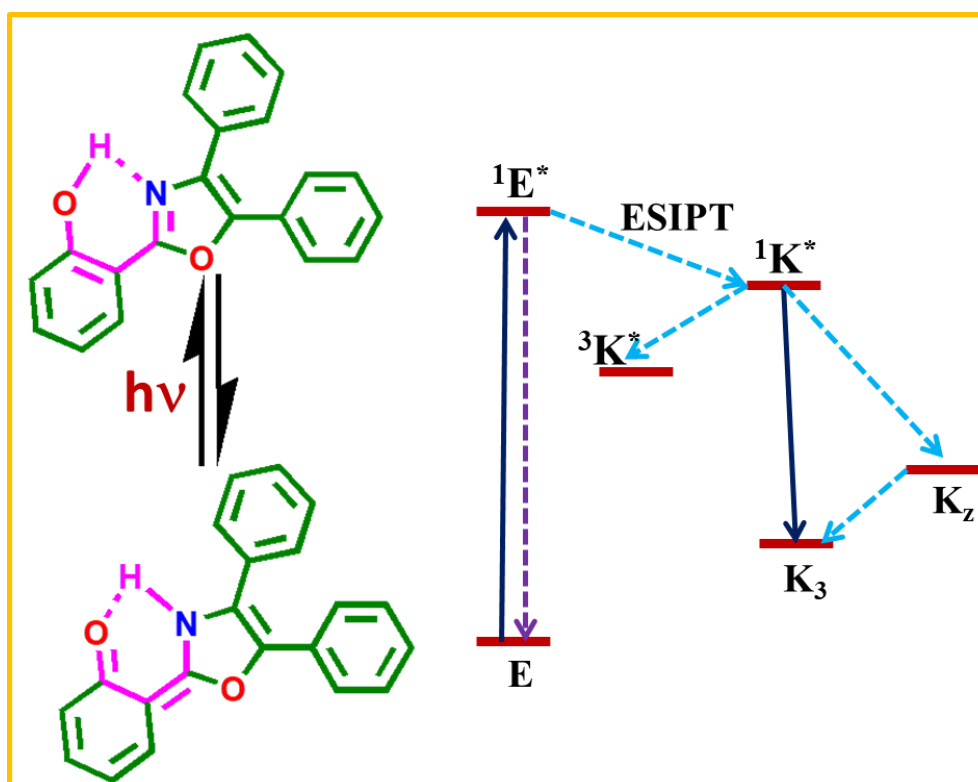
Figure 1.19 Schematic diagrams shows ESIPT processes.

1.6.4 Cation sensor

Out of 92 naturally occurring elements about 1/3 (27 elements) are involved in the origination, sustenance and death of living cells. Metal ions[99] are fundamental to life; some of the cations appear in bulk amount (Na, K, Mg, Ca) and some other present in trace amount (Cr, V, Mn, Co, Fe, Cu, Ni, Zn, Mo, Al, Si, Se, Sn). Any change in balance of concentration of the ions shows huge impact on the metabolic, electrical charge balance, neural signalling and muscular activities, osmotic pressure, photosynthesis, redox processes, DNA stability and activity, DNA transcription etc. Thus they are essential in right concentration for the maintenance of life.

Therefore, their quantitative measurement is of first truck information to the sustainability in the environment. Herein three such metal ions are discussed. These are Cu^{2+}, $Fe^{2+/3+}$ and Pd^{2+}. Selection of these three metal ions in this research is considered due to their much involvement in the environment and health issues but literature review shows these are relatively less handled from analytical perspective.

(i) Cu^{2+} sensor

Third most abundant element is copper and it is important in the biological system. It plays a vital role in the physiological and co-factor of numerous enzyme. Many researchers are developing various fluorescence probes who selectively detect the Cu^{2+} ion through the turn off/turn on sensing process. In 2020, Zhao-Feng Wu[100] et al. synthesized calcium based coordination polymer and selectively detect the Cu^{2+} with a detection limit 0.064 ppm. Another fluorescent probe to detect the Cu^{2+} is done by Komthep Silpcharu[101] et al in 2021. Here, spirobifluorene derivative was used to detect the Cu^{2+} with a limit of detection 98.2 nM. Maksim Royzen[102] et al. ware prepared dye compound to detect the Cu^{2+} selectively. Here, in presence Cu^{2+} exhibits the radiometric sensing and paramagnetic substance (Cu^{2+}) is detected by the chelation-enhanced fluorescence method. Prabhakaran Srinivasan[103] et al. characterized two fluorescent probes, BDICB (4-butyl-N-((1,3-dioxo-1H-benzo[de]isoquinolin-2(3H)-yl)carbamothioyl)benzamide) and BTHCB (4-butyl-N-(2-(thiophene-2-carbonyl)hydrazine-1-carbonothioyl)benzamide) and used them to detect Cu^{2+} in solid state with limit of detection 0.38 and 0.45 ppb.

(ii) Fe^{3+}/ Fe^{2+}sensor

Fe is the essential trace element which shows important role in the evolution of life. Iron is extensively used in the industry, housing, railways, bridges, construction of the road, medical equipment and the growth of the human civilization. Fe is main component of oxygen binding centre in the blood, redox centre in the cytochromes, ferritin and ferredoxins etc. In the presence of excess amount of the iron is causes the DNA damage, lipid peroxidation that is related to the tumour in liver and colon etc. Hence, Fe detection is most important. Few groups designed the fluorescence probes for the selective sensing of Fe. In 2023, S. Prajapati[104] et al. published a paper containing two fluorescence probes for the selective sensing of the Fe^{2+}. In the presence of the Fe^{2+} ion, both probe exhibits the turn on sensing in the MeOH-H_2O (1:1) medium. Limit of detection (LOD) values are the 1.91 μM, 3.54 μM and the Fe^{2+} sensing happens through the PET inhibition mechanism. A FRET based rhodamine B Schiff base sensor was designed for

the detection of Fe^{3+} ion. K. Chantarasunthon[105] et al. (2023) reported a Schiff base for the detection of Fe^{3+} with LOD, 83 nM. The probe is changing their color from colorless to pink. In 2016, B. -L. Hou et al.[106] synthesized water stable Zn-MOF that was used for the detection of Fe^{3+} ions with LOD, 0.20 mmol L^{-1} and in presence of the Fe^{3+} ion followed by the quenching. Total Fe was determined by the colorimetry and fluorometric methods by the probe, (2-((2-(naphthalen-1-ylamino)ethylimino)methyl)phenol) with a limit of the detection for Fe^{3+} as 20.85 μM. In presence of the Fe^{2+} and Fe^{3+} color of the probe changes to yellow-brown and purple respectively and the detection of Fe^{2+} and Fe^{3+} were reported by K. Ghosh et al.[107] in 2014. Song-Liang Cai et al.[108] (2011) synthesized a Tb–organic framework with 3D network which had shown green emission and detected Fe^{3+} ion in water.

(iii) Pd^{2+} sensors

Pd is mostly used in the catalysis for the synthesis of large number of important organic molecules, pharmaceuticals, polymers etc. Besides, it is used in the making of jewellery, watch making, electrical contact and surgery equipment etc. In the organic and organometallic complexes; it is used in different type of coupling reaction like Heck reaction, Suzuki coupling, Wacker oxidation process etc. Because of this, sensing of Pd is important in the field of fluorescence field. In 2015, S. Sanda et al.[109] synthesized a Zn(II)-constructed coordination polymer for the sensing of Pd^{2+} ion. Here, the CP exhibits blue emission and in presence of Pd^{2+} the emission is quenched. M. H. Mir et al.[110] synthesized a 1D CP, [Cd(4-nvp)2(5-ssa)], (4-nvp = 4-(1-Naphthylvinyl)pyridine and 5-ssa = 5-Sulfosalicylic acid). This 1D CP is selectively sensing of Pd^{2+} in aqueous medium. In the presence of the Pd^{2+} emission intensity of the CP is decreased due to the incorporation of Pd^{2+} in the CP network. A. K. Adak et al.[111] characterized Rhodamine-Appended Benzophenone Probe for the detection of Pd^{2+} by changing 'blue' colour of the probe to 'pink' emission in the UV-chamber. Emission intensity of the probe is increased in presence of Pd^{2+} with a detection limit (LOD) 34 nM. B. Dutta et al. synthesized the [Zn(cit)(4-nvp)]n coordination polymer[112] for the sensing of Pd^{2+} in water, where 4-nvp = 4-(1-Naphthylvinyl)pyridine and H_2cit = citraconic acid. It exhibits the machanochromism in the detection of Pd^{2+} ion.

1.7   Aim and Scope of the Dissertation

In this research, a group of CPs of Zn(II) and Cd(II) will be reported using dicarboxylato, polypyridyl-N based ligands as organic linkers. The CPs will be structurally characterized and their application in the various fields will be discussed. For the synthesis of the CPs mainly multidentate N-donating heterocycles and dicarboxylate linkers are used. In this dissertation the main focus of the study is: (a) Design and synthesis of coordination polymers with interesting structural framework, (b) Role of the supramolecular interaction in the formation of coordination polymer, (c) Physical significance of the supramolecular interaction and their role in the application as sensor and electrical conductivity field, (d) To explore the biological application of the synthesized coordination polymers.

In **Chapter 2** the design, synthesis and structural characterization of two Zn(II) based 1D coordination polymers, [Zn(adc)(4-Cltpy)(H$_2$O)] (CP**1**) and [Zn(*trans*-muca)(4-Cltpy)] (CP**2**) (4-Cltpy = 4′-Chloro-2,2′:6′,2″-terpyridine, H$_2$adc = Acetylene-dicarboxylic acid, *trans*-H$_2$muca = *trans*, *trans*-muconic acid) are described. The sensing efficiency of the CPs are examined and it is found that the CPs selectively detect the Cu^{2+} in the aqueous medium with limit of detection : 0.14 μM (CP**1**) and 0.06 μM (CP**2**). The internalization of the CPs within the HepG2 cells are examined and subsequent microscopic cell imaging are collected.
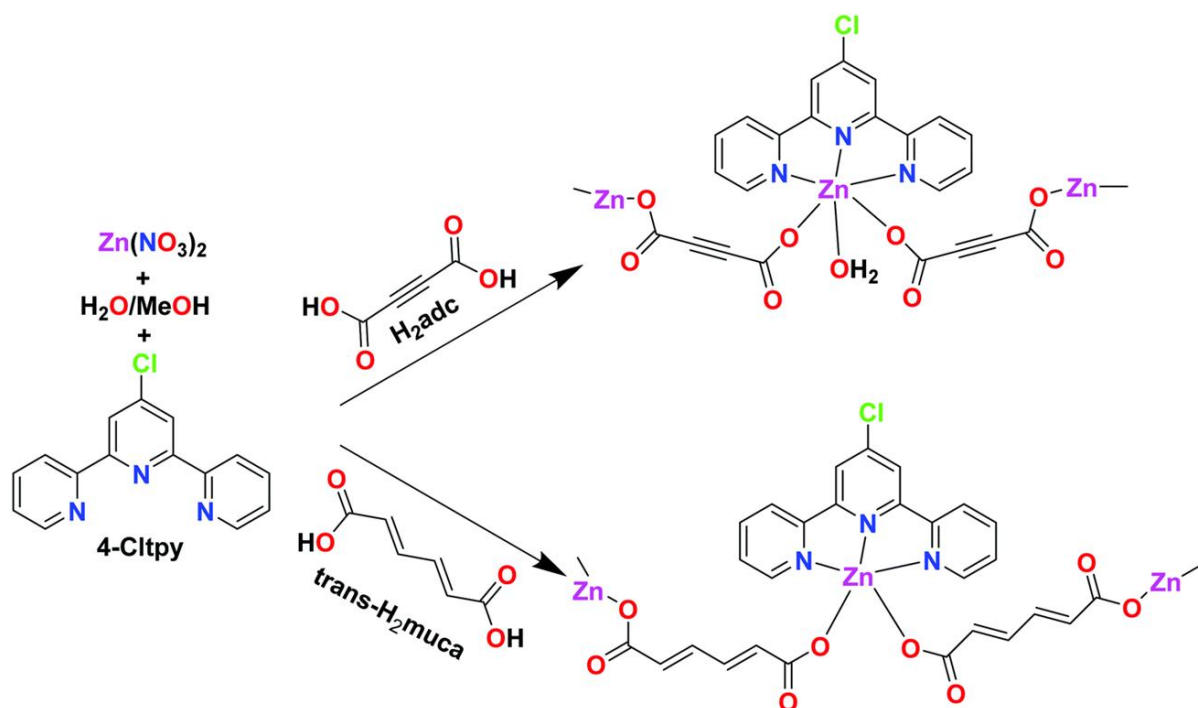
Scheme 1. Synthesis of CP**1**/CP**2** upon reaction of Zn(NO$_3$)$_2$ with 4-Cltpy and H$_2$adc/*trans*-H$_2$muca.

Zn(II) based 1D coordination polymer, {[Zn(2,6-NDC)(4-Cltpy)](H$_2$O)$_4$} (4-Cltpy = 4′-chloro-[2,2′;6′,2″]terpyridine and 2,6-NDC = 2,6-Naphthalene dicarboxylic acid) is described in **Chapter 3**. The complex is spectroscopically characterized and has been confirmed by the Single Crystal X-Ray diffraction measurements. Here, the CP has shown sensitivity to Fe$^{2+/3+}$ *via* absorption spectroscopic measurement. Zn(II) coordinated metal centre was substituted *via* Fe and color of CP was changed from colorless to pink in aqueous medium. Limit of detection (LOD) are 0.11 µM (Fe^{2+}) and 0.15 µM (Fe^{3+}). The Zn-CP also exhibits microscopic cell imaging using MDA-MB 231 cells.
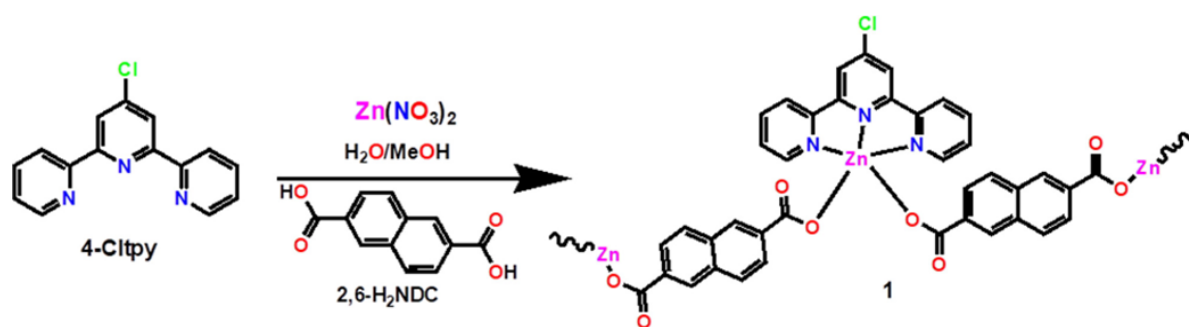
Scheme 2. Synthesis of Coordination Polymer **1**, Reaction of Zn(NO$_3$)$_2$ with 4-Cltpy and 2,6-H$_2$NDC

In **Chapter 4** the design and synthesis the Cd(II) based 2D coordination polymer, {[Cd(HAIPA)(tppz)(OH)].3H$_2$O}$_n$ (2,3,5,6-Tetrakis(2-pyridyl)pyrazine (tppz), and 5-Aminoisophthalic acid (H$_2$AIPA)) is reported. Single crystal X-ray diffraction data had helped to evaluate the structure. In presence of different secondary interaction, a 2D network was assembled. The 2D-CP uses selectively and specifically to detect Pd^{2+} in aqueous medium with a limit of detection is 0.08 µM even in presence of large number of cations. The CP shows exhibited electrical conductivity in light and dark condition and upon incorporation of Pd^{2+} in the CP the electrical conductivity is increased.

Scheme 3. Synthesis of CP**1**, using Cd(NO₃)₂.4H₂O and tppz followed by addition of 5-Aminoisophthalic acid.

The **Chapter 5** reports three Cd(II) based 3D coordination polymers, [Cd(tppz)(adc)(MeOH)] (**1**), [Cd(tppz)(trep)] (**2**) and [Cd(tppz)(2,6-ndc)] (**3**) (tppz = 2,3,5,6-Tetrakis(2-pyridyl)pyrazine, acetylene dicarboxylic acid (H₂adc), terephthalic acid (H₂trep) and 2,6 naphthalene dicarboxylic acid (2,6 H₂ndc)). Different spectral techniques have helped to characterise these CPs. The CPs **1** and **2** form 2D network and compound **3** forms 1D chain. DFT computational study of CPs helped to evaluate the band gap that supported the electrical conductivity results.

Scheme 4. Synthesis of **1,2** and **3** using Cd(NO₃)₂.4H₂O, tppz and corresponding acid.

The **Chapter 6** describes the design and sythesis of one coordination complex [CdI$_2$(4-nvp)$_2$] (**1**) using CdI$_2$ and 4-(1-naphthylvinyl)pyridine (4-nvp). This complex is assembled through the combination of non-covalent interactions, $\pi\cdots\pi$ and C–H$\cdots$I to form a supramolecular entity. This complex selectively detects TNP (trinitrophenol) with a detection limit 16.55×10^{-7} M.
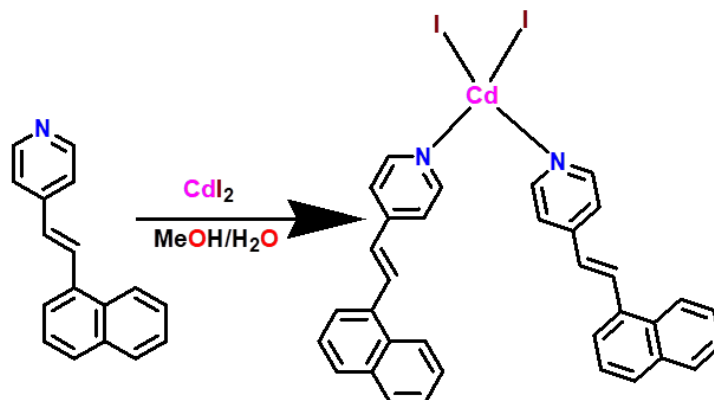
Scheme 4. Synthesis of **1** using CdI$_2$ and 4-(1-naphthylvinyl)pyridine ligand.

1.8. References

1. (a) Batten, S. R., Neville, S. M. and Turner, D. R. Coordination Polymers: Design, Analysis, and Application, *The Royal Society of Chemistry*., **2009**. (b) Kitagawa, S., Kitaura, R. and Noro, S.I. Functional porous coordination polymers. *Angew. Chem. Int. Ed.,* **2004**, *43*, 2334-2375.

2. Chen, L. and Hong, M.C. eds., Design and construction of coordination polymers. *John Wiley & Sons.*, **2009.**

3. Janiak, C., Engineering coordination polymers towards applications**.** *Dalton Trans., **2003**, *14*, .2781-2804.

4. Biradha, K., Ramanan, A. and Vittal, J.J., Coordination polymers versus metal-organic frameworks. *Cryst. Growth Des***, 2009,** *9*, .2969-2970.

5. Eddaoudi, M., Moler, D.B., Li, H., Chen, B., Reineke, T.M., O'keeffe, M. and Yaghi, O.M. Modular chemistry: secondary building units as a basis for the design of highly

porous and robust metal− organic carboxylate frameworks. *Acc. Chem. Res*, **2001**, *34,* .319-330.

6. Shetgaonkar, S.Y. Chemistry of S-block Metal Coordination Polymers: Synthesis, Reactivity Characteristics, Spectroscopic and Structural Investigations (Doctoral dissertation, Goa University).7. *Jr J. C. Bailar, Prep. Inorg. React.* **2013**, *1*, 1.

8. Janiak, C. and Vieth, J. K., MOFs, MILs and more: concepts, properties and applications for porous coordination networks (PCNs). *New J Chem*., **2010** *34*, .2366-2388.

9. Yaghi, O.M., Li, H., Davis, C., Richardson, D. and Groy, T. L., Synthetic strategies, structure patterns, and emerging properties in the chemistry of modular porous solids. *Acc. Chem. Res.,* **1998***, 31*, 474-484.

10. Kahn, O. Chemistry and physics of supramolecular magnetic materials., *Acc. Chem. Res,* **2000**, *33*, .647-657. (b) O.R. Evans and W.L Crystal engineering of NLO materials based on metal-organic coordination networks. *Acc. Chem. Res.* **2002**, *35*, 511.

11. Sun. L, Sun, M.G. Campbell and M. Dincă, Electrically conductive porous metal–organic frameworks, *Angew. Chem., Int. Ed*., **2016**, *55*, 3566.

12. Kitagawa, S., Kitaura, R. and Noro, S. I., Functional porous coordination polymers. *Angew. Chem.,* **2004**, *43*, 2334-2375.

13. (a) Li, H., Eddaoudi, M., O'Keeffe, M. and Yaghi, O.M. Design and synthesis of an exceptionally stable and highly porous metal-organic framework. *Nature.,* **1999**, *402*, 276-279.

(b) Chae, H. K., Siberio-Pérez, D. Y., Kim, J., Go, Y., Eddaoudi, M., Matzger, A.J., O'Keeffe, M., Yaghi, O. M. and Materials Design and Discovery Group. A route to high

surface area, porosity and inclusion of large molecules in crystals. *Nature*, **2004**, *427*, 523-527.

(c) Eddaoudi, M., Kim, J., Rosi, N., Vodak, D., Wachter, J., O'Keeffe, M. and Yaghi, O.M. Systematic design of pore size and functionality in isoreticular MOFs and their application in methane storage. *Science*, **2002,** *295*, 469-472.

14. (a) Rowsell, J. L., Millward, A.R., Park, K. S. and Yaghi, O.M. Hydrogen sorption in functionalized metal-organic frameworks, *J. Am. Chem. Soc.,* **2004,** *126,* 5666-5667. (b) Cote, A. P., Benin, A. I., Ockwig, N.W., O'Keeffe, M., Matzger, A. J. and Yaghi, O.M. Porous, crystalline, covalent organic frameworks. *Science***, 2005**. *310*, 1166-1170. (C) El-Kaderi, H. M., Hunt, J. R., Mendoza-Cortés, J. L., Côté, A. P., Taylor, R. E., O'Keeffe, M. and Yaghi, O.M. Designed synthesis of 3D covalent organic frameworks. *Science.*, **2007**, *316*, 268-272.

15. (a) Ockwig, N.W., Delgado-Friedrichs, O., O'Keeffe, M. and Yaghi, O.M. Reticular chemistry: occurrence and taxonomy of nets and grammar for the design of frameworks. *Acc. Chem. Res.*, **2005,** *38*, 176-182.

16. (a) Kitagawa, S. and Matsuda, R. Chemistry of coordination space of porous coordination polymers. *Coord. Chem. Rev*., **2007**, *251* ,2490-2509. (b) Kitagawa, S. and Uemura, K. Dynamic porous properties of coordination polymers inspired by hydrogen bonds. *Chem Soc Rev*, **2005**, *34*,109-119. (c) Ghosh, S.K., Zhang, J. P. and Kitagawa, S. Reversible topochemical transformation of a soft crystal of a coordination polymer. *Angew. Chem.*, **2007**, *46* ,7965-7968. (d) Matsuda, R., Kitaura, R., Kitagawa, S., Kubota, Y., Belosludov, R.V., Kobayashi, T. C., Sakamoto, H., Chiba, T., Takata, M., Kawazoe, Y. and Mita, Y. Highly controlled acetylene accommodation in a metal–organic microporous material. *Nature.,* **2005**. *436*, 238-241. (e) Ghosh, S. K.,

Bureekaew, S. and Kitagawa, S. A Dynamic, Isocyanurate-Functionalized Porous Coordination Polymer. *Angew. Chem. Int. Ed.*, **2008,** *47,* 3403-3406.

17. Mir, M. H., Koh, L. L., Tan, G.K. and Vittal, J. J. Single-Crystal to Single-Crystal Photochemical Structural Transformations of Interpenetrated 3D Coordination Polymers by [2+ 2] Cycloaddition Reactions. *Angew. Chem.*, **2009**, *2,* 400-403.

18. Schmidt, G. M. J. Photodimerization in the solid state. *Pure Appl. Chem.*, **1971**, *27*, 647-678.

19. (a) Desiraju, G. R. and Parshall, G.W. Crystal engineering: the design of organic solids. *Mater. Sci. Monogr.*, **1989**, *54*. (b) Desiraju, G. R. Crystal engineering: from molecule to crystal. *J. Am. Chem. Soc.*, **2013,** *135*, 9952-9967.

20. (a) Addadi, L. and Lahav, M. Photopolymerization of chiral crystals. 1. The planning and execution of a topochemical solid-state asymmetric synthesis with quantitative asymmetric induction. *J. Am. Chem. Soc.*, **1978,** *100*, 2838-2844. (b) Thomas, J. M. Diffusionless reactions and crystal engineering. *Nature.*, **1981,** *289***,** 633-634. (c) Copp, S. B., Subramanian, S. and Zaworotko, M. J. Supramolecular chemistry of manganese complex [Mn (CO)$_3$(μ_3-OH)]$_4$: assembly of a cubic hydrogen-bonded diamondoid network with 1, 2-diaminoethane. *J. Am. Chem. Soc.*, **1992**, *114*, 8719-8720. (d) Aakeröy, C. B. and Seddon, K. R. The hydrogen bond and crystal engineering. *Chem Soc Rev.*, **1993**, *22*, 397-407. (e) Bishop, R.. Designing new lattice inclusion hosts. *Chem Soc Rev.*, **1996,** *25*, 311-319. (f) Nassimbeni, L. R. Physicochemical aspects of host-guest compounds. *Acc. Chem. Res.*, **2003**, *36*, 631-637. (g) D. Braga, *Angew Chem Int.,* **2004**. 43, *2.* (h) Almarsson, Ö. and Zaworotko, M. J. Crystal engineering of the composition of pharmaceutical phases. Do pharmaceutical co-crystals represent a new path to improved medicines*?. Chem comm.*, **2004**, *17,* 1889-1896. (i) Hosseini, M.W.

Molecular tectonics: from simple tectons to complex molecular networks. *Acc. Chem. Res.*, **2005**, *38*, 313-323. (j) Desiraju, G. R., Vittal, J. J. and Ramanan, A. *Crystal engineering: a textbook. World Scientific.* **2011.** (k) Bond, A.D. Pharmaceutical crystallography: is there a devil in the details?. *CrystEngComm.*, **2012**, *14*, 2363-2366.

21.   (a) Nangia, A. Organic nanoporous structures, *Curr Opin Solid State Mater Sci*, **2001**, *5*, 115-122. (b) Addadi, L. and Geva, M. Molecular recognition at the interface between crystals and biology: generation, manifestation and detection of chirality at crystal surfaces. *CrystEngComm.,* **2003**, *5*, 140-146.

22.   Steed, J. W. and Atwood, J. L. *Supramolecular chemistry*. **2022**, *John Wiley & Sons*.

23.   (a) Lehn, J. M. Cryptates: inclusion complexes of macropolycyclic receptor molecules. *In Chemistry for the Welfare of Mankind*,**1979**,871-892*. Pergamon*. (b) Lehn, J. M . Toward self-organization and complex matter. *Science*, **2002**, *295*, 2400-2403. (c) Lehn, J. M. *Supramolecular Science: Where it is and Where it is Going. Dordrecht: Kluwer.*, **1999**, *287*, 4763. (d) Lehn, J.M. Supramolecular chemistry. *Science*, **1993**, *260*, 1762-1763.

24.   Schmeck Jr, H. M. Chemistry and Physics Nobels hail discoveries on life and superconductors; Three share prize for synthesis of vital enzymes. *New York Times*, **1987***, 15*.

25.   Atwood, J. L. and W, J. Steed,Supramolecular chemistry, *Wiley.*, **2013**.

26.   Oshovsky, G.V., Reinhoudt, D. N. and Verboom, W. Supramolecular chemistry in water. *Angew. Chem. Int. Ed.*, **2007***, 46*, 2366-2393.

27.   Cainelli, G., Panunzio, M., Giacomini, D., Martelli, G., Spunta, G., Bandini, E., Chatgilialoglu, C. and Snieckus, V. *Chemical Synthesis: Gnosis to Prognosis*. **1996.**

28. Ariga, K., Hill, J.P., Lee, M.V., Vinu, A., Charvet, R. and Acharya, S. Challenges and breakthroughs in recent research on self-assembly. *Sci Technol Adv Mate*,**2008**.

29. Lehn, J.M. *Supramolecular chemistry. Concepts and perspectives*.**1995.**

30. Cosic, I. Macromolecular bioactivity: is it resonant interaction between macromolecules?-theory and applications. *IEEE. Trans. Biomed. Eng*,**1994,** *41,* 1101-1114.

31. Baron, R., Setny, P. and McCammon, J. A. Water in cavity-ligand recognition. *J. Am. Chem. Soc*., **2010,** *132*, 12091-12097. (b) Baron, R. and McCammon, J. A. Molecular recognition and ligand association. *Annu. Rev. Phys. Chem*., **2013**, *64,* 151-175.

32. (a) Shinkai, S., Ikeda, M., Sugasaki, A. and Takeuchi, M. Positive allosteric systems designed on dynamic supramolecular scaffolds: Toward switching and amplification of guest affinity and selectivity. *Acc. Chem. Res*., **2001**, *34*, 494-503. (b) Grunenberg, J. Complexity in molecular recognition. *Phys. Chem. Chem. Phys*., **2011,** *13*, 10136-10146.

33. (a) Nørgaard, K. and Bjørnholm, T. Supramolecular chemistry on water-towards self-assembling molecular electronic circuitry. *Chem. Commun.*, **2005**, *14*, 1812-1823. (b) Kepert, C.J. Advanced functional properties in nanoporous coordination framework materials. *Chem. Commun,* **2006,** *7*, 695-700.

34. Cram, D. J. Preorganization-from solvents to spherands. *Angew. Chem. Int. Ed*., **1986**, *25*, 1039-1057.

35. Pedersen, C. J. Cyclic polyethers and their complexes with metal salts. *J. Am. Chem. Soc*., **1967**, *89*, 7017-7036.

36. C. J. Pedersen,Cyclic polyethers and their complexes with metal salts. *J. Am. Chem. Soc*., **1967,** *89,* 7017.

37. Mir, M. H., Wang, L., Wong, M. W. and Vittal, J. J. Water helicate $(H_2O)_7$, hosted by a diamondoid metal–organic framework. *Chem. Commun.*, **2009***, 30,* 4539-4541.

38. (a) Desiraju, G. R. Chemistry beyond the molecule, *Nature.*, **2001**, *412*, 397. (b) Desiraju, G. R. Supramolecular synthone for crystal engineering-a new organic synthesis, *Angew. Chem.*, **1995**, *107*, 2541. *Angew. Chem., Int. Ed. Engl.,* **1995**, *34*, 2311. (c) Brammer, L. Developments in inorganic crystal engineering, *Chem. Soc. Rev.*, **2004**, *33*, 476. (e) Braga, D. Brammer, L. and Champness, N. New trends in crystal engineering, *CrystEngComm.*, **2005**, *7,* 1. (f) Metrangolo, P. and Resnati, G. Halogen bonding: a paradigm in supramolecular chemistry. *Chemistry, Chem. Eur. J.,* **2001**, *7*, 2511.

39. (a) Lehn, J. M. From supramolecular chemistry towards constitutional dynamic chemistry and adaptive chemistry. *Chem Soc Rev.*, **2007,** *36*, 151-160.

    (b) Special issue dedicated to Supramolecular Chemistry: *Chem. Soc. Rev.* **2007**, *36*, 125.

40. (a) Aakeröy, C. B. and Beatty, A. M. Crystal engineering of hydrogen-bonded assemblies-a progress report. *Aust. J. Chem.,* **2001,** *54,* 409-421. (b) Aakeröy, C. B. and Beatty, A. M. Crystal engineering of hydrogen-bonded assemblies-a progress report. *Aust. J. Chem.*, **2001,** *54*, 409-421. (c) Lutz, H. D. Structure and strength of hydrogen bonds in inorganic solids. *J. Mol. Struct.*, **2003**, *646*, 227-236.

41. (a) Braga, D. and Grepioni, F. How to make weak hydrogen bonds less weak. *New J. Chem*,**1998,** *22*, 1159-1161.(b) Desiraju, G.R. and Steiner, T., The weak hydrogen bond: in structural chemistry and biology (Vol. 9). *IUCrJ.*, **2001**. (c) Langley, P. J., Hulliger, J., Thaimattam, R. and Desiraju, G. R. Supramolecular synthons mediated by weak hydrogen bonding: forming linear molecular arrays via C [triple bond, length as

m-dash] C–H··· N [triple bond, length as m-dash] C and C [triple bond, length as m-dash] C–H··· O_2N recognition. *New J. Chem.*, **1998,** *22*, 1307-1309.

42. Arunan, E., Desiraju, G. R., Klein, R. A., Sadlej, J., Scheiner, S., Alkorta, I., Clary, D. C., Crabtree, R. H., Dannenberg, J. J., Hobza, P. and Kjaergaard, H. G. Definition of the hydrogen bond (IUPAC Recommendations 2011). *Pure Appl. Chem.,***2011,** *83*, 1637-1641.

43. (a) Umeyama, H. and Morokuma, K. The origin of hydrogen bonding. An energy decomposition study. *J. Am. Chem. Soc*., **1977**, *99*, 1316-1332. (b) Desiraju G. R, Hydrogen bridges in crystal engineering: interactions without borders. *Acc. Chem. Res*., **2002**, *35*, 565.

44. Larson, J. W. and McMahon, T. B. Gas-phase bihalide and pseudobihalide ions. An ion cyclotron resonance determination of hydrogen bond energies in XHY-species (X, Y= F, Cl, Br, CN). *Inorganic Chemistry.*, **1984**, *23*, 2029-2033.

45. Emsley, J. Very strong hydrogen bonding. *Chem. Soc. Rev.,* **1980***, 9*, 91-124.

46. (a) Scheiner, S. Hydrogen bonding: a theoretical perspective. *Oxford University Press* on Demand,**1997**. (c) Desiraju, G. R. and Steiner, T. The Weak Hydrogen Bond in Structural Chemistry and Biology New York: *Oxford University Press Inc.,* **1999.**

47. Coulson, C. A., *Pauling's Chemical Bond.*, **1961.**

48. Steiner, T., Majerz, I. and Wilson, C. C. First OHN Hydrogen Bond with a Centered Proton Obtained by Thermally Induced Proton Migration. *Angew.Chem*., **2001,** *40*, 2651-2654.

49. Vishweshwar, P., Nangia, A. and Lynch, V. M. Molecular complexes of homologous alkanedicarboxylic acids with isonicotinamide: X-ray crystal structures, hydrogen bond synthons, and melting point alternation*,Cryst. Growth Des*., **2003***, 3*, 783-790.

50. Etter, M. C. Encoding and decoding hydrogen-bond patterns of organic compounds. *Acc. Chem. Res.*, **1990,** *23*, 120-126.

51. (a) Desiraju, G. R. and Parthasarathy, R. The nature of halogen.cntdot..cntdot..cntdot. halogen interactions: are short halogen contacts due to specific attractive forces or due to close packing of nonspherical atoms?*J. Am. Chem. Soc.,* **1989**, *111*, 8725. (b) Jagarlapudi, A. R. Sarma, P. Desiraju, G. R. The role of Cl. cntdot..cntdot.. cntdot. Cl and CH. cntdot..cntdot.. cntdot. O interactions in the crystal engineering of 4-. ANG. short-axis structures. *Acc. Chem. Res.,* **1986**, *19,* 222. (c) Reddy, C. M.; Kirchner, M. T.; Padmanabhan, R. V.; Gundakaram, K. A. and Desiraju, G. R. Isostructurality, polymorphism and mechanical properties of some hexahalogenated benzenes: the nature of halogen··· halogen interactions. *Chem. Eur. J.,* **2006**, *12*, 2222. (d) Nyburg, S. C.; Wong-Ng, W. Proc. *R. Soc. London, Ser. A.,* **1979**, *29,* 367.

52. Price, S. L.; Stone, A.J.; Lucas, J.; Rowland, R.S.; Thornley, A. E. The Nature of-Cl. cntdot.. cntdot.. cntdot. Cl-Intermolecular Interactions. *J. Am. Chem. Soc.,* **1994**, *116*, 4910.

53. (a) Awwadi, F. F.; Willett, R. D.; Peterson, K.A.; Twamley, B. The nature of halogen··· halogen synthons: Crystallographic and theoretical studies. *Chem. Eur. J.,* **2006**, *12*, 8952. (b) Ahmed, F., Roy, S., Naskar, K., Sinha, C., Alam, S.M., Kundu, S., Vittal, J.J. and Mir, M.H. Halogen··· halogen interactions in the supramolecular assembly of 2D coordination polymers and the CO_2 sorption behavior. *Cryst. Growth Des.*, **2016**, *16*, 5514-5519.

54. (a) Amabilino, D. B.; Stoddart, J. F. Interlocked and intertwined structures and superstructures.*Chem. Rev.,* **1995**, *95*, 2725. (b) Claessens, C.G.; Stoddart, J. F. π–π Interactions in self-assembly. *J. Phys. Org. Chem.,* **1997**, *10*, 254. (c) Hirsch, K.A.;

Wilson, S. R.; Moore, J. S. A packing model for interpenetrated diamondoid structures-an interpretation based on the constructive interference of supramolecular networks. *Chem. Eur. J.,* **1997**, *3*, 765.

55. (a) Lightfoot, M. P.; Mair, F. S.; Pritchard, R.G.; Warren, J. W. New supramolecular packing motifs: π-stacked rods encased in triply-helical hydrogen bonded amide strands. *Chem.Comm.,* **1999**, 1945. (b) Ning, G. L.; Wu, L.P.; Sugimoto, K.; Munakata, M.; Kuroda-Sowa, T. and Maekawa, M. Construction of 2-D multilayer structures: silver (I) complexes with linear aromatic compounds. *J. Chem. Soc., Dalton Trans.,* **1999**, **2529**. (c) Brown, S.P.; Schnell, I.; Brand, J. D.; Müllen, K.; Spiess, H. W. An Investigation of π···π Packing in a Columnar Hexabenzocoronene by Fast Magic-Angle Spinning and Double-Quantum 1H Solid-State NMR Spectroscopy. *J. Am. Chem. Soc.,* **1999**, *121*, 6712. (d) Lämsä, M.; Huuskonen, J.; Rissanen, K.; Pursiainen, J. X-ray and NMR Studies on Host–Guest Inclusion Complex Formation between Crown Ethers and Pyridinium Compounds. *Chem. Eur. J.,* 1998, *4*, 84. (e) Dance, I. and Scudder, M. Supramolecular Motifs: Concerted Multiple Phenyl Embraces between Ph_4P^+ Cations Are Attractive and Ubiquitous. *Chem. Eur. J.,* **1996**, *2*, 481.

56. (a) Hunter, C. A. Hammett correlations 'beyond the molecule'1. *Chem. Soc. Rev.*, **1994**, 101. (b) Hunter, C. A. Arene—arene interactions: electrostatic or charge transfer? *Angew. Chem.Int. Ed. Engl.,* **1993**, *32*, 1653. (c) Hunter, C. A. and Sanders, J. K. M. The nature of. π···π Interactions. *J. Am. Chem. Soc.,* **1990**, *112*, 5525.

57. (a) Lee, E. C.; Kim, D.; Jurečka, P.; Tarakeshwar, P.; Hobza, P. and Kim, K.S. Understanding of assembly phenomena by aromatic− aromatic interactions: benzene dimer and the substituted systems. *J. Phys. Chem. A.,* **2007**, *111*, 3446 and references therein. (b) Martinez, C. R.; Iverson, B. L. Rethinking the term "pi-stacking". *Chem. Sci.,* **2012**, 3, 2191.

58. Jorgensen, W. L. and Severance, D. L. Aromatic-aromatic interactions: free energy profiles for the benzene dimer in water, chloroform, and liquid benzene. *J. Am. Chem. Soc.,* **1990**, *112*, 4768.

59. Janiak, C. A critical account on π–π stacking in metal complexes with aromatic nitrogen-containing ligands. *J. Chem. Soc., Dalton Trans.,* **2000**, **3885** and references therein.

60. Wheeler, S. E. and Houk, K. N. Substituent effects in the benzene dimer are due to direct interactions of the substituents with the unsubstituted benzene. *J. Am. Chem. Soc.,* **2008**, *130,* 10854.

61. Bhattacharyya, R.; Samanta, U. and Chakrabarti, P. Aromatic–aromatic interactions in and around α-helices. *Protein. Eng.,* **2002**, *15*, 91 and references therein.

62. Kannan, N. and Vishveshwara, S. Aromatic clusters: a determinant of thermal stability of thermophilic proteins. *Protein Eng.,* **2000**, *13*, 753.

63. (a) Umezawa, Y.; Tsuboyama, S.; Takahashi, H.; Uzawa, J. and Nishio, M. CH…π interaction in the conformation of organic compounds. A database study. *Tetrahedron.,* **1999**, *55*, 10047. (b) Matsumoto, A.; Tanaka, T.; Tsubouchi, T.; Tashiro, K.; Saragai, S. and Nakamoto, S. Crystal engineering for topochemical polymerization of muconic esters using halogen− halogen and CH/π interactions as weak intermolecular interactions. *J. Am. Chem. Soc.,* **2002**, *124*, 8891.

64. (a) Cantrill, S. J.; Preece, J.A.; Stoddart, J. F.; Wang, Z. H.; White, A. J. P.; Williams, D. J. The idiosyncrasies of tetrabenzo [24] crown-8 in the solid state. *Tetrahedron.,* **2000**, *56*, 6675. (b) Arduini, A.; Giorgi, G.; Pochini, A.; Secchi, A.; Ugozzoli, F. Interactions of the aromatic cavity of rigid calix [4] arene cone conformers with acid CH_3 and CH_2 containing guests in apolar solvents. *Tetrahedron.,* **2001**, *57*, 2411.

65. (a) Akazome, M.; Ueno, Y.; Ooiso, H.; Ogura, K. Enantioselective Inclusion of Methyl Phenyl Sulfoxides and Benzyl Methyl Sulfoxides by (R)-Phenylglycyl-(R)-phenylglycine and the Crystal Structures of the Inclusion Cavities. *J. Org. Chem.,* **2000**, *65*, 68. (b) Kinbara, K.; Harada, Y.; Saigo, K. Enantiopure trans- and cis-3-Aminoindan-1-ols: Preparation and Application as Novel Basic Resolving Agents. *J. Chem. Soc., Perkin Trans.,* **2000**, *2* 1339.

66. (a) Andreetti, G. D.; Pochini, A. and Ungaro,R. Molecular inclusion in functionalized macrocycles. Part 6. The crystal and molecular structures of the calix[4]arene from p-(1,1,3,3-tetramethylbutyl)phenol and its 1 : 1 complex with toluene. *J. Chem. Soc., Perkin Trans.,* **1983**, *2*, 1773. (b) Ungaro, R.; Pochini, A.; Andreetti, G. D.; Sangermano, V. Molecular inclusion in functionalized macrocycles. Part 9. The crystal and molecular structure of p-t-butylcalix[4]arena–anisole (2 : 1) complex: a new type of cage inclusion compound. *J. Chem. Soc., Perkin Trans.,* **1984**, *2*, 1979. (c) Ungaro, R.; Pochini, A.; Andreetti, G. D.; Domiano, P. *J. Chem. Soc., Perkin Trans.,* **1985**, *2*, 197. (d) Andreetti, G. D.; Ori, O.; Ugozzoli, F.; Alfieri, C.; Pochini, A.; Ungaro, R. Molecular inclusion in functionalized macrocycles. Part 9. The crystal and molecular structure of p-t-butylcalix[4]arena–anisole (2 : 1) complex: a new type of cage inclusion compound. *J. Incl.Phenom.,* **1988***, 6*, 523.

67. (a) Quiocho, F. A. and Vyas, N. K. Novel stereospecificity of the L-arabinose-binding protein. *Nature.,* **1984***, 310*, 381. (b) Vyas, N. K.; Vyas, M. N. and Quiocho, F. A. A novel calcium binding site in the galactose-binding protein of bacterial transport and chemotaxis. *Nature.,* **1987**, *327*, 635. (c) Tatko, C. D. and Waters, M. L. Comparison of C− H⊙⊙⊙ π and Hydrophobic Interactions in a β-Hairpin Peptide: Impact on Stability and Specificity. *J. Am. Chem. Soc.,* **2004**, *126*, 2028.

68. (a) Novoa, J. J. and Mota, F. The C–H··· π bonds: strength, identification, and hydrogen- bonded nature: a theoretical study. *Chem. Phys. Lett.,* **2000,** *318*, 345. (b) Takahashi, O.; Kohno, Y. and Saito, K. Molecular orbital calculations of the substituent effect on intermolecular CH/π interaction in $C_2H_3X–C_6H_6$ complexes (X= H, F, Cl, Br, and OH). *Chem. Phys. Lett.,* **2003**, *378,* 509.

69. Hirota, M.; Sakakibara, K.; Suezawa, H.; Yuzuri, T.; Ankai, E. and Nishio, M. Intramolecular CH–π interaction. Substituent effect as a probe for hydrogen bond-like character. *J. Phys. Org. Chem.,* **2000**, *13*, 620.

70. Tsuzuki, S.; Honda, K.; Uchimaru, T.; Mikami, M. and Tanabe, K. The interaction of benzene with chloro-and fluoromethanes: effects of halogenation on CH/π interaction. *J. Phys.Chem. A.,* **2002**, *106*, 4423.

71. (a) Nakagawa, N.; Nikki, K.; Takeuchi, Y. and Kumagai, I. Application of aromatic solvent induced shifts in organic chemistry. *Chem. Lett.,* **1972**, 1239. (b) Nikki, K.; Nakagawa, N. and Takeuchi, Y. Aromatic solvent-induced shift (ASIS). I. An interpretation based on the dipole-quadrupole interaction. *Bull. Chem. Soc. Jpn.,* **1975**, *48*, 2902. (c) Nikki, K. and Nakagawa, N. Aromatic Solvent-induced Shifts (ASIS). II. Interpretation of Benzene and Hexafluorobenzene Induced Shifts by Means of the Electrostatic Interaction Model. *Bull. Chem. Soc. Jpn.,* **1978**, *51*, 3267.

72. Nishio, M.; Hirota, M. and Umezawa, Y. The CH-π Interaction. *Evidence, Nature, and Consequences. Wiley-VCH, New York,* **1998**.

73. Singh, M. K. and Rajaraman, G. Can CH··· π Interactions Be Used To Design Single-Chain Magnets? *Chem. Eur. J.,* **2015**, *21*, 980.

74. U.S. Environmental Protection Agency. Risk Assessment, Management and Communication of Drinking Water Contamination; US EPA 625/4-89/024, EPA: Washington, DC, **1989**.

75. Sorenson, J. R. J.; Campbell, I. R.; Tepper, L. B. and Lingg, R. D. Aluminum in the Environment and Human Health, Environ. *Health Perspect.,* **1974**, *8*, 3–95.

76. Flaten, T. P. Aluminium as a risk factor in Alzheimer's disease, with emphasis on drinking water, *Brain Res. Bull.,* **2001**, *55*, 187–196.

77. Baral, M.; Sahoo, S. K. and Kanungo, B. K. Tripodal amine catechol ligands: A fascinating class of chelators for aluminium(III), *J. Inorg. Biochem.,* **2008**, *102*, 1581–1588.

78. Gupta, V. K.; Jain, A. K. and Maheshwari, G. Aluminum(III) selective potentiometric sensor based on morin in poly(vinyl chloride) matrix, *Talanta,* **2007**, *72*, 1469–1473.

79. Berg, C. M. G. Chemical Speciation of Iron in Seawater by Cathodic Stripping Voltammetry with Dihydroxynaphthalene, *Anal. Chem.,* **2006**, *78*, 156–163.

80. Cerchiaro, G.; Manieri, T. M. and Bertuchi, F. R. Analytical methods for copper, zinc and iron quantification in mammalian cells, *Metallomics.,* **2013**, *5*, 1336-1345.

81. Pomazal, K.; Prohaska, C.; Steffan, I.; Reich, G. and Huber, J. F. K. Determination of Cu, Fe, Mn, and Zn in blood fractions by SEC-HPLC-ICP-AES coupling, *Analyst.,* **1999**, *124*, 657–663.

82. Vanloot, P.; Coulomb, B.; Brach-Papa, C.; Sergent, M. and Boudenne, J. L. Multivariate optimization of solid-phase extraction applied to iron determination in finished waters, *Chemosphere.,* **2007**, *69*, 1351–1360.

83. Ammann, A. A. Inductively coupled plasma mass spectrometry (ICP MS): a versatile tool, *J. Mass Spectrom.,* **2007**, *42*, 419-427.

84. Shamspur, T.; Sheikhshoaie, I. and Mashhadizadeh, M. H. Flame atomic absorption spectroscopy (FAAS) determination of iron(III) after preconcentration on to modified analcime zeolite with 5-((4-nitrophenylazo)-N-(2′,4′-dimethoxyphenyl))salicylaldimine by column method, *J. Anal. At. Spectrom.,* **2005**, *20*, 476–478.

85. McIlwee, H. A.; Schauer, C. L.; Praig, V. G.; Boukherroub, R. and Szunerits, S. Thin chitosan films as a platform for SPR sensing of ferric ions, *Analyst.,* **2008**, *133*, 673–677.

86. Mehta, V. N.; Kailasa, S. K.; Wu, H.-F. Sensitive and Selective Colorimetric Sensing of Fe^{3+} Ion by Using P-Amino Salicylic Acid Dithiocarbamate Functionalized Gold Nanoparticles. *New J. Chem.*, **2014**, *38*, 1503–1511.

87. Yin, Z.-Z.; Li, Y.; Jiang, L.-P.; Rana, R. K.; Zhu, J.-J. Synthesis and Electrocatalytic Activity of Haemin-Functionalised Iron (II, III) Oxide Nanoparticles. *Anal. Chim. Acta.,* **2013**, *781*, 48–53

88. Miller, G. C.; Pritsos, A. Cyanide: social, industrial and economic aspects: the proceedings of a symposium held at Annual Meeting of TMS (The Minerals, Metals & Materials Society), *New Orleans, Louisiana*, **2001**.

89. Martínez-Máñez, R.; Sancenón, F. Fluorogenic and Chromogenic Chemosensors and Reagents for Anions. *Chem. Rev.*, **2003**, *103*, 4419–4476.

90. Bissell, R. A.; Silva, A. P. de; Gunaratne, H. Q. N.; Lynch, P. L. M.; Maguire, G. E. M.; Sandanayake, K. R. A. S. Molecular Fluorescent Signalling with 'Fluor–Spacer–

Receptor' Systems: Approaches to Sensing and Switching Devices via Supramolecular Photophysics. *Chem. Soc. Rev.,* **1992**, *21*, 187–195.

91. Wiskur, S. L.; Ait-Haddou, H.; Lavigne, J. J.; Anslyn, E. V. Teaching Old Indicators New Tricks. *Acc. Chem. Res.*, **2001**, *34* , 963–972.

92. Martínez-Máñez, R.; Sancenón, F. Chemodosimeters and 3D Inorganic Functionalised Hosts for the Fluoro-Chromogenic Sensing of Anions. *Coord. Chem. Rev.,* **2006**, *250*, 3081–3093.

93. Chang, J. H.; Choe, Y. M.; Sin, Y. G. A Significant Fluorescence Quenching of Anthryl amino benzo crown Ethers by Paramagnetic Metal Cations. *Bull. Korean Chem. Soc.,* **2001**, *22*, 527–530.

94. Vlček, A. Highlights of the Spectroscopy, Photochemistry and Electrochemistry of [M(CO)$_4$(α-Diimine)] Complexes, M=Cr, Mo, W. *Coord. Chem. Rev.,* **2002**, *230*, 225–242.

95. Xu, Z.; Xiao, Y.; Qian, X.; Cui, J.; Cui, D. Ratiometric and Selective Fluorescent Sensor for CuII Based on Internal Charge Transfer (ICT). *Org. Lett.,* **2005**, *7*, 889–892.

96. Serin, J. M.; Brousmiche, D. W.; Fréchet, J. M. J. A FRET-Based Ultraviolet to Near-Infrared Frequency Converter. *J. Am. Chem. Soc.*, **2002**, *124*, 11848–11849.

97. Guha, S.; Lohar, S.; Sahana, A.; Banerjee, A.; Safin, D. A.; Babashkina, M. G.; Mitoraj, M. P.; Bolte, M.; Garcia, Y.; Mukhopadhyay, S. K.; Das, D. A Coumarin-Based "Turn-on" Fluorescent Sensor for the Determination of Al^{3+}: Single Crystal X-Ray Structure and Cell Staining Properties. *Dalton Trans.,* **2013**, *42*, 10198–10207.

98. Zhao, J.; Ji, S.; Chen, Y.; Guo, H.; Yang, P. Excited State Intramolecular Proton Transfer (ESIPT): From Principal Photophysics to the Development of New

Chromophores and Applications in Fluorescent Molecular Probes and Luminescent Materials. *Phys. Chem. Chem. Phys.,* **2012**, *14*, 8803–8817.

99. Carter, K. P., Young, A. M. and Palmer, A. E. Fluorescent sensors for measuring metal ions in living systems. *Chem. Rev.,* **2014**, *114*, 4564-4601.

100. Wu, Z.-F.; Velasco, E.; Shan, C.; Tan, K.; Zhang, Z.-Z.; Hu, Q.-Q.; Xing, K.; Huang, X.-Y.; Li, J. Robust Fluorescent Calcium Coordination Polymers as Cu^{2+} Sensors with High Sensitivity and Fast Response. *J. Mater. Chem. C.,* **2020**, *8*, 6820–6825.

101. Silpcharu, K.; Soonthonhut, S.; Sukwattanasinitt, M.; Rashatasakhon, P. Fluorescent Sensor for Copper(II) and Cyanide Ions via the Complexation–Decomplexation Mechanism with Di(Bissulfonamido)Spirobifluorene. *ACS Omega.,* **2021**, *6*, 16696–16703.

102. M., Royzen, Dai, Z. and Canary, J. W., Ratiometric displacement approach to Cu (II) sensing by fluorescence. *J. Am. Chem.*, **2005**, *127*, 1612-1613.

103. Srinivasan, P. and Deivasigamani, P. Solid-state naked-eye sensing of Cu (II) from industrial effluents and environmental water samples using probe integrated polymeric sensor materials. *Microchem. J.*, **2023**, *185*, 108224.

104. Prajapati, S., Sinha, P., Hindore, S. and Jana, S. Selective turn-on fluorescence sensing of Fe^{2+} in real water samples by chalcones. *Spectrochim. Acta A Mol. Biomol. Spectrosc.,* **2023**, *287*, 122107.

105. Chantarasunthon, K., Promkatkaew, M., Waranwongcharoen, P., Sueksachat, A., Prasop, N., Norasi, T., Sonsiri, N., Sansern, S., Chomngam, S., Wechakorn, K. and Thana, C.,. A novel highly selective FRET sensor for Fe (III) and DFT mechanistic evaluation. *Spectrochim. Acta A Mol. Biomol. Spectrosc.*, **2023**, *286*, 122031.

106. Hou, B. L., Tian, D., Liu, J., Dong, L. Z., Li, S. L., Li, D. S. and Lan, Y. Q., A water-stable metal–organic framework for highly sensitive and selective sensing of Fe^{3+} ion. *Inorg. Chem.*, **2016**, *55*, 10580-10586.

107. Ghosh, K. and Rathi, S., A novel probe for selective colorimetric sensing of Fe (II) and Fe (III) and specific fluorometric sensing of Fe (III): DFT calculation and logic gate application. *RSC advances.*, **2014**, *4*, 48516-48521.

108. Cai, S. L., Zheng, S. R., Fan, J., Xiao, T.T., Tan, J. B. and Zhang, W. G., A new sensor based on luminescent terbium–organic framework for detection of Fe^{3+} in water. *Inorg. Chem. Comm.*, **2011**, *14*, 937-939.

109. Sanda, S., Parshamoni, S., Biswas, S. and Konar, S., Highly selective detection of palladium and picric acid by a luminescent MOF: a dual functional fluorescent sensor. *Chem. Comm.*, **2015**, *51*, 6576-6579.

110. Mir, M. H., Bera, S., Khan, S., Maity, S., Sinha, C. and Dutta, B., Sunlight assisted SCSC dimerization of a 1D coordination polymer impacts the selectivity of Pd (II) sensing in water. *Chem. Comm.*, **2021**, *57*, 6197-6200.

111. Adak, A. K., Purkait, R., Manna, S. K., Ghosh, B. C., Pathak, S. and Sinha, C., Fluorescence sensing and intracellular imaging of Pd^{2+} ions by a novel coumarinyl-rhodamine Schiff base. *New J. Chem.*, **2019**, *43*, 3899-3906.

112. Dutta, B., Debsharma, K., Dey, S., Naaz, S., Sinha, C. and Mir, M. H., Designing of Interdigitated Coordination Polymer for Fluorogenic Sensing of Pd (II) in Water with Reversible Nonphase Mechanochromism. *Adv. Mater. Interfaces.*, **2022**, *9*, 2201120.

Chapter 2

Ultratrace level detection of Cu^{2+} in aqueous medium by novel Zn(II)-dicarboxylato – pyridyl coordination polymers and cell imaging with HepG2 cells
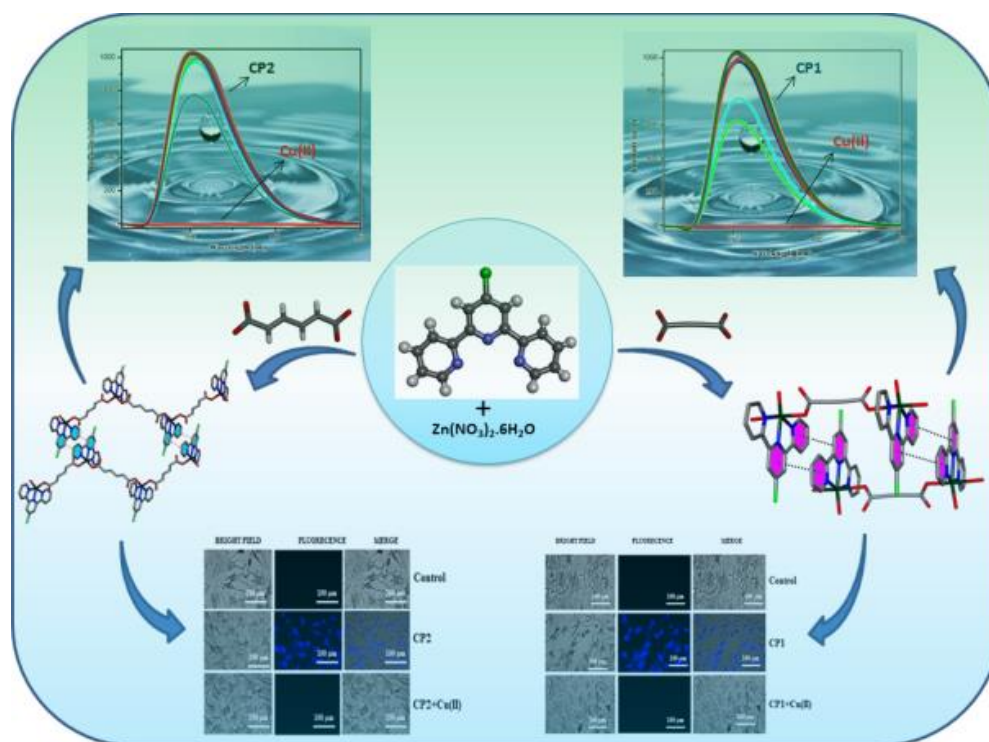
Chapter 2

Abstract

Two newly designed coordination polymers (CPs), [Zn(adc)(4-Cltpy)(H$_2$O)] (CP**1**) and [Zn(*trans*-muca)(4-Cltpy)] (CP**2**) (4-Cltpy = 4′-Chloro-2,2′:6′,2″-terpyridine, H$_2$adc = Acetylene-dicarboxylic acid, *trans*-H$_2$muca = *trans*, *trans*-muconic acid), are synthesized and structurally characterized by single crystal X-ray crystallography, PXRD, TGA, IR and elemental analysis. The coordination unit gets polymerized through the bridging of dicarboxylic acids and a 1D chain has been constructed. Self-assembly of 1D chain *via* H-bonding, C–H···π and π···π interactions makes supramolecular geometry. Interestingly, the 4′-chloro-2,2′:6′,2″-terpyridine appended CPs are highly emissive in aqueous media and exhibit selective quenching by Cu^{2+} ions; the calculated (3σ method) limits of detection (LODs) are 0.14 μM (CP**1**) and 0.06 μM (CP**2**), respectively. Microscopic cell imaging determines the internalization of CPs within HepG2 cells. An MTT assay displays a tolerance limit of 100 μM.

2.1. Introduction

In the history of inorganic chemistry (after the winning of the Nobel prize by Alfred Werner in 1913), the coordination polymers (CPs)[1–11] have been most stimulating in the field of materials science (**Chapter 1**). CPs are the polymeric form of a coordination moiety, and are composed of inorganic and organic components. On judicious selection of the metal and ligands, a variety of CPs can be designed that could exhibit different properties who are the key factor for application. Thus, there is a vital relationship among the structure, properties and applications. CPs are employed for numerous applications, like gas absorption, electrical conductivity, catalysis, water splitting, electrochemistry, magnetism, dye degradation, drug delivery, device fabrication and sensing, *etc*.[12–19] The sensing properties of CPs are utilized as a powerful tool for fluorescence chemosensors[20–28] because of their high sensitivity, selectivity, rapid response, reusability and low cost. Recently, fluorescent materials have been used intensively for the detection of toxic or useful cations, anions and small organic molecules, explosive materials, *etc*. by achieving perceivable changes *via* quenching or enhancement of the luminescence. Fluorescence sensing of CPs has also been applied to detect volatile organic compounds[29,30] (styrene *etc*.), heavily toxic metal ions, chemical sensing and temperature sensing[31]*etc*. However, the fluorescence properties of CPs have been recognised in few cases.[32,33]

Copper is the 3rd most abundant element[34] among the heavy metals (next to Fe, Zn) in biological systems and is a naturally occurring element in the soil, rocks, air, sediment and water. It has played a major role in the growth of civilization by contributing to building construction, electrical equipment, industrial machinery and so forth. It also plays a pivotal role in several physiological processes and is a co-factor of numerous enzymes. But excess uptake of copper is injurious to health as it causes Menkes disease, Wilson's disease, Alzheimer's disease, hypoglycaemia, gastrointestinal disease, dyslexia, infant liver

damage, *etc.*[35] Therefore, it is important to measure Cu^{2+} in food stuffs, drinks, beverages *etc.* as well as in living systems for public health management. Due to its essentiality and toxic nature, intracellular copper absorption and distribution is strictly controlled by cells. One of the methods is to utilise fluorophoric chemosensors for copper detection. There are a few reports[36–38] where CPs are used for Cu^{2+} detection in aqueous solution. Sensor applications in aqueous media are scarce, which may be mainly due to poor solubility and complicated synthetic strategies.

In this aspect, some fluorescence chemosensors have been designed based on coordination compounds, which are mostly 0D, 1D or 3D in nature.[32,33,39–42] This work is focused on the synthesis of two Zn(II)-based CPs of H_2adc (Acetylene dicarboxylic acid)/*trans*-H_2muca (*trans*, *trans*-muconic acid) along with 4-Cltpy (4′-Chloro-2,2′:6′,2″-terpyridine) as a capping agent. Both coordination polymers can specifically detect Cu^{2+} ions in aqueous media with high sensitivity. They are 1D coordination polymers that can undergo H-bonding, C–H···π, π···π and C–Cl···π interactions and form a 3-D supramolecular network. The coordination of carboxylato-O of the CPs to Cu^{2+} may be the reason for the detection of Cu^{2+} in aqueous media by quenching of the emission. Cell imaging experiments support the biocompatibility of the respective CPs and the detection of intracellular Cu^{2+} within HepG2 cells.

2.2. Experimental Section

2.2.1. Materials and Physical Measurements

$Zn(NO_3)_2·6H_2O$, acetylene dicarboxylic acid (H_2adc), *trans*, *trans*-muconic acid (*trans*-H_2muca) and 4′-chloro-2,2′:6′,2″-terpyridine (4-Cltpy) were purchased in reagent grade from different commercial sources and were used without any further purification. The elemental analysis (C, H, N) was executed by a PerkinElmer 240C elemental analyser. FT-IR spectra were obtained with a PerkinElmer spectrometer following the technique of attenuated total reflectance (ATR). The powder X-ray diffraction (PXRD) data collection was performed at

room temperature in a Bruker D8 Advance X-ray diffractometer using a Cu Kα radiation source having a wavelength of 1.548 Å. Thermogravimetric analysis was performed by a PerkinElmer TGA 4000 System, at 100–240 V/50–60 Hz in the temperature range of 30–900 °C with a 10 °C min^{-1} (CP**1**) and 20 °C min^{-1} (CP**2**) heating rate, under a nitrogen atmosphere. The fluorescence spectra were examined by a PerkinElmer spectrofluorometer model LS55 and UV-vis spectra were obtained using a PerkinElmer Lambda 25 spectrophotometer. Measurements of fluorescence lifetime were carried out using a Horiba Jobin Yvon fluorescence spectrophotometer.
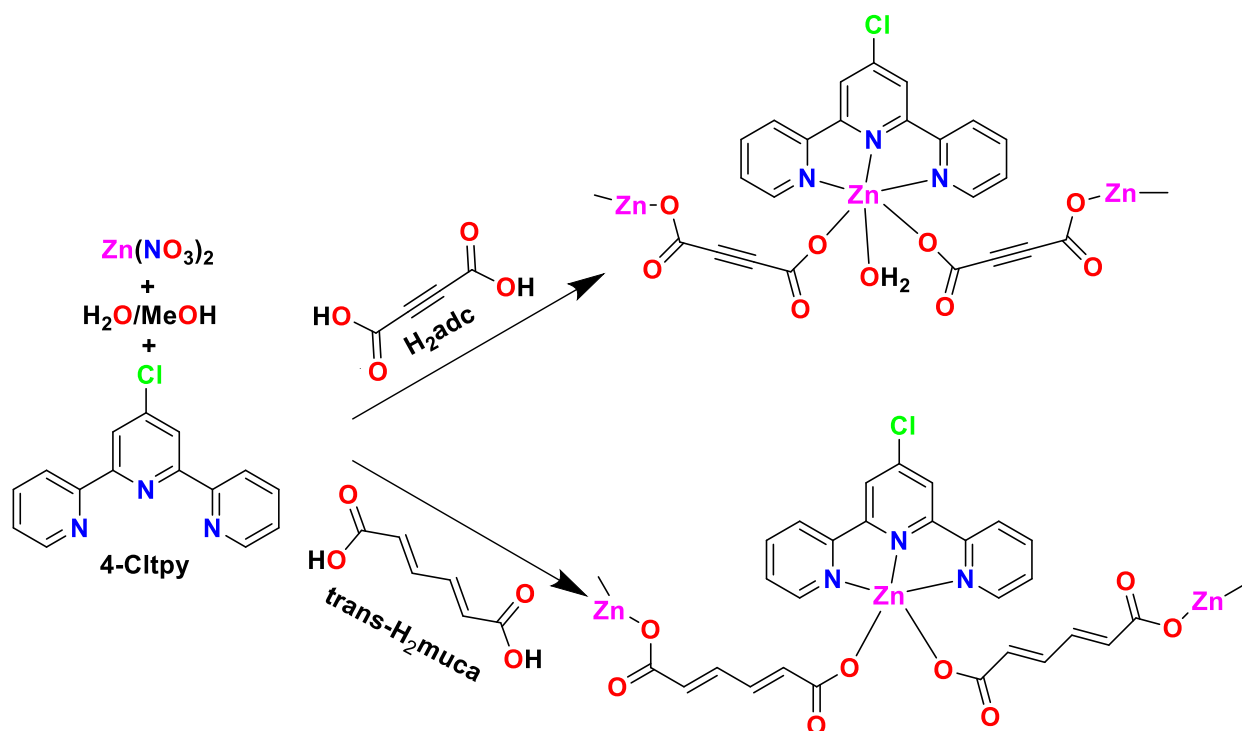
Scheme 2.1. Synthesis of CP**1**/CP**2** upon reaction of Zn(NO$_3$)$_2$ with 4-Cltpy and H$_2$adc/trans-H$_2$muca

2.2.2. Preparation of CPs (CP1, CP2)

The coordination polymer of CP**1** and CP**2** (**Scheme 2.1**) was synthesized by the layering method at room temperature (27 °C). Firstly, an aqueous solution (2 ml) of Zn(NO$_3$)$_2$·6H$_2$O (0.06 g, 0.2 mmol) was taken in a tube and a buffer solution of H$_2$O–MeOH (1 : 1, v/v; 2 ml) was added slowly; then, a methanol (2 ml) solution of 4-Cltpy (0.084 g, 0.05 mmol) was

carefully layered. Finally, the solution of H_2adc (0.023 g, 0.2 mmol) neutralized by Et_3N (0.042 g, 0.4 mmol) in EtOH (2 ml) was coated. Colourless block crystals of (**CP1**) were produced after three days (0.090 g, yield 64%). Elemental analysis (%) Calculated for $C_{19}H_{12}ClN_3O_5Zn$: C, 49.27; H, 2.61; N, 9.07. Found: C, 49.34; H, 2.66; N, 9.12. IR $\bar{\nu}$ (cm^{-1}) 1640 $\nu(-C=O)$, 1558 $\nu_{as}(COO)$, 1311 $\nu_{sys}(COO)$, 775 $\nu(C-Cl)$, 3078 $\nu(H_2O)$ (**Figure 2.1a**).

The coordination polymer **CP2** was also synthesized following an identical procedure using *trans*-H_2muca. The crystals of (**CP2**) were produced after seven days (0.096 g, yield 65%). Micro analytical: (%) Calculated for $C_{21}H_{15}ClN_3O_5Zn$: C, 51.45; H, 3.08; N, 8.57. Found: C, 51.54; H, 3.16; N, 8.66. IR $\bar{\nu}$ (cm^{-1}) 1624 $\nu(-C=O)$, 1553 $\nu_{as}(COO)$, 1351 $\nu_{sys}(COO)$, 866 $\nu(C-Cl)$ (**Figure 2.1b**).
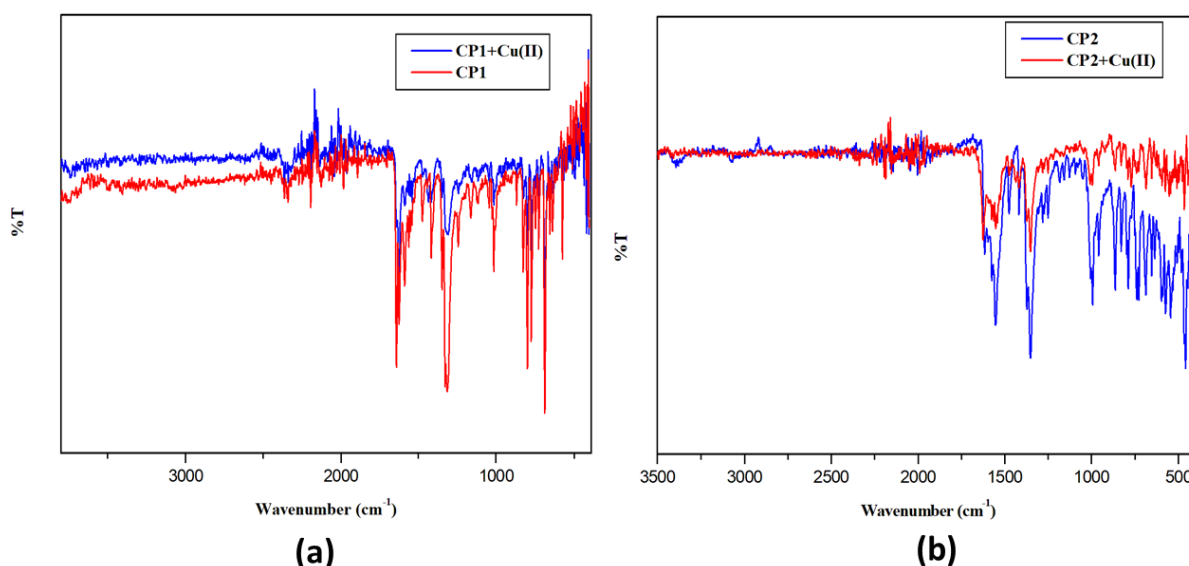
Figure 2.1 (a) IR spectra of CP**1** and CP**1**+Cu(II) ion, **(b)** IR spectra of CP**2** and CP**2**+Cu(II) ion.

2.2.3. X-Ray crystal structure determination

Two colourless crystals with suitable dimensions (size $0.29 \times 0.14 \times 0.08$ Å (CP**1**)/$0.29 \times 0.14 \times 0.07$ Å (CP**2**)) were used for data collection for single crystal X-ray diffraction with the help of a Bruker APEX-II CCD diffractometer equipped with a graphite-monochromated MoKα

radiation source (λ = 0.71073 Å) for CP**1** and CP**2** at 273(2) K. Determination of the single

crystal structures was done with the help of the SHELX-97[43] package. Non-hydrogen

Table 2.1 Crystal data and refinement parameters of CP**1** and CP**2.**

Compounds	CP**1**	CP**2**
Formula	$C_{19} H_{12} Cl N_3 O_5 Zn$	$C_{21} H_{15} Cl N_3 O_5 Zn$
fw	461.19	490.20
crystsyst	triclinic	Triclinic
space group	*P -1*	*P-1*
a (Å)	9.0876(7)	8.697(5)
b (Å)	10.0804(8)	10.798(6)
c (Å)	11.7778(9)	13.165(7)
α(deg)	66.626(2)	100.543(14)
β(deg)	75.962(2)	105.004(14)
γ (deg)	65.717(2)	113.587(14)
V (Å^3)	898.68(12)	1035.5(10)
Z	2	2
D_{calcd}(g/cm^3)	1.704	1.572
μ(mm^{-1})	1.515	1.354
λ(Å)	0.71073	0.71073
data[$I > 2\sigma(I)$]/params	3093/268	3529/286
GOF on F^2	1.343	1.073
final R indices[$I > 2\sigma(I)$]^{a,b}	$R1 = 0.0270$ $wR2 = 0.0990$	$R1 = 0.0766$ $wR2 = 0.2159$

$^aR1 = \Sigma||F_o| - |F_c||/ \Sigma|F_o|$, $^bwR2 = [\Sigma w(F_o^2 - F_c^2)^2/\Sigma w(F_o^2)^2]^{1/2}$

atoms were refined with anisotropic thermal parameters. Hydrogen atoms are situated in their

geometrically idealised positions and constrained to ride over their parent atoms. The

crystallographic data of CP**1** and CP**2** are summarised in **Table 2.1** and selected bond angles

and bond lengths are tabulated in **Table 2.2** and **2.3**.

Table 2.2 Selected bond lengths and bond angles in CP**1.**

Zn(1) - O(1)	1.9870(19)	N(1) - Zn(1) - O(4)b	87.32(8)
Zn(1) - O(3)	2.082(2)	N(2) - Zn(1) - N(3)	75.55(8)
Zn(1) - N(1)	2.154(2)	N(2) - Zn(1) - O(4)b	82.66(7)
Zn(1) - N(2)	2.080(2)	N(3) - Zn(1) - O(4)b	86.46(8)
Zn(1) - N(3)	2.166(2)	Zn(1) - O(3) - C(1)	120.03(17)
Zn(1) - O(4)b	2.510(2)	C(4) - O(4) - Zn(1)a	122.45(18)
O(1) - Zn(1) - O(3)	100.39(8)	Zn(1) - N(1) - C(15)	115.47(17)
O(1) - Zn(1) - N(1)	110.65(8)	Zn(1) - N(1) - C(19)	125.85(16)
O(1) - Zn(1) - N(2)	163.19(8)	Zn(1) - N(2) - C(10)	119.84(16)
O(1) - Zn(1) - N(3)	95.85(8)	Zn(1) - N(2) - C(14)	118.93(16)
O(1) - Zn(1) - O(4)b	82.41(7)	Zn(1) - N(3) - C(5)	124.97(16)
O(3) - Zn(1) - N(1)	95.18(8)	Zn(1) - N(3) - C(9)	115.85(17)
O(3) - Zn(1) - N(2)	94.03(7)	N(1) - Zn(1) - N(3)	151.69(7)
O(3) - Zn(1) - N(3)	89.46(8)	N(1) - Zn(1) - N(2)	76.27(8)
O(3) - Zn(1) - O(4)b	175.29(8)		

a = x,-1+y,z   b = x,1+y,z

Table 2.3 Selected bond lengths and bond angles in CP**2.**

Zn(1) - O(1)	1.961(4)	N(1) - Zn(1) - N(2)	74.7(2)
Zn(1) - O(3)	1.951(5)	N(1) - Zn(1) - N(3)	150.69(18)
Zn(1) - N(1)	2.211(6)	N(2) - Zn(1) - N(3)	76.2(2)
Zn(1) - N(2)	2.092(5)	Zn(1) - O(1) - C(19)	119.5(4)
Zn(1) - N(3)	2.174(7)	Zn(1) - O(3) - C(3)	115.4(4)
O(1) - Zn(1) - O(3)	98.53(18)	Zn(1) - N(1) - C(14)	116.1(4)
O(1) - Zn(1) - N(1)	92.3(2)	Zn(1) - N(1) - C(18)	125.6(4)

O(1) - Zn(1) - N(2)	132.83(19)	Zn(1) - N(2) - C(9)	117.8(4)
O(1) - Zn(1) - N(3)	104.9(2)	Zn(1) - N(2) - C(13)	119.9(4)
O(3) - Zn(1) - N(1)	105.0(2)	Zn(1) - N(3) - C(4)	126.3(5)
O(3) - Zn(1) - N(2)	128.6(2)	Zn(1) - N(3) - C(8)	115.4(5)
O(3) - Zn(1) - N(3)	95.8(2)	N(1) - Zn(1) - N(3)	150.69(18)

a = x,-1+y,z   b = x,1+y,z

2.2.4. UV-Visible and Fluorescence experiments

Finely powdered **CP1** was mixed in 10 ml of CH_3CN to make a suspension (1.0×10^{-3} M). An acetonitrile solution of **CP2** (1×10^{-3} M) was also prepared in a similar way. All required metal $M(OAc)_x$ (M = Zn^{2+}, Cu^{2+}, Cd^{2+}, Hg^{2+}), $M(NO_3)_x$ (M = Al^{3+}, Pb^{2+}, Co^{2+}) and MCl_x (M = Mn^{2+}, Ni^{2+}, Fe^{3+}, Mg^{2+}, Ca^{2+}, Ba^{2+}, Na^{+}, K^{+}) solutions (1×10^{-3} M) were prepared in methanol. For all the spectral measurements (UV-visible, Fluorescence), a 50 μM working solution was prepared in H_2O (HEPES buffer, pH 7.2) by taking 50 μl of the above stock solution and into this solution 1.00 equivalent of metal salt was added. A similar experiment was also performed using a solution of **CP2** and the sensor experiments were performed at pH 7.2. Fluorescence measurements of CPs were carried out using excitation slit 15, emission slit 5 (**CP1**) and excitation slit 15, emission slit 7 (**CP2**). Excitation wavelengths of 285 nm (**CP1**) and 260 nm (**CP2**) were used for the fluorescence experiments. In the absence of quencher (Q), the lifetime is abbreviated as τ_0 of CPs and the corresponding fluorescence quantum yield is abbreviated as ϕ_0. According to the following equation: $\phi_0/\phi = 1 + K_q\tau_0[Q]$, where K_q is the rate constant and ϕ is the fluorescence quantum yield in the presence of the quencher. The fluorescence quantum yield is proportional to the emission intensity. The quenching rate constant were calculated using $I_0/I = K_{SV}[Q] + 1$, where I_0 is the intensity of the coordination polymer (**CP1/CP2**), I is the intensity after the addition of Cu^{2+} ions and $K_{SV} = K_q\tau_0$ (Stern–Volmer constant).

2.2.5. Cell line culture

Hep G2 (Human liver cancer cell line) and WI-38 (human lung fibroblast cells) were procured from the National Center for Cell Science (NCCS) Pune, India. These human cells were cultured in DMEM, 10% FBS (Fetal Bovine Serum), and penicillin/streptomycin (100 units per ml) at a temperature of 37 °C and CO_2 pressure of 5%. All the treatments were performed at a cell density that facilitates growth of the cells exponentially.

2.2.6. Cell Imaging

The HepG2 cells were cultured for 24 h in coverslips. The cultured cells were then either mock-exposed or exposed to CP**1**/CP**2** at a concentration of 10 μM of CP**1**/CP**2** in the absence or presence of Cu^{2+} salts (10 μM) and were incubated for a span of 24 h at a temperature of 37 °C.[44] Thorough washing was then carried out with $1 \times$ PBS buffer solution and the cells were used for investigation under a fluorescence microscope (Leica).

2.2.7. Cell survivability assay

The cell survivability study of CP**1** and CP**2** was performed against the human lung fibroblast cells, WI-38.[45] To carry out the MTT assay, the viability of WI-38 cells was assessed after exposure to several concentrations of the ligand. The cells were seeded at 1×10^4 cells per well in 96-well plates and were treated with the ligand at different concentrations (0–100 μM) for a span of 24 h. The cultured cells were washed twice with $1 \times$ PBS and incubated at a temperature of 37 °C with a solution of MTT (450 μg ml^{-1}) for a period of 3–4 h. The MTT solubilisation buffer was employed to dissolve the produced formazan crystals and the peak of absorbance was observed at 570 nm with the aid of a spectrophotometer (BioTek).

2.3. Results and Discussion

2.3.1. Structural Description of CP1 and CP2

Single crystal X-ray data reveal that CP**1** crystallises in the triclinic space group $P\bar{1}$ with $Z = 2$. In the molecular unit, Zn(II) appears in a distorted octahedral geometry with a ZnO_3N_3 coordination

61

sphere. Three-Ns are coming from 4-Cltpy in a chelating fashion, two-O atoms coordinate from two adc^{2-} anions in a monodentate fashion and one H_2O molecule is also coordinated (**Figure 2.2a**). Hence, dicarboxylate anions bridge two Zn^{2+} centres and form a linear 1D polymeric chain (**Figure 2.2b**) [Zn1–O1, 1.987(19), Zn(1)–O(3), 2.082(2), Zn1–O4, 2.510(2), Zn1–N2, 2.085(2), Zn1–N1, 2.147(2), Zn1–N3, 2.211(3) Å]. Strong intermolecular hydrogen bond formation occurs between the coordinated H_2O and carboxylato-O of adc^{2-} with the O···H separation of 1.958 Å (**Figure 2.3**). This intermolecular H-bonding interaction has been employed for the formation of a 2D supramolecular assembly.

Figure 2.2. (a) The coordination atmosphereof hexa-coordinated Zn(II) in CP**1**, **(b)** View of 1D coordination polymer with four Zn(II) center, **(c)** π···π interaction in CP**1**,**(d)** Supramolecular assembly of linear 1D coordination polymer.
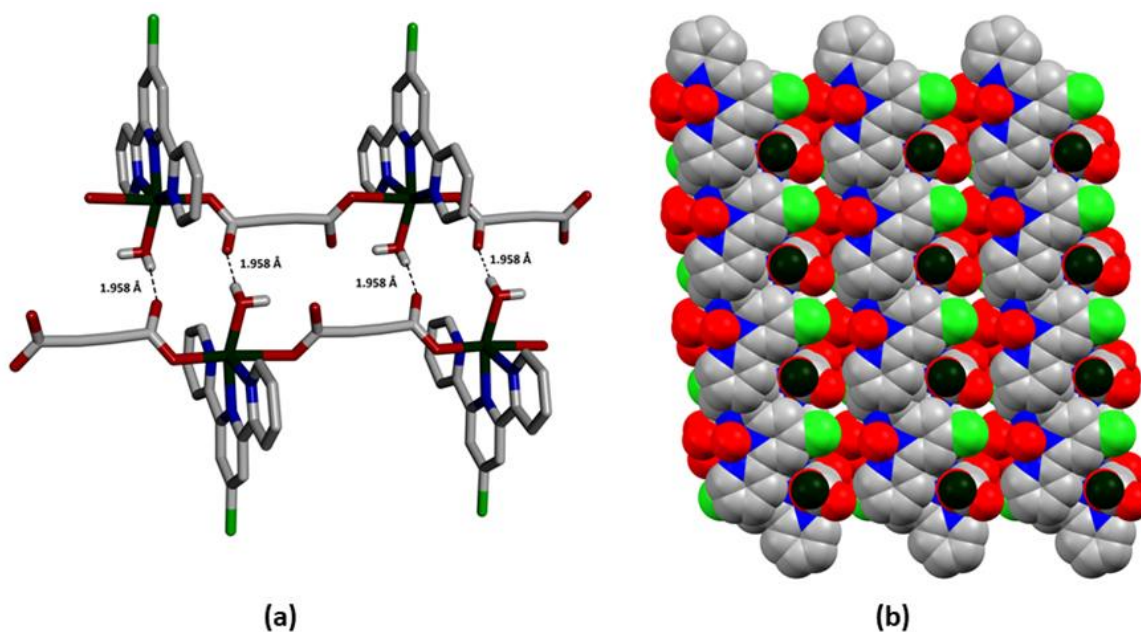
Figure 2.3. **(a)** H-bonding interaction between water and adc^{2-} ion in CP**1**. **(b)** spell field model of CP**1.**

There are $\pi\cdots\pi$ stacking interactions between the adjacent pyridine rings of 4-Cltpy (**Figure 2.2c**). Thus H-bonding along with $\pi\cdots\pi$ stacking gives rise to supramolecular aggregates (**Figure 2.2d**). Dutta *et al.* designed a Zn(II)-based 1D CP of the same ligands, but the coordination atmosphere and the structural architecture are different.[46]

The asymmetric unit of the block shaped colourless crystals of CP**2**, space group-triclinic, *P* $\bar{1}$ and *Z* = 2, displays a distorted trigonal bipyramidal geometry where Zn(II) is coordinated with three N atoms of 4-Cltpy in a tridentate fashion and two carboxylate-O of the muca^{2-} moiety coordinated in a monodentate fashion (**Figure 2.4a**). This coordination repeating unit is extended into a 1D linear polymeric structure through muca^{2-} bridging with two Zn(II) centres. Elongation of the asymmetric unit along the "a" axis generally forms a beautiful zig zag structure (**Figure 2.4b**). The connectivity of the neighbouring carboxylate-O with the Zn(II) centres generates a 1D CP [Zn1–O1 1.961(4), Zn1–O3 1.951(5), Zn1–N2 2.092(5), Zn1–N1 2.211(6), Zn1–N3 2.174(7) Å] which assembles through $\pi\cdots\pi$ interaction (**Figure 2.5**) and displays a chair-like structure (**Figure 2.4c**). The distance between the neighbouring π clouds

of two 1D coordination polymers is 3.843 Å. The supramolecular aggregate ion of the 1D coordination polymer due to C–Cl···π, C–H···π and π···π interactions is shown in **Figure 2.4d**. The phase purities of CP**1** (**Figure 2.6a**) and CP**2** (**Figure 2.6b**) were determined from PXRD data.
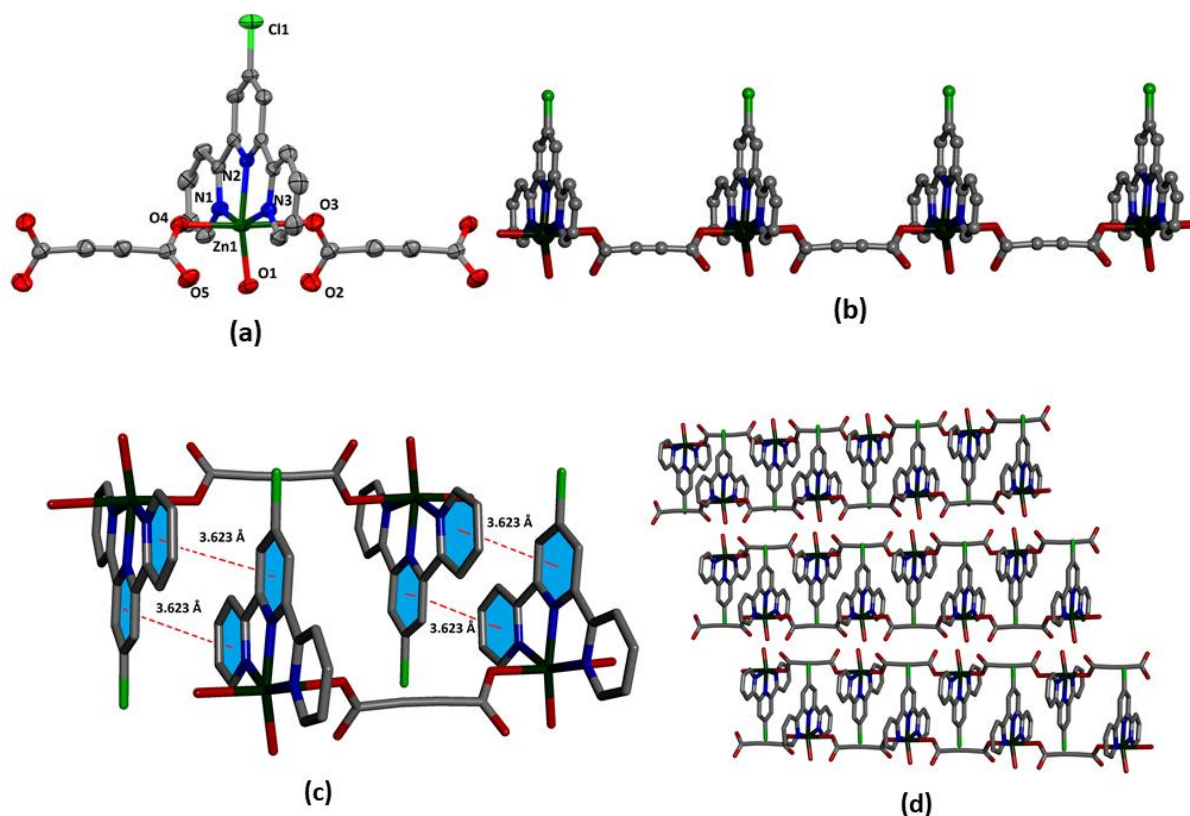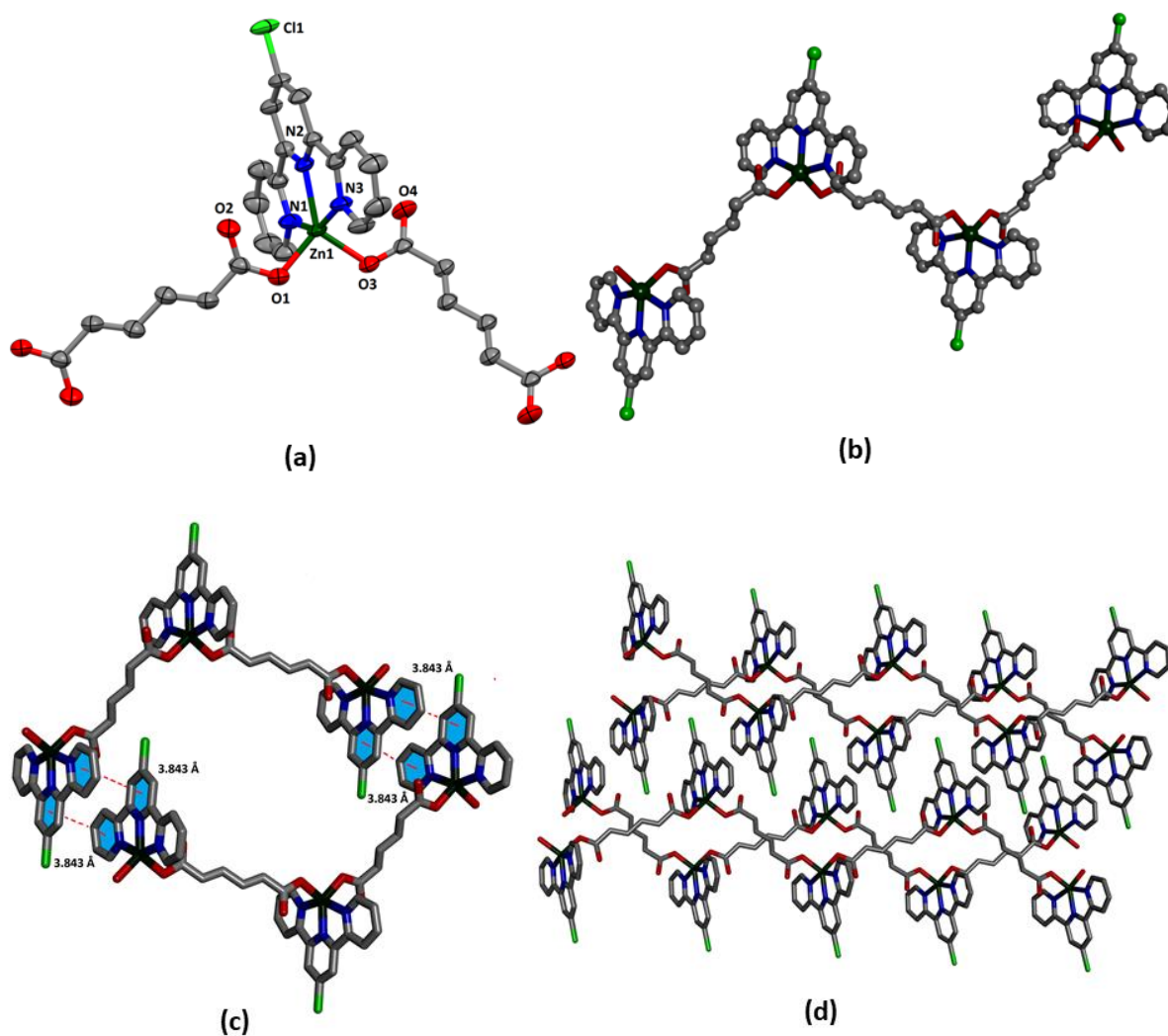

Figure 2.4 (a) The coordination atmosphereof penta-coordinatedZn(II) in CP**2**,**(b)**View of 1D Coordination polymer with four Zn(II) centre,**(c)** View of π···π interaction in CP**2**,**(d)**Supramolecular assembly of linear 1D coordination polymer.
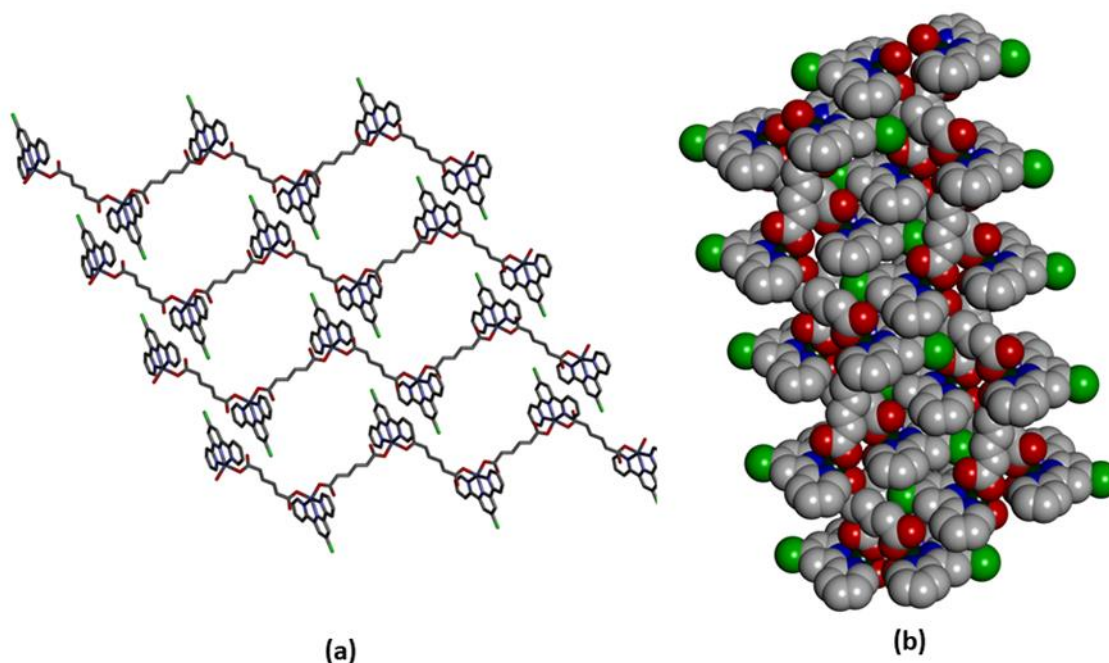
Figure 2.5. (a) Supramolecular aggregate of 1D coordination polymer. **(b)** Spell field model of CP**2**.
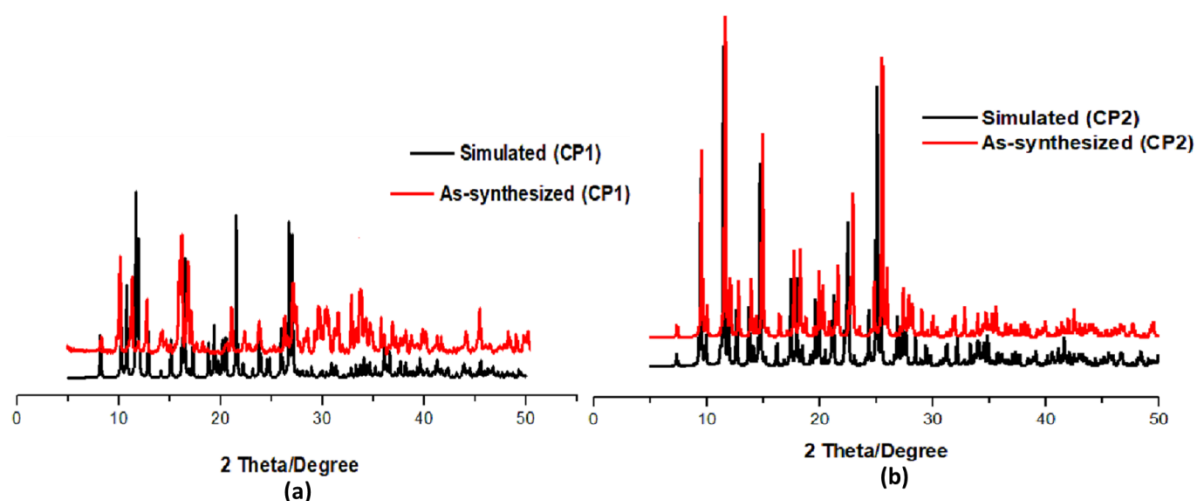
Figure 2.6. Powder X-ray Diffraction analysis of CP**1 (a)** and CP**2 (b)**.

The thermal stability of the CP**1**/CP**2** coordination polymers was checked by thermogravimetric analysis (TGA), which was performed in the temperature range of 30–900 °C, at a rate of 10 °C min^{-1} under a N$_2$ atmosphere. For CP**1**, the first weight loss of 3.82% (calcd. 3.90%) was observed in the temperature range of 175–180 °C, which is due to the loss of a water molecule from the crystal lattice. This compound is stable up to 350 °C and then decomposes (**Figure 2.7a**). For CP**2**, weight loss starts at 300 °C, and it is stable up to 340 °C and then decomposes (**Figure 2.7b**). The TGA

analysis of CP**1** shows that there is one water molecule in the lattice. But below 200 °C, no weight loss for CP**2** is observed, which means that there is no coordinated water molecule in the crystal lattice.
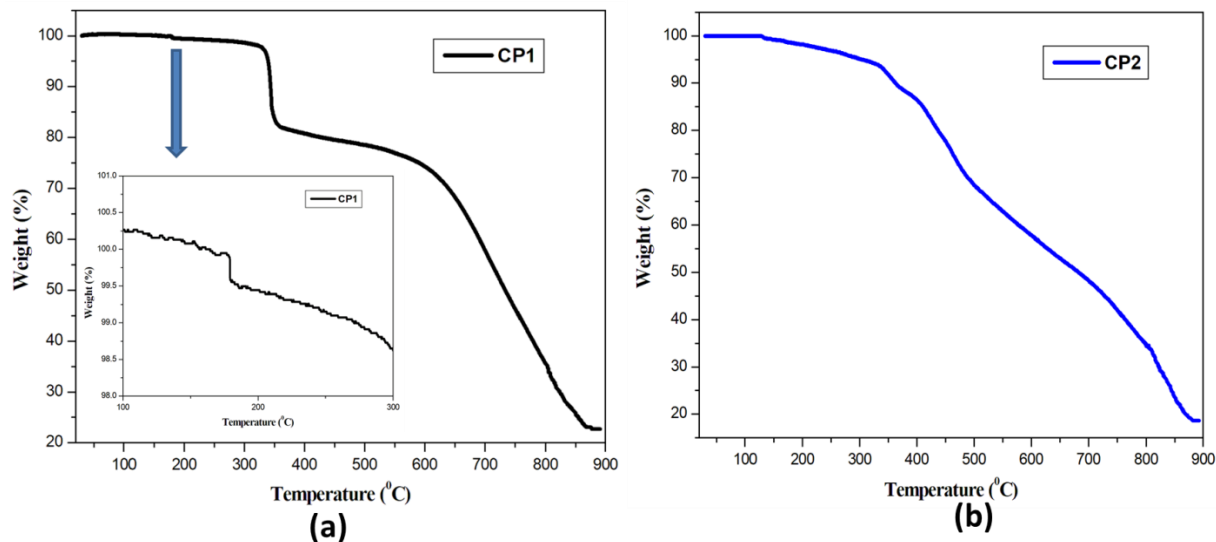
Figure 2.7. Thermogravimetric analysis (TGA) spectra of CP**1 (a)**, CP**2 (b).**
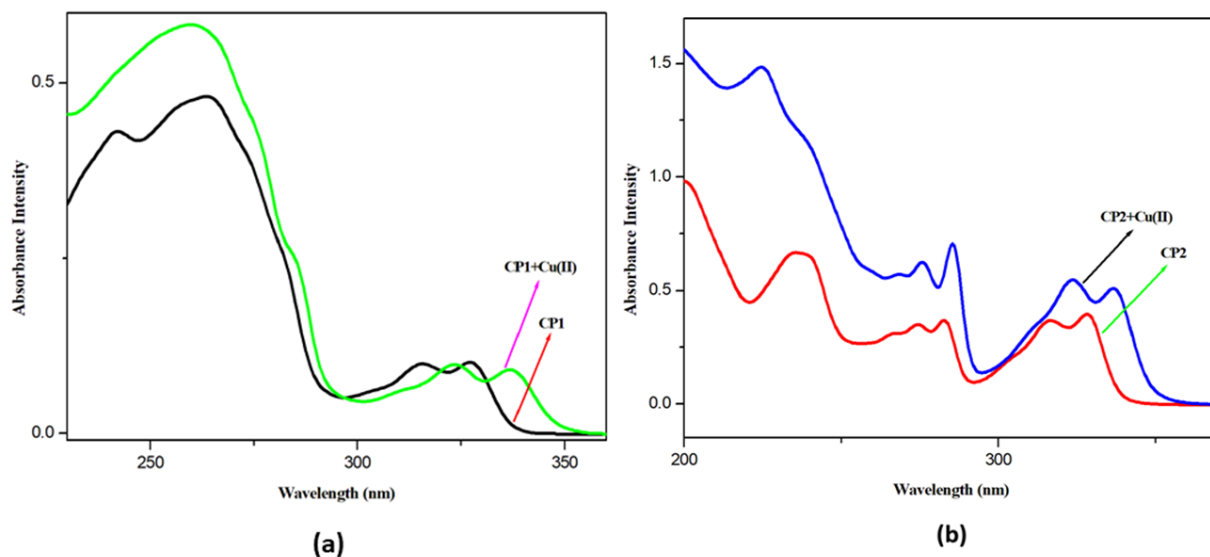
Figure 2.8. (a) UV Visible spectra of CP**1** and CP**1**+Cu^{2+} in aqueous medium. **(b)** UV-Visible spectra of CP**2** and CP**2**+Cu^{2+} in aqueous medium.
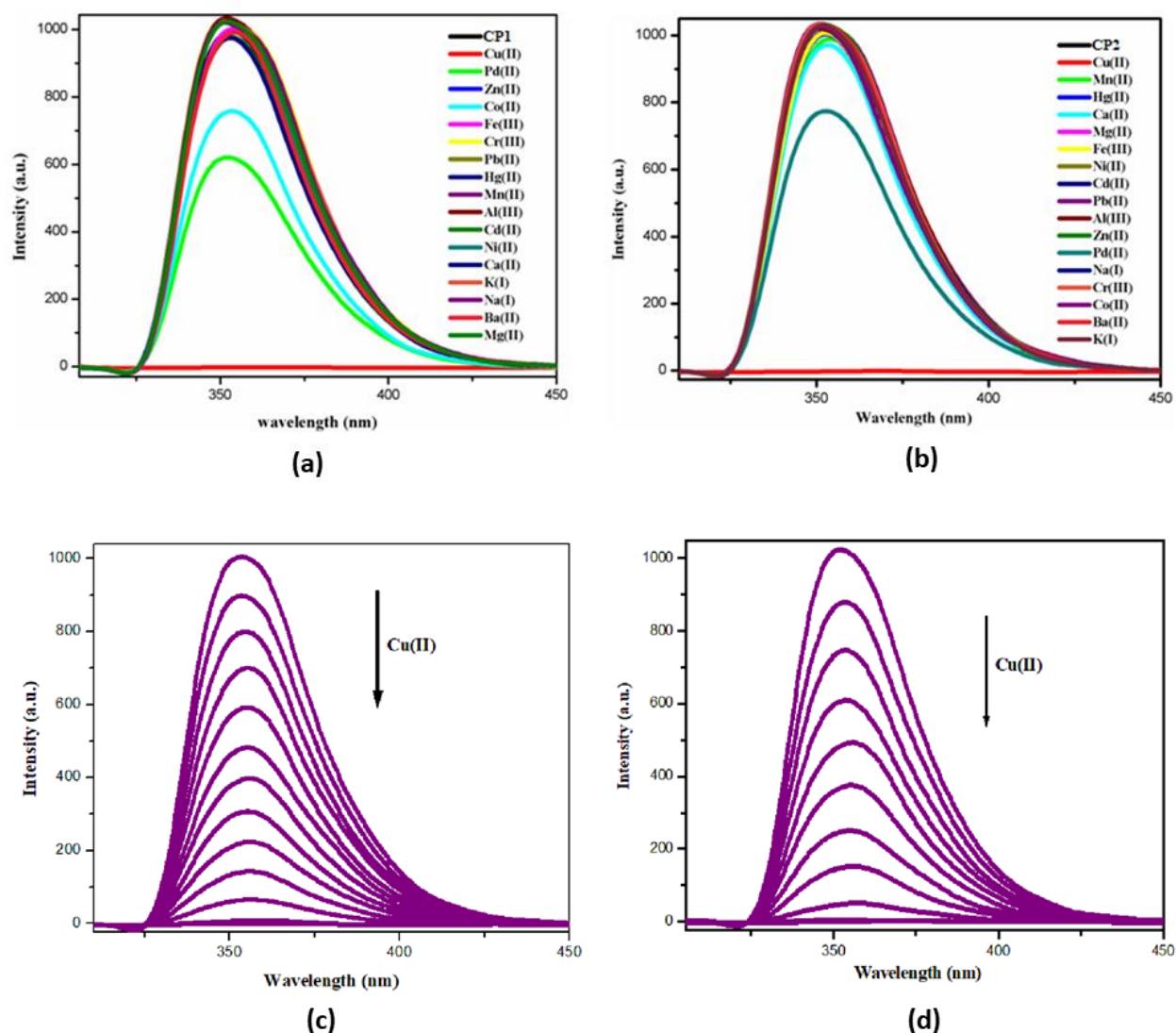
Figure 2.9. **(a)** Emission spectra of **CP1** in presence of different metals ion solutionwith excitation wavelength 285 nm in water medium; **(b)** Emission spectra of **CP2** in presence of different metals ion solution with excitation wavelength 260 nm in water medium; **(c)** Change in fluorescence emission spectra of **CP1** upon addition of Cu^{2+} ion with excitation wavelength 285 nm in aqueous medium; **(d)** Fluorescence quenching of **CP2** on adding Cu^{2+} ion with excitation wavelength 260 nm in aqueous medium.

2.3.2. Fluorescence quenching performance of CP1/CP2 towards Cu^{2+}

The UV-visible spectrum of **CP1** in aqueous solution displays two absorption bands at 327 and 315 nm (**Figure 2.8a**). Similarly, **CP2** also shows peaks at 327 and 316 nm (**Figure 2.8b**). **CP1** and **CP2** exhibit emission in aqueous media at 354 nm (**CP1**) and 352 nm (**CP2**) (room

temperature 27 °C) upon excitation at 285 and 260 nm, respectively. Polypyridines are excellent π-acidic fluorophoric scaffolds and Zn(II) coordination (d^{10} configuration) complexes of polypyridines are highly emissive due to the elimination of photo-induced electron transfer (PET) and inclusion of chelation enhanced fluorescence (CHEF). Thus, the Zn(4-Cltpy)-scaffold is emissive in nature.[47] The emission intensity (354 nm/352 nm) drastically decreases upon addition of Cu^{2+} ions (**Figure 2.9a-b**), but other metal ions (Zn^{2+}, Cd^{2+}, Hg^{2+}, Al^{3+}, Pb^{2+}, Co^{2+}, Mn^{2+}, Ni^{2+}, Fe^{3+}, Mg^{2+}, Ca^{2+}, Ba^{2+}, Na^{+}, K^{+} (MCl_n, $M(OAc)_n$, $M(NO_3)_n$, where $n = 1, 2, 3$)) do not exhibit any significant change in emission property. To examine the effect of anions, the copper salts of different anions (Cl^- NO_3^-, SO_4^-, OAc^-, ClO_4^-) were used and no significant change of fluorescence behaviour is observed (**Figure 2.10a** (CP**1**) and **Figure 2.10b** (CP**2**)). Hence, the emission property of CPs is indifferent to anions. For quantitative detection of Cu^{2+} ions, fluorometric titration was also performed for CP**1** (**Figure 2.9c**) and CP**2** (**Figure 2.9d**). The emission intensity (354 nm (CP**1**) and 352 nm (CP**2**)) gradually decreases upon addition of Cu^{2+} ions (1.5 µL in every step). The emission intensity
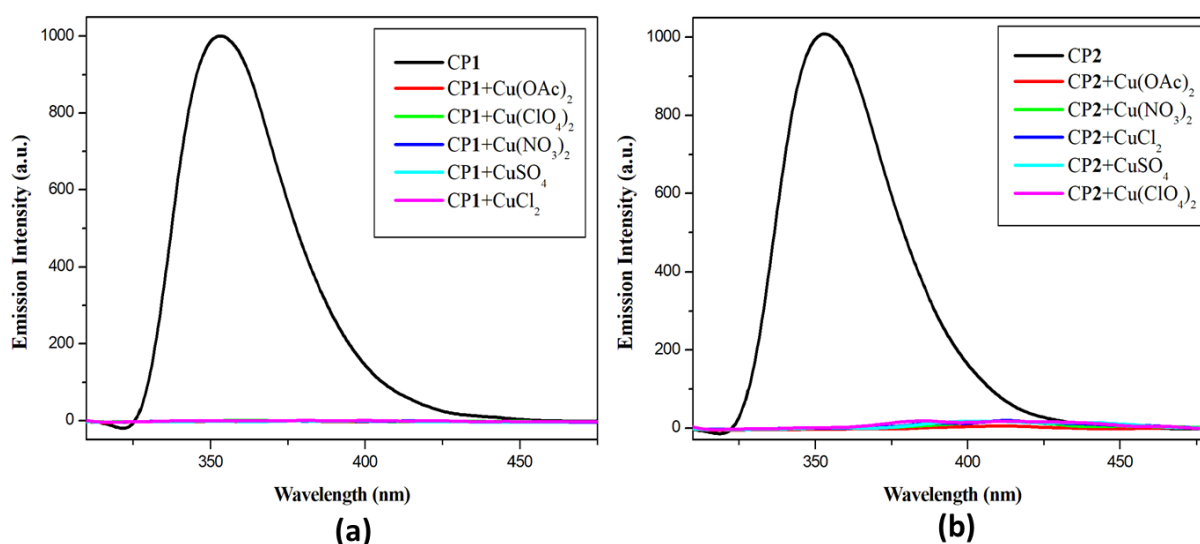
Figure 2.10. (a) Emission Intensity of CP**1** in presence of different Cu^{2+} salts, **(b)** Emission Intensity of CP**2** in presence of different Cu^{2+} salts.

of CP**1** and CP**2** does not change with variation of the pH (2 to 12), the complexes are emissive in the pH range used and in the presence of Cu^{2+} ions, the emission is quenched without preferring any pH (**Figure 2.11**). The fluorometric experiments were evaluated at pH = 7.2 maintained by HEPES buffer. The Stern–Volmer constant, K_{SV}, is calculated from $I_0/I = K_{SV}[Q] + 1$ (I_0, the intensity of the coordination polymer (CP**1**/CP**2**) only; I, the intensity after the addition of Cu^{2+} ions) and it is 2.30393×10^5 M^{-1} (CP**1**; **Figure 2.12**) and 3.685×10^5 M^{-1} (CP**2**, **Figure 2.13**). The calculated lifetime (τ_0) is 1.5145×10^{-9} s (CP**1**) and 1.6478×10^{-9} s (CP**2**) before addition of the quencher. Here, $K_{SV} = K_q\tau_0 \gg 1$; this indicates static quenching for both CPs. The results display that the Ksv value of CP**2** is higher than that of CP**1** and the lifetime ((τ_0) values are nearly the same for both CPs.
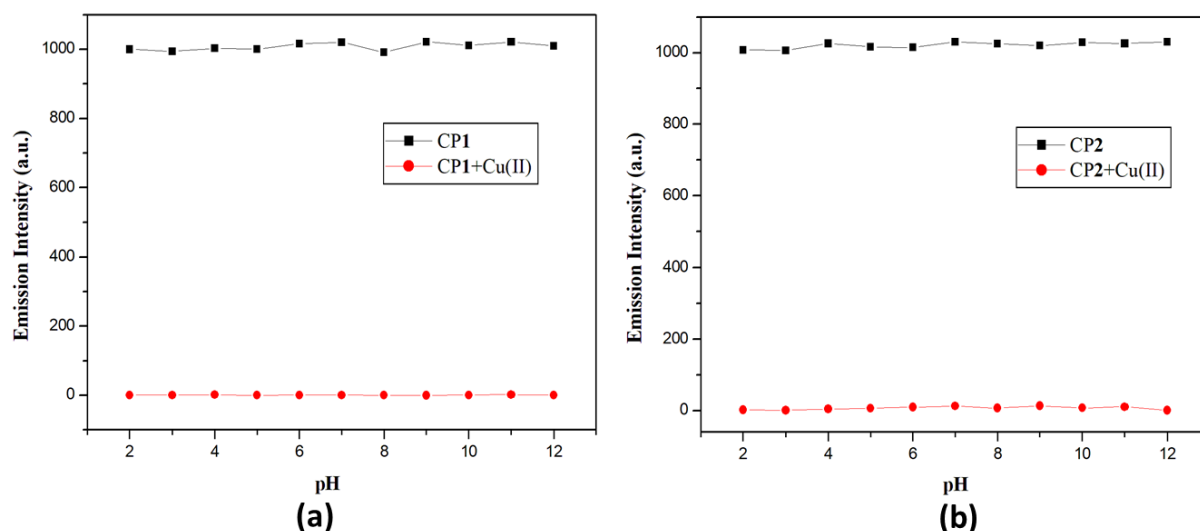
Figure 2.11. (a) Emission Intensity of CP**1** and CP**1** in presence of Cu(II) ion at different pH, **(b)** Emission Intensity of CP**2** and CP**2** in presence of Cu(II) ion at different pH.

As a result, the quenching rate constant K_q is higher in CP**2** than CP**1**. In addition, the quencher Cu^{2+} is more efficient for CP**2** than CP**1**, *i.e.*, CP**2** is more sensitive towards Cu^{2+} quenching. From the above experimental evidence, it is concluded that the CPs (CP**1** and CP**2**) are efficient Cu^{2+} ion sensors; the efficiency of the Zn(II)-coordination
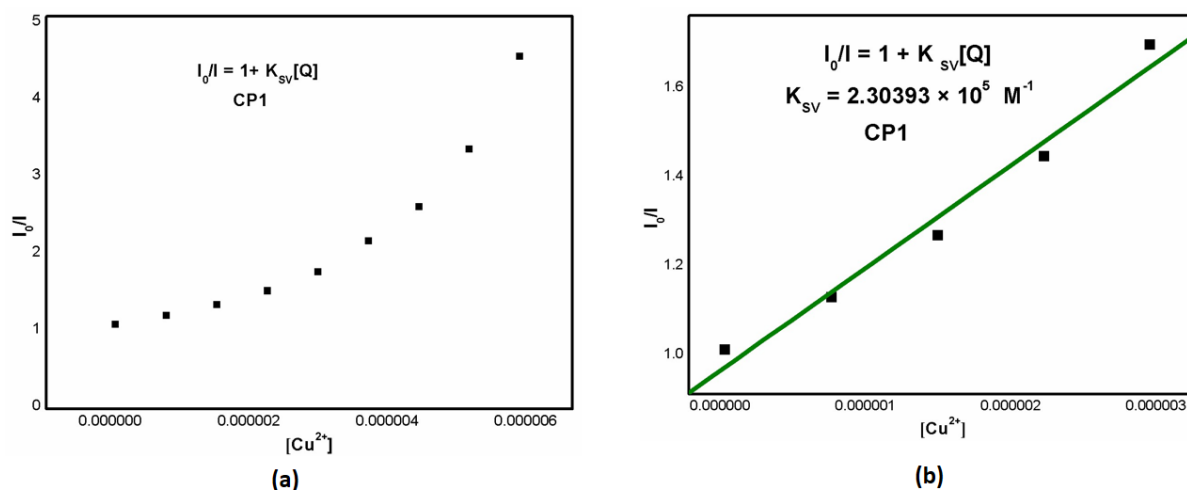
Figure 2.12. (a) Stern-Volmer plot of CP**1. (b)** Stern-Volmer plot of CP**1** at lower range of quencher [Cu^{2+}] (in M) concentration.
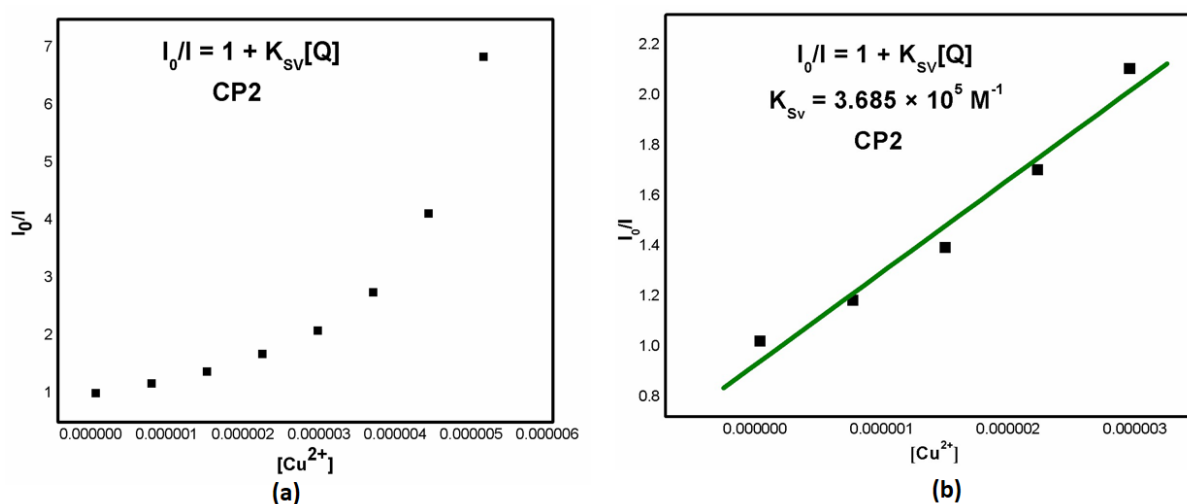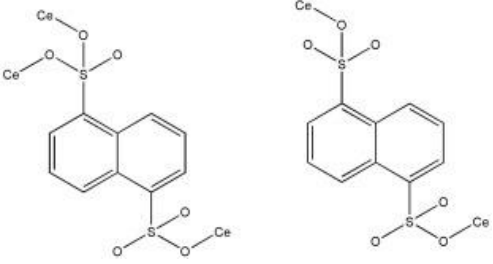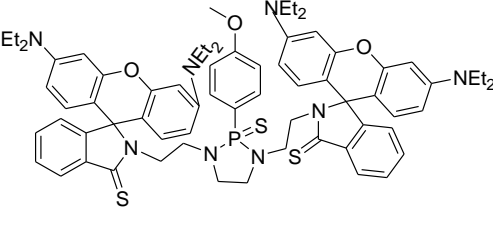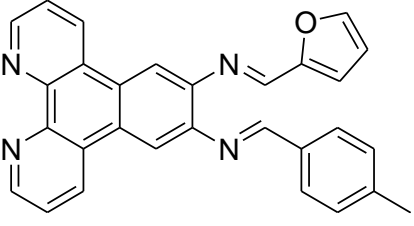
Figure 2.13. Stren-Volmer plot of CP**2**. **(b)** Stern-Volmer plot of CP**2** at lower range of quencher [Cu^{2+}] (in M) concentration.

polymers has been compared with some other reported results in the literature.[37,48–50] However, Cu^{2+} quenching in an aqueous medium with a low limit of detection is still challenging. The Zn(II) CPs in this work are highly selective to Cu^{2+} ions compared to the reported data (**Table 2.4**). According to the World Health Organization (WHO) and U.S. Environmental Protection Agency (EPA), the limit of copper concentration is 2 ppm and 1.3 ppm in drinking water, respectively. Here, the detection limits of CP**1** (0.06 ppm) and CP**2** (0.03 ppm) (calculated by $3\sigma/M$, where M = slope, σ = standard deviation) mean that very low concentrations of Cu(II)

are easily detectable by the present CPs (**Figure 2.14**). The Cu(II) sensitivity of CP**2** (LOD, 0.06 μM or 0.03 ppm) is about twice that of CP**1** (LOD, 0.14 μM or 0.06 ppm).

Table 2.4. Comparison data for Cu^{2+} ion sensor.

Sl. No.	Ligand	Selectivity (LOD)	Solvent	Live Cell Imaging	Reference
1.		3.0 μM.	Water	No	51
2.	SSA/AMP-Tb, 5-sulfosalicylic acid (SSA), adenosine monophosphate (AMP) and terbium ion (Tb^{3+}),	0.3 μM	HEPES buffer (0.1 M, pH 7.4)	No	52
3.		0.01 μM.	MeCN	No	53
4.		0.45 μM.	MeOH	No	54
5.	CP**1** and CP**2**	0.14 μM and 0.06 μM respectively.	Water	Yes	**This Work**
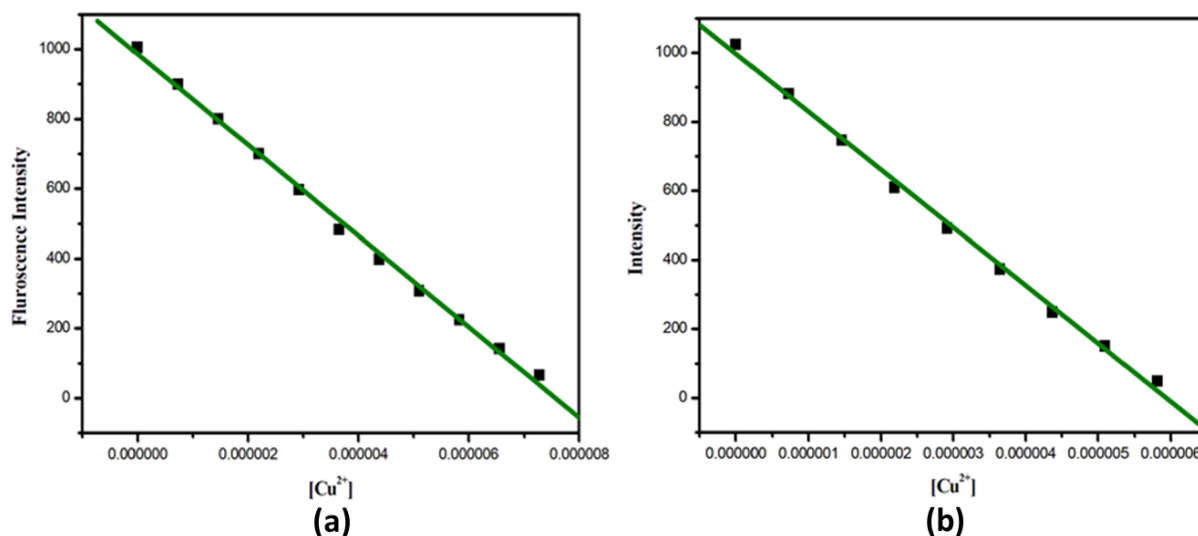
Figure 2.14. (a) The linear dynamic response of CP**1** for Cu^{2+} ion and the determination of the limit of detection (LOD) of Cu^{2+} ion. **(b)** The linear dynamic response of CP**1** for Cu^{2+} ion and the determination of the limit of detection (LOD) of Cu^{2+} ion.
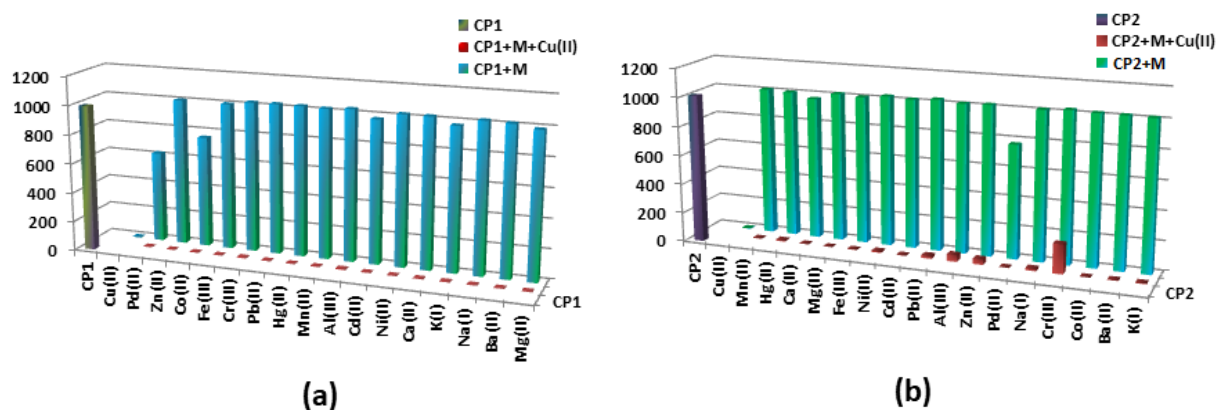
Figure 2.15. Interference of various metal ions with Cu^{2+} in CP**1** (**a**) and CP**2** (**b**).

The results may have some correlation with the structure of the CPs; Zn(II) is six coordinated (bond length C(1)–O(2) = 1.224 Å and ∠O(1)–Zn(1)–O(4) = 82.40°) and distorted octahedrally arranged in CP**1**, while it is five coordinated (bond length C(1)–O(2) = 1.243 Å and ∠O(1)–Zn(1)–O(3) = 98.53°) and distorted trigonal pyramidal in CP**2**. Interaction of carboxylato-O towards Cu^{2+} ions become easier in CP**2** than in CP**1**. This is because the longer –'CO' bond length and less steric hindrance (six coordinate and higher bond angle) in CP**2** may allow better energy transfer in the excited state.

72
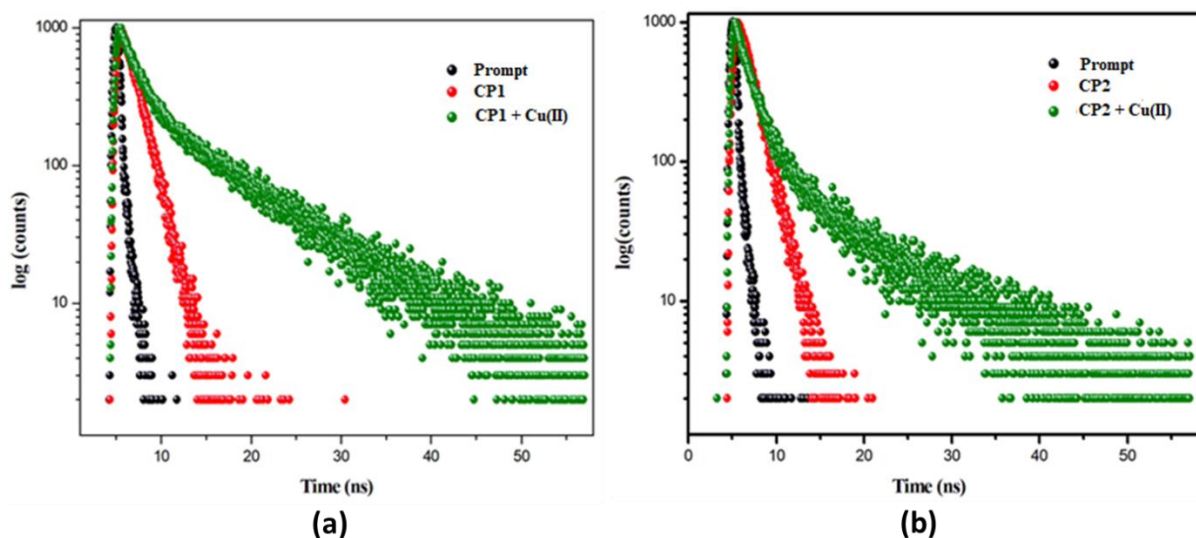
Figure 2.16 (a) Excited state decay profile of prompt, CP**1** and Cu^{2+} ion with CP**1** in aqueous medium. **(b)** Excited state decay profile of prompt, CP**2** and Cu^{2+} ion with CP**2** in aqueous medium.

The quenching effect of Cu^{2+} in the presence of different competitive cations, like Zn^{2+}, Cd^{2+}, Hg^{2+}, Al^{3+}, Pb^{2+}, Co^{2+}, Mn^{2+}, Ni^{2+}, Fe^{3+}, Mg^{2+}, Ca^{2+}, Ba^{2+}, Na^{+}, and K^{+}, is shown in **Figure 2.15**. Comparing the interference plots of the two CPs, it is shown that the quenching effect of Cu^{2+} ions in CP**2** is interfered with by Cr^{3+} ions. The fluorescence lifetimes (τ) of CP**1** and CP**2** in the presence of Cu^{2+} ions are 3.4755×10^{-9} s and 2.5095×10^{-9} s, respectively, but the free CPs have a life time (τ_0) of 1.5145×10^{-9} s (CP**1**) and 1.6478×10^{-9} s (CP**2**) (**Figure 2.16**). In the selective sensing of Cu^{2+} by CP**1** and CP**2** have no effect of constituent ligands (**Figure 2.17**).
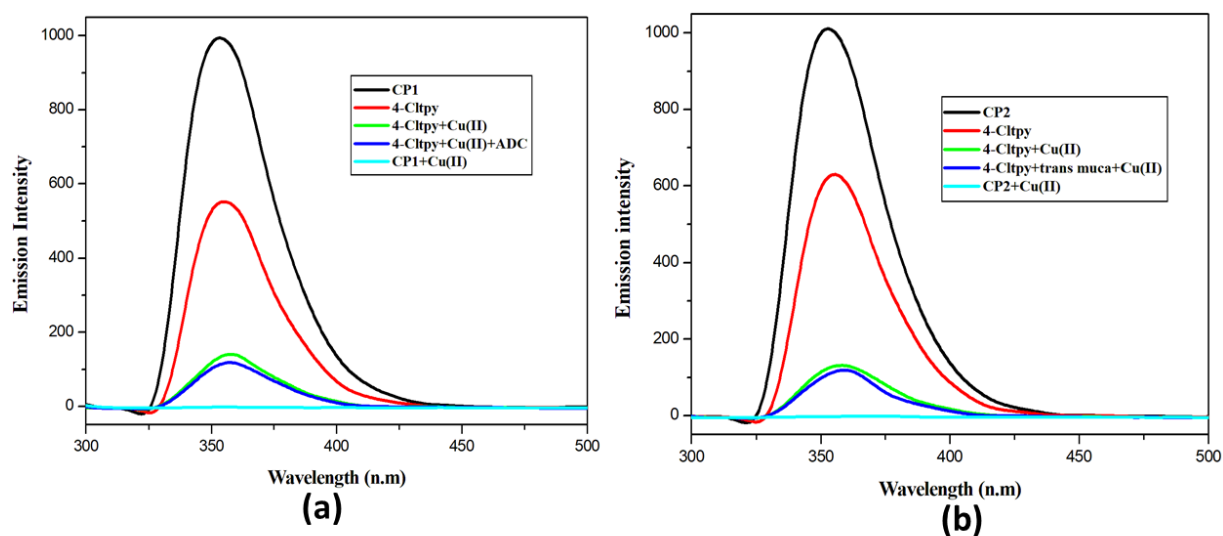
Figure 2.17 (a) Emission intensity of CP**1**, constitute materials of CP**1** and their intensity change in presence of Cu(II) ion. **(b)** Emission intensity of CP**2**, constitute materials of CP**2** and their intensity change in presence of Cu(II) ion.
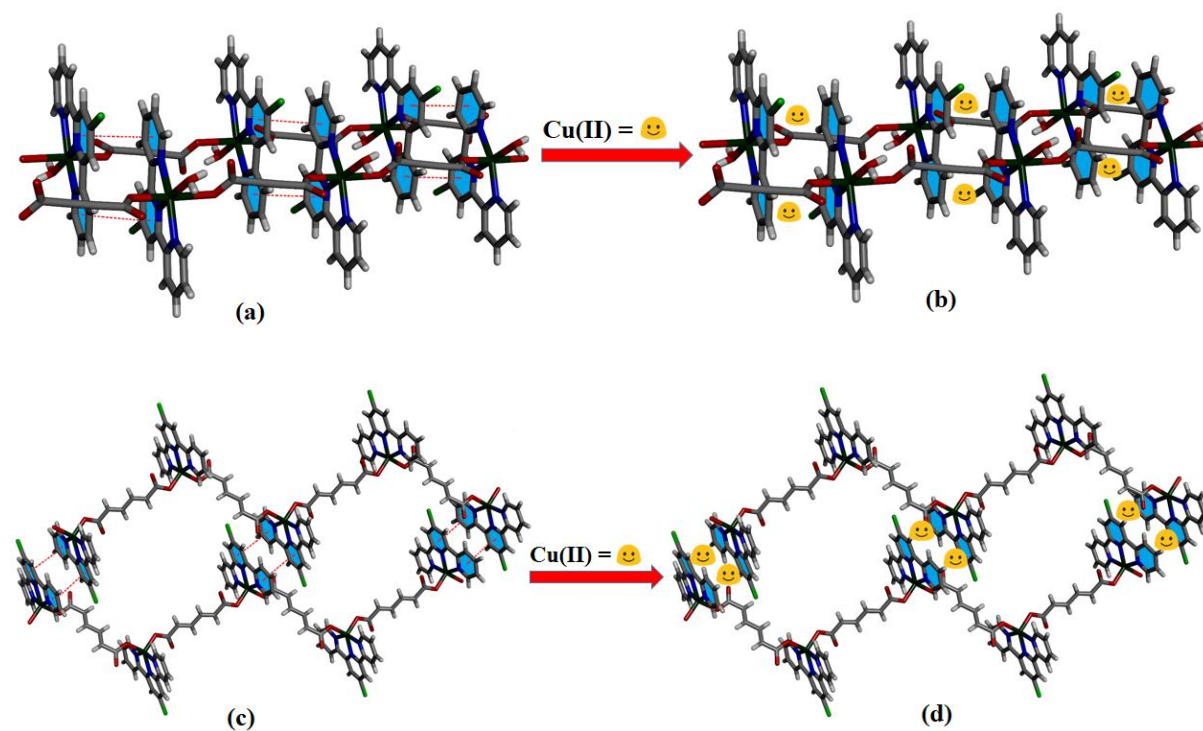
Figure 2.18. (a) $\pi\cdots\pi$ interaction between CP**1** moiety, **(b)** interaction between Cu(II) and CP**1**, **(c)** $\pi\cdots\pi$ interaction between CP**2** moiety, **(d)** interaction between Cu(II) and CP**2**.

74

The mechanism of luminescence quenching in the CP system has been explored in various ways. As these hybrid materials are constructed of a metal centre connected through organic ligands, upon introduction of analytes (ions or small molecules) there is a chance of collapse of the framework. But in the case of CP**1** and CP**2**, the PXRD (**Figure 2.6**), IR (**Figure 2.1**) (before and after Cu^{2+} addition) and absorption spectra (**Figure 2.8**) remain undistorted and indicate the retention of the structural architecture. The 1D chain of the coordination polymers are self-assembled by C–H···π, π···π and C–Cl···π interactions, and the emission of the CPs is significant. Upon interaction with paramagnetic Cu^{2+}, the excited energy transfer causes quenching (**Figure 2.18**).

2.3.3. Cell imaging study

The cellular uptake of CP**1** and CP**2** (10 μM) by hepatocellular carcinoma cells, HepG2, has been examined by fluorescence microscopy. A promiscuous blue signal is evident for the cells treated with CP**1** (**Figure 2.19a**) and CP**2** (**Figure 2.19b**). The blue signal immediately disappears after the addition of Cu^{2+} (10 μM). Thus, it can be concluded that the cells internalize the compounds CP**1** and CP**2** readily.

2.3.4. Cell survivability assay

The *in vitro* cytotoxicity of the ligands is testified by the biocompatibility against the normal human lung fibroblast cells, WI-38. The cells were exposed to various concentrations (20 μM, 40 μM, 60 μM, 80 μM and 100 μM) of the ligand for a span of 24 h and afterwards an MTT assay was performed. The results clearly depict the lack of any toxicity of the CPs against WI-38 cells, even when they are treated with a 100 μM concentration (**Figure 2.19c**). Henceforth, the CPs are non-hazardous and can be effectively implemented in various biological arenas.
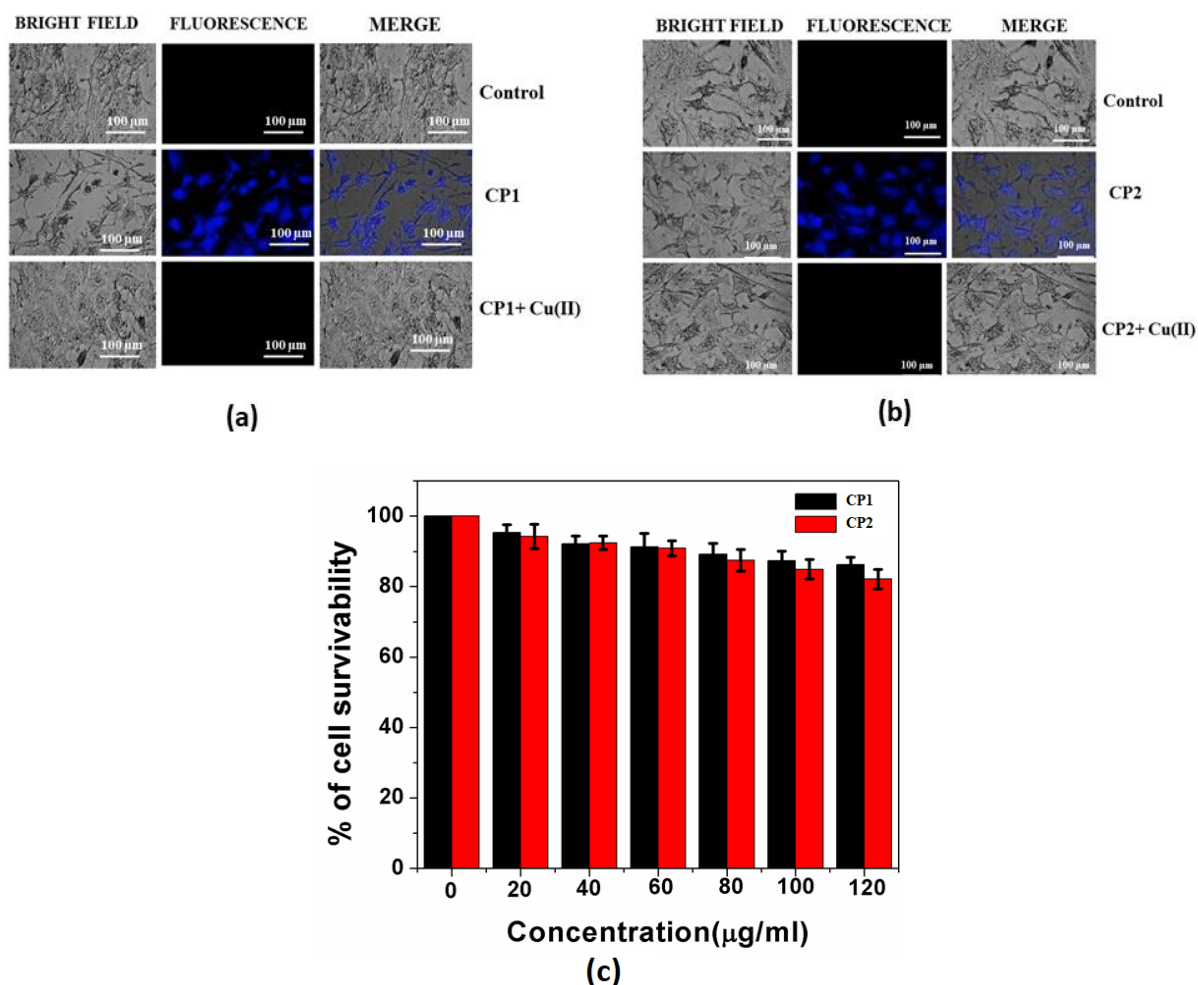
Figure 2.19. Image depicting the internalization of CP**1** **(a)** and CP**2** (**b**) within HepG2 cells, **(c)** Cell survivability assay on normal lung fibroblast cells, WI38 which confirms the biocompatibility of CP**1** and CP**2**.

2.4. Conclusion

4-Cltpy serves as an end capping ligand and dicarboxylates adc^{2-}/$muca^{2-}$ are chain propagating ligands to constitute Zn(II)-based 1D CPs. These CPs displayed strong emission in aqueous solution. Significantly, in an aqueous medium, these compounds are able to detect Cu^{2+} ions at LOD 0.14 μM (0.06 ppm) (CP**1**)/0.06 μM (0.03 ppm) (CP**2**). Cell imaging supports the biocompatibility of the respective CPs and intracellular Cu^{2+} detection in HepG2 cells. The cell survivability assay displays the tolerance limit as 100 μM.

2.5. Reference

1.   Fuku, K., Miyata, M., Takaishi, S., Yoshida, T., Yamashita, M., Hoshino, N., Akutagawa, T., Ohtsu, H., Kawano, M. and Iguchi, H., Emergence of electrical conductivity in a flexible coordination polymer by using chemical reduction. *Chem. Comm.*, **2020**, *56*, 8619-8622.

2.   Chen, W., Fan, R., Zhang, H., Dong, Y., Wang, P. and Yang, Y. Tunable white-light emission PMMA-supported film materials containing lanthanide coordination polymers: preparation, characterization, and properties. *Dalton Trans.*, **2017**, *46*, 4265-4277.

3.   Dutta, B., Dey, A., Sinha, C., Ray, P.P. and Mir, M.H. Photochemical structural transformation of a linear 1D coordination polymer impacts the electrical conductivity. *Inorg. Chem.,* **2018**, *57*, 8029-8032.

4.   Biradha, K., Su, C.Y. and Vittal, J.J. Recent developments in crystal engineering. *Cryst. Growth Des.*, **2011**, *11*, 875-886.

5.   Duan, J., Jin, W. and Kitagawa, S., Water-resistant porous coordination polymers for gas separation. *Coord. Chem. Rev.*, **2017**, *332*, 48-74.

6.   Wang, F., Li, F.L., Xu, M.M., Yu, H., Zhang, J.G., Xia, H.T. and Lang, J.P., Facile synthesis of a Ag (I)-doped coordination polymer with enhanced catalytic performance in the photodegradation of azo dyes in water. *J. Mater. Chem. A.,* **2015**, *3*, 5908-5916.

7.   O'Keeffe, M. and Yaghi, O.M. Deconstructing the crystal structures of metal–organic frameworks and related materials into their underlying nets. *Chem. Rev.*, **2012**, *112*, 675-702.

8. Naskar, K., Dey, A., Dutta, B., Ahmed, F., Sen, C., Mir, M.H., Roy, P.P. and Sinha, C., Intercatenated coordination polymers (ICPs) of carboxylato bridged Zn (II)-isoniazid and their electrical conductivity. *Cryst. Growth Des.*, **2017**, *17*, 3267-3276.

9. Dutta, B., Pal, K., Jana, K., Sinha, C. and Mir, M.H. Fabrication of a Zn (II)-Based 2D Pillar Bilayer Metal-Organic Framework for Antimicrobial Activity. *ChemistrySelect., **2019**, *4*, .9947-9951.

10. Wu, S., Min, H., Shi, W. and Cheng, P. Multicenter metal–organic framework-based ratiometric fluorescent sensors. *Adv.Mater.*, **2020**, *32*, 1805871.

11. Horike, S., Nagarkar, S.S., Ogawa, T. and Kitagawa, S. A new dimension for coordination polymers and metal–organic frameworks: towards functional glasses and liquids. *Angew. Chem., Int. Ed.*, **2020**, *59*, 6652-6664.

12. Brozek, C.K. and Dincă, M. Cation exchange at the secondary building units of metal–organic frameworks. *Chem. Soc. Rev.*, **2014**, *43*, 5456-5467.

13. Ma, Z. and Moulton, B., Recent advances of discrete coordination complexes and coordination polymers in drug delivery. *Coord. Chem. Rev.*, **2011**, *255*, 1623-1641.

14. Xu, Z., Han, L.L., Zhuang, G.L., Bai, J. and Sun, D., In Situ Construction of Three Anion-Dependent Cu (I) Coordination Networks as Promising Heterogeneous Catalysts for Azide–Alkyne "Click" Reactions. *Inorg. Chem.*, **2015**, *54*, 4737-4743.

15. Dutta, B., Jana, R., Sinha, C., Ray, P.P. and Mir, M.H., Synthesis of a Cd (II) based 1D coordination polymer by in situ ligand generation and fabrication of a photosensitive electronic device. *Inorg. Chem. Front.*, **2018**, *5*, 1998-2005.

16. Dey, S., Sil, S., Dutta, B., Naskar, K., Maity, S., Ray, P.P. and Sinha, C. Designing of Pb (II)-based novel coordination polymers (CPs): structural elucidation and optoelectronic application. *ACS omega.,* **2019**, *4*, 19959-19968.

17. Chakraborty, A., Roy, S., Eswaramoorthy, M. and Maji, T.K., Flexible MOF–aminoclay nanocomposites showing tunable stepwise/gated sorption for C_2H_2, CO_2 and separation for CO_2/N_2 and CO_2/CH_4. *J. Mater. Chem. A.,* **2017**, *5*, 8423-8430.

18. Dutta, B., Maity, S., Ghosh, S., Sinha, C. and Mir, M.H., An acetylenedicarboxylato-bridged Mn (II)-based 1D coordination polymer: electrochemical CO_2 reduction and magnetic properties. *New J. Chem.*, **2019**, *43*, 5167-5172.

19. Yin, Z., Zhou, Y.L., Zeng, M.H. and Kurmoo, M., The concept of mixed organic ligands in metal–organic frameworks: design, tuning and functions. *Dalton Trans.*, **2015**, *44*, 5258-5275.

20. Lv, R., Wang, J., Zhang, Y., Li, H., Yang, L., Liao, S., Gu, W. and Liu, X., An amino-decorated dual-functional metal–organic framework for highly selective sensing of Cr (III) and Cr (VI) ions and detection of nitroaromatic explosives. *J. Mater. Chem. A.,* **2016**, *4*, 15494-15500.

21. Wang, H., Qin, J., Huang, C., Han, Y., Xu, W. and Hou, H. Mono/bimetallic water-stable lanthanide coordination polymers as luminescent probes for detecting cations, anions and organic solvent molecules. *Dalton Trans*., **2016**, *45*, 12710-12716.

22. Meng, X., Wei, M. J., Wang, H. N., Zang, H.Y. and Zhou, Z.Y. Multifunctional luminescent Zn (II)-based metal–organic framework for high proton-conductivity and detection of Cr^{3+} ions in the presence of mixed metal ions. *Dalton Trans.*, **2018**, *47*, 1383-1387.

23. Chen, M. M., Chen, L., Li, H. X., Brammer, L. and Lang, J.P., Highly selective detection of Hg^{2+} and MeHgI by di-pyridin-2-yl-[4-(2-pyridin-4-yl-vinyl)-phenyl]-amine and its zinc coordination polymer. *Inorg. Chem. Front.*, **2016**, *3*,1297-1305.

24. Rath, B.B. and Vittal, J.J. Water stable Zn (II) metal–organic framework as a selective and sensitive luminescent probe for Fe (III) and chromate ions. *Inorg. Chem.*, **2020**, *59*, 8818-8826.

25. Allendorf, M. D., Bauer, C.A., Bhakta, R.K. and Houk, R.J.T. Luminescent metal–organic frameworks. *Chem. Soc. Rev.*, **2009**, *38*, 1330-1352.

26. Gogoi, C., Yousufuddin, M. and Biswas, S. A new 3D luminescent Zn (II)–organic framework containing a quinoline-2, 6-dicarboxylate linker for the highly selective sensing of Fe (III) ions. *Dalton Trans.*, **2019**, *48*, 1766-1773.

27. Liang, Y. T., Yang, G.P., Liu, B., Yan, Y.T., Xi, Z.P. and Wang, Y.Y., Four super water-stable lanthanide–organic frameworks with active uncoordinated carboxylic and pyridyl groups for selective luminescence sensing of Fe^{3+}. *Dalton Trans.*, **2015**, *44*, 13325-13330.

28. Wu, Y., Li, Y., Zou, L., Feng, J., Wu, X., Yang, S., Liu, W., Fan, G., Singh, A. and Kumar, A. A 2D Cd (II)-MOF as a multifunctional luminescencent sensor for nitroaromatics, iron (III) and chromate ions. *J. Coord. Chem.*, **2017**, *70*, 1077-1088.

29. Feng, L., Dong, C., Jiang, W., Gu, X., Xiao, M., Li, C., Ning, Z. and Gao, D., A facile synthesized Eu-based metal–organic frameworks sensor for highly selective detection of volatile organic compounds. Journal of Materials Science: Materials in Electronics, **2019**, *30*, 19247-19253.

30. Feng, L., Dong, C., Li, M., Li, L., Jiang, X., Gao, R., Wang, R., Zhang, L., Ning, Z., Gao, D. and Bi, J. Terbium-based metal-organic frameworks: Highly selective and fast

respond sensor for styrene detection and construction of molecular logic gate. *J. Hazard. Mater.*, **2020**, *388*, 121816.

31. Liu, J., Pei, L., Xia, Z. and Xu, Y., Hierarchical accordion-like lanthanide-based metal–organic frameworks: solvent-free syntheses and ratiometric luminescence temperature-sensing properties. *Cryst. Growth Des.*, **2019**, *19*, 6586-6591.

32. Naskar, K., Bhanja, A.K., Paul, S., Pal, K. and Sinha, C. Trace quantity detection of H2Po4–by fluorescent metal–organic framework (F-MOF) and bioimaging study. *Cryst. Growth Des.*, **2020**, *20*, 6453-6460.

33. Dutta, B., Jana, R., Bhanja, A.K., Ray, P.P., Sinha, C. and Mir, M.H. Supramolecular aggregate of Cadmium (II)-based one-dimensional coordination polymer for device fabrication and sensor application. *Inorg. Chem.*, **2019**, *58*, 2686-2694.

34. Zhu, R., Zhou, G., Tang, F., Tong, C., Wang, Y. and Wang, J. Detection of Cu2+ in water based on histidine-gold labeled multiwalled carbon nanotube electrochemical sensor. *Int.J.Anal. Chem.,* **2017**, 1–8.

35. Barnham, K. J., Masters, C. L. and Bush, A. I. Neurodegenerative diseases and oxidative stress. *Nat. Rev. Drug. Discov.*, **2004**, *3*, 205-214.

36. Dong, C.L., Li, M.F., Yang, T., Feng, L., Ai, Y.W., Ning, Z.L., Liu, M.J., Lai, X. and Gao, D.J. Controllable synthesis of Tb-based metal–organic frameworks as an efficient fluorescent sensor for Cu^{2+} detection. *Rare Met.,* **2021**, *40*, 505-512.

37. Geranmayeh, S., Mohammadnejad, M. and Mohammadi, S. Sonochemical synthesis and characterization of a new nano Ce (III) coordination supramolecular compound; highly sensitive direct fluorescent sensor for Cu2+. *Ultrason. Sonochem.*, **2018**, *40*, 453-459.

38. Chakraborty, C., Singh, P., Maji, S.K. and Malik, S., Conjugated polyfluorene-based reversible fluorescent sensor for Cu (II) and cyanide ions in aqueous medium. *Chem. Lett.*, **2013**, *42*, 1355-1357.

39. Dutta, B., Hazra, A., Dey, A., Sinha, C., Ray, P.P., Banerjee, P. and Mir, M.H., Construction of a succinate-bridged Cd (II)-based two-dimensional coordination polymer for efficient optoelectronic device fabrication and explosive sensing application. *Cryst. Growth Des.*, **2020**, *20*, 765-776.

40. Dutta, B., Purkait, R., Bhunia, S., Khan, S., Sinha, C. and Mir, M.H., Selective detection of trinitrophenol by a Cd (II)-based coordination compound. *RSC Adv.*, **2019**, *9*, 38718-38723.

41. Dutta, B., Dey, S., Pal, K., Bera, S., Naaz, S., Jana, K., Sinha, C. and Mir, M.H., Supramolecular assembly of a 4-(1-naphthylvinyl) pyridine-appended Zn(II) coordination compound for the turn-on fluorescence sensing of trivalent metal ions (Fe^{3+}, Al^{3+}, and Cr^{3+}) and cell imaging application. *New J. Chem.*, **2020**, *44*, 13163-13171.

42. Ghorai, P., Dey, A., Hazra, A., Dutta, B., Brandão, P., Ray, P.P., Banerjee, P. and Saha, A., Cd (II) based coordination polymer series: fascinating structures, efficient semiconductors, and promising nitro aromatic sensing. *Cryst. Growth Des.*, **2019**, *19*, 6431-6447.

43. Sheldrick, G.M., Phase annealing in SHELX-90: direct methods for larger structures. Acta Crystallographica *Sect. A: Found. Crystallogr.,* **1990**, *46*, 467-473.

44. Pal, K., Roy, S., Parida, P.K., Dutta, A., Bardhan, S., Das, S., Jana, K. and Karmakar, P., Folic acid conjugated curcumin loaded biopolymeric gum acacia microsphere for

triple negative breast cancer therapy in invitro and invivo model. *Mater. Sci. Eng. C.*, **2019**, *95*, 204-216.

45. Samui, A., Pal, K., Karmakar, P. and Sahu, S.K., In situ synthesized lactobionic acid conjugated NMOFs, a smart material for imaging and targeted drug delivery in hepatocellular carcinoma. *Mater. Sci. Eng. C.*, **2019**, *98*, 772-781.

46. Dutta, B., Das, D., Datta, J., Chandra, A., Jana, S., Sinha, C., Ray, P.P. and Mir, M.H., Synthesis of a Zn (II)-based 1D zigzag coordination polymer for the fabrication of optoelectronic devices with remarkably high photosensitivity. *Inorg. Chem. Front.*, **2019**, *6*, 1245-1252.

47. Zhang, Q., Tian, X., Hu, Z., Brommesson, C., Wu, J., Zhou, H., Li, S., Yang, J., Sun, Z., Tian, Y. and Uvdal, K., A series of Zn (II) terpyridine complexes with enhanced two-photon-excited fluorescence for in vitro and in vivo bioimaging. *J Mater Chem. B.*, **2015**, *3*, 7213-7221.

48. Huang, P., Wu, F. and Mao, L., Target-triggered switching on and off the luminescence of lanthanide coordination polymer nanoparticles for selective and sensitive sensing of copper ions in rat brain. *Anal. Chem.*, **2015**, *87*, 6834-6841.

49. She, H., Song, F., Xu, J., Xiong, X., Chen, G., Fan, J., Sun, S. and Peng, X., A new tridentate sulfur receptor as a highly sensitive and selective fluorescent sensor for Cu^{2+} ions. *Chem. Asian J.*, **2013**, *8*, 2762-2767.

50. Sangeetha, S., Sathyaraj, G., Muthamilselvan, D., Vaidyanathan, V.G. and Nair, B.U. Structurally modified 1, 10-phenanthroline based fluorophores for specific sensing of Ni^{2+} and Cu^{2+} ions. *Dalton Trans.*, **2012**, *41*, 5769-5773.

51. Geranmayeh, S., Mohammadnejad, M. and Mohammadi, S., Sonochemical synthesis and characterization of a new nano Ce (III) coordination supramolecular compound;

highly sensitive direct fluorescent sensor for Cu^{2+}. *Ultrason. Sonochem.*, **2018**, *40*, 453-459.

52.   Huang, P., Wu, F. and Mao, L., Target-triggered switching on and off the luminescence of lanthanide coordination polymer nanoparticles for selective and sensitive sensing of copper ions in rat brain. *Anal. Chem.*, **2015**, *87*, 6834-6841.

53.   She, H., Song, F., Xu, J., Xiong, X., Chen, G., Fan, J., Sun, S. and Peng, X., A new tridentate sulfur receptor as a highly sensitive and selective fluorescent sensor for Cu^{2+} ions. *Chem. Asian J.*, **2013**, *8*, 2762-2767.

54.   Sangeetha, S., Sathyaraj, G., Muthamilselvan, D., Vaidyanathan, V.G. and Nair, B.U., Structurally modified 1, 10-phenanthroline based fluorophores for specific sensing of Ni^{2+} and Cu^{2+} ions. *Dalton Trans.*, **2012**, *41*, 5769-5773.

Chapter 3

Spectrophotometric Determination of Trace Amount of Total Fe^{II}/Fe^{III} and Live Cell Imaging of a Carboxylato Zn(II) Coordination Polymer
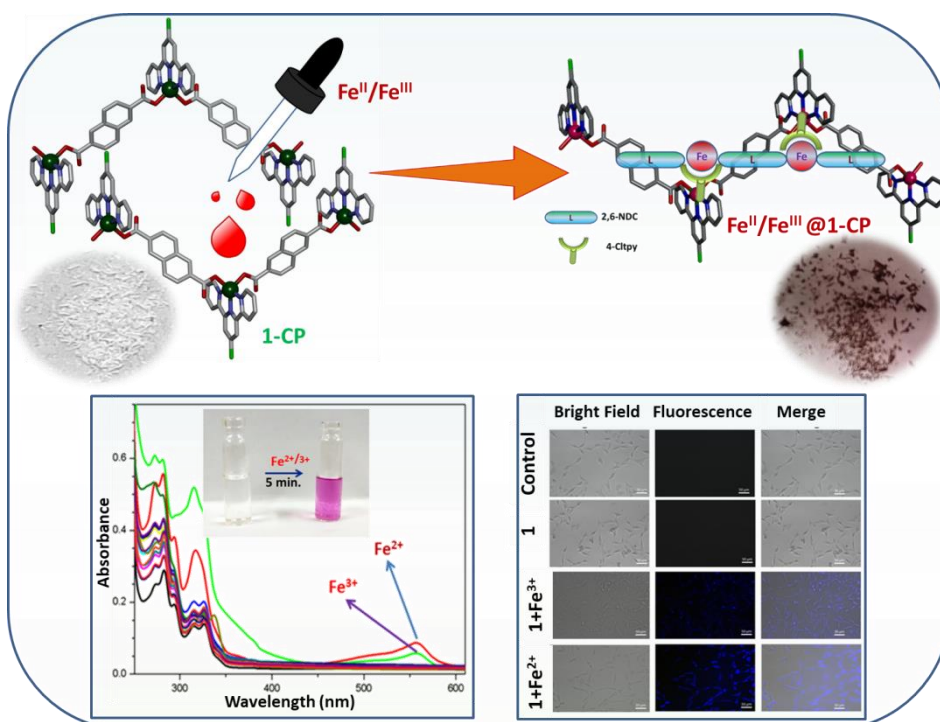
Chapter 3

Abstract

The coordination polymer, (**1**), {[Zn(2,6-NDC)(4-Cltpy)](H$_2$O)$_4$} (**1**) (2,6-H$_2$NDC = 2,6-Naphthalene dicarboxylic acid and 4-Cltpy = 4′-chloro-[2,2′;6′,2″]terpyridine) is structurally characterised by Single Crystal X-Ray Diffraction measurement and other physicochemical studies (PXRD, FTIR, Thermal analysis, Microanalytical data). 4-Cltpy acts as end capping ligand and NDC^{2-} is a carboxylato bridging motif to constitute ZnN$_3$O$_2$ distorted trigonal bi-pyramid core that propagates to construct 1D chain. The coordination polymer, **1** detects total iron (Fe^{3+} and Fe^{2+}) in aqueous solution by visual colour change, colourless to pink. Absorption spectrophotometric technique in aqueous medium measures the limit of detection (LOD) 0.11 μM (Fe^{2+}) and 0.15 μM (Fe^{3+}) and binding constants (K$_d$) are 6.7 × 10^4 M^{-1} (Fe^{2+}) and 3.33 × 10^4 M^{-1} (Fe^{3+}). Biocompatibility of **1** is examined in live cells and intracellular Fe^{2+} and Fe^{3+} are detected in MDA-MB 231 cells. Zn(II) substitution is assumed upon addition of Fe^{III}/Fe^{II} solution to the suspension of the coordination polymer, **1** in water-acetonitrile (41:1) (LZn^{II} + Fe$^{III/II}$→LFe^{III} + Zn^{II}, where L is defined as coordinated ligand) which is accompanied by changing colourless to pink at room temperature. The colour of the mixture may be assumed to the charge transfer transition from carboxylate-O to Cltpy via Fe(II/III) bridging centre (carboxylate-O-Fe-CltPy). The product isolated from the reaction is finally characterized as **Fe(III)@1-**CP. It is presumed that product **Fe(II)@1-**CP may undergo fast aerial oxidation to transform **Fe(III)@1-**CP. The Fe^{III} exchanged framework (**Fe(III)@1-**CP) has been characterized by PXRD, IR, TGA and energy dispersive X-Ray analysis (EDX)-SEM. The MTT assay calculates the Cell viability (%) and the tolerance limit is 100 μM to total of Fe^{2+} and Fe^{3+}.

3.1. Introduction

In the field of material chemistry, the coordination polymers (CPs) [1-13] are receiving great attention (**Chapter 1**) due to their novel applications like gas absorption, catalysis, electrical conductivity, magnetism, photocatalytic reduction and oxidation, chromatographic Separation, water splitting, electrochemistry, drug delivery, energy saving device fabrication, sensing and dye degradation etc.[14-34] Use of CPs as sensor[35-40] for the detection of trace quantity of ions, various pollutants, explosive materials, volatile organic compounds[41-43] is currently focused in chemical, environmental, engineering and biomedical research. The sensing property of CPs (**Chapter 2**) in aqueous medium is a challenging task because biologically important ions are sorbed in living cells mainly from food, drinks, beverages etc. In comparison to molecular sensors CPs are beneficial and sustainable because of stability, flexibility and reusability. However, the sensing of paramagnetic ions/molecules is troublesome by fluorescence process because of paramagnetic quenching; absorption spectrophotometric process is more useful in this respect.

The stable CPs/MOFs may be formulated following the selection of metal ion(s) and ligand centres using the Hard and Soft Acid Base (HSAB) principle.[44-47] The -COO and pyridyl-N donor ligands are considered as a hard base and binding with the hard acid like Fe^{3+}, Cr^{3+}, Ti^{4+}, Zr^{4+} etc. to form stable CPs. Sometimes, the post synthetic metathesis (PSM) and red-ox reactions[48-50] may be used to transform more stable and useful CPs. The metal exchange reaction by the post-synthetic method is one of the common tools for the synthesis of new CPs.[49-55]

Iron (Fe) is an essential element in the growth of civilization and life. Iron oxides form the outer layer and inner core of the earth. It is widely used in equipment manufacturing, construction of road, railway, bridge, housing, industry, surgical instrument and the growth of

human society.[56] In living organism iron is an important trace element; it is the main component of oxygen binding centre in blood and nitrogen fixation of nitrogenase enzyme, redox centre in Cytochromes, ferredoxins, ferritin etc. Fe is important for the electron transfer process at the time of formation of DNA and RNA in biological system.[57-59] In the ecosystem, Fe is increasing due to massive discharge of industrial wastes. Excess amount of Fe in body causes DNA damage, lipid peroxidation, imbalance of oxidant and antioxidant system which is related to the tumour in liver, colon and other organs.[60-63] Some of the CPs/MOFs are known for the quantitative estimation of trace amount of $Fe^{2+/3+}$.[64-74] However, very few CPs are available to sense total amount of Fe^{2+} and Fe^{3+} .[75,76] Therefore, it is urgently needed to design a suitable probe which can detect selectively and sensitively total iron (Fe^{3+} and Fe^{2+}) in the consumable media.

With this consideration in mind, we synthesise a compound (**1**) of 2,6-Naphthalene dicarboxylic acid (H₂NDC) where 4′-chloro-[2,2′;6′,2″]terpyridine (4-Cltpy) serves as tridentate end capping ligand. The coordination polymer (**1**) is used to detect trace amount of total Fe (Fe^{2+} and Fe^{3+}) by absorption spectrophotometric method in aqueous solution in presence of other cations (Al^{3+}, Cr^{3+}, Zn^{2+}, Pb^{2+}, Co^{2+}, Mn^{2+}, Ni^{2+}, Cu^{2+}, Mg^{2+}, Ca^{2+}, Ba^{2+}, Cd^{2+}, Hg^{2+}, Na^+). Isolation of **Fe(III)@1-**CP from the reaction of compound (**1**) in water-acetonitrile (41:1) suspension with Fe(II) or Fe(III) solution in air and the physicochemical characterisation (PXRD, IR, TGA, (EDX)-SEM) of the product has accounted the plausible substitution of Zn(II) by Fe(II)/Fe(III) from **1** (followed by fast air oxidation of Fe(II) in case of substitution by Fe(II)). The cell line efficiency of **1** is examined by MTT assay and the cell survivability is determined for MDA-MB 231 and WI38. The effects of **1** on the growth of MDA-MB 231 cells in presence of Fe^{2+} and Fe^{3+} are also examined.

3.2. Experimental Section

3.2.1. Materials and physical methods

$Zn(NO_3)_2 \cdot 6H_2O$, 4′-Chloro-[2,2′;6′,2″]terpyridine (4-Cltpy), 2,6-Naphthalene dicarboxylic acid (H_2NDC) were procured from Sigma-Aldrich Chemical company. All other reagents were collected Mark, India and used without further purification. PerkinElmer 2400 CHNS/O elemental analyser were collected the Microanalytical data (C, H, N). FTIR spectra have been investigated using a KBr disc on a PerkinElmer RX-1 FTIR Spectrophotometer in the 4000-400 cm^{-1} range. Utilizing a Pyris Diamond Thermogravimetric Analyzer (TGA) in the temperature range of 30-850 °C, the thermal stability of the coordination polymer was evaluated. Powder X-ray diffraction (PXRD) data were recorded using a X-ray diffractometer (Bruker D8 Advance). Carl Zeiss SUPRA 55VP FESEM was used to record the morphological characterization via FESEM micrograph. Oxford Instruments X-Max linked to the FESEM with INCA software was used to evaluate the elemental analysis via EDX. Fluorescence and UV-Vis spectra were recorded on a PerkinElmer spectrofluorometer model LS55 and PerkinElmer Lambda 25 spectrophotometer, respectively. Horiba Jobin Yvon Fluorescence Spectrophotometer was used for measurement of Fluorescence lifetime. Cell line Study was examined using fluorescence microscope (Leica) using 350 nm monochromatic laser beams.

3.2.2. Synthesis of coordination polymer 1,

Methanol solution (2 mL) of 4-Cltpy (0.054 g, 0.2 mmol) was slowly injected into aqueous solution $Zn(NO_3)_2 \cdot 6H_2O$ (0.06 g, 0.2 mmol, 2 mL) and H_2O-MeOH buffer (1:1, v/v; 2 mL), followed by the subsequent addition of ethanolic solution (2 mL) of H_2NDC (0.023 g, 0.2 mmol) neutralized by Et_3N (0.042 g, 0.4 mmol). Block shaped colourless crystals were obtained by slow evaporation for a week. Synthesis of **1** is following the route of **Scheme 3.1**. Elemental analysis (%) for $C_{27}H_{24}ClN_3O_{11}Zn$: Calcd.: C, 49.59; H, 3.62; N, 6.30. Found: C,

49.65; H, 3.67; N, 6.38. FTIR data: ν (cm^{-1}); ν(C=O), 1614; ν$_{as}$(COO), 1551 ν$_{sys}$(COO), 1341; ν(C-Cl), 905 cm^{-1} (**Figure 3.1**).
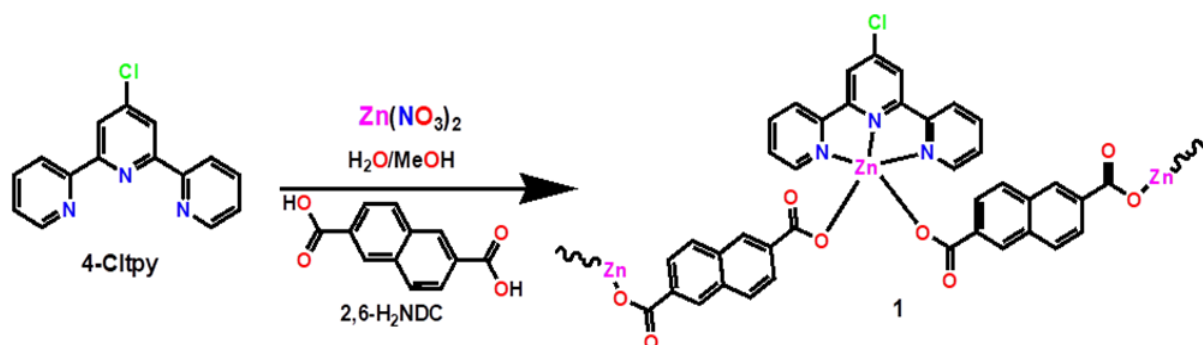
Scheme 3.1. Synthesis of Coordination polymer **1**, reaction of Zn(NO$_3$)$_2$ with 4-Cltpy and 2,6-H$_2$NDC.
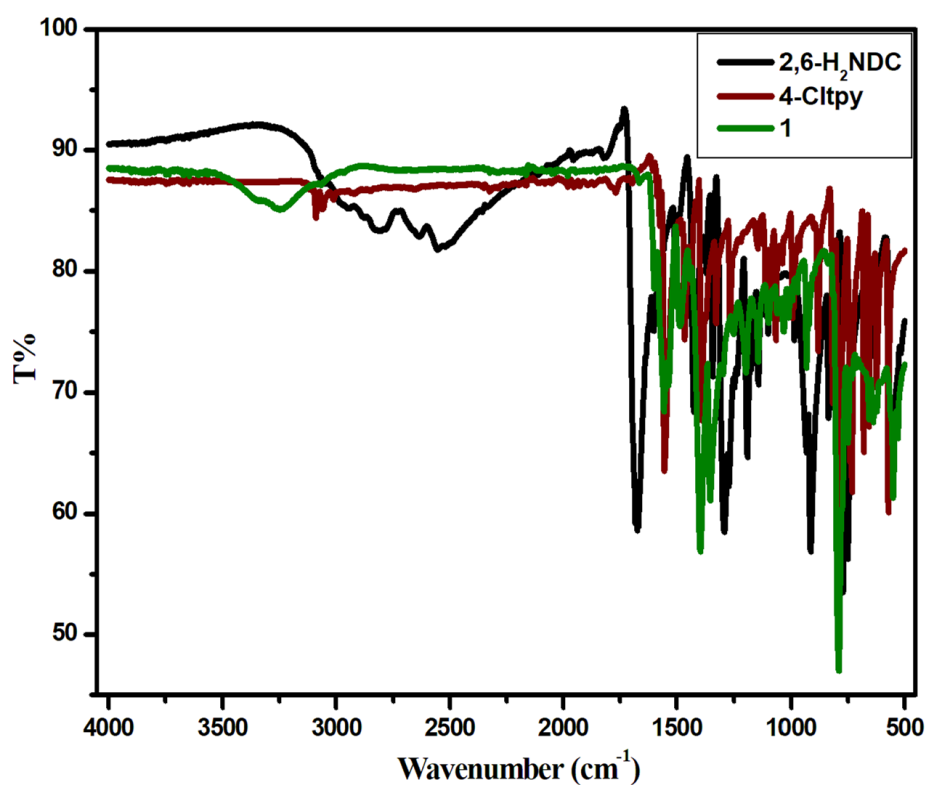
Figure 3.1. IR spectra of constitute ligands and compound **1**.

3.2.3. Structure determination by Single Crystal X-Ray Diffraction Studies

The crystal of compound **1**, with suitable dimension ($0.15 \times 0.08 \times 0.05$ Å^3) was used for data collection from the Single Crystal X-Ray diffraction using Bruker APEX-II CCD diffractometer equipped with graphite-monochromatized Mo-Kα radiation ($\lambda = 0.71073$ Å) at 273(2) K. SHELX-97 package helped to evaluate single crystal structure. The indexing and

Table 3.1. Crystal data and refinement parameters for compound **1**

Formula	$C_{27} H_{29} Cl N_3 O_{11} Zn$
CCDC No.	2117331
fw	672.37
Crystal system	monoclinic
space group	*C 2/c*
a (Å)	13.4146(10)
b (Å)	24.4795(19)
c (Å)	11.5313(9)
α(deg)	90
β(deg)	124.357(2)
γ (deg)	90
V (Å^3)	3126.1(4)
Z	4
D_{calcd}(g/cm^3)	1.429
μ(mm^{-1})	0.932
λ(Å)	0.71073
data[$I > 2\sigma(I)$]/params	2527/ 215
GOF on F^2	1.04
final R indices[$I > 2\sigma(I)$][a,b]	$R_1 = 0.0289$ $wR_2 = 0.0870$

[a]$R1 = \Sigma||F_o| - |F_c||/ \Sigma|F_o|$, [b] $wR2 = [\Sigma w(F_o{}^2 - F_c{}^2)^2/\Sigma w(F_o{}^2)^2]^{1/2}$

scaling of the data set, as well as cell refinement, were accomplished using the Bruker Smart Apex and Bruker Saint packages[77]. Direct method was used and subsequent Fourier analyses,[78]

to solve the structure. The structure was refined using the F^2 based full-matrix least-squares technique with all detected reflections[79] and anisotropic thermal parameters were applied to optimize non-hydrogen atoms. Hydrogen atoms are forced to ride over their parent atoms in their geometrically perfect position. The WinGX System, Ver 2018.3.39 was used for the calculations. Mercury 3.10.3 and Discovery Studio 2017R2 were used to prepare all the Molecular pictures. The crystallographic data of **1** were summarised in **Table 3.1** and **Table 3.2** recorded the bond angle and bond lengths.

Table 3.2 Selected bond lengths and bond angles in **1**.

Zn(3) - O(12)	1.9817(19)	N(7)-Zn(3)-N(6)	75.52(5)
Zn(3) - O(12_a)	1.9817(19)	O(12_a)-Zn(3)-N(6)	105.84(7)
Zn(3) - N(7)	2.083(2)	O(12_a)-Zn(3)-N(6_a)	93.81(7)
Zn(3) - N(6)	2.1564(16)	N(7)-Zn(3)-N(6_a)	75.52(5)
Zn(3) - N(6_a)	2.1564(16)	N(6)-Zn(3)-N(6_a)	151.05(7)
O(12)-Zn(3)-O(12_a)	94.52(8)	C(27)-O(12)-Zn(3)	112.74(13)
O(12)-Zn(3)-N(7)	132.74(5)	C(37_a)-N(7)-Zn(3)	119.42(12)
O(12)-Zn(3)-N(6)	93.81(7)	C(42)-N(6)-C(38)	118.87(17)
O(12)-Zn(3)-N(6_a)	105.84(7)	C(38)-N(6)-Zn(3)	116.16(13)
O(12_a)-Zn(3)-N(7)	132.74(5)	C(27)-O(12)-Zn(3)	112.74(13)
O(12_a)-Zn(3)-N(6)	105.84(7)	C(37)-N(7)-Zn(3)	119.42(12)
		O(12_a)-Zn(3)-N(6_a)	93.81(7)

3.2.4. Sensing Experiments

A stock solution of **1** (1×10^{-3} M) was prepared by dissolving requisite amount of compound **1**, in acetonitrile solution. NaCl, KCl, $CuCl_2$, $ZnCl_2$, $CdCl_2$, $HgCl_2$, $AlCl_3$, $PbCl_2$, $CoCl_2$, $MnCl_2$, $FeCl_3$, $MgCl_2$, $CaCl_2$, $BaCl_2$, $MnCl_2$, $NiCl_2$, $CrCl_3$ and $(NH_4)_2Fe(SO_4)_2\cdot6H_2O$ salts were used

to prepare (1×10^{-3} M) aqueous solution using deionised water. For the measurement of UV-Visible experiments, 50 μM main solutions was prepared in water (HEPES buffer, pH 7.2) by taking the above stock solution and 1.00 equivalent metal salts were added into this solution. After mixing the metal ions in the coordination polymer **1** solution and then examined their spectra at 25°C.

Limit of detection (LOD) of Fe (Fe^{2+} and Fe^{3+} separately) were calculated using titration of UV-Visible measurement. Standard deviation was scrutinized from absorbance of coordination polymer (**1**). The LODs were evaluated using $3\sigma/M$ method, where σ is the standard deviation and M is slope of the calibration curve. Binding constant values of Fe^{2+} and Fe^{3+} with **1** were calculated using absorbance data following Benesi–Hildebrand equation, $1/\Delta A = 1/\Delta A_{max} + (1/K_d[C])(1/\Delta A_{max})$. Here $\Delta A = A-A_0$ and $\Delta A_{max} = A_{max}-A_0$, where A_0 = absorbance value of **1** measured in the absence of Fe^{n+}, A = absorbance values at an intermediate Fe^{n+} concentration, A_{max} = Absorbance at saturation concentration of Fe^{n+} and [C] = concentration of cation, K_d = binding constant. The value of K_d calculated from slope of this plot $(A_{max}-A)/(A-A_0)$ vs. $1/[C]$ for Fe^{n+}, where n = 2, 3. Thermal stability of the compound **1** was determined using thermogravimetric analysis (TGA) with the temperature range 30-850 °C. Stability in excited state of **1** in presence and absence of Fe^{3+} was evaluated from life time plot.

3.2.5. Cell line study

Human cancer cell line MDA-MB 231 and normal lung fibroblast cell line WI-38 (NCCS in Pune, India) was used in the present studies. The cell lines were cultivated in a T25 flask with DMEM supplemented with sodium pyruvate (1 mM), non-essential amino acids, 10% FBS, penicillin (100 units/L), gentamycin (50 mg/L), L-glutamine (2 mM), streptomycin (100 mg/L), and in a humidified incubator with 5% CO_2 at 37°C.

The cell survival test of **1** was investigated using the MTT cell proliferation assay. MDA-MB 231 and WI-38 cells were seeded at a concentration of 1×10^4 cells per well in 96-well plates for 24 h of incubation which would be exposed at different concentrations of solution **1** ranging from (0 μM-100 μM) for the time period of 24 h. After incubation PBS (1X) was washed and MTT solution (0.5 mg/mL, 100 μL) was added to each well and incubated for 3-4 h (37°C) in humidified incubator (5% CO_2). The solution of formazan crystals in DMSO was used and the absorbance data were collected at 570 nm as usual.[80]

The fluorescence of **1** in the presence of Fe^{2+} and Fe^{3+} was envisioned using MDA-MB-231 cells. MDA-MB -231 cells were grown in cover slips for 24 h and then added with 10 μM of **1** in the presence or absence of 10 μM Fe^{2+}/Fe^{3+} separately and incubated for the time period of 30 min in dark at 37ºC and washed with 1×PBS and detected under fluorescence microscope (Leica) using 350 nm monochromatic laser beams.[81]

3.3. Results and Discussion

3.3.1. Structure of 1

Single Crystal X-Ray structure determination has shown that the asymmetric unit of **1** consists of ZnN_3O_2 core in a distorted trigonal bipyramid geometry about Zn(II) with monoclinic crystal system, space group *C 2/c*, Z = 4. Dicarboxylato-O (-OOC-R-COO-) of NDC^{2-} bridges adjacent Zn(II) centres and propagates zig-zag 1D coordination polymer (**Figure 3.2**). 4-Cltpy acts as tridentate-NNN end capping motif. Bond lengths [Zn(3)-O(12), 1.9829(13); Zn(3)-O(12_a), 1.9830(13); Zn(3)-N(7), 2.081(2); Zn(3)-N(6), 2.1559(16); Zn(3)-N(6_a), 2.1559(16) Å] and bond angles [O(12)-Zn(3)-O(12_a), 94.49(8); N(7)-Zn(3)-N(6), 75.53(4); N(7)-Zn(3)-N(6_a), 75.53(4); N(6)-Zn(3)-N(6_a), 151.06(9)°] (**Figure 3.2a, Table 3.2**) are comparable with the reported data.[54] 1D chain (**Figure 3.2b**) of CP forms
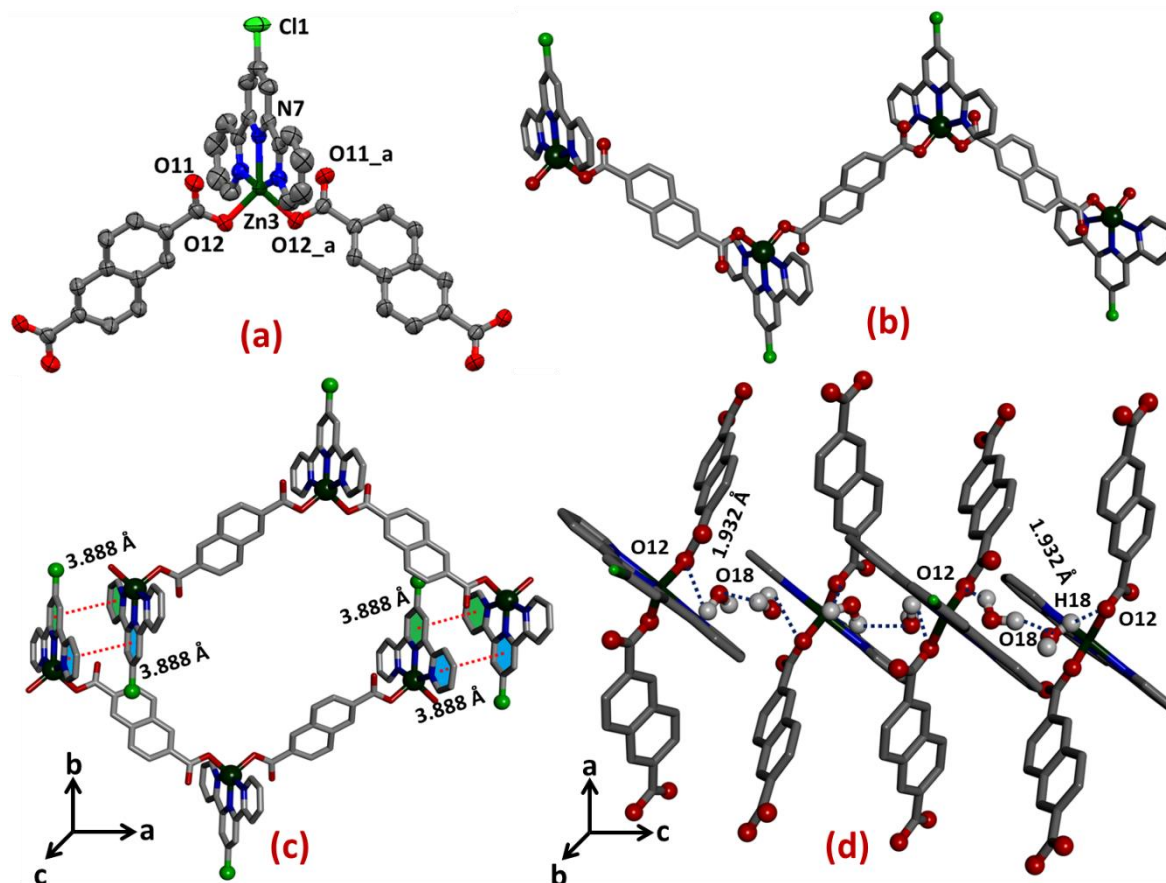
Figure 3.2. (a) Asymmetric unit of **1**, **(b)** View of 1D chain of **1** along crystallographic c axis, **(c)** View π···π interaction (3.888 Å) along crystallographic c axis of two 1D chain with short distance between two π-cloud 3.887 Å, **(d)** H-bonding (1.932 Å) between CP and water molecules along crystallographic b axis.

supramolecular (2D) assemble (**Figure 3.3a-c, Table 3.3**) by π···π (3.887 Å, **Figure 3.2c**), hydrogen bonding and C-Cl···π (**Figure 3.3d**) interaction. H-boding between CP and water molecules also make a strong 1D chain (**Figure 3.2d**). 4-Cltpy ligand has shown nearly planer structure with a dihedral angel 3.11° (**Figure 3.3e**).
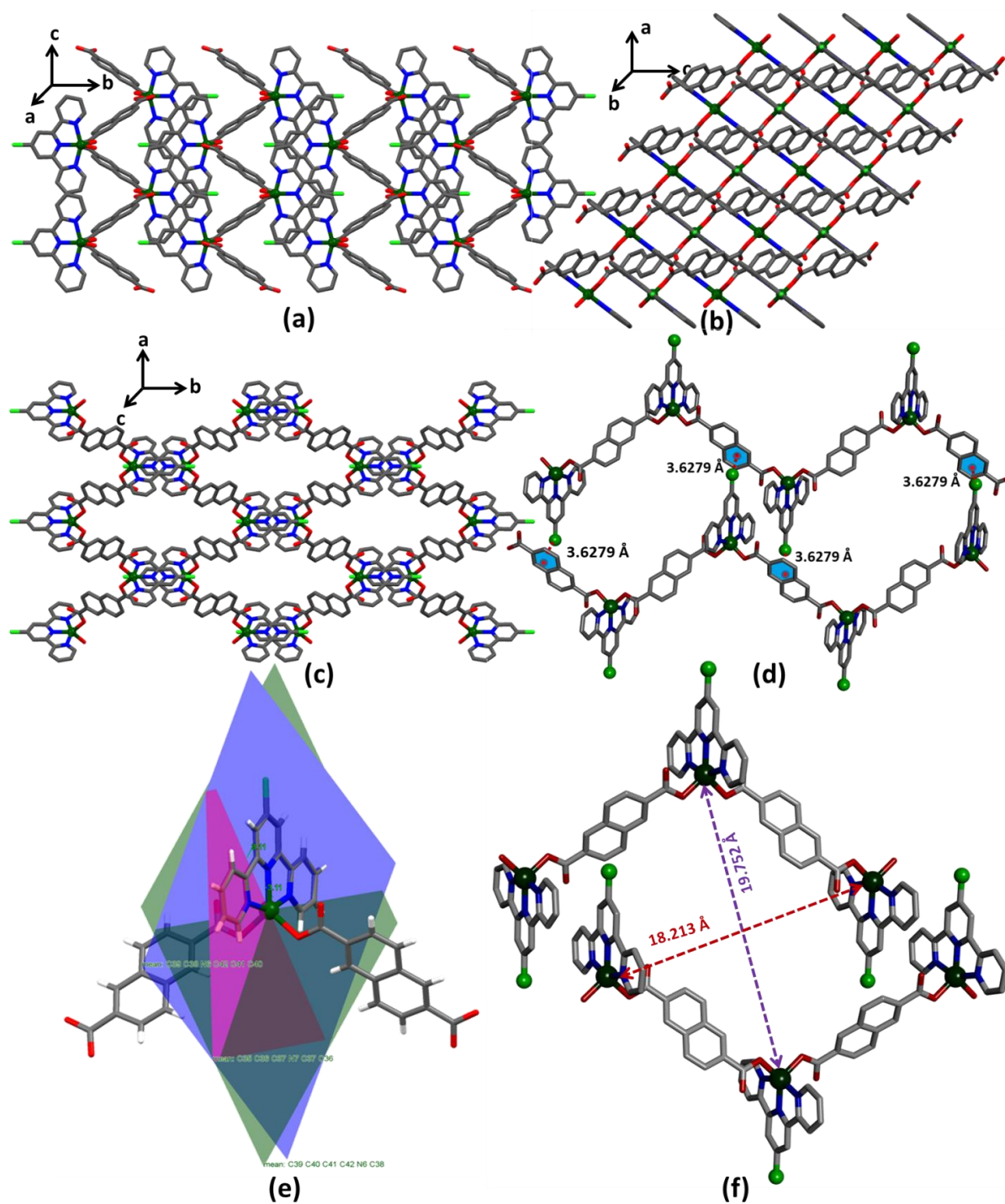
Figure 3.3. View of supramolecular assemble along a **(a)**, b **(b)** and c **(c)** axis. **(d)** C-Cl···π

interaction with a distance 3.6279 Å **(e)** Planarity checked in terpyridine moiety. **(f)** diameter

determination.

Table 3.3. List of π···π, C–Cl···π and H-bonding interaction in compound **1**.

π···π interaction		
Ring(i) → Ring(j)	Distance between the (i, j) ring centroids (Å) in the crystal	[ARU(j)]
R(4) → R(3)	3.8884(16)	[3666.01]
R(4) → R(3)	3.8873(14)	[4564.01]

C-Cl···π interaction				
C-Cl(i) ···Ring(j)	Cl..R(j)	C···Ring (Å)	∠C-Cl..R(j) (°)	[ARU(j)]
C(35) - Cl(1)→R(5)	3.6274(9)	4.590(2)	113.09(2)	[3666.01]
C(35) - Cl(1)→R(6)	3.6274(9)	4.590(2)	113.09(2)	[5555.01]

H-bonding interaction						
Type	Donor--- H	Acceptor	D - H	H...A	∠D - H...A	[ARU]
Intermolecular (Classical)	O(1) -- H(1A)	O(19)	0.85	2.09	150	[1655.05]
Intermolecular (Classical)	O(1) -- H(1B)	O(19)	0.85	2.02	159	[3665.05]
Intermolecular (Classical)	O(2) --H(2)	O(19)	1.12(9)	2.42(8)	105(5)	[7555.05]
Intermolecular (Classical)	O(18) -- H(18B)	O(12)	0.87(4)	1.93(4)	173(6)	-
Intermolecular (Classical)	O(19) -- H(19A)	O(11)	0.84(3)	1.98(3)	179(7)	-
Intermolecular (Classical)	O(19) -- H(19B)	O(2)	0.86(4)	2.09(4)	164(5)	[7555.03]
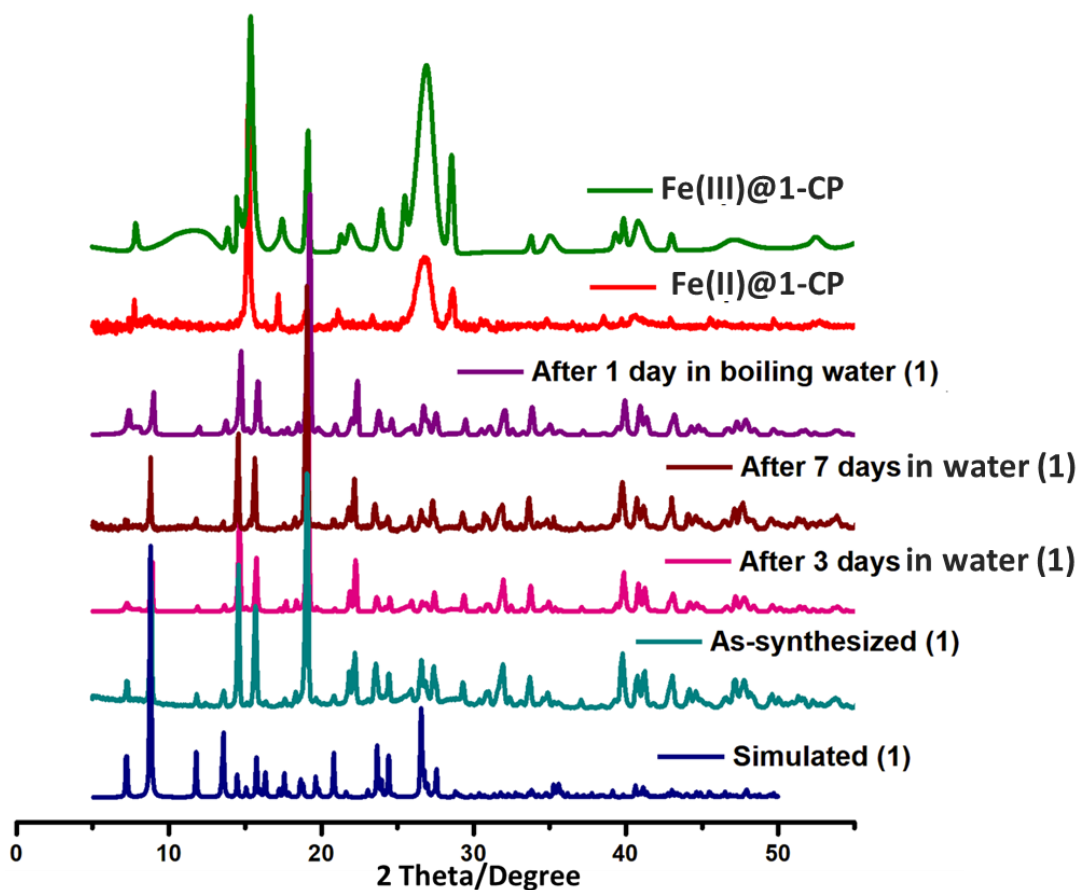
Figure 3.4. Powder X-ray Diffraction analysis of **1**, **1** in different aqueous condition, **Fe(II)@1-CP** and **Fe(III)@1-CP.**

Phase purity of coordination polymer **1** is determined by the PXRD (**Figure 3.4**). The stability of **1** has been checked by measuring the PXRD of water immersed compound **1** for seven days and also in boiling water for 24 h who does not show any change in the spectral pattern and supports the stability of **1** in water medium (**Figure 3.4**).

3.3.2. Spectroscopic detection of Fe^{2+}/ Fe^{3+}

Absorption spectra of **1** suspended in water shows band at 325 and 282 nm. UV-Visible spectra of **1** show absorption at 558 nm in presence of Fe^{3+} and Fe^{2+} ion. In presence of other metal ions Al^{3+}, Cr^{3+}, Zn^{2+}, Pb^{2+}, Co^{2+}, Mn^{2+}, Ni^{2+}, Cu^{2+}, Mg^{2+}, Ca^{2+}, Ba^{2+}, Cd^{2+}, Hg^{2+}, Na^+, K^+ the

spectra of **1** did not show any noticeable difference of the spectra of the compound **1** (**Figure 3.5a**). UV-Visible experiments determine the Fe^{3+} and Fe^{2+} in aqueous medium. The

(a)

(b)

(c)
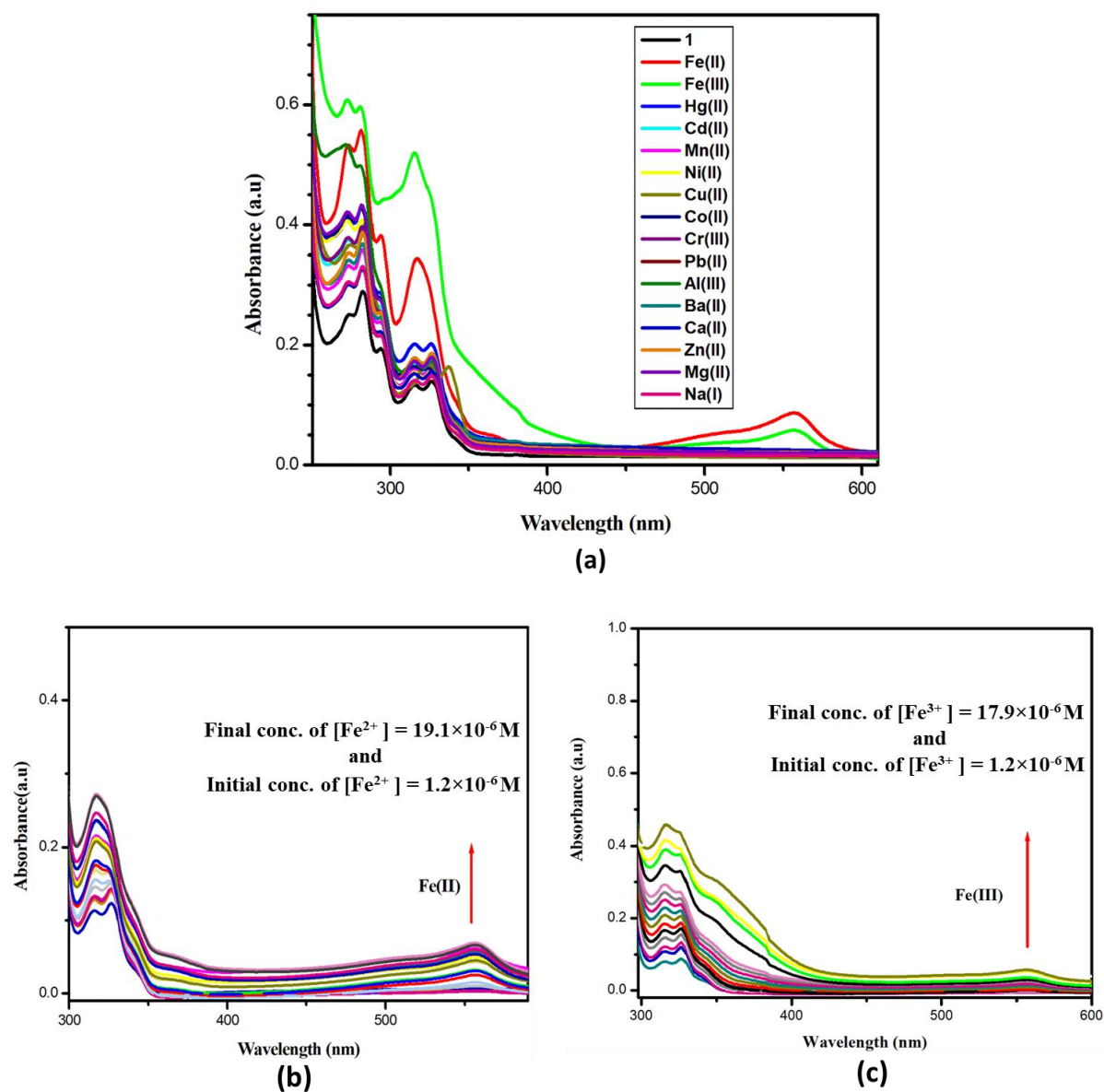
Figure 3.5. (a) Change of absorption spectra with addition of different metal ions in probe **1**, **(b)** Change of absorption intensity of probe **1** upon addition of Fe^{2+} gradually in an aqueous medium at the peak 558 nm, **(c)** Change of absorption intensity of probe **1** upon addition of Fe^{3+}gradually in a aqueous medium at the peak 558 nm.

absorption peak at 558 nm shows visual colour change from colourless to pink. Aqueous solution of **1** is weakly emissive (**Figure 3.6**). A The absorption peak at 558 nm observed after

adding $Fe^{3+/2+}$ to **1** suspension may be due to the coordination of free oxygen donor centre of carboxylate-O of Ar-C(O)-O-Zn followed by substitution of Zn(II) by Fe(III)/Fe(II) which may allow charge transfer from carboxylato moiety to metal center (Fe) which consecutively transfer charge to π-acidic chloroterpyridine (Cltpy) (Ar-COO-Fe-Cltpy).[82-84]
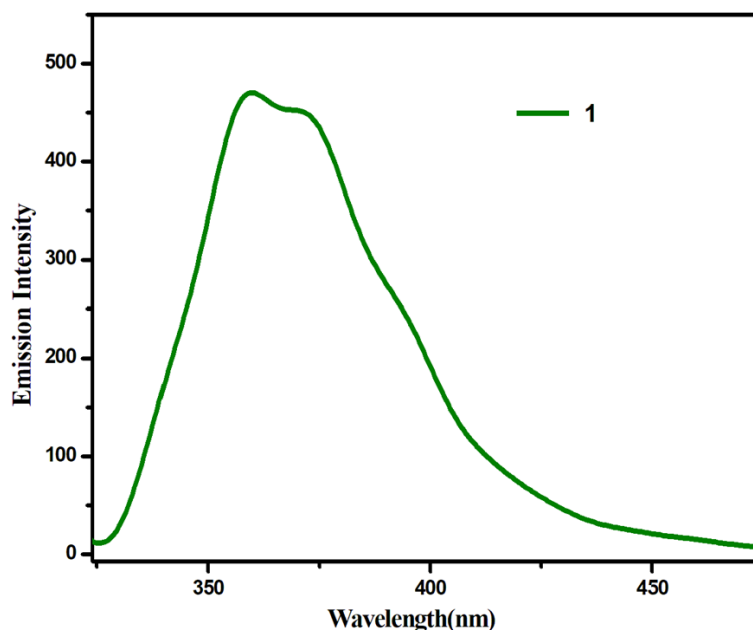
Figure 3.6. Fluorescence spectra of **1** in water with excitation wavelength 325 nm.

For quantitative detection of Fe^{3+} and Fe^{2+}, titration was performed for **1** in aqueous medium. The absorption of coordination polymer **1** is increased gradually with addition (2.5 μL in every step) of Fe^{2+} (**Figure 3.5b**) /Fe^{3+} (**Figure 3.5c**) at 558 nm. The experiment was performed at pH=7.2 maintained by HEPES buffer. Absorption intensity of **1** does not change in appreciably at the pH range 2 to 11 (**Figure 3.7**). Similarly, the absorption intensity remains insensitive to the variation of pH in the range of 2 – 11 even after addition of $Fe^{2+/3+}$ ions (**Figure 3.7**). Thermal stability of coordination polymer **1** was examined by thermogravimetric analysis (TGA). Temperature range 30 – 850 °C with rate 10 °C/ min was performed TGA under the N$_2$ atmosphere.
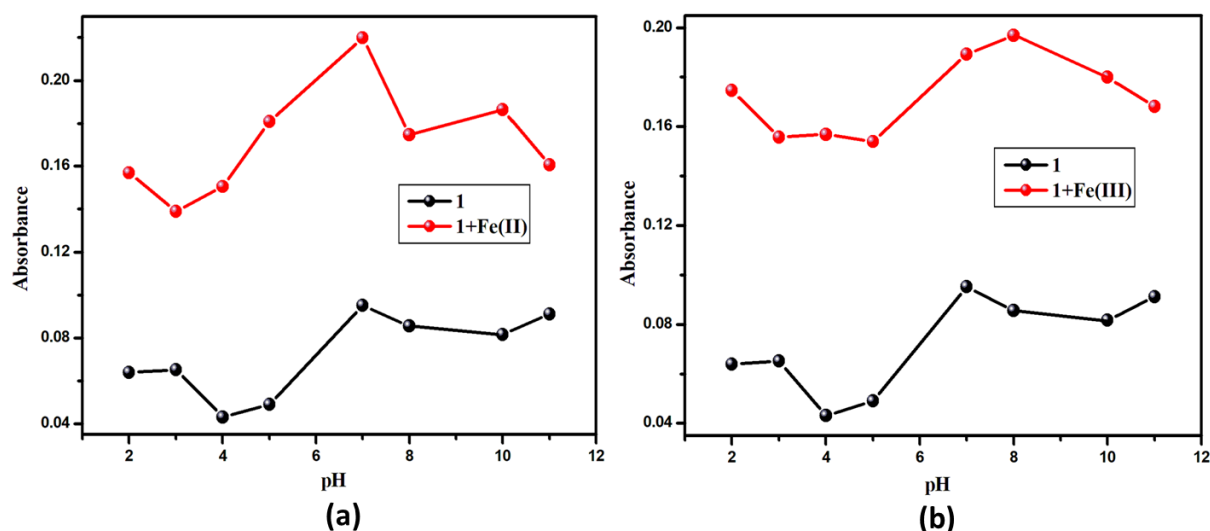
Figure 3.7. (a) pH plot of **1** and **1** in presence of Fe(II) ion. **(b)** pH plot of **1** and **1** in presence of Fe(III) ion.
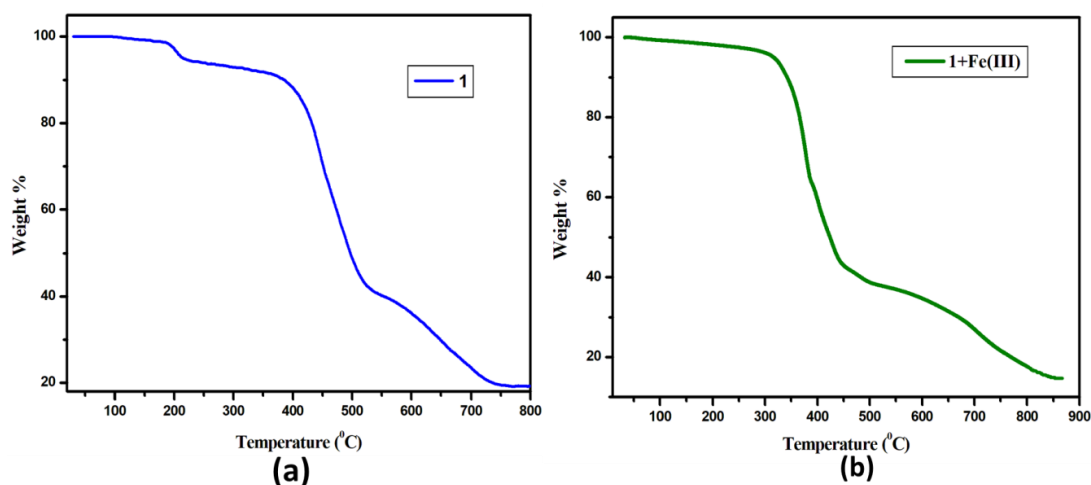
Figure 3.8. (a) TGA of **1**, **(b)** TGA of **Fe(III)@1-CP**.

For the coordination polymer **1**, first weight loss 5.37 % (calcd. 5.35 % for $2H_2O$) at the range of 180-220 °C was observed, which is due to loss of more weakly bounded two water molecule from crystal lattice. The compound is moderately stable upto 390 °C (**Figure 3.8**) and decomposition started at 390 °C. This decomposition has been completed at 727 °C.

Excited state life time of **1** is 2.62 ns and in presence of Fe^{3+} is decreased to 1.87 ns (**Figure 3.9**) and life time of **1** after addition Fe^{2+} is nearly same with the Fe^{3+} (**Figure 3.9b**).
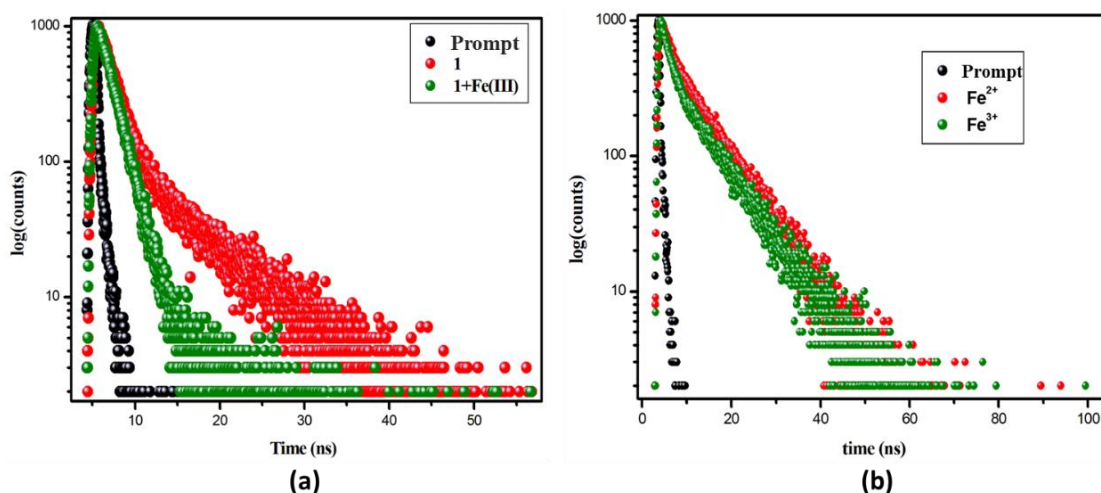
Figure 3.9. (a) Excited state decay profile of prompt, **1** and Fe^{3+} ion with **1** in aqueous medium. **(b)** Life time plot of **1+ Fe(II)** and **1+ Fe(III)**.
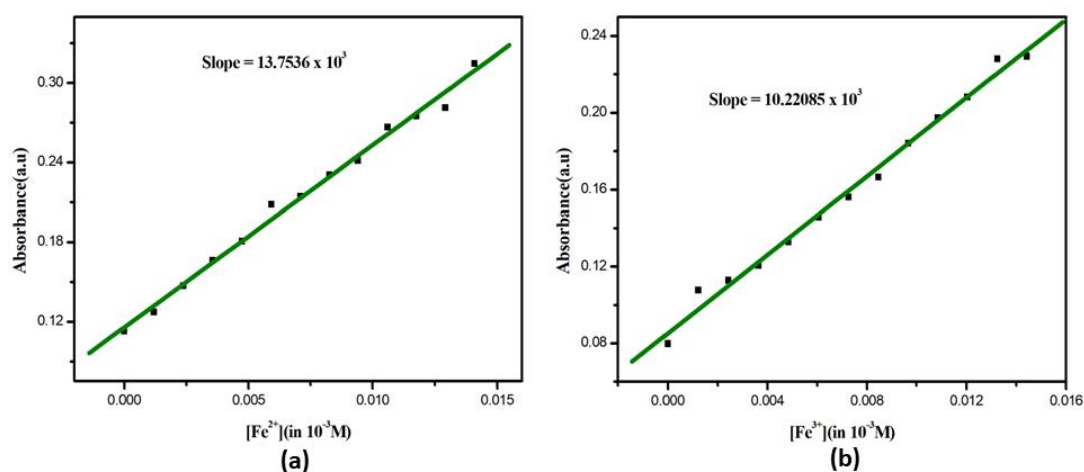
Figure 3.10. (a) Limit of detection (LOD) plot of **1** in presence of Fe(II) ion. **(b)** Limit of detection (LOD) plot of **1** in presence of Fe(III) ion.

Hence, the excited state stability of pure **1** is higher than in presence of $Fe^{2+/3+}$ ions. This implies that $Fe^{2+/3+}$ affects the integrity of the CP **1**. Limit of detections (LOD) are 0.11 μM and 0.15 μM for Fe^{2+} and Fe^{3+} respectively (**Figure 3.10**). Literature shows that sensing of $Fe^{2+/3+}$ by CPs are scarce and the present result of Zn(II)-CP (**1**) is highly selective and sensitive (**Table 3.4**). Binding constant (K_d) of **1** with Fe^{2+} (**Figure 3.11a**) and Fe^{3+} (**Figure 3.11b**) are 3.33×10^4 M^{-1} and 6.7×10^4 M^{-1} respectively which shows that stronger binding with Fe^{3+} than the

Fe^{2+}. The spectral effect of Fe^{2+} and Fe^{3+} in presence of other metal ions Al^{3+}, Cr^{3+}, Zn^{2+}, Pb^{2+}, Co^{2+}, Mn^{2+}, Ni^{2+}, Cu^{2+}, Mg^{2+}, Ca^{2+}, Ba^{2+}, Cd^{2+}, Hg^{2+}, Na^+, K^+ is shown in **Figure 3.12**. Absorption intensity of **1**, intensity change with different metal ions (**M**) and intensity diagram with Fe^{3+} along with different metal ions in aqueous medium.
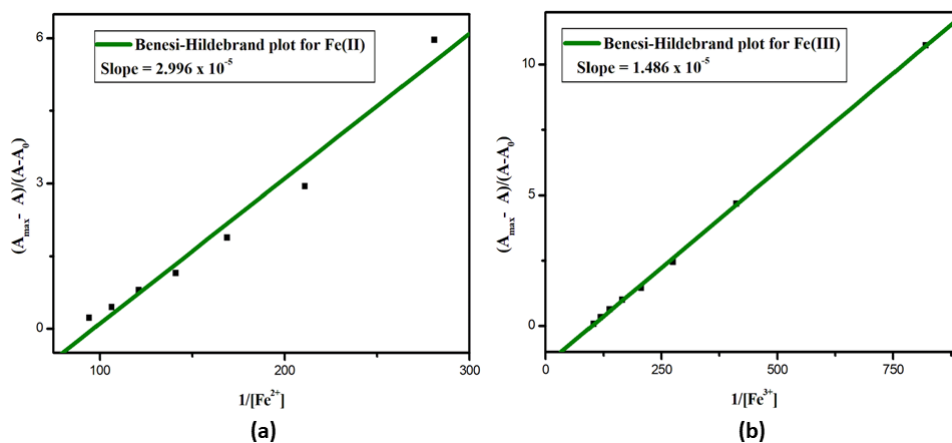
Figure 3.11. (a) Benesi-Hildebrand plot of **1** in presence of Fe(II) ion. **(b)** Benesi-Hildebrand plot of **1** in presence of Fe(III) ion.
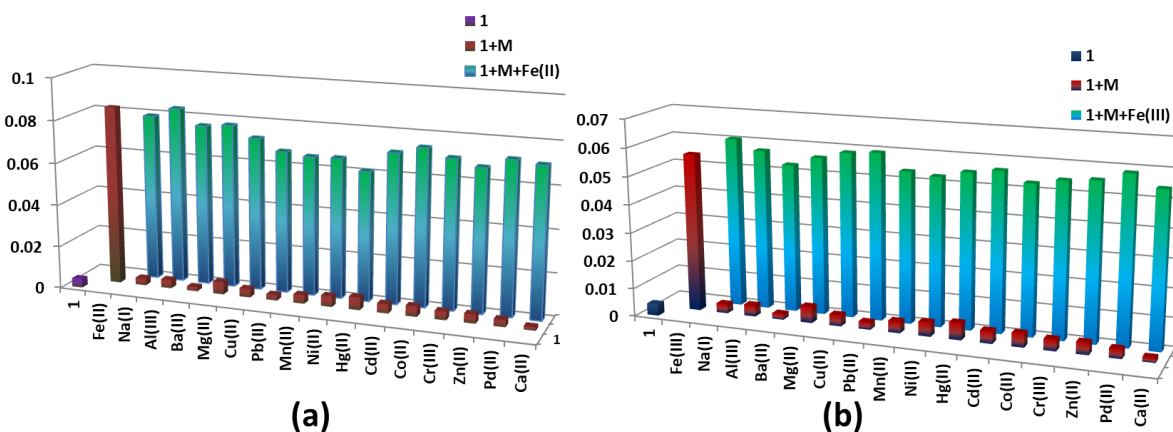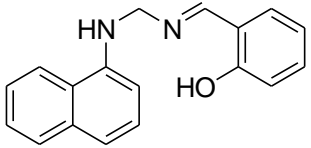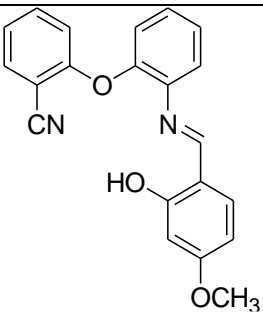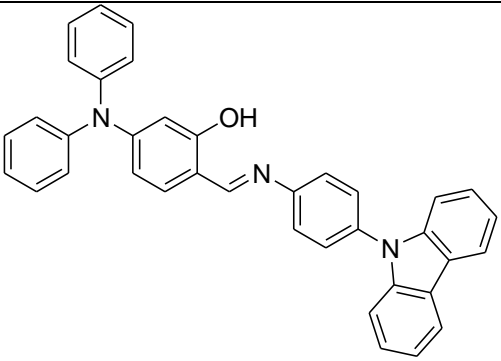
Figure 3.12. (a) Absorption intensity of **1**, intensity change with different metal ions (**M**) and intensity diagram with Fe^{2+} along with different metal ions in aqueous medium (**b**).

Table 3.4. Comparison of the sensitivities of **1** with previously reported CPs to Fe^{3+} and Fe^{2+} ions.

Sl. No.	Ligand	Selectivity (LOD)	Solvent	Live Cell Imaging	Reference
1.		20.85 μM	Water-Methanol (1:4)	No	85
2.		14.53 μM	Acetonitrile	No	86
3.		10 μM	MeCN	No	87
4.	[Zn(L)0.5(2,6-NDC)]n (L = 1,6-bis(1-(pyridin-4-ylmethyl)-1H-benzo[d]imidazol-2-yl)hexane, 2,6-H2NDC = 2,6-naphthalenedicarboxylic acid)	0.82 μM	MeOH	No	88
5.	[Zn5(hfipbb)4(trz)2(H2O)2] (H2hfipbb = 4,4′(hexafluoroisopropylidene)bis(benzoic acid), Htrz = 1H-1,2,3-triazole)	0.20 μM	Water	No	89

6.	[Co(OBA)(L1)$_{0.5}$]$_n$ (**1**) and [Co(HBTC)(L2)]$_n$ (**2**) (H2OBA = 4,4′-oxybis(benzoic acid), H3BTC = 1,3,5-benzenetricarboxylic acid, 1,3-bis(1-(pyridin-4-ylmethyl)-1H-benzimidazol-2-yl)propane (L1) and 1,4-bis(benzimidazol-1-yl)-2-butene (L2)).	6.92 μM (**1**) and 10.16 (**2**)μM	water	No	90
7.	**1**	0.11 μM (Fe^{2+}) and 0.15 μM (Fe^{3+})	Water	Yes	**This Work**

3.3.3. Kinetic Study of compound (1) with aqueous solution of FeCl₃

The crystals of compound (**1**) was suspended in aqueous solution of FeCl₃. The colourless crystals of **1** turned to dark brown (**Figure 3.13**). Energy Dispersive X-Ray Analysis (EDX) study reveals the exchange of Zn(II) by Fe(III). The metal exchange process may explain that the Zn-N and Zn-O bonds are dissociated and Fe-N and Fe-O bonds are formed.
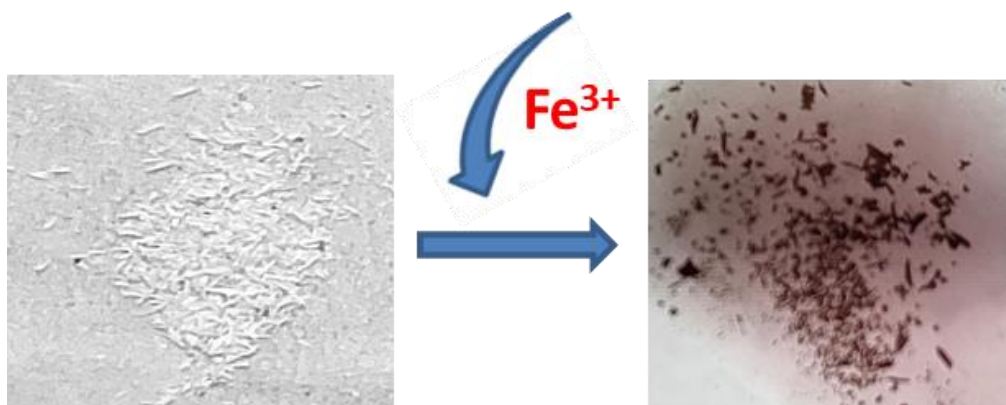
Figure 3.13. Color changes colorless to dark brown of crystal **1** uptake of Fe^{3+}.

The table in figure (a):

Time (min)	$[Fe^{3+}]$ (uptake, in M)
05	4.9×10^{-5}
10	5.2×10^{-5}
15	5.5×10^{-5}
20	6.02×10^{-5}
25	6.3×10^{-5}
30	6.5×10^{-5}
35	6.7×10^{-5}
40	6.9×10^{-5}
45	7.17×10^{-5}
50	7.4×10^{-5}
55	7.69×10^{-5}
60	7.92×10^{-5}
65	8.26×10^{-5}
70	8.56×10^{-5}
75	8.9×10^{-5}
80	9.39×10^{-5}
85	9.65×10^{-5}
90	9.94×10^{-5}
95	10.17×10^{-5}
100	10.69×10^{-5}
105	11.0×10^{-5}
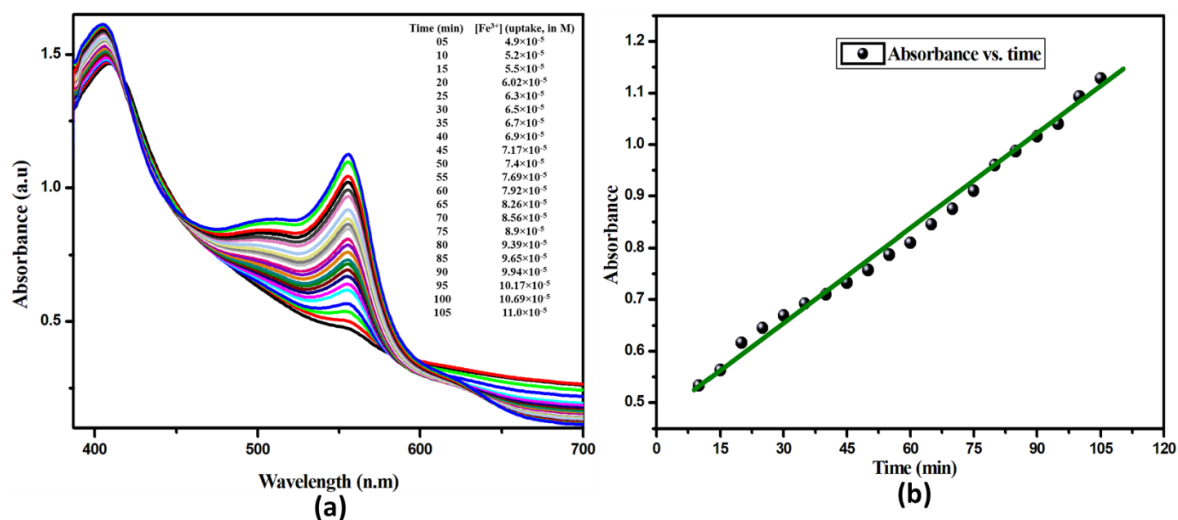
Figure 3.14. **(a)** Fe^{3+} uptake kinetic of **1** monitored via UV-Visible spectroscopy in water medium, **(b)** Absorbance vs. time (min) plot for Fe^{3+} uptake kinetic.

The UV-Visible spectroscopy was used to determine the concentration of Fe^{3+} in solution after absorption by **1** (**Figure 3.14, Figure 3.16**) via substitution reaction; the uptake level of Fe^{3+} concentration was increased with increasing time. Crystal colour was changed from
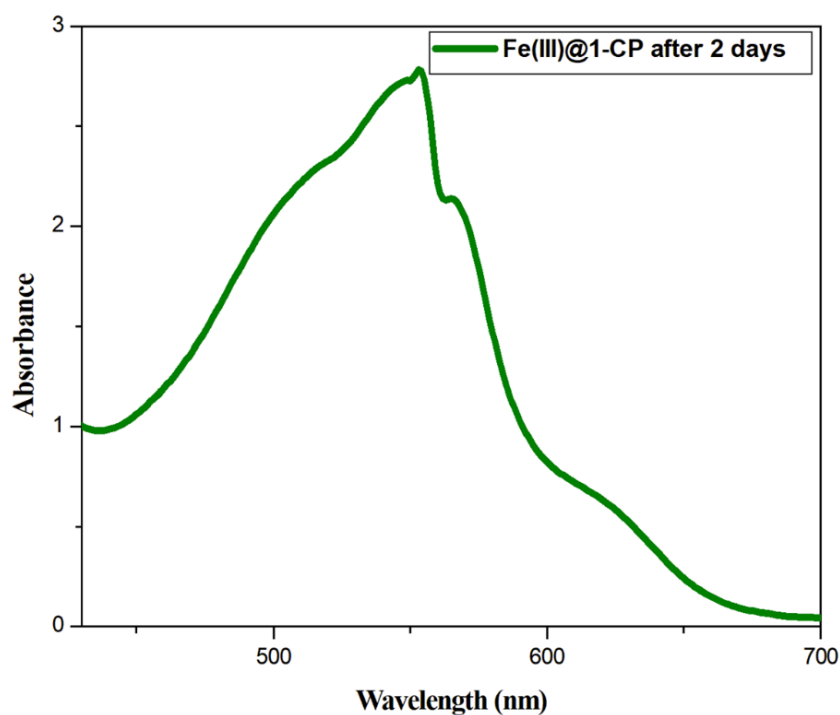
Figure 3.15. Absorbance of **1** in presence of Fe^{3+} after 2 days.

106

colourless to dark brown (**Figure 3.13**). Fe^{3+} uptake by coordination polymer is a substitution reaction that follows first order kinetics[48] (like I_2 sorption[15]) and rate constant (k) value is 2.20 $\times 10^{-3}$ min^{-1} (**Table 3.5**) calculated from the plot of, log(qe – qt) vs t (min) (**Eq. 3.1, 3.2**). No further change of absorbance after 2 days (**Figure 3.15**) is observed, which indicates that the system has reached at equilibrium. Rate constant (k) of the process (uptake of Fe^{3+} by coordination polymer **1**) was determined using UV-Visible spectroscopy.[91,92]

(a)

(b)
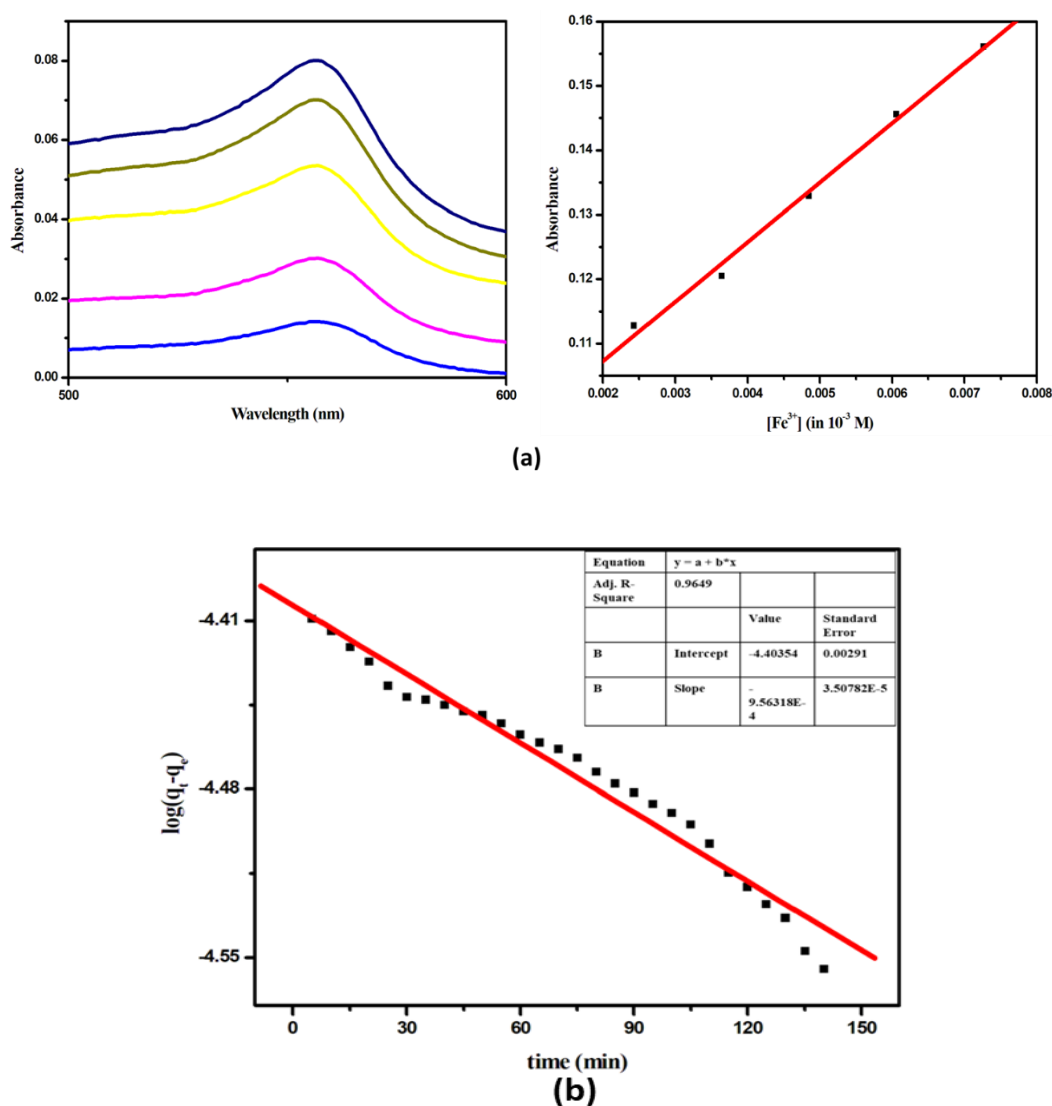
Figure 3.16. (a) Fe(III) uptake UV-Visible experiments and calibration curve under five different concentration solutions at wavelength 558 nm, **(b)** Plot log(q_t – q_e) vs. time (min.) for calculation of rate constant (k) during the Fe(III) uptake kinetics of **1**.

The following equation[7-8] define the amount of Fe^{3+} uptake at the time t,

$$qe(t) = \frac{V(Ci - Ce(t))}{m} \qquad (3.1)$$

Where, Ce and Ct are the concentration at equilibrium (mol/L) and at time t, Ci is the initial concentration of Fe^{3+} in water (mol/L), qe and qt are the amount of Fe^{3+} uptake at equilibrium (mol/mg) and at time t, m is the mass of CP of **1** were used (mg).

The linear form of pseudo first order kinetic model is expressed by the following equation[91-93], Where, qe and qt are previously defined, k is the pseudo first order rate constant for the adsorption process (min^{-1}).

$$\log(qe - qt) = \log qe - \left(\frac{k}{2.303}\right)t \qquad (3.2)$$

Table 3.5. Determination rate constant (k) using the UV-Visible spectroscopy.

Rate constant (k, min^{-1})	Slope	Intercept
0.0022	9.56318×10^{-4}	4.40354

This substitution reaction is also substantiated by the PXRD, IR and SEM-EDX study data. The IR spectra, in general, show the shifting of the frequency (cm^{-1}) to the higher values (**Figure 3.17**). Frequency of –COO group is shifted 1601 cm^{-1} (**1**) →1683 cm^{-1} (**Fe(III)@1-CP**) and 1673 cm^{-1} (**Fe(II)@1-CP**). TGA also shows the decomposition temperature is higher for **Fe(III)@1**-CP (796 °C) than the **1** (727 °C) (**Figure 3.8**). The PXRD pattern shows the crystalline nature of the product **Fe(III)@1**-CP after reaction (**Figure 3.4**) where phase pattern of **Fe(III)@1**-CP remains same as **1** with some additional signals.
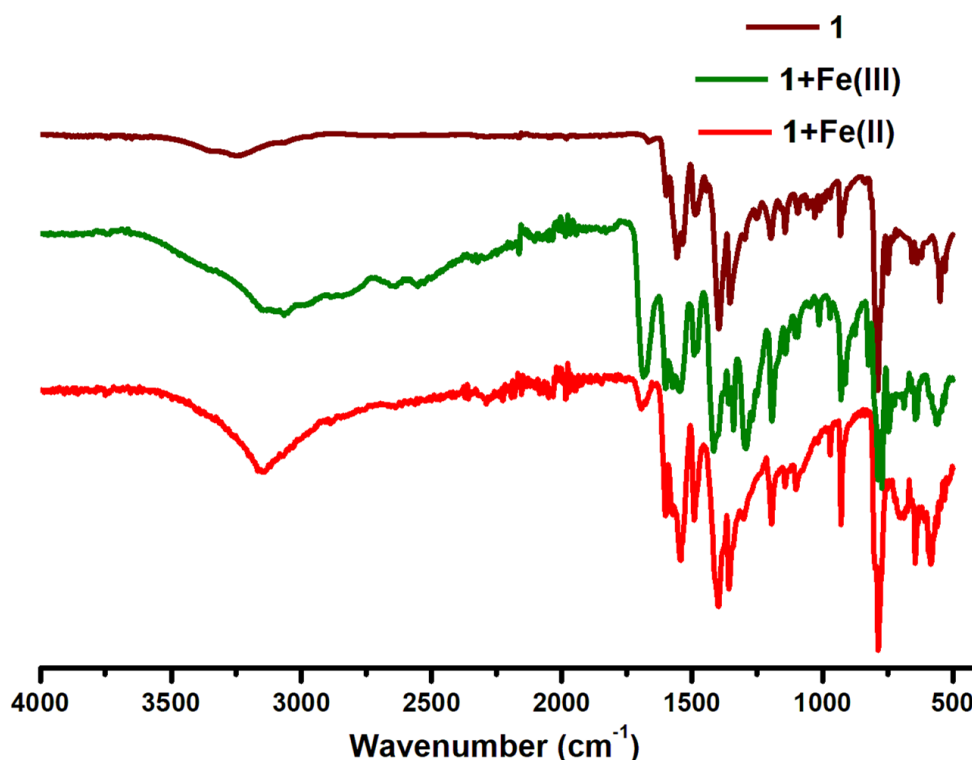
Figure 3.17. IR spectrum of **1**, **1+Fe(II)** and **1+Fe(III)**.

To support the substitution of Zn(II) by Fe(II/III) the SEM mapping and EDX analysis were performed. The SEM image shows the crystalline morphologies of **1, Fe(III)@1-**CP and **Fe(II)@1-**CP in the range of 10 μm to 50 μm respectively (**Figures 3.18a-c**) and **Figures 3.18d-f** show mapping of Fe; and Zn mapping is shown in **Figures 3.18g-h** of the sample **1, Fe(III)@1-**CP and **Fe(II)@1-**CP respectively. Similary, Cl and N mapping of **1, Fe(III)@1-**CP and **Fe(II)@1-**CP was shown in **Figure 3.19**. However, PXRD at higher angle of diffraction ($2\theta > 30°$) shows signal shifting from that of simulated spectrum which is not very uncommon. Elemental data analysis and SEM mapping clearly show the increase in Fe percentage (**Figure 3.20, Table 3.6**) and decrease in Zn percentage (**Figure 3.20**) during substitution reaction.
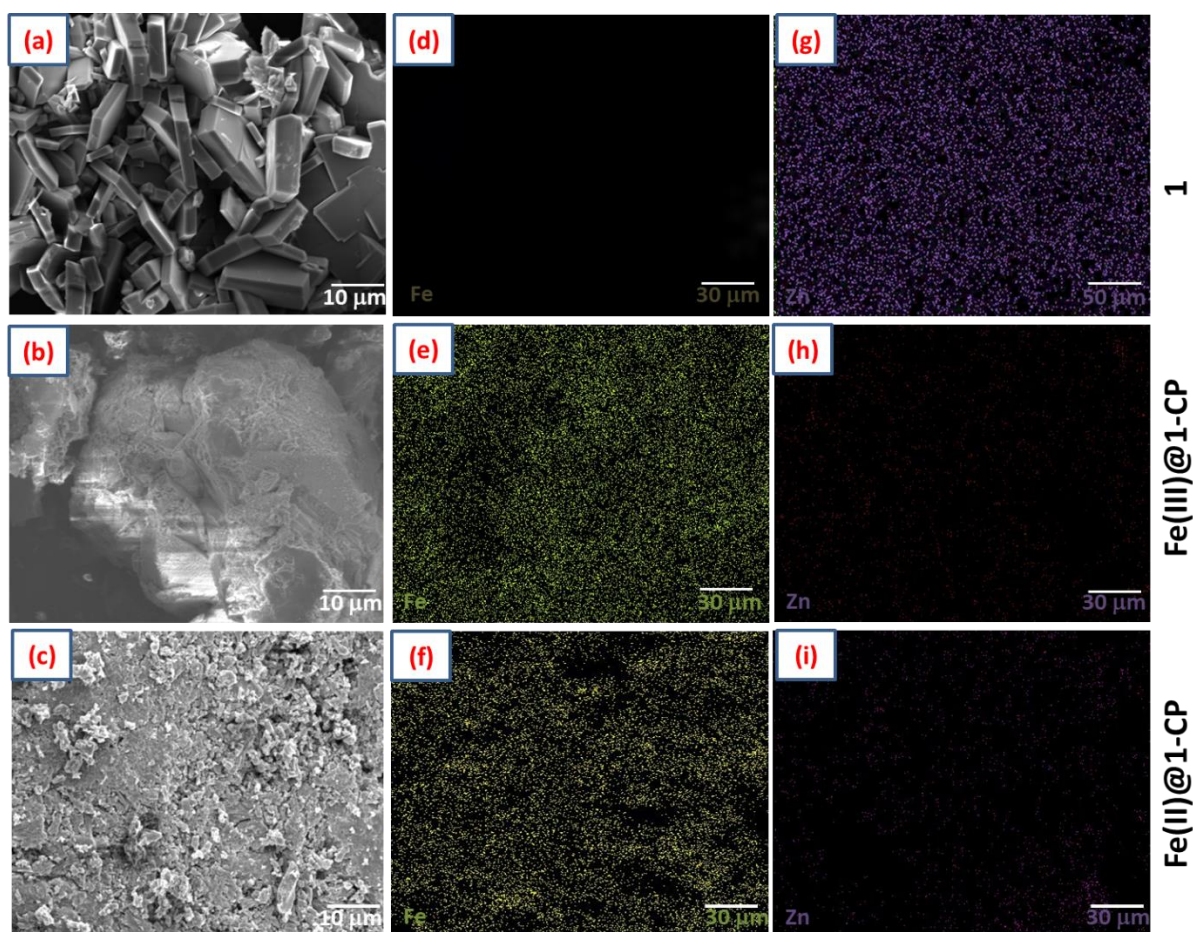
Figure 3.18. SEM images of **1 (a), Fe(III)@1-CP (b)** and **Fe(II)@1-CP (c)** in the range of 10 μm. EDX mapping of Fe in **1 (d), Fe(III)@1-CP (e)** and **Fe(II)@1-CP (f);** EDX mapping of Zn in **1 (g), Fe(III)@1-CP (h)** and **Fe(II)@1-CP (i)**.

Table 3.6. Atom% of **1**, **Fe(II)@1-CP** and **Fe(III)@1-CP** in the EDX spectrum.

Sample	N%	Zn%	Fe%
1	4.18	24.08	-
Fe(III)@1-CP	3.27	-	30.47
Fe(II)@1-CP	2.47	1.12	19.68
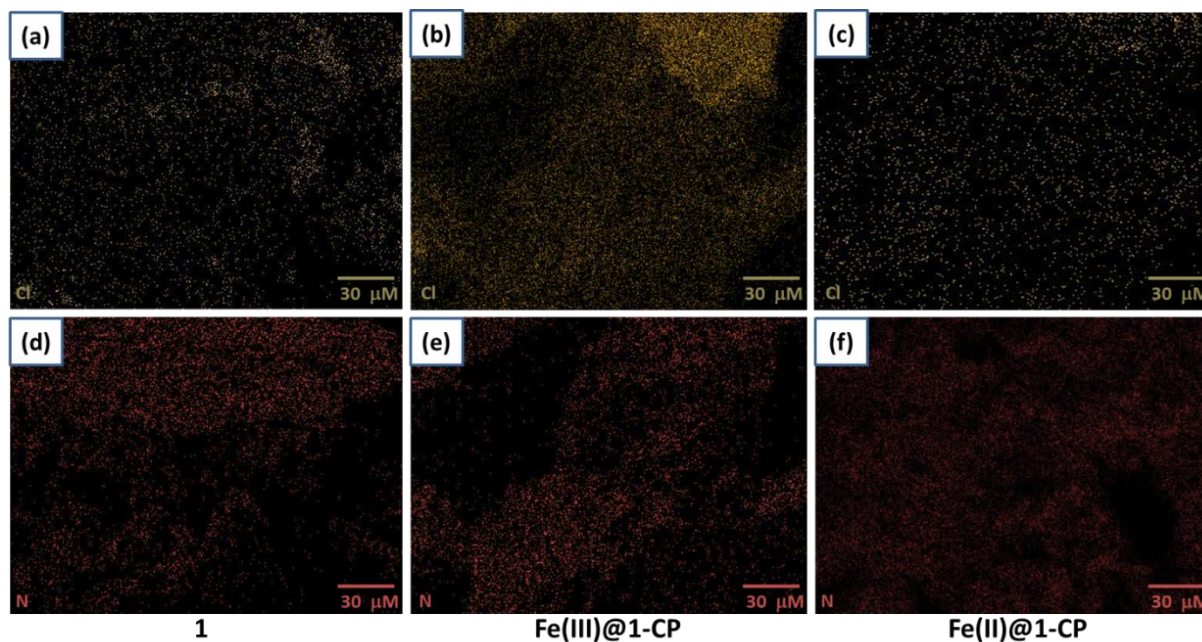
Figure 3.19. EDX mapping of Cl in **1 (a), Fe(III)@1-CP (b)** and **Fe(II)@1-CP (c);** EDX mapping of N in **1 (d), Fe(III)@1-CP (e)** and **Fe(II)@1-CP (f)**.

In colorimetric experiment, the colour of suspension of **1** in water has changed from colorless to pink upon addition of $Fe^{2+/3+}$ (**Figure 3.21**). Zn(II) ion is exchanged with Fe^{3+} ion and formed the **Fe(III)@1-**CP. In presence of Fe(II) the coordination polymer **1** also joined in the exchange reaction along with fast air oxidation to Fe(III) as it is evidenced from same spectral pattern (IR, EDX) and formed **Fe(III)@1-**CP.[48]

All inorganic salts (NaCl, KCl, $CuCl_2$, $ZnCl_2$, $CdCl_2$, $HgCl_2$, $AlCl_3$, $PbCl_2$, $CoCl_2$, $MnCl_2$, $FeCl_3$, $MgCl_2$, $CaCl_2$, $BaCl_2$, $MnCl_2$, $NiCl_2$, $CrCl_3$ and $(NH_4)_2Fe(SO_4)_2 \cdot 6H_2O$ were used (1×10^{-3} M) to prepare aqueous solution using deionised water. Cl^- presence as a counter ion was observed by $AgNO_3$ test (**Figure 3.22**). Stability of the compound **1** (**Figure 3.23**) and reversibility (in presence of EDTA) was checked (**Figure 3.24**).

3.3.4. Cell imaging study

Upon addition of MDA-MB 231 cells to the solution of **1** (10 μM), [**1**+ Fe^{2+} (10 μM)] and [**1** + Fe^{3+} (10 μM)] at the incubation time frame of 30 min a bright blue fluorescence was recorded by Fluorescence microscopy imaging technique, while no fluorescence has been
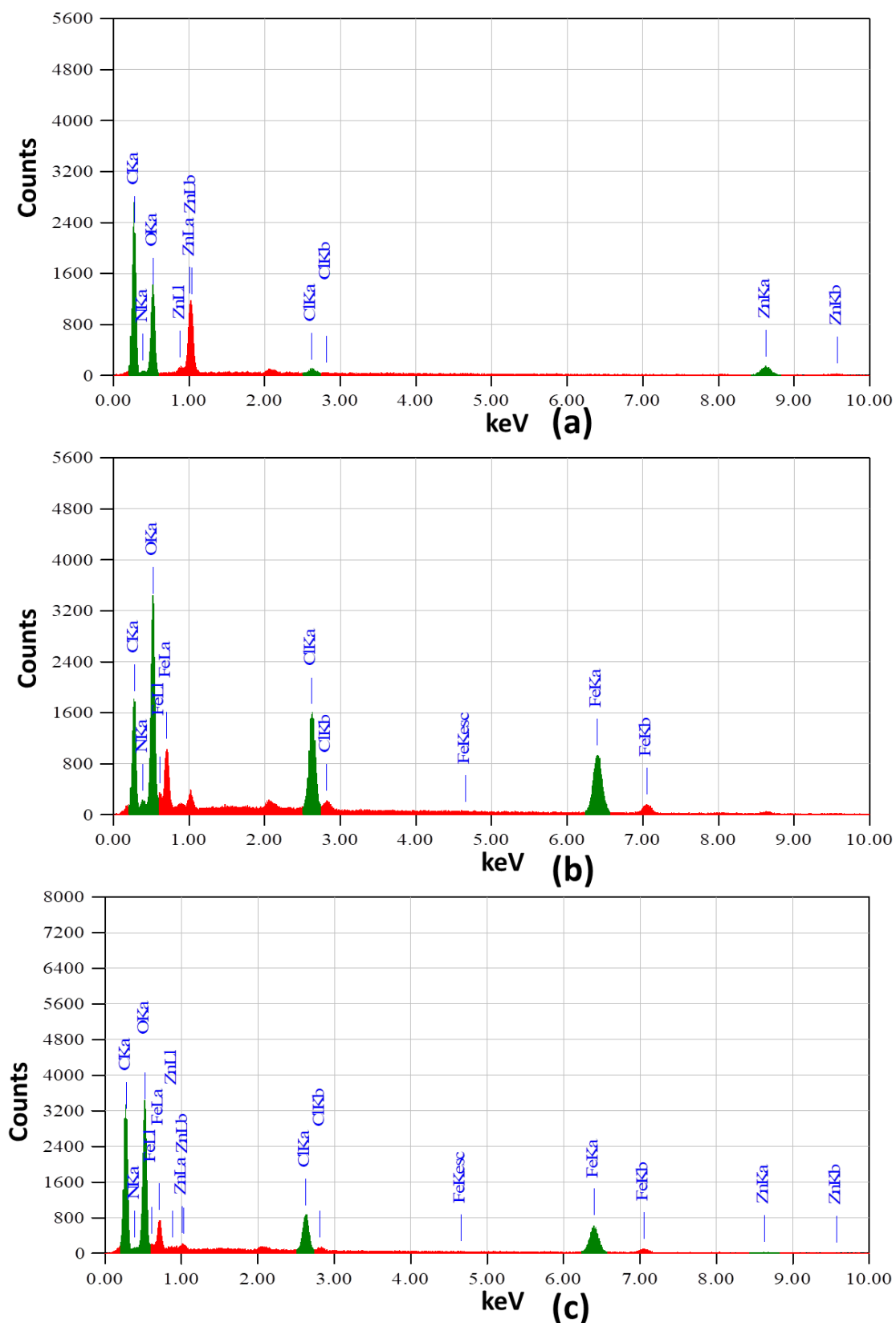
Figure 3.20. (a) EDX spectrum of **1 (b)** EDX spectrum of **Fe(III)@1-CP**, **(c)** EDX spectrum

of **Fe(II)@1-CP**

112

Figure 3.21. Visualization test of Coordination polymer, **1** with different metal ions.

Figure 3.22. $AgNO_3$ test for presence of Cl^- as counter ion in **Fe(III)@1-CP**.

observed in untreated as well as cells treated with only the coordination polymer, **1** (**Figure 3.25a**). This experiment confirms that the cells readily uptake the **1** (10 μM) in the presence of Fe^{2+} and Fe^{3+}. Results from fluorescence microscopy also justified that in the presence of Fe^{2+} and Fe^{3+}, **1** has shown that the blue emission is not an artefact of one of either added compounds.
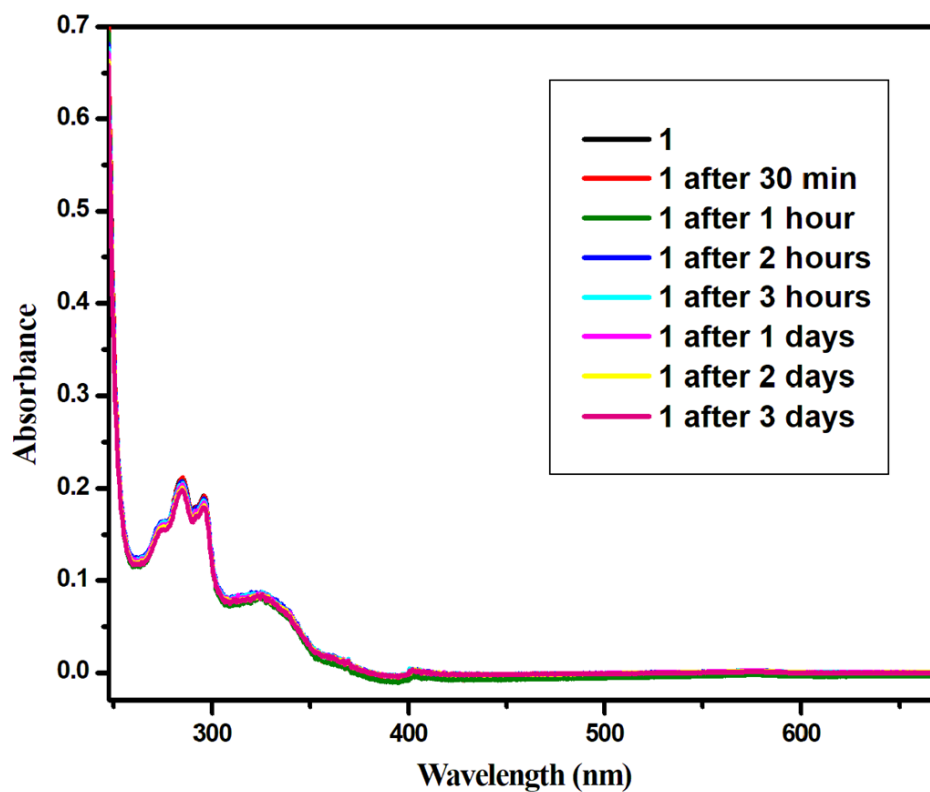
Figure 3.23. Water stability of **1** examined via UV-Visible experiments.
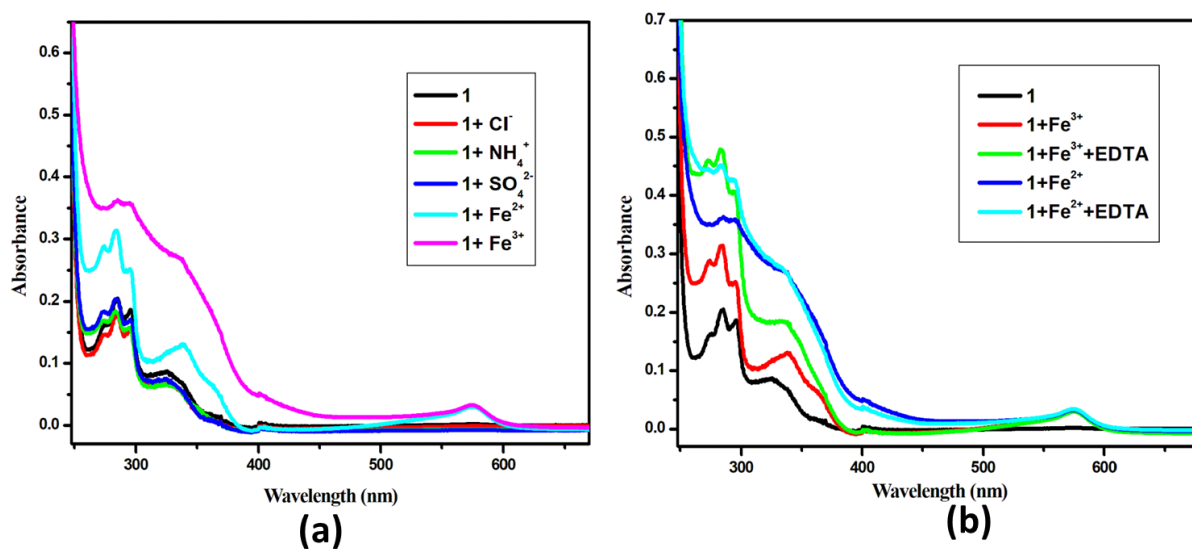
Figure 3.24. (a) Effect of constitute ions in the colorimetry by $Fe^{2+/3+}$, **(b)** reversibility checked by UV-Visible experiments.

114
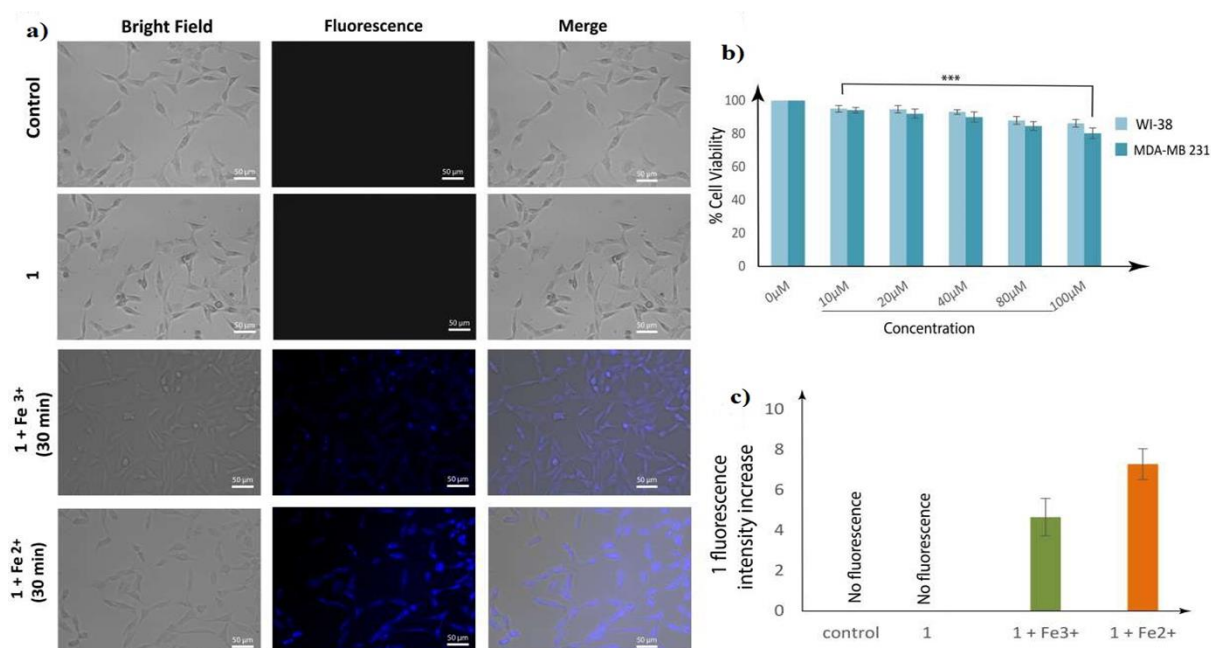
Figure 3.25. (a) Microscopic images of untreated MDA-MB 231 cells (Control), cells treated with **1**(10µM), [**1** (10 µM) + Fe^{2+} (10 µM)] and [**1**(10 µM) + Fe^{3+} (10 µM)] after 30 min, incubation period under bright, fluorescence and merged field, **(b)** Cell survivability of MDA-MB 231 and WI-38 cells exposed to various concentration of **1**. The data are from at least three independent experiments, and the bar graph shows the mean $\pm$ SEM, ***$p < 0.001$ were interpreted as statistically significant, as compared with the control, **(c)** histogram of the fluorescence intensity,

3.3.5. Cell survivability assay

In-vivo cell survivability and cytotoxicity of the **1** was checked on MDA-MB 231 and WI-38 cell line. MTT assay data revealed no significant toxicities, even at higher concentration of 100 µM of **1** (**Figure 3.25b**). Hence, **1** is biocompatible and favourable for biological applications.

3.4. Conclusion

The coordination polymer **1** is formed with the capping ligand 4-Cltpy, linked with dicarboxylate NDC^{2-} and Zn(II) ions. This 1D CP is assembling through $\pi\cdots\pi$, C-Cl$\cdots\pi$ and H-bonding interactions to make a supramolecular geometry. In aqueous medium, it detects total Fe (Fe^{2+} and Fe^{3+}) through colour change, colourless to pink and in solid state changes colourless to dark brown while other fifteen ions do not show any impact on the absorption spectra of **1**. The product analysis by the SEM, EDX mapping, PXRD, TGA and IR spectral data support the substitution of Zn(II) from **1** by Fe(II/III) to isolate **Fe(III)@1-CP**. Moreover, the biocompatible Cell imaging study of this coordination polymer revealed that the intracellular Fe^{II}, Fe^{III} detects in MDA-MB 231 cells line and the cell viability (%) tolerance limit to 100 μM displays in the MTT assay.

3.5. Reference

1. Wen, Y.; Rentería-Gómez, A.; Day, G. S.; Smith, M. F.; Yan, T. H.; Ozdemir, R. O. K.; Gutierrez, O.; Sharma, V. K.; Ma, X.; Zhou, H. C. Integrated Photocatalytic Reduction and Oxidation of Perfluorooctanoic Acid by Metal–Organic Frameworks: Key Insights into the Degradation Mechanisms. *J. Am. Chem. Soc.,* **2022**.

2. Chen, W.; Fan, R.; Zhang, H.; Dong, Y.; Wang, P.; Yang, Y. Tunable white-light emission PMMA-supported film materials containing lanthanide coordination polymers: preparation, characterization, and properties. *Dalton Trans.* **2017**, *46*, 4265–4277.

3. Xu, M.; Cai, P.; Meng, S. S.; Yang, Y.; Zheng, D. S.; Zhang, Q. H.; Gu, L.; Zhou, H. C.; Gu, Z. Y. Linker Scissoring Strategy Enables Precise Shaping of Metal–Organic Frameworks for Chromatographic Separation. *Angew. Chem.,* **2022**, 202207786.

4. Dutta, B.; Dey, Arka.; Sinha,C.; Ray,P. P.; Mir,M. H. Photochemical Structural Transformation of a Linear 1D Coordination Polymer Impacts the Electrical Conductivity. *Inorg. Chem.* **2018**, *57*, 14, 8029–8032.

5. Biradha. K.; Su. C.-Y.; Vittal, J. J. Recent developments in crystal engineering. *Cryst. Growth Des.***2011**, *11*, 875–886.

6. Duan, J.; Jin, W.; Kitagawa, S. Water-resistant porous coordination polymers for gas separation. *Coord. Chem. Rev.***2017**, *332*, 48−74.

7. Wang, F.; Li, F.-L.; Xu, M.-M.; Yu, H.; Zhang, J.-G.; Xia, H.-T.; Lang, J.-P. Facile synthesis of a Ag(I)-doped coordination polymer with enhanced catalytic performance in the photo degradation of azo dyes in water. *J. Mater. Chem. A.* **2015**, *3*, 5908−5916.

8. O'Keeffe, M.; Yaghi, O. M. Deconstructing the crystal structures of metal–organic frameworks and related materials into their underlying nets. *Chem. Rev.***2012**, *112*, 675–702.

9. Naskar, K.; Dey, A.; Dutta, B.; Ahmed, F.; Sen, C.; Mir, M. H.; Roy, P. P.; Sinha, C. Intercatenated coordination polymers (ICPs) of carboxylato bridged Zn(II)-isoniazid and their electrical conductivity. *Cryst. Growth Des.* **2017**, *17*, 3267-3276.

10. Dutta, B.; Pal, K.; Jana, K.; Sinha, C.; Mir, M. H. Fabrication of a Zn (II)-Based 2D Pillar Bilayer Metal-Organic Framework for Antimicrobial Activity. *ChemistrySelect.* **2019**, *4*, 9947-9951.

11. Wu, S.; Min, H.; Shi, W.; Cheng, P. Multicenter Metal–Organic Framework-Based Ratiometric Fluorescent Sensors. *Adv.Mater.***2020**, *32*, 1805871.

12. Horike, S.; Nagarkar, S. S.; Ogawa, T.; Kitagawa, S. A New Dimension for Coordination Polymers and Metal–Organic Frameworks: Towards Functional Glasses and Liquids. *Angew. Chem., Int. Ed.* **2020**, *59*, 6652-6664.

13. Brozek, C. K.; Dinca, M. Cation exchange at the secondary˘ building units of metal-organic frameworks. *Chem. Soc. Rev.* **2014**, *43*, 5456−5467.

14. Ma, Z.; Moulton, B. Recent advances of discrete coordination complexes and coordination polymers in drug delivery. *Coord. Chem. Rev.* **2011**, *255*, 1623−1641.

15. Naskar, K.; Dey, A.; Maity, S.; Bhunia, M, K.; Ray, P, P.; Sinha, C. Novel porous polycatenated Iodo–cadmium coordination polymer for iodine sorption and electrical conductivity measurement. *Cryst. Growth Des*. **2019**, *19*, 2206-2218.

16. Naskar, K.; Bhanja, A. K.; Paul, S.; Pal, K.; Sinha, C. Trace Quantity Detection of H_2PO^{4-} by Fluorescent Metal Organic Framework (F-MOF) and Bio-Imaging Study. *Cryst. Growth Des.* **2020**, *20*, 6453-6460.

17. Dey, S.; Sil, S.; Dutta, B.; Naskar, K.; Maity, S.; Ray, P, P.; Sinha, C. Designing of Pb (II)-Based Novel Coordination Polymers (CPs): Structural Elucidation and Optoelectronic Application. *ACS omega*. **2019**, *4*, 19959-19968.

18. Chakraborty, A.; Roy, S.; Eswaramoorthy, M.; Maji, T, K. Flexible MOF–aminoclay nanocomposites showing tunable stepwise/gated sorption for C_2H_2, CO_2 and separation for CO_2/N_2 and CO_2/CH_4. *J. Mater. Chem.A.*, **2017**, *5*, 8423−8430.

19. Dutta, B.; Maity, S.; Ghosh, S.; Sinha, C.; Mir, M, H.; An acetylenedicarboxylato-bridged Mn (II)-based 1D coordination polymer: electrochemical CO_2 reduction and magnetic properties. *New J. Chem.*, **2019**, *43*, 5167-5172.

20. Yin, Z.; Zhou, Y, L.; Zeng, M, H.; Kurmoo, M. The concept of mixed organic ligands in metal–organic frameworks: design, tuning and functions. *Dalton Trans*. **2015**, *44*, 5258−5275.

21. Du, J.; Wang, R.; Lv, Y, R.; Wei, Y, L.; Zang, S, Q.; One-step MOF-derived Co/Co 9 S 8 nanoparticles embedded in nitrogen, sulfur and oxygen ternary-doped porous carbon: an efficient electrocatalyst for overall water splitting. *Chem. Comm.,***2019**, *55*, 3203-3206.

22. Gao, J.; He, M.; Lee, Z, Y.; Cao, W.; Xiong, W, W.; Li, Y.; Ganguly, R.; Wu, T.; Zhang, Q. A surfactant-thermal method to prepare four new three-dimensional heterometal–organic frameworks. *Dalton Trans.,* **2013**, *42*, 11367-11370.

23. Guo, Y.; Wang, K.; Hong, Y.; Wu, H.; Zhang, Q. Recent progress on pristine two-dimensional metal-organic frameworks as active components in supercapacitors. *Dalton Trans.,* **2021**, *50*, 11331-11346.

24. Li, C.; Wang, K.; Li, J.; Zhang, Q. Nanostructured potassium–organic framework as an effective anode for potassium-ion batteries with a long cycle life. *Nanoscale,***2020,***12*, 7870-7874.

25. Zhang, X, D.; Hou, S, Z.; Wu, J, X.; Gu, Z, Y. Two-Dimensional Metal–Organic Framework Nanosheets with Cobalt-Porphyrins for High-Performance CO_2 Electroreduction. *Eur. J. Chem.,***2020**, *26*, 1604-1611.

26. Naskar, K.; Dey, A.; Maity, S.; Ray, P, P.; Sinha, C. Charge Transportation in Zn (II)/Cd (II)-Based 2D MOFs of 5-Nitro-isophthalate with Isonicotinic Hydrazide. *Cryst. Growth Des*. **2021**, *21*, 4847-4856.

27. Jana, S.; Datta, J.; Maity, S.; Thakurta, B.; Ray, P, P.; Sinha, C. Tetrameric and Polymeric Zn (II) Coordination Complexes of 4-Diallylaminobenzoic Acid and Their

Applications in the Electroreduction of CO2 and Schottky Diode Behavior. *Cryst. Growth Des*. **2021**, *21*, 5240-5250.

28. Chandra, A.; Das, D.; Castro, J, O.; Naskar, K.; Jana, S.; Frontera, A.; Ray, P, P.; Sinha, C. Cd (II) coordination polymer of fumaric acid and pyridyl-hydrazide Schiff base: Structure, photoconductivity and theoretical interpretation. Inorganica Chim. Acta., **2021**, *518*, 120253.

29. Khan, S.; Medishetty, R.; Ekka, A.; Mir, M, H.; Mechanical Motion in Crystals Triggered by Solid State Photochemical [2+ 2] Cycloaddition Reaction. *Chem. Commun*. **2021**, *57*, 6197-6200.

30. Dey, S.; Sil, S.; Dutta, B.; Naskar, K.; Maity, S.; Ray, P, P.; Sinha, C. Designing of Pb (II)-Based Novel Coordination Polymers (CPs): Structural Elucidation and Optoelectronic Application. *ACS omega*. **2019**, *4*, 19959-19968.

31. Chandra, A.; Das, M.; Pal, K.; Jana, S.; Dutta, B.; Ray, P, P.; Jana, K.; Sinha, C. Three-Dimensional-Coordination Polymer of Zn (II)-Carboxylate: Structural Elucidation, Photoelectrical Conductivity, and Biological Activity. *ACS omega*. **2019**, *4*, 17649-17661.

32. Jana, S.; Karim, S.; Paul, S.; Zangrando, E.; El Fallah, M, S.; Das, D.; Sinha, C. Carboxylato bridging Cu (II) coordination polymer: Structure, magnetism and catalytic reduction of nitrophenols. *J. Mol. Struct*. **2021**, *1245*, 131058.

33. Naskar, K.; Maity, S.; Maity, H, S.; Sinha, C. A Reusable Efficient Green Catalyst of 2D Cu-MOF for the Click and Knoevenagel Reaction. *Molecules*. **2021**, *26*, 5296.

34. Naskar, K.; Maity, S.; Jana, S.; Dutta, B.; Tanaka, S.; Mallick, D.; Akitsu, T.; Sinha, C. Arylazoimidazole coordinated and naphthalene-dicarboxylato bridged polymers of Co (II) and photochromic Zn (II) complexes. *Cryst. Growth Des*. **2018**, *18*, 2986-2997.

35. Rath, B. B.; Vittal, J. J. Water Stable Zn(II) Metal–Organic Framework as a Selective and Sensitive Luminescent Probe for Fe(III) and Chromate Ions. *Inorg. Chem.***2020**, *59*, 8818-8826.

36. Allendorf, M.; Bauer, C.; Bhakta, R.; Houk, R. Luminescent metal−organic frameworks. *Chem. Soc. Rev*. **2009**, *38*, 1330−1352.

37. Dutta, B.; Purkait, R.; Bhunia, S.; Khan, S.; Sinha, C.; Mir, M.H. Selective detection of trinitrophenol by a Cd (II)-based coordination compound. *RSC Adv.* **2019**, *9*, 38718-38723.

38. Bhunia, S.; Dutta, B.; Pal, K.; Chandra, A.; Jana, K.; Sinha, C. Ultra-trace level detection of Cu^{2+} in an aqueous medium by novel Zn (ii)-dicarboxylato–pyridyl coordination polymers and cell imaging with HepG2 cells. *New J. Chem*. **2021**, *45*, 13941-13948.

39. Li, H, Y.; Zhao, S, N.; Zang, S, Q.; Li, J.; Functional metal–organic frameworks as effective sensors of gases and volatile compounds. *Chem. Soc. Rev.,***2020**, *49*, 6364-6401.

40. Dutta, B.; Jana, R.; Bhanja, A, K.; Ray, P, P.; Sinha, C.; Mir, M, H. Supramolecular aggregate of Cadmium (II)-based one-dimensional coordination polymer for device fabrication and sensor application. *Inorg. Chem*. **2019**, *58*, 2686-2694.

41. Lv, R.; Wang, J. Y.; Zhang, Y. P.; Li, H.; Yang, L. Y.; Liao, S. Y.; Gu, W.; Liu, X. An Amino-Decorated Dual-Functional Metal Organic Framework for Highly Selective Sensing of Cr(III) and Cr(VI) Ions and Detection of Nitroaromatic Explosives. *J. Mater.Chem. A*. **2016**, *4*, 15494−15500.

42. Wang, H. R.; Qin, J. H.; Huang, C.; Han, Y. B.; Xu, W. J.; Hou, H. W. Mono/Bimetallic Water-Stable Lanthanide Coordination Polymers as Luminescent Probes for Detecting

Cations, Anions and Organic Solvent Molecules. *Dalton Trans*. **2016**, *45*, 12710−12716.

43. Meng, X.; Wei, M.-J.; Wang, H.-N.; Zang, H.-Y.; Zhou, Z.-Y. Multifunctional luminescent Zn(II)-based metal−organic framework for high proton-conductivity and detection of Cr^{3+} ions in the presence of mixed metal ions. *Dalton Trans.* **2018**, *47*, 1383−1387.

44. Pearson, R. G. Hard and soft acids and bases. *J. Am. Chem. Soc*. **1963**, *85*, 3533.

45. Wang, B.; Lv, X. L.; Feng, D.; Xie, L. H.; Zhang, J.; Li, M.; Xie, Y.; Li, J. R.; Zhou, H. C. Highly stable Zr (IV)-based metal–organic frameworks for the detection and removal of antibiotics and organic explosives in water. *J. Am. Chem. Soc.*, **2016**, *138*, 6204-6216.

46. He, T.; Kong, X. J.; Bian, Z. X.; Zhang, Y. Z.; Si, G. R.; Xie, L. H.; Wu, X. Q.; Huang, H.; Chang, Z.; Bu, X. H.; Zaworotko, M. J. Trace removal of benzene vapour using double-walled metal–dipyrazolate frameworks. *Nat. Mater.,* **2022**, *21*, 689-695.

47. Lv, X. L.; Wang, K.; Wang, B.; Su, J.; Zou, X.; Xie, Y.; Li, J. R.; Zhou, H. C. A base-resistant metalloporphyrin metal–organic framework for C–H bond halogenation. *J. Am. Chem. Soc.*, **2017**, *139*, 211-217.

48. Liu, T, F.; Zou, L.; Feng, D.; Chen, Y, P.; Fordham, S.; Wang, X.; Liu, Y.; Zhou, H, C. Stepwise synthesis of robust metal–organic frameworks via postsynthetic metathesis and oxidation of metal nodes in a single-crystal to single-crystal transformation. *J. Am. Chem. Soc.***2014**, *136*, 7813-7816.

49. Lalonde, M.; Bury, W.; Karagiaridi, O.; Brown, Z.; Hupp, J. T.; Farha, O. K. Transmetalation: routes to metal exchange within metal–organic frameworks.*J. Mater. Chem.A***2013**, *1*, 5453.

50. He, T.; Kong, X. J.; Zhou, J.; Zhao, C.; Wang, K.; Wu, X. Q.; Lv, X. L.; Si, G. R.; Li, J. R.; Nie, Z.R. A practice of reticular chemistry: Construction of a robust mesoporous palladium metal–organic framework via metal metathesis. *J. Am. Chem. Soc.*, **2021**, *143*, 9901-9911.

51. Brozek, C, K.; Cozzolino, A, F.; Teat, S, J.; Chen, Y, S.; Dincă, M. Quantification of site-specific cation exchange in metal–organic frameworks using multi-wavelength anomalous x-ray dispersion.*Chem. Mater.***2013**,*25*, 2998.

52. Kim, M.; Cahill, J, F.; Fei, H.; Prather, K, A.; Cohen, S, M. Postsynthetic ligand and cation exchange in robust metal–organic frameworks.*J. Am. Chem. Soc.***2012**, *134*, 18082.

53. Brozek, C, K.; Dincă, M. Ti^{3+}-, V$^{2+/3+}$-, Cr$^{2+/3+}$-, Mn^{2+}-, and Fe^{2+}-substituted MOF-5 and redox reactivity in Cr-and Fe-MOF-5. *J. Am. Chem. Soc.***2013**, *135*, 12886.

54. Dincă, M.; Long, J, R. High-enthalpy hydrogen adsorption in cation-exchanged variants of the microporous metal− organic framework $Mn_3[(Mn_4Cl)_3$ $(BTT)_8(CH_3OH)_{10}]_2$. *J. Am. Chem. Soc.,* **2007**, *129*, 11172.

55. Kim, Y.; Das, S.; Bhattacharya, S.; Hong, S.; Kim, M, G.; Yoon, M.; Natarajan, S.; Kim, K.Metal-Ion Metathesis in Metal–Organic Frameworks: A Synthetic Route to New Metal–Organic Frameworks.*Chem.Eur. J.,* **2012**, *18*, 16642.

56. Seenan, S.; Kulathu Iyer, S.; Colorimetric Metal Sensing of Fe^{3+} and Cr^{3+} and Photophysical and Electrochemical Studies Based on Benzo [4, 5] thiazolo [3, 2-a] pyrimidine-3-carboxylate and Its Derivatives. *J. Org. Chem.*, **2020**, *85*, 1871-1881.

57. Cao, L, H.; Shi, F.; Zhang, W, M.; Zang, S, Q.; Mak, T, C. Selective Sensing of Fe^{3+} and Al^{3+} Ions and Detection of 2, 4, 6-Trinitrophenol by a Water-Stable Terbium-Based Metal–Organic Framework. *Chem. Eur. J.***2015**, *21*, 15705-15712.

58. Zhao, X, Y.; Liang, B.; Xiong, K, C.; Shi, Y,W.; Yang, S, L.; Wei, T, Y.; Zhang, H.; Zhang, Q, F.; Gai, Y, L. Two novel lead-based coordination polymers for luminescence sensing of anions, cations and small organic molecules. *Dalton Trans*. **2020**, *49*, 5695-5702.

59. Dong, Y.; Zhang, H.; Lei, F.; Liang, M.; Qian, X.; Shen, P.; Xu, H.; Chen, Z.; Gao, J.; Yao, J. Benzimidazole-functionalized Zr-UiO-66 nanocrystals for luminescent sensing of Fe^{3+} in water. *Solid State Chem.***2017**, *245* , 160-163.

60. Wang, H.; Gao, T.; Zhang, Y. Synthesis of two 3D supramoleculars and their fluorescent sensing for nitroaromatic compounds/Fe^{3+} ions in aqueous medium. *Inorg. Chem. Commun*. **2019**, *108*, 107491-107495.

61. Chen, Z.; Sun, Y.; Zhang, L.; Sun, D.; Liu, F.; Meng, Q.; Wang, R.; Sun, D. A tubular europium–organic framework exhibiting selective sensing of Fe^{3+} and Al^{3+} over mixed metal ions. *Chem. Commun*. **2013**, *49*, 11557-11559.

62. Hyman, L, M.; Franz, K, J.; Probing oxidative stress: Small molecule fluorescent sensors of metal ions, reactive oxygen species, and thiols. *Coord. Chem. Rev*. **2012**, *256*, 2333-2356.

63. Zhao, Q.; Li, F.; Huang, C. Phosphorescent chemosensors based on heavy-metal complexes. *Chem. Soc. Rev*. **2010**, *39*, 3007-3030.

64. Yang, J.; Ni, W.; Ruan, B.; Tsai, C, L.; Ma, N.; Shi, D.; Jiang, T.; Tsai, C, F. Review—Design and Synthesis of Fluorescence Sensing Metal-Organic Frameworks. *ECS J Solid State Sci Technol*. **2021**, *10*, 056003.

65. Liu, Y.; Ren, L.; Cui, Gm, H. Two Co (ii)-based coordination polymers as multi-responsive luminescent sensors for the detection of levofloxacin, benzaldehyde and Fe^{3+} ions in water media. *Cryst. Eng. Comm*. **2021**, *23*, 7485-7495.

66. Wang, Y.; Ma, J, X.; Zhang, Y.; Xu, N.; Wang, X, L.; A Series of Cobalt-Based Coordination Polymer Crystalline Materials as Highly Sensitive Electrochemical Sensors for Detecting Trace Cr (VI), Fe (III) Ions, and Ascorbic Acid. *Cryst. Growth Des*. **2021**, *21*, 4390–4397.

67. Lin, Y.; Zhang, X.; Chen, W.; Shi, W.; Cheng, P. Three cadmium coordination polymers with carboxylate and pyridine mixed ligands: luminescent sensors for FeIII and CrVI ions in an aqueous medium. *Inorg. Chem*. **2017**, *56*, 11768-11778.

68. Zhou, X.; Liu, L.; Kou, H.; Zheng, S.; Song, M.; Lu, J.; Tai, X. A Multifunctional 3D Supermolecular Co Coordination Polymer With Potential for CO2 Adsorption, Antibacterial Activity, and Selective Sensing of Fe^{3+}/Cr^{3+} Ions and TNP. *Front. Chem*. **2021**, *9,* 678993.

69. Chen, C, H.; Wang, X, S.; Li, L.; Huang, Y, B.; Cao, R. Highly selective sensing of Fe^{3+} by an anionic metal–organic framework containing uncoordinated nitrogen and carboxylate oxygen sites. *Dalton Trans*. **2018**, *47,* 3452-3458.

70. Wang, H.; Wang, X.; Kong, R, M.; Xia, L.; Qu, F. Metal-organic framework as a multi-component sensor for detection of Fe^{3+}, ascorbic acid and acid phosphatase. *Chem. Lett*. **2021**, *32*, 198-202.

71. Xie, W.; Xu, M, Y.; Jiang, W.; Xu, G, J.; Zhang, S, R.; Xu, Y, H.; Su, Z, M. A stable Cd metal–organic framework as efficient fluorescent probe for sensing Fe^{3+} in water. *Inorganica Chim. Acta*., **2021**, *528*, 120635.

72. Hou, B, L.; Tian, D.; Liu, J.; Dong, L, Z.; Li, S, L.; Li, D, S.; Lan, Y, Q. A water-stable metal–organic framework for highly sensitive and selective sensing of Fe^{3+} ion. *Inorg. Chem*. **2016**, *55*, 10580–10586.

73. Dong, X, Y.; Wang, R.; Wang, J, Z.; Zang, S, Q.; Mak, T, C. Highly selective Fe^{3+} sensing and proton conduction in a water-stable sulfonate–carboxylate Tb–organic-framework. *J. Mater. Chem.,* **2015**, *3*, 641-647.

74. Chen, M. –L. Chen, Z. –L. Qi, W. –T. Jin, Z. Xu, Y. –H. Cheng and Z. –H. Zhou, Cation exchange in a fluorescent zinc-based metal–organic framework for cadmium ion detection, *CrystEngComm.*, **2021**, *23*, 7442-7449.

75. Ghosh, K.; Rathi, S. A novel probe for selective colorimetric sensing of Fe (II) and Fe (III) and specific fluorometric sensing of Fe (III): DFT calculation and logic gate application. *RSC Adv*. **2014**, *4*, 48516-48521.

76. Trigo-López, M.; Muñoz, A.; Ibeas, S.; Serna, F.; García, F, C.; García, J, M. Colorimetric detection and determination of Fe (III), Co (II), Cu (II) and Sn (II) in aqueous media by acrylic polymers with pendant terpyridine motifs. *Sens. Actuators, B*. **2016**, *226*, 118-126.

77. Bruker, 2000. SMART, SAINT. Software Reference Manual Bruker AXS Inc. Madison, Wisconsin, USA.

78. Sheldrick, G, M. A short history of SHELX. *Acta Cryst A*, **2008**, *64*, 112-122.

79. Farrugia, L, J. WinGX and ORTEP for Windows: an update. *J. Appl. Crystallogr*. **2012**, *45*, 849-854.

80. Twentyman, P, R.; Luscombe, M. A study of some variables in a tetrazolium dye (MTT) based assay for cell growth and chemosensitivity. *Br. J. Cancer*. **1987**, *56*, 279-285.

81. Mandal, M.; Sain, D.; Islam, M, M.; Banik, D.; Periyasamy, M.; Mandal, S.; Mahapatra, A, K.; Kar, A. A ratiometric triazine-based colorimetric and fluorometric sensor for the

recognition of Zn $^{2+}$ ions and its application in human lung cancer cells. *Anal. Methods*. **2021**, *13*, 3922.

82. Pozdnyakov, I. P.; Melnikov, A. A.; Tkachenko, N.; Chekalin, S. V.; Lemmetyinen, H.; Plyusnin, V. F. Ultrafast photophysical processes for Fe (III)-carboxylates. *Dalton Trans.,* **2014**, *43*, 17590-17595.

83. Kjær, K. S.; Kaul, N.; Prakash, O.; Chábera, P.; Rosemann, N. W.; Honarfar, A.; Gordivska, O.; Fredin, L. A.; Bergquist, K. E.; Häggström, L.; Ericsson, T. Luminescence and reactivity of a charge-transfer excited iron complex with nanosecond lifetime. *Science.,* **2019**, *363*, 249-253.

84. Chábera, P.; Liu, Y.; Prakash, O.; Thyrhaug, E.; Nahhas, A. E.; Honarfar, A.; Essén, S.; Fredin, L. A.; Harlang, T. C.; Kjær, K. S.; Handrup, K. A low-spin Fe (III) complex with 100-ps ligand-to-metal charge transfer photoluminescence. *Nature.,* **2017**, *543*, 695-699.

85. Ghosh, K.; Rathi, S. A novel probe for selective colorimetric sensing of Fe (II) and Fe (III) and specific fluorometric sensing of Fe (III): DFT calculation and logic gate application. *RSC adv*., **2014**, *4*, 48516-48521.

86. Kundu, A.; Hariharan, P, S.; Prabakaran, K.; Anthony, S, P.; Developing new Schiff base molecules for selective colorimetric sensing of Fe^{3+} and Cu^{2+} metal ions: Substituent dependent selectivity and colour change. *Sens. Actuators, B*., **2015**, *206*, 524-530.

87. Kundu, A.; Anthony, S, P.; Triphenylamine based reactive coloro/fluorimetric chemosensors: Structural isomerism and solvent dependent sensitivity and selectivity. *Spectrochim. Acta, Part A.*, **2018**, *189*, 342-348.

88. Cui, N, J.; Zhu, H.; Cui, H, G. A water-stable 3D Zn(II) luminescent coordination polymer for highly sensitive and selective sensing of acetylacetone and Fe^{3+} ion. *Inorg. Chem. Commun*. **2021**, *129*, 108654.

89. Hou, B, L.; Tian, D.; Liu, J.; Dong, L, Z.; Li, S, L.; Li, D, S.; Lan, Y, Q. A water-stable metal–organic framework for highly sensitive and selective sensing of Fe^{3+} ion. *Inorg. Chem*. **2016**, *55*, 10580–10586.

90. Liu, Y.; Ren, L.; Cui, Gm, H. Two Co (ii)-based coordination polymers as multi-responsive luminescent sensors for the detection of levofloxacin, benzaldehyde and Fe $^{3+}$ ions in water media. *Cryst. Eng. Comm*. **2021**, *23*, 7485-7495.

91. Falaise, C.; Volkringer, C.; Facqueur, J.; Bousquet, T.; Gasnot, L.; Loiseaua, T. Capture of Iodine in Highly Stable Metal–organic Frameworks: A Systematic Study. *Chem. Commun*., **2013**, *49*, 10320–10322.

92. Naskar, K.; Dey, A.; Maity, S.; Bhunia, M, K.; Ray, P, P.; Sinha, C. Novel porous polycatenated Iodo–cadmium coordination polymer for iodine sorption and electrical conductivity measurement. *Cryst. Growth Des.*, **2019**, *19*, 2206-2218.

93. Liu, T, F.; Zou, L.; Feng, D.; Chen, Y, P.; Fordham, S.; Wang, X.; Liu, Y.; Zhou, H, C. Stepwise synthesis of robust metal–organic frameworks via postsynthetic metathesis and oxidation of metal nodes in a single-crystal to single-crystal transformation. *J. Am. Chem. Soc.***2014**, *136*, 7813-7816.

Chapter 4

Aminoisophthalate Bridge Cd(II)-2D Coordination Polymer : Structure-Property Correlation Towards Aqueous Medium Pd^{2+} Detection and Fabrication of Schottky Diode
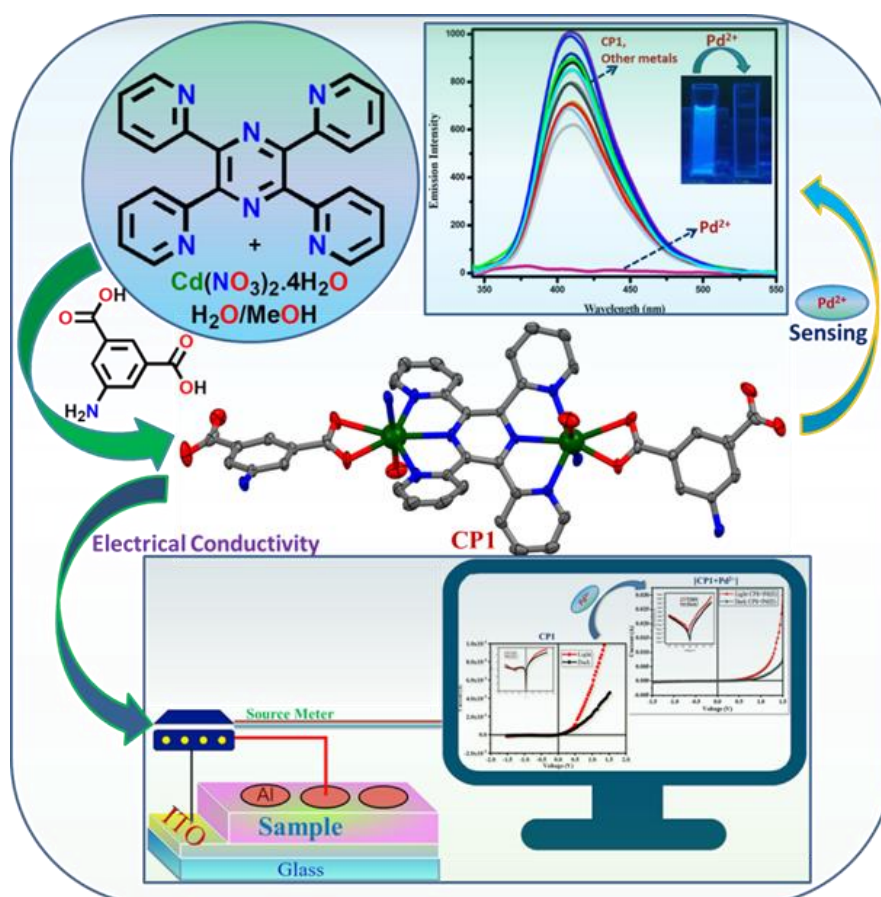
Chapter 4

Abstract

2,3,5,6-Tetrakis(2-pyridyl)pyrazine (tppz), and 5-Aminoisophthalic acid (H_2AIPA) served as bridging groups in two almost mutually perpendicular directions with Cd(II) as node and propagates to constitute a 2D coordination polymer (2D-CP), $\{[Cd(HAIPA)(tppz)(OH)].3H_2O\}_n$, (CP**1**). The 2D-CP is self-assembled via H-bonding and $\pi\cdots\pi$ interactions to constitute 3D supramolecule. The CP**1** is highly blue emissive in aqueous-acetonitrile (40:1, v/v) suspension and is selectively quenched by Pd^{2+} without any interference in presence of as many as sixteen cations. The limit of detection (LOD) is second lowest in the literature (0.08 μM). The binding constant (Ksv = 7.25 x 10^4 M^{-1}) also supports the strong interaction of CP**1** with Pd^{2+}. The optical band gap of CP**1** ((3.61 eV) lies in semiconductor region and is improved on binding with Pd^{2+} (3.05 eV [CP**1**+Pd^{2+}]). The electrical conductivity of CP**1** is enhanced upon light irradiation (Λ_{CP1}: 7.42×10^{-5} S m^{-1} (dark) and 2.45×10^{-4} S m^{-1} (light)) and has upgraded to non-Ohmic I-V relationship. Upon binding with Pd^{2+} the electrical conductivity of the composite, [CP**1**+Pd^{2+}], is increased by 1.6 times ($\Lambda_{[CP1+Pd^{2+}]}$: 1.20×10^{-4} S m^{-1} (dark) and 3.81×10^{-4} S m^{-1} (light)) and the rectification ratios (I_{on}/I_{off}) of CP**1** and [CP**1**+Pd^{2+}] are 2.5 and 2.78 times higher at light phase than at dark phase, respectively. DFT computation has been attempted to explain the electronic properties.

4.1. Introduction

Palladium (Pd), an abundant metal, is mostly used in catalytic transformation in a number of well-known name reactions in organic synthesis including the Suzuki, Stille, Heck, Buchwald-Hartwig cross-couplings; the Tsuji-Trost allylation, the Wacker process along with hydrogenation, hydrogenolysis, carbonylation, cycloisomerization, pericyclic reactions etc. [1-7]. Even after thorough purification the hazardous Pd may present in the target products at very low concentration. Out of three redox states Pd(0/II/IV), the Pd(II) is most toxic on human health and the recommended threshold limit for Pd is 5-10 ppm and the dietary intake range is 1.5-15 μg/person/day (14 - 140 nM) as per reference of the USEPA (United States Environmental Protection Agency).[7,8] Pd(II) obstructs many enzymatic functions such as, alkaline phosphatase, carbonic anhydrase, propyl hydroxylase, kinase, aldolase, succinate dehydrogenase. Besides, Pd(II) binds selectively biothiols (-SH) and becomes carcinogenic to DNA, proteins and vitamins.[6,7] Therefore, precise, accurate, easy and low-cost determination of Pd in the fine chemicals and pharmaceutical products is an important research. Therefore, different detection techniques have been designed for trace to ultra-trace amount measurement of Pd(II) in the consumable items. Use of fluorescent probes in the visual detection of Pd(II) even in presence of excess of Pd(0) and other PGMs (Platinum Group Metals) is of current interest.[9-16]

Recently, Luminescent Coordination Polymers (LCPs) or Luminescent Metal Organic Frameworks (LMOFs) are used as superior sensors of ions/molecules than that of molecular sensors[17-25] because of their thermal, mechanical, chemical, photophysical and radio-analytical stability and very low leaching affinity. Use of LMOFs for the selective and specific detection of Pd(II) is currently focused by few researchers after first report in 2013.[22-25] A luminescent 2D Cd(II)-CP, {[Cd(HAIPA)(tppz)(OH)].3H$_2$O} (CP**1**) [tppz = 2,3,5,6-Tetrakis(2-pyridyl)pyrazine, H$_2$AIPA = 5-Aminoisophthalic acid], strong emissive, is vastly quenched by

Pd^{2+} in aqueous-acetonitrile (40:1, v/v) medium (LOD, 0.08 μM) in presence of many other ions.[24,25] The optical band gap 3.61 eV (**CP1**) and 3.05 eV [**CP1**+Pd^{2+}] encourage to check their electrical conductivity at dark and under illumination. The **CP1** shows significant improvement of electrical conductivity upon addition of Pd^{2+} in both phase (light and dark) and has been thoroughly examined in this work.

4.2. Experimental Section

4.2.1. Materials and Physical Measurements

All reagents such as $Cd(NO_3)_2.4H_2O$, 5-Aminoisophthalic acid (H_2AIPA) and 2,3,5,6-Tetrakis(2-pyridyl)pyrazine (tppz) and solvents were purchased from different viable sources and used without any further purification. The micro-elemental analyses (C, H, N) were examined by Perkin-Elmer 240° C elemental analyser. FT-IR spectral data were collected from Perkin Elmer RX1 FT-IR spectrophotometer. Bruker D8 Advance X-ray diffractometer has been used for collection of Powder X-ray diffraction (PXRD) data, using the Cu Kα radiation source (λ = 1.548 Å). PerkinElmer TGA 4000 System were used in Thermogravimetric analysis using 100−240 V/50−60 Hz with temperature ranging from 30−800 °C at the heating rate 10 °C min^{-1}, under the nitrogen atmosphere. The fluorescence and UV−vis spectra were analysed from PerkinElmer spectrofluorometer model LS55 and Lambda 25 spectrophotometer, respectively. Fluorescence lifetime was measured using the Horiba Jobin Yvon fluorescence spectrophotometer. Bruker (AC) 300 MHz FT-NMR spectrometer was used to examine the ^{1}H NMR spectra where TMS was used an internal standard. Crystallographic parameters of coordination sphere of **CP1** were used in the DFT computation using Gaussian 09 software of B3LYP basis set for C, H, N, O and LanL2DZ basic set for Cd and Pd. The band gap was calculated from the energy difference of HOMO and LUMO. Fractional contribution of different ligands and metal was calculated using the GAUSSSUM.
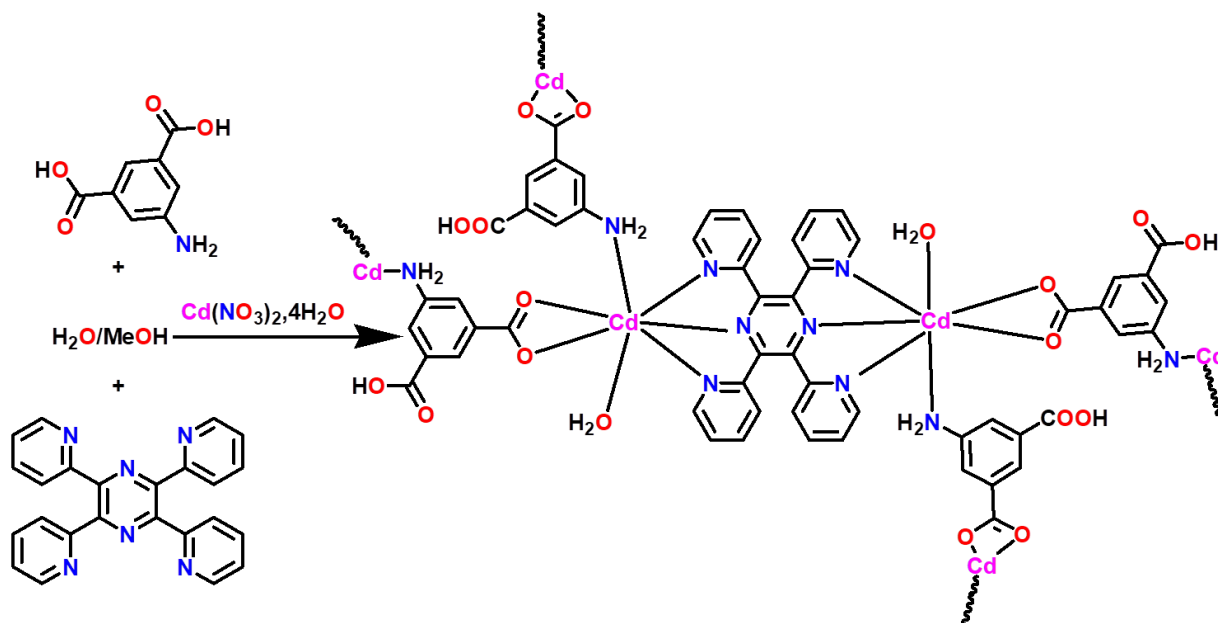
Scheme 4.1. Synthesis of **CP1**, using Cd(NO₃)₂.4H₂O and tppz followed by addition of 5-Aminoisophthalic acid.

4.2.2. Synthesis of CP1

To methanol (2 ml) solution of tppz (0.0194 g, 0.05 mmol) was carefully layered aqueous (2 ml) solution of Cd(NO₃)₂·4H₂O (0.06 g, 0.2 mmol) using buffer of H₂O-MeOH (1:1, v/v; 2 ml) followed by H₂AIPA (0.0362 g, 0.2 mmol) and neutralized with 0.042 g of Et₃N (0.4 mmol) in EtOH solution (2 ml) (**Scheme 4.1**). Block shaped yellow crystals of (**CP1**) were deposited after four days and collected and dried (0.072 g, yield 63.6%). Elemental analysis (%): Calculated for $C_{20}H_{19}CdN_4O_8$: C, 43.22; H, 3.45; N, 10.08. Found: C, 43.29; H, 3.56; N, 10.16. IR $\overline{v}$ (cm⁻¹) 3329 ν(-OH), 3218 ν(-NH), 3130 ν(-CH), 1677 ν(-COOH), 1609 ν(COO), 1371ν (-OH bending) (**Figure 4.1**).
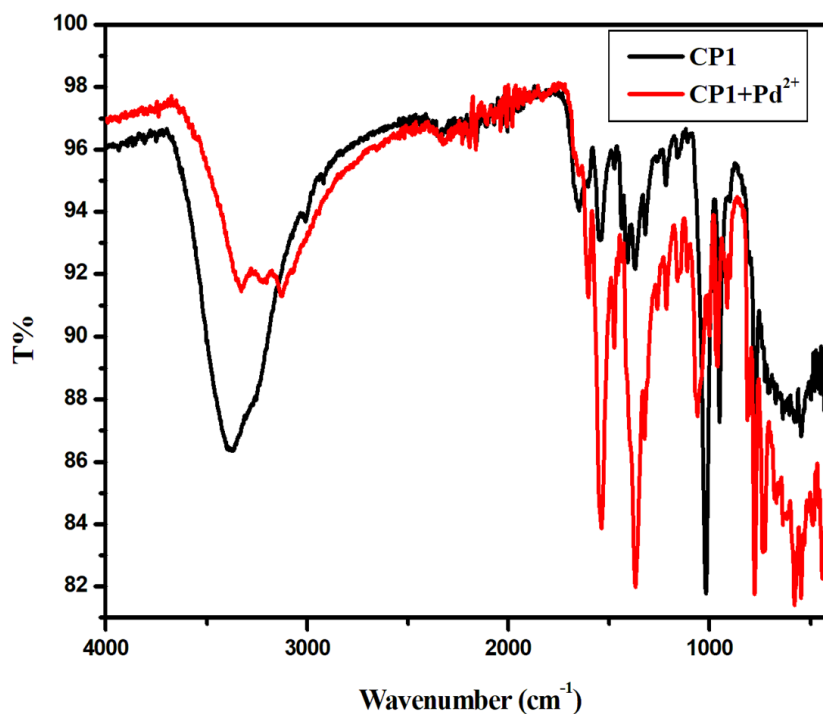
Figure 4.1. FTIR spectra of CP**1** and [CP**1**+Pd^{2+}].

4.2.3. Single Crystal X-Ray Crystallography

Yellow colored crystal with suitable dimension (0.15×0.08×0.05 mm^3) was used for data collection with Bruker APEX-II CCD diffractometer consisting of graphite-monochromated MoKα radiation (λ = 0.71073 Å) at 273(2) K. The crystal structure solution was carried out using SHELX-97[26] package. The least-square refinements of all reflections and the hkl values ($-22 \leq h \leq 22, -12 \leq k \leq 12, -27 \leq l \leq 27$) were used for the estimation of the crystal-orientation matrices and unit cell parameters. The collected data (I > 2σ(I)) were integrated by using the SAINT program,[27] and the absorption correction carried out by SADABS.[28] SHELXL-2014 and SHELX-97 package[26] were used for solving the molecular structure of single crystal. Anisotropic thermal parameters were used for refinement of the non-hydrogen atoms of crystal. All the hydrogen atoms were placed in their geometrically perfect positions and constrained to ride on their parent atoms. Details of crystallographic data for compound CP**1** is enlisted in **Table 4.1**. The selected bond lengths and bond angles were included in **Table 4.2**.

Table 4.1 Crystal data and refinement parameters for compound CP**1**

Formula	$C_{20} H_{14} Cd N_4 O_5$
fw	502.75
Crystal system	monoclinic
space group	*C 2/c*
a (Å)	18.5722(19)
b (Å)	10.2375(10)
c (Å)	23.082(2)
α(deg)	90
β(deg)	91.983(3)
γ (deg)	90
V (Å^3)	4386.1(7)
Z	8
D_{calcd}(g/cm^3)	1.523
μ(mm^{-1})	1.032
λ(Å)	0.71073
data[$I > 2\sigma(I)$]/params	3859/ 272
GOF on F^2	1.106
final *R* indices[$I > 2\sigma(I)$]^{a,b}	$R1 = 0.0532$ $wR2 = 0.1076$

$^a R1 = \Sigma||F_o| - |F_c||/ \Sigma|F_o|,$ $^b wR2 = [\Sigma w(F_o^2 - F_c^2)^2/\Sigma w(F_o^2)^2]^{1/2}$

4.2.4. Sensing experiments

The CP**1** (6.67 mg, 0.012 mmol) was crushed in powder and suspended in acetonitrile (10 ml) and used to prepare stock solution. $ZnCl_2$, $CdCl_2$, $HgCl_2$, $CuCl_2$, $NiCl_2$, $CoCl_2$, $FeCl_3$, $MnCl_2$, $CrCl_3$, $PbCl_2$, $AlCl_3$, $MgCl_2$, $CaCl_2$, $BaCl_2$, NaCl, KCl salts were used to prepare 10^{-3} M aqueous solution. For UV-Visible and Fluorescence experiments, the stock solution of CP**1** was diluted appropriately to prepare 50 mM solution in water (HEPES buffer, pH 7.2) and added the equivalent amount of metal salt solution at 27°C. The excitation wavelength was selected from UV-Vis spectra of the mixture and the Fluorescence experiments were carried

Table 4.2. Selected bond lengths and bond angles in CP**1**.

Cd(01) – O(4)	2.283(4)	O(9) – Cd(01) – N(3)	92.48(14)
Cd(01) – O(9)	2.319(4)	N(4) – Cd(01) – N(3)	92.20(14)
Cd(01) – N(4)	2.379(4)	N(1) – Cd(01) – N(3)	136.19(15)
Cd(01) – N(1)	2.390(5)	O(4) – Cd(01) – N(2)	151.40(14)
d(01) – N(3)	2.401(4)	O(9) – Cd(01) – N(2)	86.99(14)
Cd(01) – N(2)	2.406(4)	N(4) – Cd(01) – N(2)	95.62(14)
Cd(01) – O(3)	2.658(4)	N(1) – Cd(01) – N(2)	67.34(14)
O(4)– Cd(01) – O(9)	88.69(14)	N(3) – Cd(01) – N(2)	68.87(14)
O(4) – Cd(01) – N(4)	90.90(14)	C(8) – O(4) – Cd(01)	101.8(3)
O(9) – Cd(01) – N(4)	175.22(15)	C(9) – N(1) – Cd(01)	120.2(4)
O(4) – Cd(01) – N(1)	140.56(14)	C(13) – N(1) - Cd(01)	119.6(3)
O(9) – Cd(01) – N(1)	86.58(14)	C(15) – N(2) – Cd(01)	116.9(3)
N(4) – Cd(01) – N(1)	90.72(14)	C(14) – N(2) – Cd(01)	120.4(3)
O(4) – Cd(01) – N(3)	83.10(14)	C(16) –N(3) – Cd(01)	117.1(3)
C(4) – N(4) –Cd(01)	114.7(3)	Cd(01) - O(9) - H(9)	109
C(20)– N(3) –Cd(01)	122.6(4)	H(4A) - N(4) - Cd(01)	109
O(3) - Cd(01) - O(4)	52.31(13)	O(3) - Cd(01) - N(2)	155.55(13)
O(3) - Cd(01) - N(1)	88.41(13)	O(3) - Cd(01) - N(3)	135.38(14)
O(3) - Cd(01) - N(4)	87.44(13)	Cd(01) - O(3) - C(8)	83.9(3)
Cd(01) - N(3) - C(16)	117.1(3)	Cd(01) - N(3) - C(20)	122.6(4)

out. Limit of detection (LOD) of Pd(II) sensing by CP**1** in aqueous-acetonitrile (40:1, v/v) medium was determined using the $3\sigma/M$ method, where M is the slope and σ is standard deviation of calibration curve. Binding constant value K_{SV} examined using Stern-Volmerequation, $I_0/I = K_{SV} [Q] + 1$, where I_0, I are the emission intensity of CP**1** in absence of

quencher and presence of quencher (Pd^{2+}), respectively. [Q] is the concentration of quencher (Pd^{2+}). Stability of coordination polymer in the excited state was evaluated using life time plot. Thermal stability of CP**1** was evaluated using the Thermogravimetric analysis (TGA) with temperature range 30-800°C under the N_2 atmosphere. Phase purity was examined using PXRD data.

4.2.5. The Electrical Device fabrication
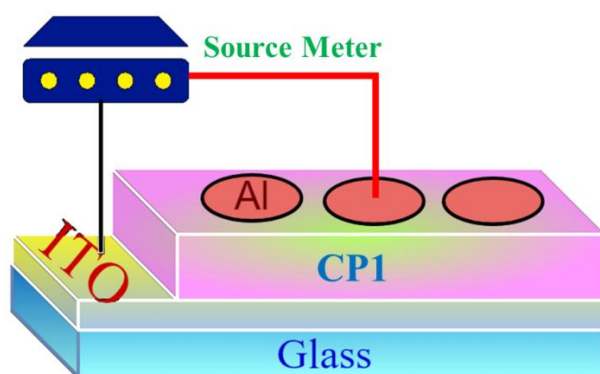
Figure 4.2. Metal-semiconductor (MS) junction Schottky device architecture

The metal-semiconductor Schottky junction devices were made by coating fresh ITOs with CP**1** and [CP**1**+Pd^{2+}] then covering it with Al-electrode (ITO/CP**1**/Al or ITO/[CP**1**+Pd^{2+}]/Al) (**Figure 4.2**). The ITO-coated glass substrates were cleaned in an ultrasonic bath, and then washed for 15 minutes in deionized, ethanol, acetone, and 2-propanol then dried at 80° C hot plate. The composites (20 mg) dispersed in N, N-dimethylformamide (DMF, 500 µl) by mixing and sonicating in two separate vials. A thin film of the synthesized material was obtained by spin coating of a well-dispersed solution (50 µl) of the material at 1000 rpm for 30 sec. This spin coating process was repeated one more time at 1500 rpm. The process of film formation was same for the palladium-based composite. Then films were dried in a vacuum oven at 90°C for 30 min to completely remove the solvent portion. Finally, aluminium (Al) electrodes were

formed on the spin coated film using a vacuum coating unit with adequate masking to maintain a cross-sectional area of 35×10^{-6} m^2.

4.3. Results and Discussion

4.3.1. Structure Description of CP1

The compound **CP1** crystallises in the Monoclinic Crystal System and space group C 2/c with Z=8. The geometry around Cd(II) is distorted pentagonal bipyramidal (**Figure 4.3a**) with CdN$_4$O$_3$ coordination environment. Ligand tppz carries six pyridyl-N donor centres where
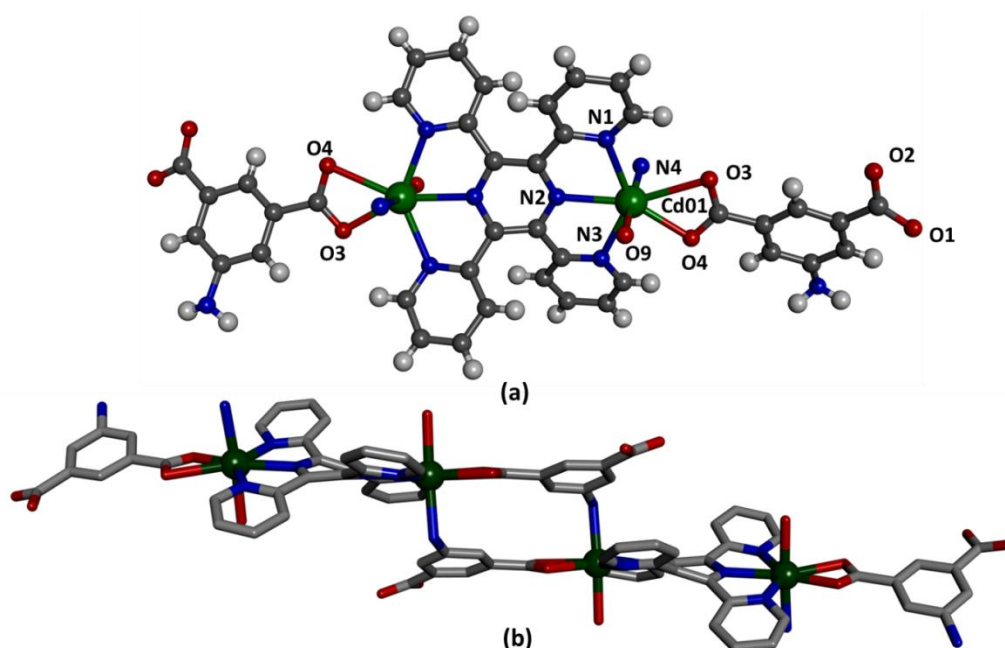
Figure 4.3. (a) View molecular unit of CP**1**, **(b)** Two molecular units binding via. Cd-N bond.

three Ns are in terpyridyl mode and 5-aminoisophthalate (HAIPA$^-$) bears two -COO and one -NH$_2$ group. The coordination sphere is constituted by three pyridyl-N from tppz and one N (-NH$_2$) from HAIPA$^-$ while one -COO chelates and charge is balanced by coordinated OH$^-$. Thus a 2D coordination polymer is constituted. One of the carboxylic acid groups (-COOH of HAIPA$^-$) remains free and is engaged with H-bonding with next layer. Thus, a 2D network is started to develop (**Figure 4.4**).
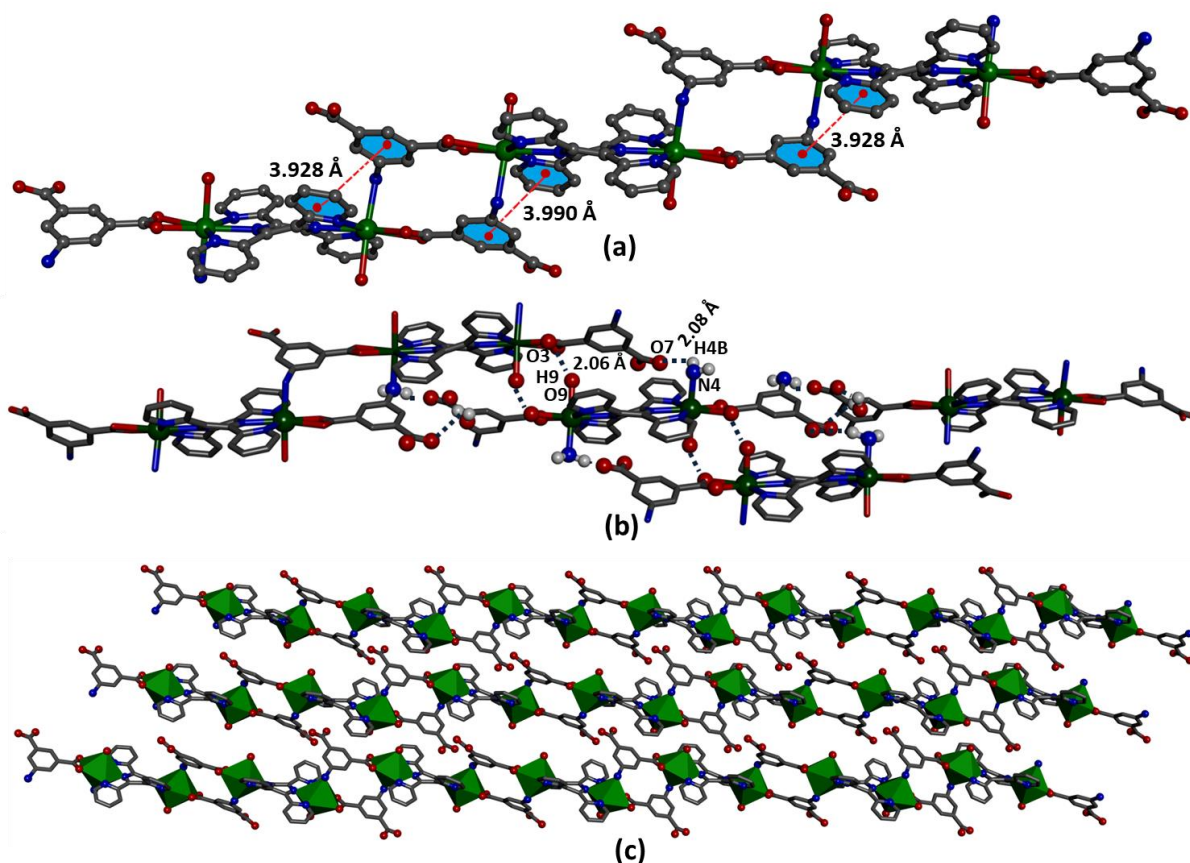
Figure 4.4. (a) View of π···π interaction, **(b)** View H-bonding in different molecular unit of CP**1**, **(c)** Polyhedron Structure of coordination polymer CP**1**.

Bond lengths of Cd-N(tppz) (Cd(01) – N(4), 2.379(4); Cd(01) – N(1), 2.390(5); Cd(01) – N(3), 2.401(4); Cd(01) – N(2), 2.406(4) Å) are comparable with reported data.[29-33] The chelated bond angles and bond lengths lie within acceptable limit.[34-36] The Cd-O(carboxylate) lengths and angles (Cd(01) – O(3), 2.658(4); Cd(01) – O(4), 2.283(4); Cd(01) – O(9), 2.319(4) Å and O(4) – Cd(01) – O(9), 88.69(14)°) also lie within experimental perimeter.[18,19,29] Two Cd(II) centres are bridged by –NH$_2$ of HAIPA$^-$ unit (**Figure 4.3b**) and forms a thirteen member metallo-macrocycle which propagates in 1D pattern. It is also noted that accessible solvent molecules are there with in crystal lattice which are masked for clarity.

The H-bonds (2.06, 2.08 Å) are formed using the $-NH_2$ and carboxylate function of adjacent coordination units (**Figure 4.4b**) and makes the 2D network. The H-bonding and $\pi\cdots\pi$ interactions (3.928, 3.990 Å) (**Table 4.3**) in the 2D network lead to self-assembly for the construction of supramolecule (**Figure 4.4c**, **Figure 4.5**). The architecture is formed via four nodal net, with the point symbol for net with loops {2} (**Figure 4.6**) and point symbol for net is {0}3{4}4.
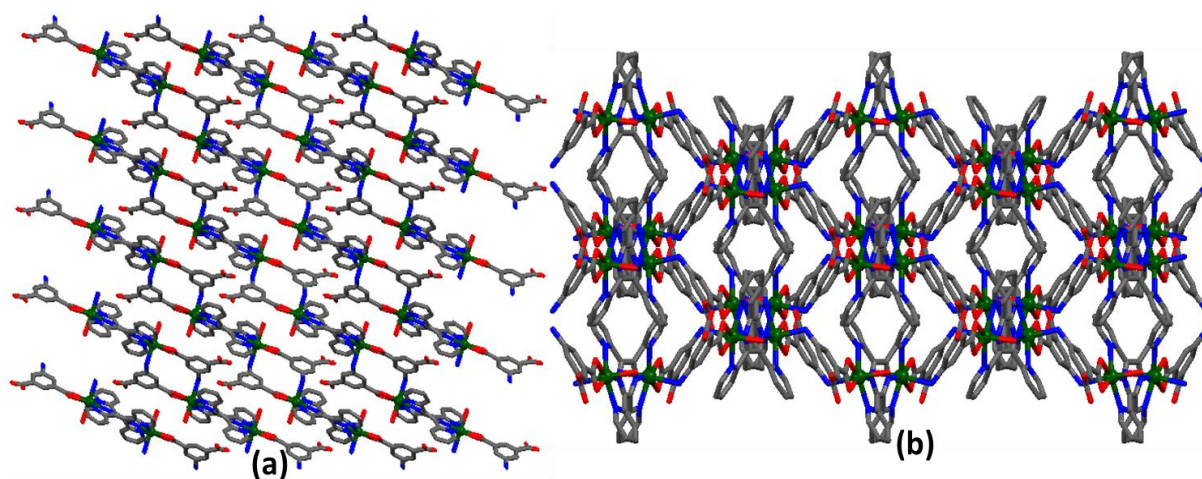
Figure 4.5. Packing of CP**1** along b axis **(a)** and c axis **(b)**.

Table 4.3. $\pi\ldots\pi$ interaction and H-bonding interaction related data of CP**1**.

$\pi\ldots\pi$ interaction		
Ring(i) → Ring(j)	Distance between the (i, j) ring centroids (Å) in the crystal	[ARU(j)]
R(1) → R(4)	3.990(3)	[3666.01]
R(3) → R(4)	3.928(3)	[7556.01]

H-bonding interaction						
Type	Donor--- H	Acceptor	D - H	H...A	∠D - H...A	[ARU]
Intermolecular (Classical)	N4 -- H4B	O7	0.89	2.08	155	[6545.01]
Intermolecular (Classical)	O9 -- H9	O3	0.85	2.06	149	[3666.01]
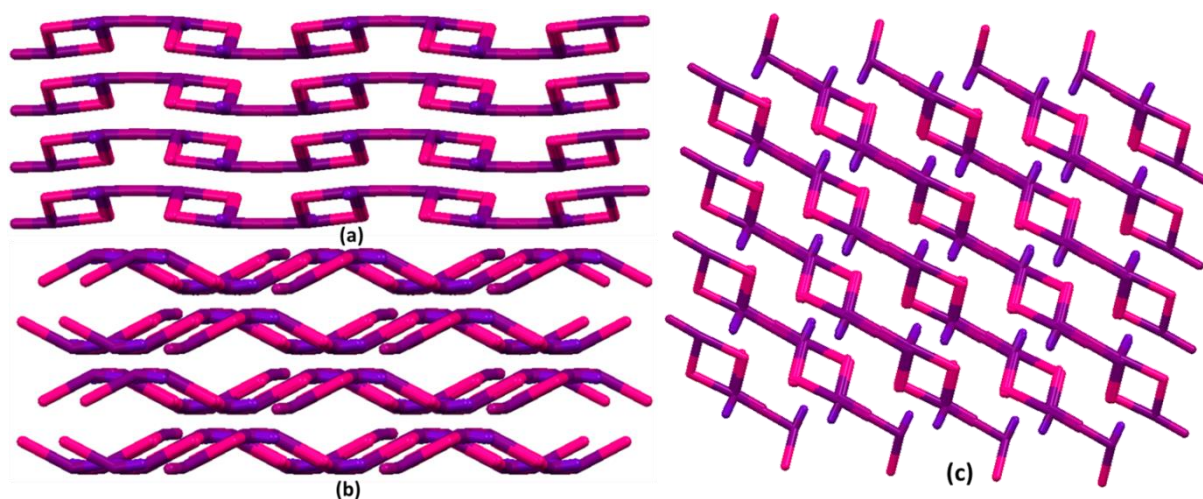
Figure 4.6. 1D +1D rectangular topological structure view in ab (**a**), ac (**b**) and bc (**c**) plane.
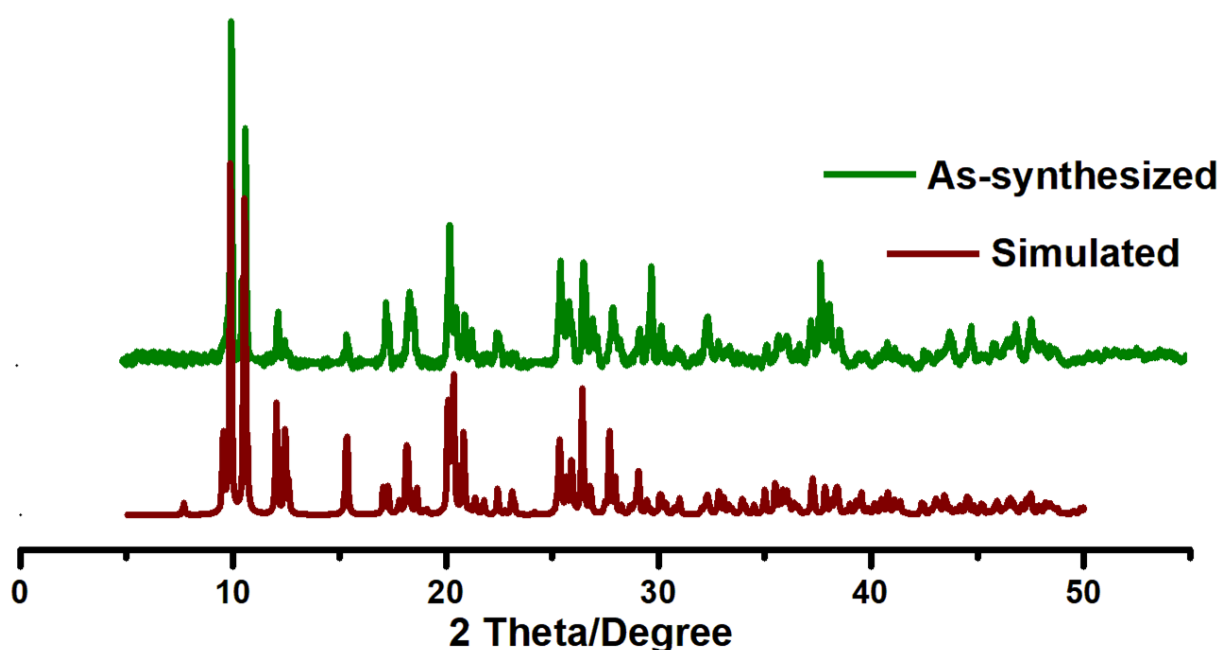
Figure 4.7. Powder X-ray Diffraction analysis of CP**1**.

Phase purity of the coordination polymer has been determined by using the powder crystal X-ray in the range of 2θ is 0-50°. PXRD pattern of powdered as-synthesized sample well matched with simulated pattern (**Figure 4.7**) which have confirmed the bulk purity of material. TGA curve reveals the thermal stability (in the range 30 – 800°C) of CP**1** at a heating rate of 10° C/min. Water molecule is removed from the lattice site at 105°C. This first weight loss of 9.63 % (calculated 9.71 %) corresponds to the loss of three water molecules. The compound has

141

remained stable up to 350°C; exhibiting that high range of framework consistency tempted towards the material application along with device fabrication (**Figure 4.8**).
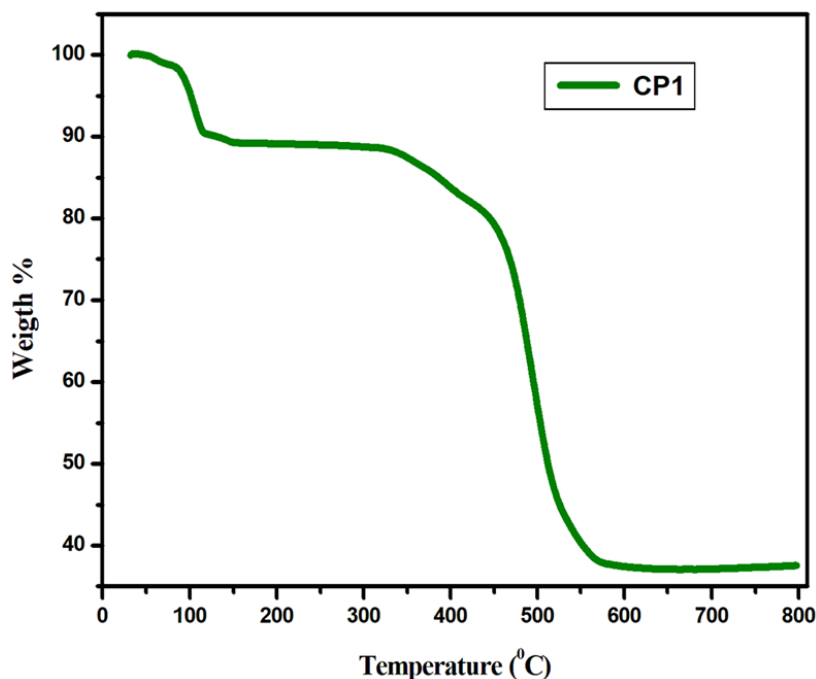
Figure 4.8. TGA plot of CP**1.**

4.3.2. Sensing of Pd^{2+}

Finely powdered CP**1** is dispersed and sonicated in acetonitrile and has been used for stock solution. The UV-Visible spectrum is collected with properly diluted solution by water which shows absorption at 315 nm with a shoulder at 363 nm (**Figure 4.9**). Upon irradiation at 315 nm (excitation slit 15 and emission slit 10) the strong emission is observed at 412 nm (**Figure 4.10a**). Repeated irradiation at UV wavelength (315 nm) followed by the absorption spectrum of CP**1** solution does not show any photodegradation which suggests photostability of the material. On addition of aqueous solution of salts of the metal ions like Fe^{3+}, Al^{3+}, Cr^{3+}, Cd^{2+}, Zn^{2+}, Mn^{2+}, Ni^{2+}, Co^{2+}, Cu^{2+}, Pb^{2+}, Hg^{2+}, Ba^{2+}, Ca^{2+}, Mg^{2+}, K^+, Na^+ do not hamper the intensity
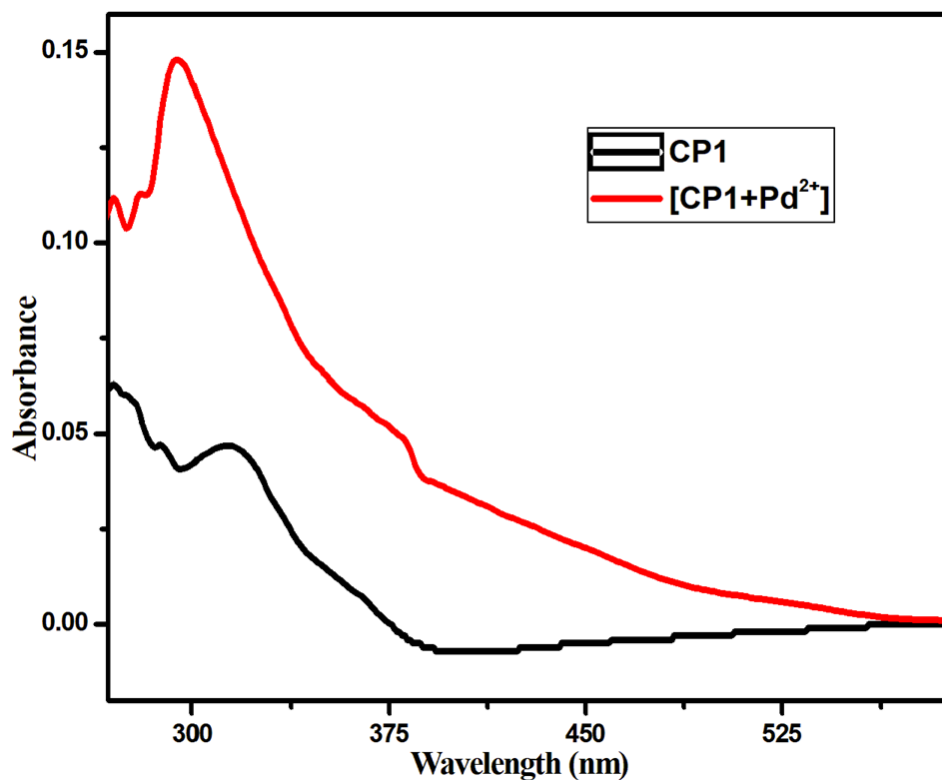
Figure 4.9. UV-Visible spectra of CP**1** and [CP**1**+Pd^{2+}].

of emission of CP**1** significantly while the addition of Pd^{2+} solution shows substantial quenching (**Figure 4.10a**) that may be due to the heavy atom effect of Pd^{2+}.[24] The calculated LOD is 0.08 μM (3σ/M method, **Figure 4.10b**) (**Figure 4.11**) which is second lowest in the literature (**Table 4.4**). There are significant numbers of molecular fluorescence sensor available for the detection of Pd^{2+} at trace level[17-22] while first report of Pd^{2+} sensing by luminescent MOF appeared in 2013[22] and so far a few reports are available in literature (**Table 4.4**)[23-25].
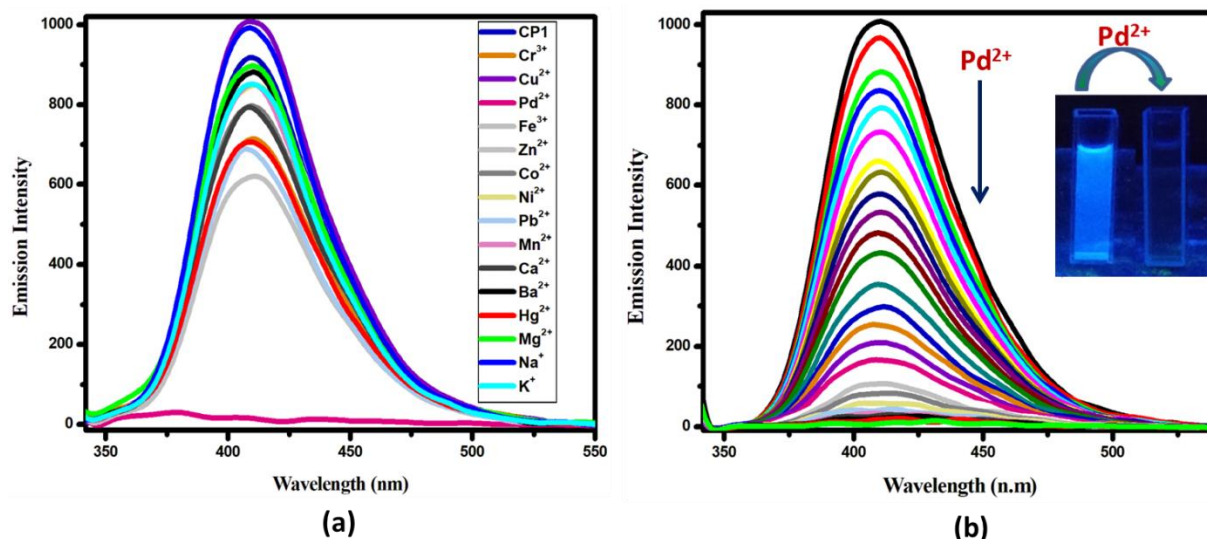
Figure 4.10. (a) Fluorescence intensity of CP**1** and presence of different metal salts solution with CP**1**; **(b)** Quenching of emission intensity by adding Pd^{2+} gradually in the suspension of CP**1** in aqueous-acetonitrile (40:1, v/v) medium.
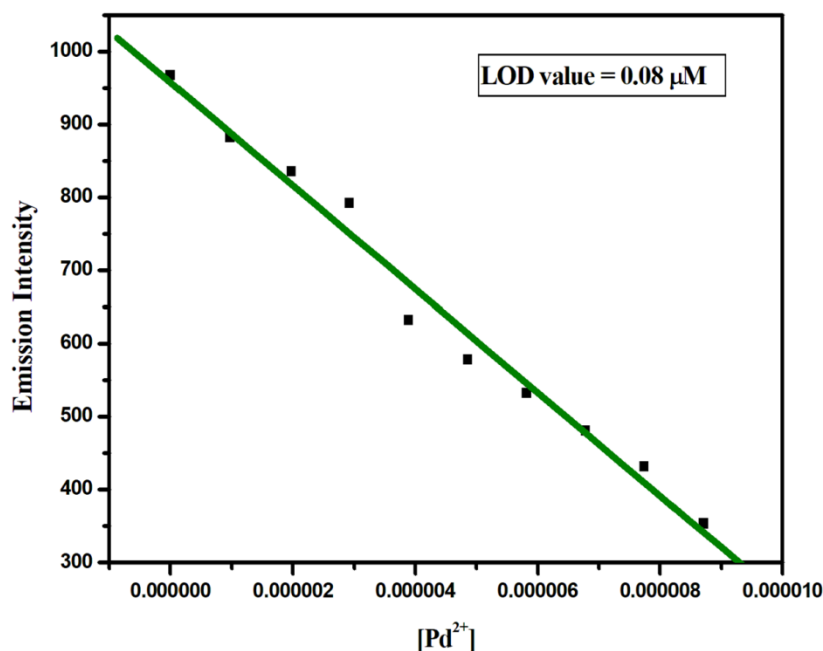
Figure 4.11. LOD determination plot of CP**1** in presence of Pd(II) ion.

The pH (2-12) effect on the intensity of the CP**1** and [CP**1**+Pd^{2+}] is examined by measuring the change of emission intensity which shows no observable variation with tuning of pH (**Figure 4.12**). The chemical stability of CP**1** has been checked by IR, PXRD and SEM images in different pH range (2 to 12)). Results show that the IR spectra (**Figure 4.13**),

Table 4.4. Comparison of the sensitivities of CP**1** with previously reported CPs to Pd^{2+} ions.

Sl. No.	Ligand	Selectivity (LOD)	Solvent	Electrical Conductivity	Reference
1.	**[Cd(4-nvp)2(5-ssa)]** [4-nvp = 4-(1-naphthylvinyl)pyridine and 5-ssa = 5-sulfosalicylic acid]	0.05 μM	Water	No	55
2.	**[Tb(ppda)(npdc)0.5(H$_2$O)$_2$]n** 4-(pyridin-3-yloxy)-phthalic acid (H$_2$ppda) and 1,4 naphthalenedicarboxylic acid (H$_2$nbdc)	94.4 μM.	Water	No	56
3.	**{[Zn(fum)(4-nvp)2]·2H2O}n (1)** **{[Zn(mes)(4-nvp)2]·H2O}n (2)** **[Zn(glu)(4-nvp)]n (3)** (H$_2$fum =fumaric acid, 4-nvp = 4-(1-naphthylvinyl)pyridine, H$_2$mes = mesaconic acid and H$_2$glu-glutaric acid)	0.132μM **(1)** 0.146μM **(2)** 0.152μM **(3)**	Water	No	57
4.	**[Zn2(1,2,3,4-tcpb)4(bpeb)2]** (bpeb=1,4-bis[2-(4-pyridyl)ethenyl]benzene), (H$_4$tcpb = 1,2,4,5-tetrakis(4-carboxyphenyl)benzene)	0.05 μM	DMF	No	58
5.	**CP1**	0.08 μM	Water	Yes	**This Work**

Figure 4.12. Emission intensity of CP**1** and [CP**1**+Pd^{2+}] at different pH range (2 to 12).
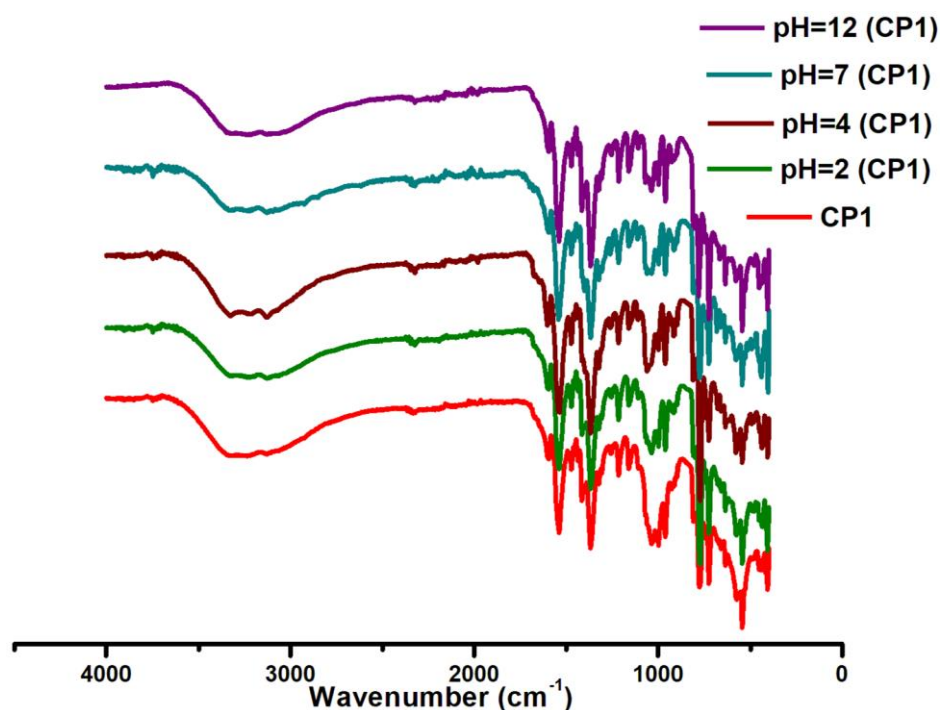
Figure 4.13. IR spectra of CP**1** at different pH

PXRD pattern (**Figure 4.14**) and SEM images (**Figure 4.15**) were quite indifferent with respect to original material. Binding constant, (K$_{SV}$), 7.25×10^4 M^{-1} (**Figure 4.16**) is evaluated using Stern-Volmer equation, (I$_0$/I $-$ 1) = K$_{SV}$[Q]. The plot shows upward curvature which
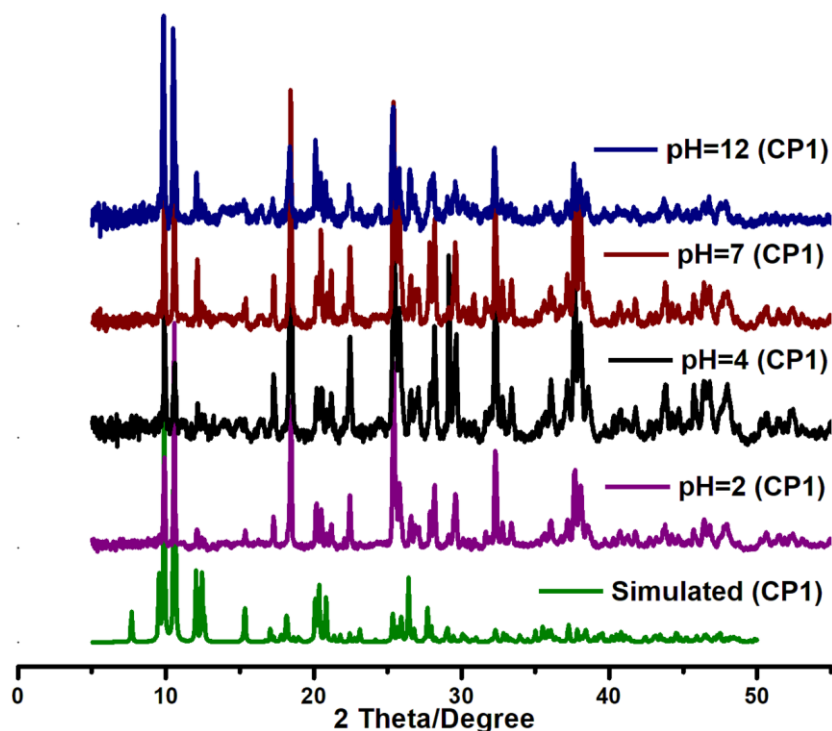
Figure 4.14. Powder X-ray pattern of CP**1** at different pH.
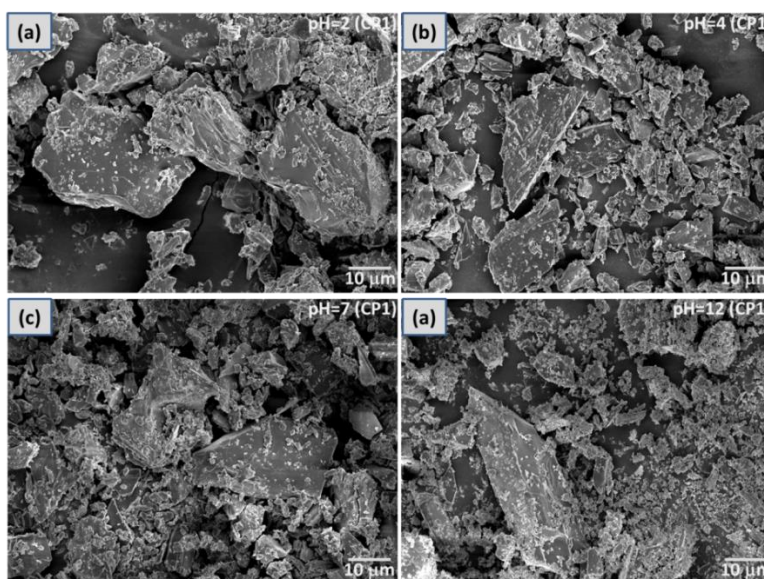
Figure 4.15. FESEM image of CP**1** at different pH : pH = 2 (**a**), pH = 4 (**b**), pH = 7 (**c**) and pH = 12 (**d**)

suggests both static and dynamic quenching of the emission of CP**1** by Pd^{2+} and the extent of quenching is high at a higher concentration of Pd^{2+}. The excited state stability of CP**1** is evaluated from the life time plot (**Figure 4.17a**) and the values are 4.50831×10^{-9} s (CP**1**) and 6.28401×10^{-10} s ([CP**1**+Pd^{2+}]). Therefore, the stability of the CP**1** in excited state is decreased in presence of Pd^{2+} ion.
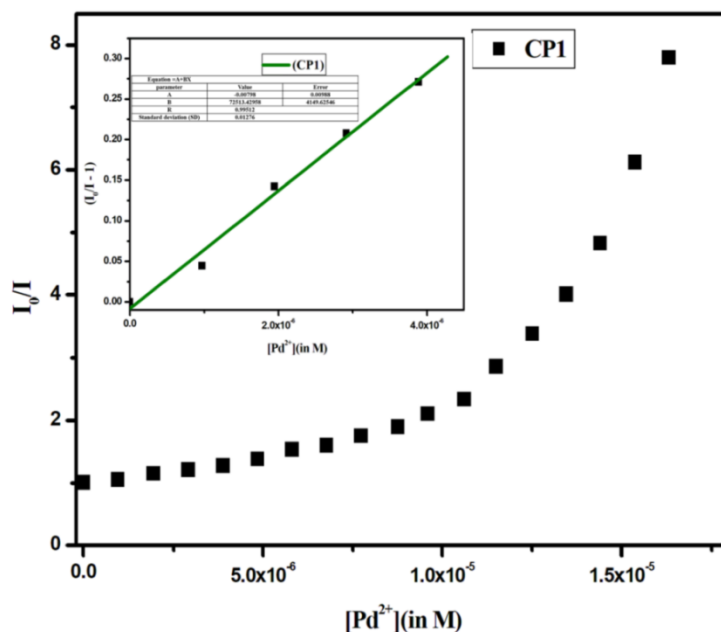
Figure 4.16. Stern-Volmer plot of CP**1**

Quenching effect of Pd^{2+} in presence of other ions like Fe^{3+}, Al^{3+}, Cr^{3+}, Cd^{2+}, Zn^{2+}, Mn^{2+}, Ni^{2+}, Co^{2+}, Cu^{2+}, Pb^{2+}, Hg^{2+}, Ba^{2+}, Mg^{2+}, Ca^{2+}, Na^+, K^+ do not show any interfering effect (**Figure 4.17b**). Also, the chemical constituent (tppz, H_2AIPA) of CP**1** do not show any emission or weakly emissive and have no effect (**Figure 4.18**) towards the Pd^{2+} ion sensing.
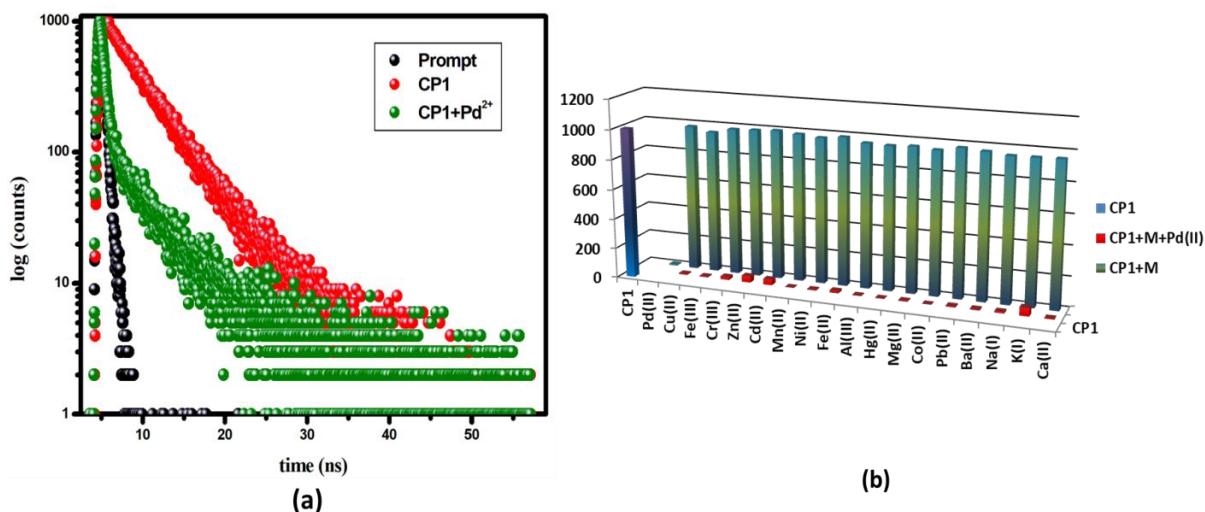
Figure 4.17. (a) Excited state stability of CP**1** and [CP**1**+Pd^{2+}] **(b)** Quenching efficiency of Pd^{2+} in presence of the other metal salts (M).
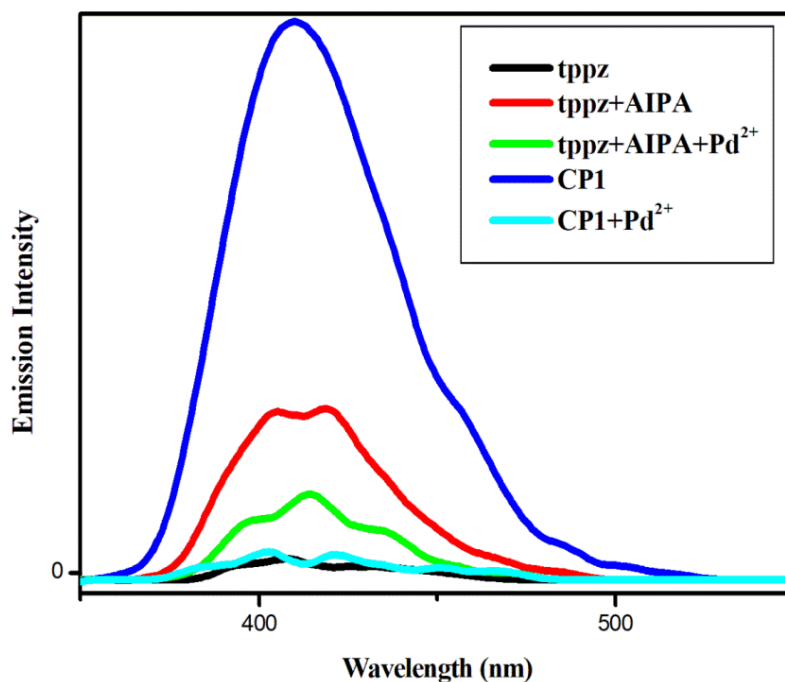
Figure 4.18. Emission of different constituent of CP**1** separately

The surface morphology of CP**1** and [CP**1**+Pd^{2+}] has been characterised by the scanning electron microscopy (SEM) (**Figure 4.19**) with energy dispersive spectroscopy (EDS) analysis and results show that Cd, O, C, N are present in the CP**1** and Cd, O, C, N, Pd exist in the [CP**1**+Pd^{2+}]. Element analyses (**Table 4.5**) and EDS have shown that the Pd appears in [CP**1**+Pd^{2+}] (**Figures 4.20**). The chemical stability of the CP**1** has also been examined by the SEM at different pH range. SEM photographs show that the morphology of the CP**1** is nearly same at the different pH range *i.e* the probe is stable in solution phase at the pH = 2-12 (**Figures 4.15**). The quantitative evaluation of Pd impression on CP**1** confirms the presence of Pd on the surface. This implies that Pd(II) is injected in the CP**1** while the chemical composition of the host and its structure remain unchanged. The cavity measurement helps to find sufficient space between the O9···O4 (2.813 Å) atoms of two layers and Pd^{2+} (VdW, 1.7 Å[37,38]) may be placed therein **(Figure 4.21)**.
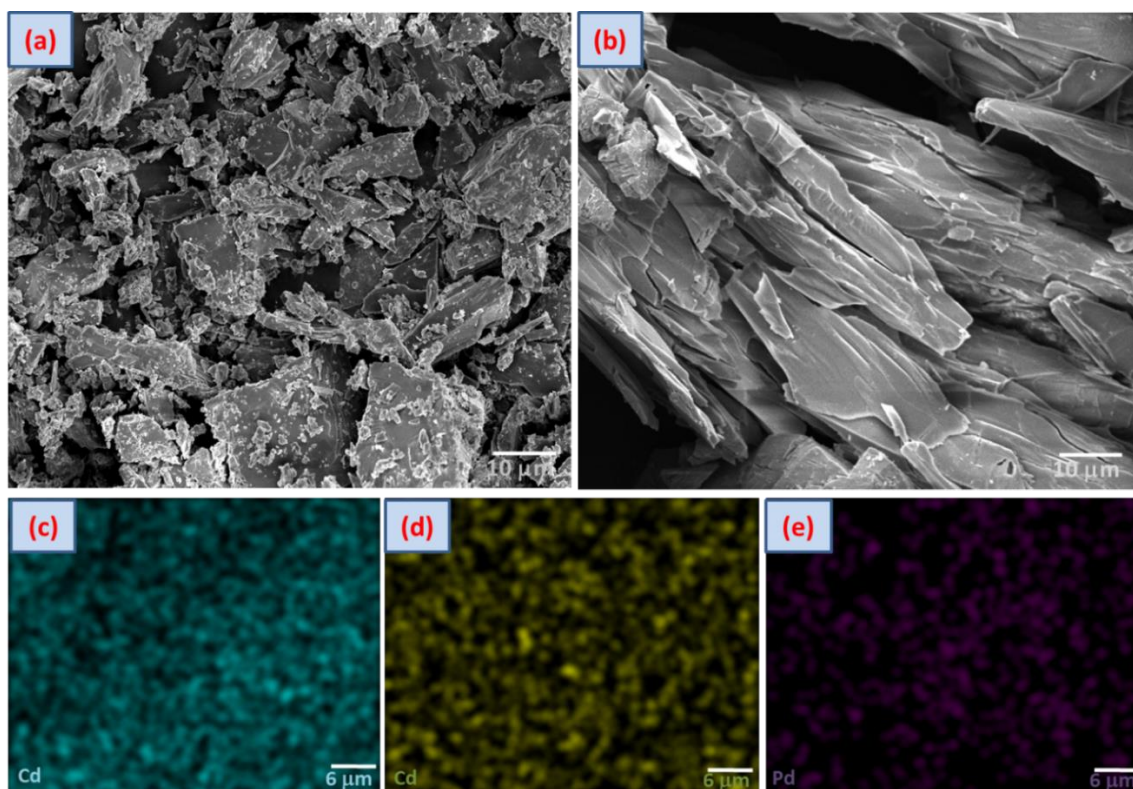
Figure 4.19. (a) SEM image of CP**1**, **(b)** SEM image of [CP**1**+Pd^{2+}], **(c)** Mapping of Cd in CP**1**, **(d)** SEM mapping of Cd in [CP**1**+Pd^{2+}], **(e)** Mapping of Pd in [CP**1**+Pd^{2+}].

Table 4.5. Atomic % of the CP**1** and [CP**1**+Pd^{2+}]

Sample	Cd%	O%	Pd%
CP**1**	18.96	77.98	-
[CP**1**+Pd^{2+}]	16.55	65.64	3.56
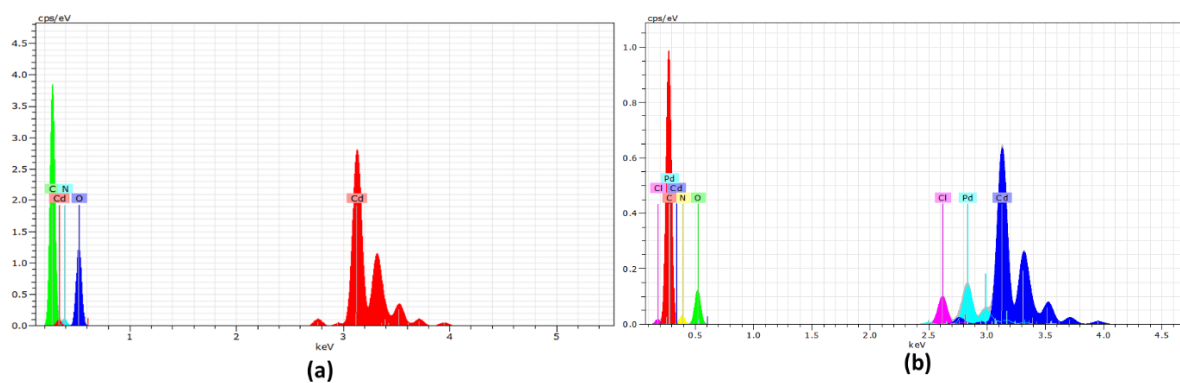
Figure 4.20. EDS spectra of CP**1** **(a)** and CP**2** **(b)**.
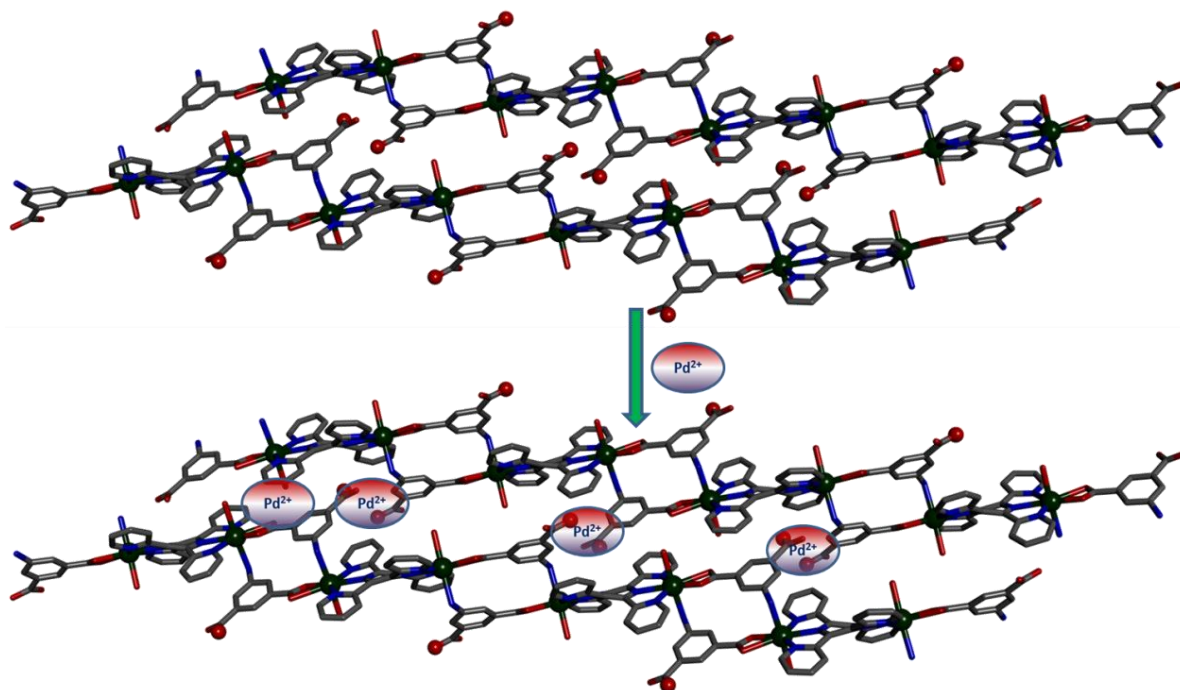
Figure 4.21. Mechanistic model for Pd^{2+} ion sensing, distance between O3···O9 is 2.813 Å.

The ^{1}H NMR spectral pattern of the CP**1** has changed upon addition of Pd^{2+} where most of the peaks of the CP**1** have been broadened. This may be due to the interaction of Pd^{2+} with CP**1**. The X-Ray structure identifies (**Figure 4.4**) the presence of free -COOH that may be able to bind Pd^{2+}; however, the cavity size may have substantial role to monitor the selectivity (interlayer O9···O4 distance is 2.813 Å and Van der Waal's radius of Pd^{2+} is 1.7 Å), as well as the π-cloud of tppz and 5-aminoisopthalate may enhance the stability of Pd(II)-π-complex of polymeric network. The ^{1}H-NMR spectral shifting to higher δ and signal broadening (**Figure 4.22**) may be the reason for electron drifting by guest Pd^{2+} in the coordination network.
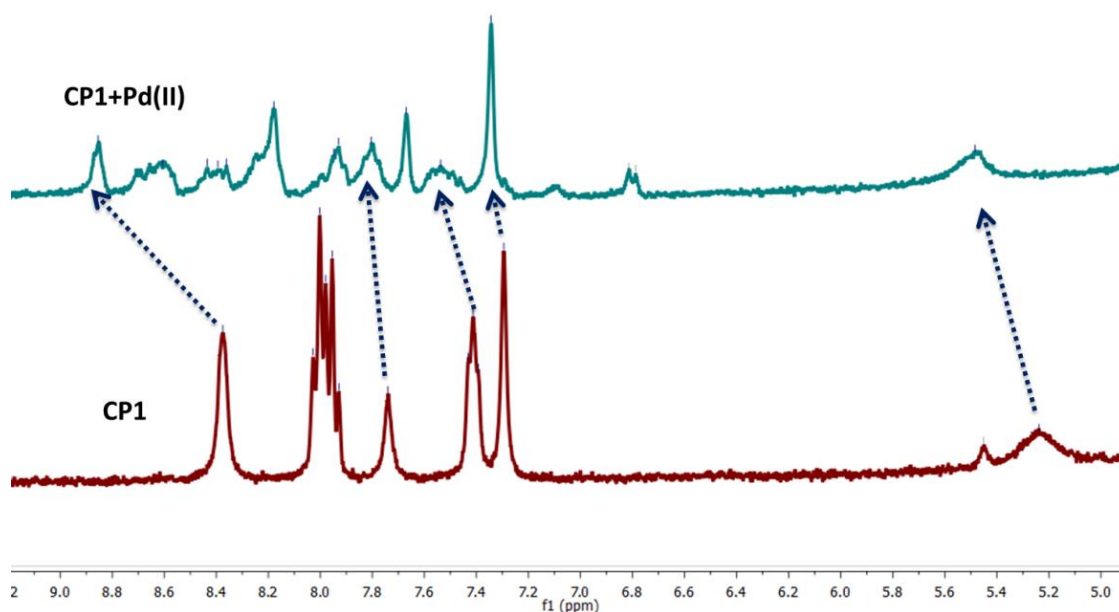
Figure 4.22. ^{1}H NMR (300 MHz, DMSO-d$_6$) spectra of CP**1** and CP**1** in presence of Pd^{2+}.

The XPS (X-ray photoelectron spectroscopy) study is useful to analyse the composition of material with oxidation state and effective interaction of analyte with donor atoms. The peaks in XPS spectra (**Figure 4.23**, **4.24)** have been assigned to C1s, N1s, O1s, Cd$_{3d}$ and Pd$_{3d}$ of CP**1** and [CP**1**+Pd^{2+}] on comparing with literature report.[39-43] After adding Pd^{2+} in the CP**1**, binding energy of C1s for -C-C/ -C-H [39] and –C=N/-C=O is shifted to higher value (ΔE~0.2 eV) which indicates the weak interaction with the Pd. The peak for carboxylate group is shifted from 287.94 eV to 286.63 eV; that corresponds to the interaction of the Pd^{2+} with the free carboxylate group. The N1s binding energy of compound shows two peaks those are assigned to -NH$_2$ (400.20 eV)[40] and –C=N[41] (399.09 eV) which are shifted to 399.91 eV and 399.19 eV respectively; this also unambiguously supports the weak interaction of CP**1** with the Pd^{2+}.
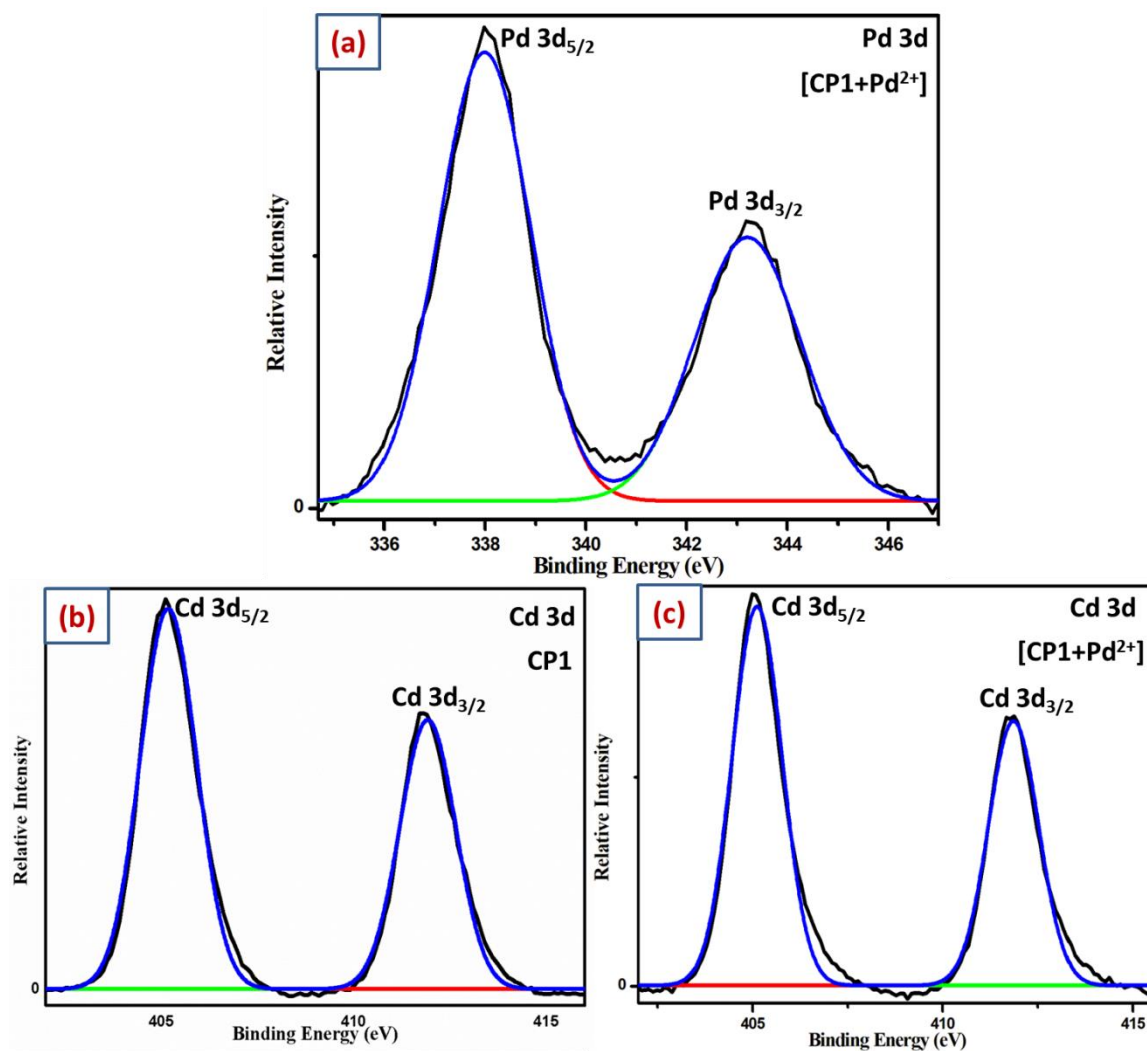
Figure 4.23. XPS spectra of (**a**) Pd for [CP**1**+Pd^{2+}], (**b**) Cd for CP**1** and (**c**) Cd for [CP**1**+Pd^{2+}].

The O1s peak[39,42] for –COO-Cd, -COOH and Cd(-OH)/-C-OH are assigned to 533.05, 532.22 and 531.02 eV, respectively. After addition of Pd^{2+}, the peak at 532.22 eV is shifted to the
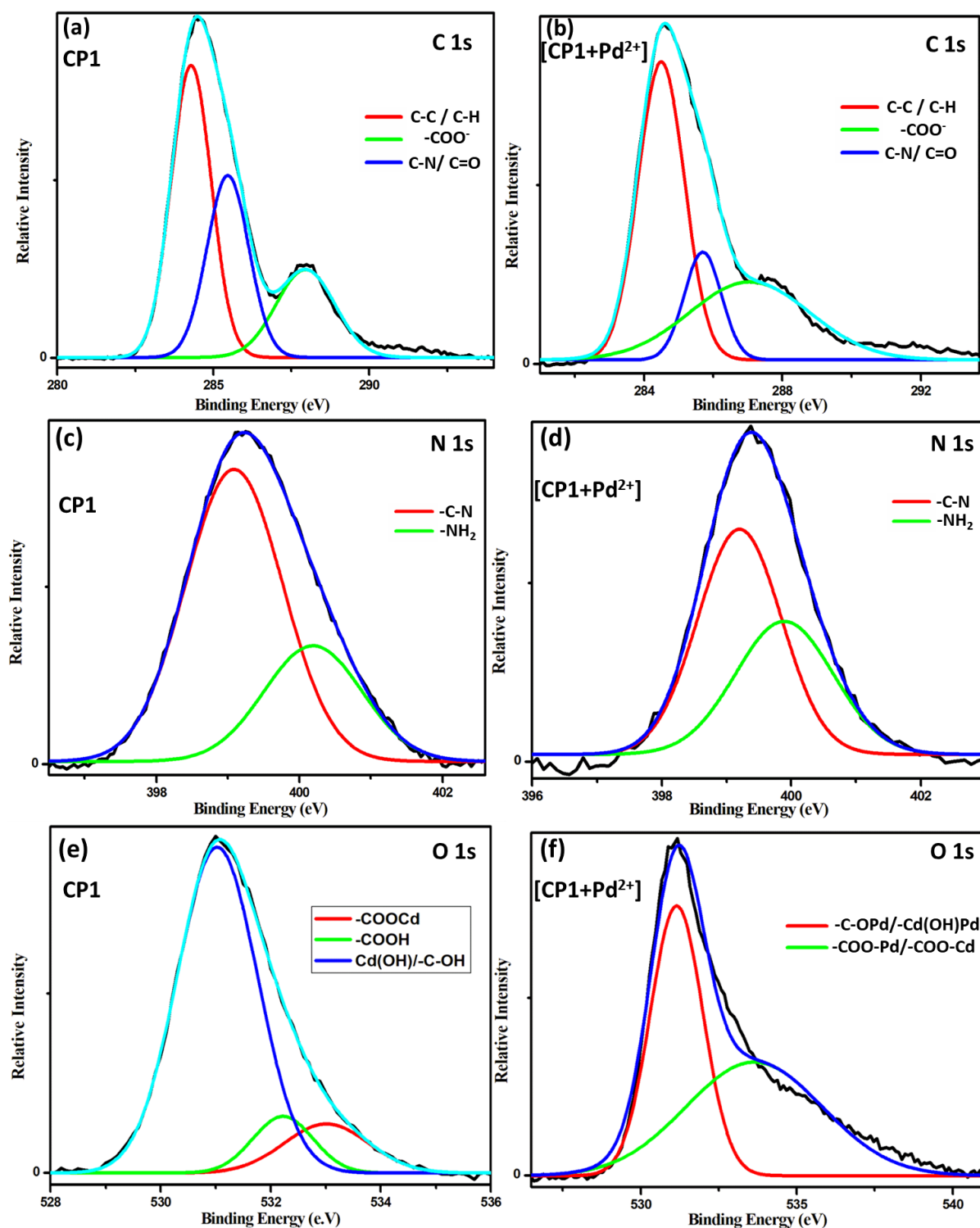
Figure 4.24. XPS pattern of C1s in **CP1** (**a**), [**CP1**+Pd^{2+}] (**b**), N1s in **CP1** (**c**), [**CP1**+Pd^{2+}] (**d**) and O1s in **CP1** (**e**), [**CP1**+Pd^{2+}] (**f**).

higher value (~533.63 eV) that superpose on the peak of –COO-Cd which also supports the binding of Pd^{2+} with -COOH of **CP1**. Another peak (at 531.02 eV) has been shifted to 531.16 eV because of weak interaction of analyte. The Cd$_{3d}$ shows two peaks at 405.18 and 411.93 eV

those remain at same position even after addition of Pd^{2+}. The XPS pattern of [CP**1**+Pd^{2+}] shows the peaks at the position of 338.00 ($3d_{5/2}$) and 343.24 eV ($3d_{3/2}$) those indicate that Pd exists in '+2' oxidation state. Therefore, the XPS has conveyed the binding of the Pd^{2+} with the free carboxylate group along with the interaction of the ligand moieties of framework.

Table 4.6. DFT table of CP**1**.

Excitation energy (eV)	Wavelength Exp. (nm)	Wavelength Thro. (nm)	Oscillation frequency (f)	Key transitions	Nature of Transitions
3.9532	314.64	313.63	0.2118	(31%) HOMO-2→LUMO+8	ILCT
3.3607	363.64	368.92	0.0701	(37%) HOMO→LUMO+4	ILCT

ILCT: Intra-ligand charge transfer.

Table 4.7. DFT table of **[CP1+Pd^{2+}]**.

Excitation energy (eV)	Wavelength Exp. (nm)	Wavelength Thro. (nm)	Oscillation frequency (f)	Key transitions	Nature of Transitions
4.0392	295.19	306.95	0.0048	(41%) HOMO-10 →LUMO+4	ILCT
3.2061	380.87	386.71	0.0391	(22%) HOMO-6→LUMO+4	ILCT

ILCT: Intra-ligand charge transfer.

Table 4.8. DFT computed bond lengths (in Å) and bond angles (°)

Bond lengths (Å)			
CP**1**		[CP**1**+Pd^{2+}]	
Cd(41)-O(45)	2.099	Cd(41)-O(45)	2.074

Cd(41)-O(61)	2.344	Cd(41)-O(61)	2.082
Cd(41)-O(46)	2.508	Cd(41)-O(46)	2.068
Cd(41)-N(69)	3.883	Cd(41)-N(69)	2.111
Cd(41)-N(43)	2.432	Cd(41)-N(43)	2.131
Cd(41)-N(42)	2.552	Cd(41)-N(42)	2.132
Cd(41)-N(44)	2.456	Cd(41)-N(44)	2.141
Bond angels (°)			
O(61)-Cd(41)-O(46)	55.20	O(61)-Cd(41)-O(46)	59.36
N(42)-Cd(41)-N(44)	66.14	N(42)-Cd(41)-N(44)	73.64
N(42)-Cd(41)-N(43)	65.55	N(42)-Cd(41)-N(43)	74.02

DFT optimization and TDDFT data of CP**1** and [CP**1**+Pd^{2+}] to evaluate the electronic transition (**Tables 4.6, 4.7**) which may match with the Tauc's plot (**Figure 4.27**). A small decrease in theoretical calculated band gap is reasonably due to the electron withdrawing nature of ligand and geometry strain of polymer. In this case, band gap of CP**1** and [CP**1**+Pd^{2+}] was calculated using the single motif (**Figure 4.25**). Corresponding transition at 314.64 (HOMO-2 →LUMO+8), 363.64 nm (HOMO→LUMO+4) were observed for CP**1** and 295.19 (HOMO-10→LUMO+4), 380.87 nm (HOMO-6→LUMO+4) for the [CP**1**+Pd^{2+}]; this transition were nearly matched with the theoretical values (**Tables 4.7**, **4.8**). After addition of Pd^{2+} in the CP**1** wavelength was shifted to the higher wavelength that was observed in theoretically and experimentally.

To get insight the binding mode, the DFT computation has been carried out using crystallographic parameters. Use of full polymeric network in the DFT computation is formidable and only coordination repeating motif is considered. The bond length and bond angles of CP**1** are compared with theoretical (DFT computed, **Table 4.8**) and experimental (Single Crystal X-Ray) data (**Table 4.2; Figure 4.25**) and match well. The energy difference between highest occupied molecular orbital (HOMO, -5.34 eV) and lowest unoccupied
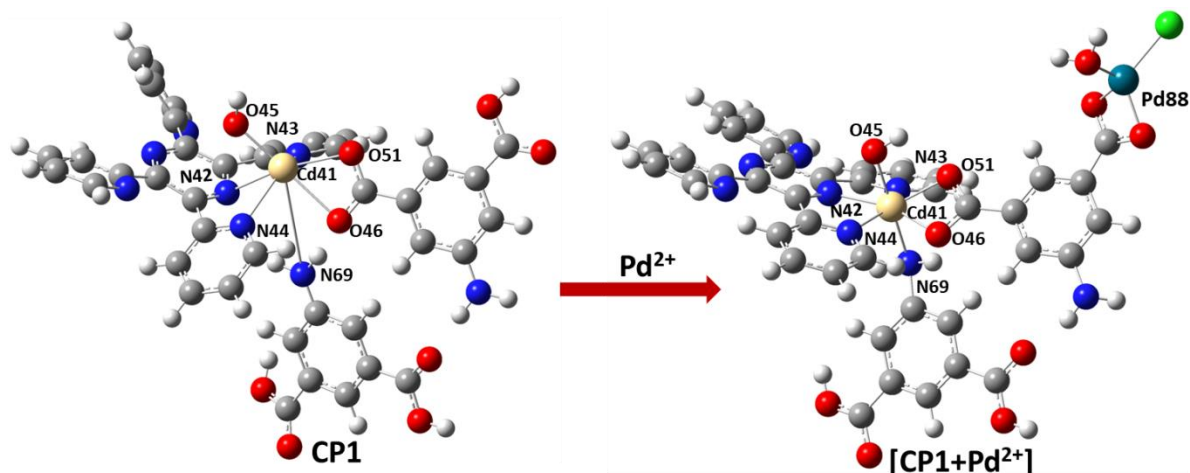
Figure 4.25. DFT optimized structure of CP**1** and [CP**1**+Pd^{2+}].
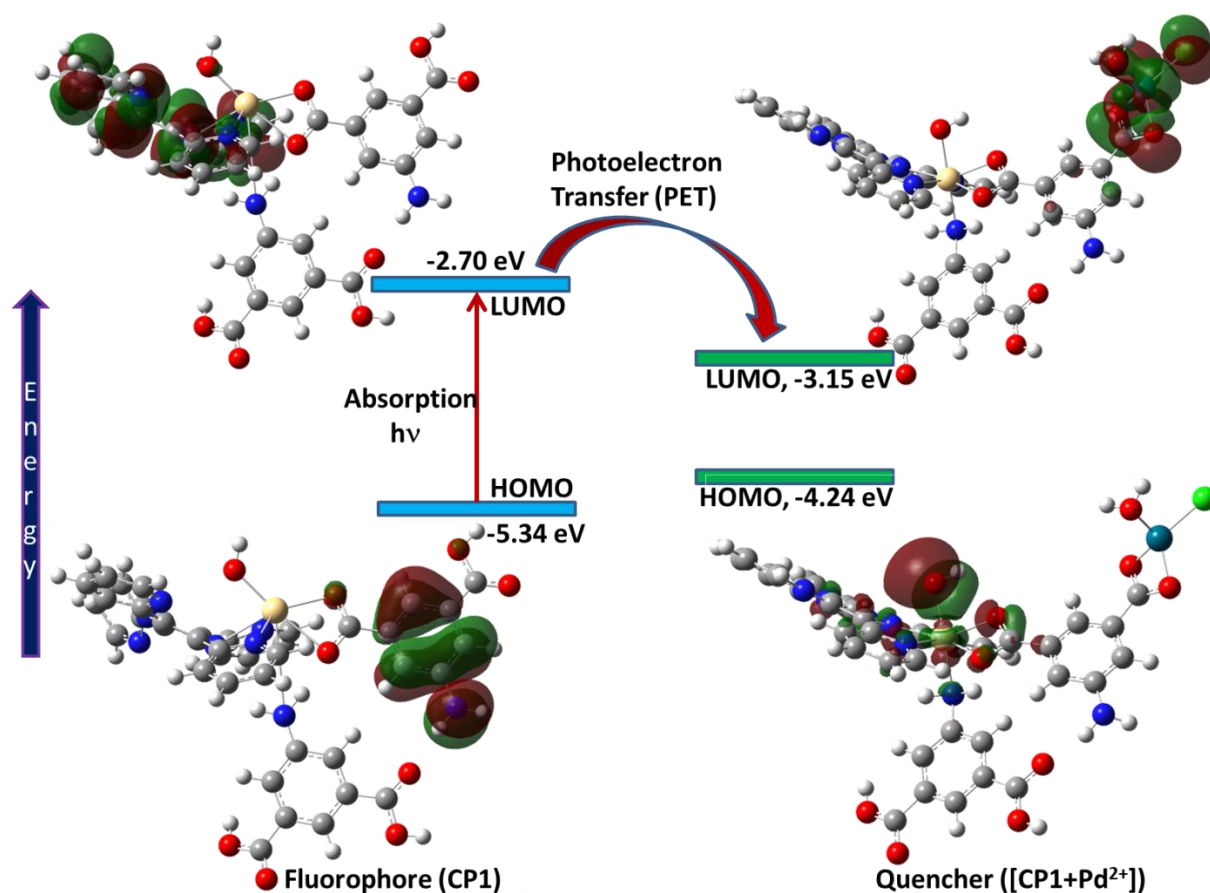
Figure 4.26. DFT calculated energy and band gap of CP**1**.

molecular orbital (LUMO, -2.70 eV) in CP**1** is 2.64 eV that corresponds to 470 nm. The

observed λ$_{max}$, 315 and 363 nm, differ at length which may be due to the consideration of only

coordination unit in calculation. In [CP**1**+Pd^{2+}] the HOMO (-3.15 eV) lies at lower in energy

than that of LUMO (-2.70 eV) of CP**1**. Upon excitation, the electron from HOMO→LUMO in

CP**1** may transfer energy to the LUMO of quencher, [CP**1**+Pd^{2+}]. This may be defined as PET

(Photoinduced electron transfer) process in presence of Pd^{2+} as heavy atom quencher (**Figure**

4.26).

4.3.3. Optical Characterization

The solid-state absorption spectra (**Figure 4.27**) have been recorded using thin films of CP**1**

and [CP**1**+Pd^{2+}] prepared by the dispersion of the composites in DMF. The Tauc's equation

(**Eq. 4.1**)[43] has been used to measure the optical band gap (3.61 eV (CP**1**) and 3.05 eV

[CP**1**+Pd^{2+}]) between the conduction and valence band in the basic absorption edge regions

(around 300–550 nm). The band gap supports semiconducting behaviour of the materials.

$$(\alpha h\nu)^m = K(h\nu - E_g) \tag{4.1}$$

Here, α = absorption coefficient, h is Planck's constant, ν is the frequency with the band gap E_g

and K is a constant.

The values of m = 2 and 1/2 indicate the permitted direct and indirect optical transitions

between the valence band and the conduction band.
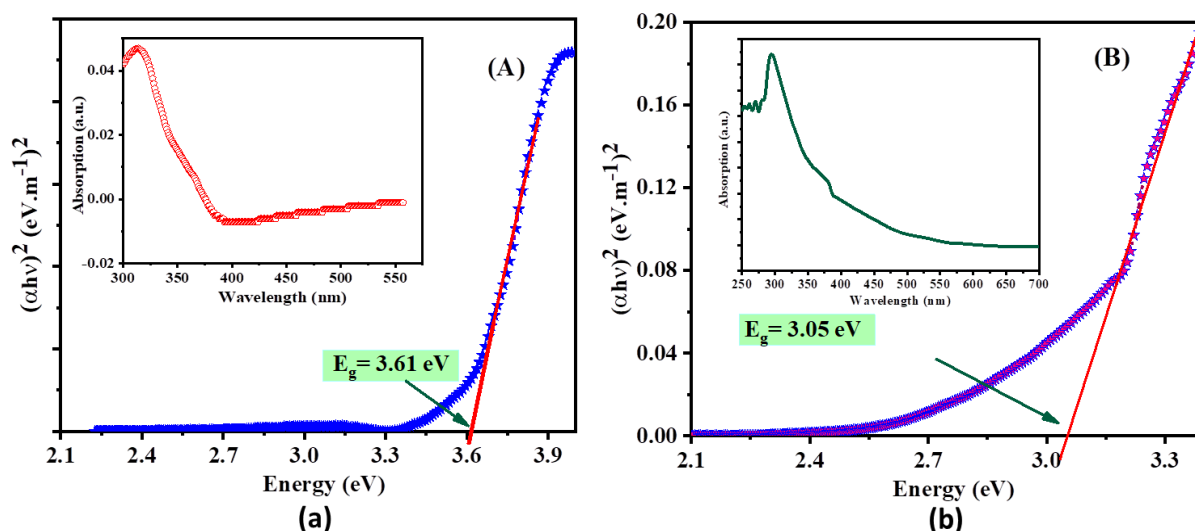
Figure 4.27. UV-vis absorption spectra (inset) and Tauc's plots for the **(a)** CP**1**, **(b)**
[CP**1**+Pd^{2+}].

4.3.4. Electrical Characterization

The current-voltage (I-V) data were collected (Keithley 2400 source meter) with and without illumination (Intensity ~ 100 mW.cm^{-2}) at 300 K by applied bias voltage within ± 1.5 V range with step size 0.03 V (**Figure 4.28**) across the thin-film metal-semiconductors (MS) junction of CP**1** (ITO/CP**1**/Al) and [CP**1**+Pd^{2+}] (ITO/[CP**1**+Pd^{2+}]/Al). The electrical conductivities are 7.42×10^{-5} S m^{-1} (CP**1**) and 1.2×10^{-4} S m^{-1} [CP**1**+Pd^{2+}] at dark and upon illumination, the conductivities are improved to 1.45×10^{-4} S m^{-1} (CP**1**) and 3.81×10^{-4} S m^{-1} [CP**1**+Pd^{2+}] (**Table 4.10**). This improvement in conductivity upon illumination is probably due to the increment of charge transportation *via* multiple routes, such as through covalent conduction bond and coordination bonds in the composite and through space charge travels *via* noncovalent interactions.[44] The DFT computation has been attempted to explain the enhancement of electrical conductivity on incorporation of Pd^{2+} into CP**1** (*Vide infra*).
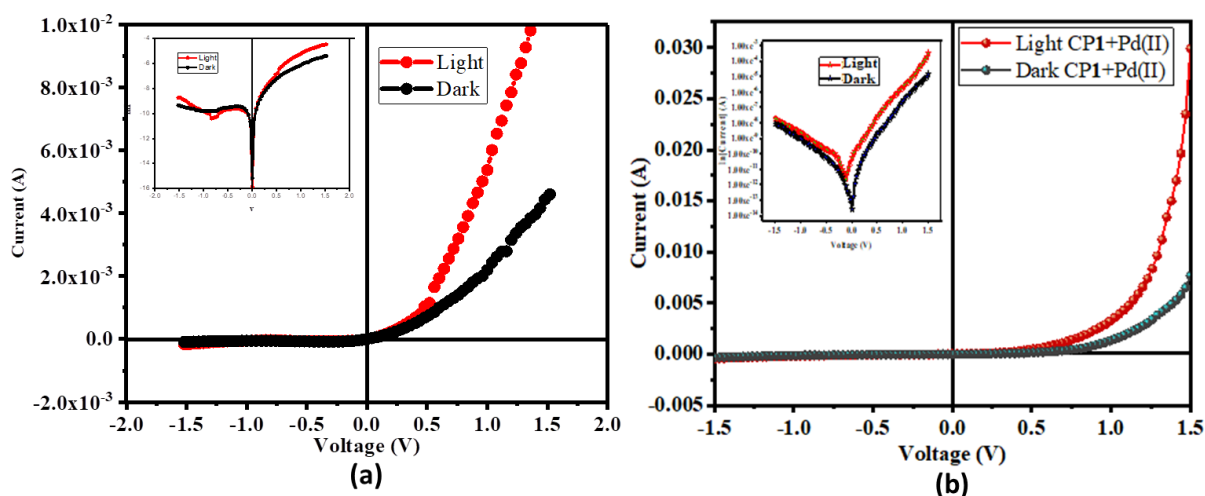
Figure 4.28. I-V characteristic curves for composite-based MS devices under light and dark conditions of **(a)** CP**1** and **(b)** [CP**1**+Pd^{2+}].

The I−V characteristic of the composite exhibits nonlinear rectifying behaviour in both dark and illumination environments. The rectification ratio (I_{on}/I_{off}) calculated from the plots reveals that the devices based on CP**1** and [CP**1**+Pd^{2+}] have 2.5 and 2.78 times higher at light phase

than at dark phase, respectively (**Table 4.9**). Hence, the photo conducting properties of the devices, such as photosensitivity (P$_S$), photoresponsivity (R), photoconductivity sensitivity (S), and specific detectivity (D*) were estimated and compared under dark and light conditions. The ratio of photocurrent generated (I$_{phc}$ = I$_{light}$ − I$_{dark}$) to the current in dark (I$_{dark}$) is known as the photosensitivity and is given by (P$_S$; **Eq. 4.2**).[45] The remarkable photosensitivity level and high specific detectivity of the proposed devices make it an appealing candidate for photovoltaic applications.

$$P_S = \frac{I_{phc}}{I_{dark}}$$
(4.2)

The ratio of photocurrent of a photodiode to the incident optical power is defined as photoresponsivity (R) and can be obtained from the **Eq. 4.3**:

$$R = \frac{I_{phc}}{P_i A_{eff}}$$
(4.3)

Where P$_i$ is incident optical power (100 mW.cm^{-2}) and A$_{eff}$ (9×10^{-6} m^2) gives the effective area of device. Diode suitability of a photo detector is judged from the specific detectivity (D*) as given in **Eq. 4.4**:

$$D^* = \frac{R}{\sqrt{2qI_{dark}}}$$
(4.4)

Where, electric charge is denoted by q. Another parameter, the photoconductivity sensitivity (S), is estimated by **Eq. 4.5**.

$$S = \frac{L.I_{phc}}{V.P_i.A_{eff}}$$
(4.5)

Table 4.9: Photosensing parameters of the Schottky junction device.

Device	Rectification ratio		Photosensitivity (P$_s$)	Responsivity (R) (AW^{-1})	Specific detectivity (D*) (Jones)	Photoconductivity sensitivity (S) (m Ω^{-1} W^{-1})
CP1	Dark	40.24	1.5	0.77	1.99×10^{10}	5.11×10^{-7}
	Light	100.2				
[CP1+Pd^{2+}]	Dark	24.78	2.9	2.46	4.97×10^{10}	1.64×10^{-6}

The thermionic emission (TE) theory has been adopted for measuring I-V characteristic of the composite-based device (**Eq. 4.6**).[46]

$$I = I_0 \left[exp\left(\frac{qV}{rkT}\right) - 1 \right] \qquad (4.6)$$

Where V, q, r, k, and T have denote the applied bias voltage, electronic charge, ideality factor, Boltzmann constant, and operating temperature in Kelvin. The reverse saturation current, I_0 calculated using **Eq. 4.7**.

$$I_0 = AA^*T^2 exp\left(-\frac{q\phi_b}{kT}\right) \qquad (4.7)$$

Where A is the effective area of Schottky diodes, which is 35×10^{-6} m^2, A^* represents effective Richardson constant, which is assumed as 1.20×10^6 AK^{-2} m^{-2}, ϕ_b is the barrier height (BH) at the junction. The reverse saturation current (I_0) is derived from the intercept of lnI vs V at V = 0. The temperature dependence of ideality factor (r) is expressed in **Eq. 4.8**.

$$\mathbf{r} = \frac{q}{kT}\left[\frac{dV}{d(lnI)}\right] \qquad (4.8)$$

The barrier height (ϕ_b) at zero bias can be achieved from **Eq. 4.7** and can be expressed as **Eq. 4.9**.

$$\phi_b = \frac{kT}{q} ln\left(\frac{AA^*T^2}{I_0}\right) \qquad (4.9)$$

The values of *r* and ϕ_b of the Schottky device are estimated from the slope and intercept of the plots respectively (**Table 4.10**). Schottky parameters like ideality factor (**r**), series resistance (*Rs*), and barrier height (ϕ_b) have been determined from the forward bias *I–V* characteristics employing Cheung's method (**Eq. 4.10**).[47]

$$\frac{dV}{d(lnI)} = IR_S + \frac{rkT}{q} \qquad (4.10)$$

Table 4.10. The Schottky Device Parameters for the Composite Based Thin Film Devices.

Device	Condition	Conductivity (S. m^{-1})	Ideality factor (r)	Series Resistance from (R$_s$ in Ω)		Barrier Height from (ϕ_b in eV)	
				dV/dlnI *vs* I	H(I)-I	I-V plot	H(I)-I
CP**1**	Dark	7.42× 10^{-5}	2.36	443.36	453.30	0.69	0.65
	Light	1.45× 10^{-4}	2.29	330.44	344.11	0.67	0.62
[CP**1**+Pd^{2+}]	Dark	1.20× 10^{-4}	2.14	412.25	421.12	0.65	0.63
	Light	3.81× 10^{-4}	1.99	342.41	355.81	0.62	0.59

From the intercept of the plot *dV/dlnI* vs. *I* (**Figure 4.29a, 4.29c**) ideality factor (**r**) for the developed devices under both condition has been estimated whereas the slope of this corresponding plot gives the value of series resistance (**R$_S$**) of the MS device (**Eq. 4.11**).[47]

$$H(I) = V - \frac{rkT}{q} ln\left(\frac{I}{AA^*T^2}\right) = r\phi_b + R_S I \qquad (4.11)$$

The y-axis intercept for the *H (I) vs. I* curve (**Figure 4.29b, 4.29d**) provides potential barrier height (ϕ_b). In general, the ideality factor (**r**) in the dark deviates from ideal behaviour due to Schottky barrier junction inhomogeneities, a high chance of electron and hole recombination in depletion zone, and the presence of series resistance as well as interfacial states.[48,49] Under dark and light conditions, values of **r** for the device based on CP**1** are 2.36 and 2.29, respectively, whereas the values for [CP**1**+Pd^{2+}] are 2.14 and 1.99, respectively. These values differ from the desired value (~1). This could be owing to the presence of Schottky barrier junction in homogeneities and series resistance at the junction.

The decrement in ideality factor (2.36 (dark) and 2.29 (light) for CP**1**; 2.14 (dark) and 1.99 (light) for [CP**1**+Pd^{2+}]) towards ideal value in presence of light suggests that the composite-based device has less carrier recombination at the junction.[50]

As a result, under lighting condition, the barrier potential height is likewise reduced. The accumulation of photo-induced charge carriers near the conduction band possibly is the primary cause of this decrease. Series resistances (R_s) achieved by both procedures are consistent. The resulting series resistances were shown to decrease when exposed to light (**Table 4.10**), indicating their usefulness in the area of optoelectronic devices.
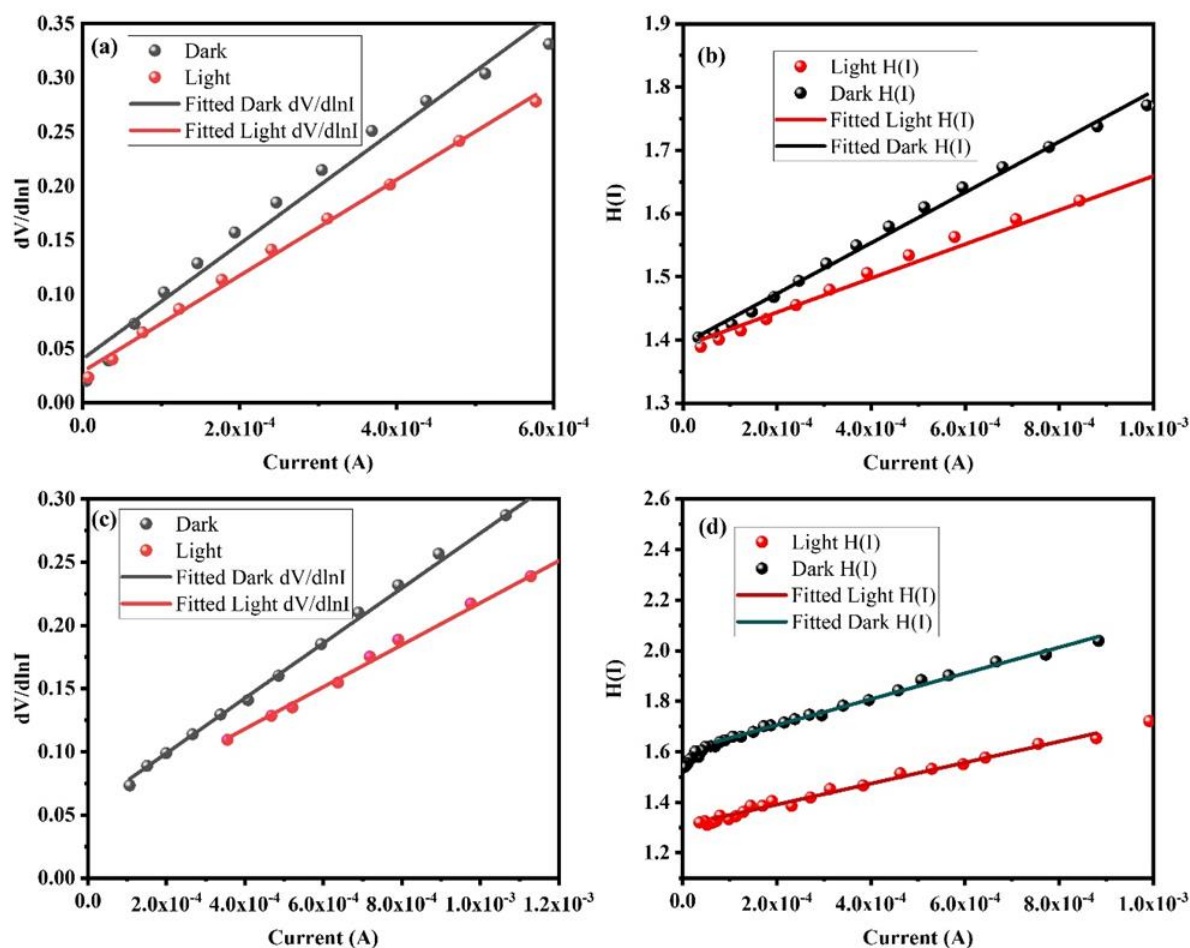
Figure 4.29. **(a)** *dV/dlnI vs. I (A)*, **(b)** *H (I) vs. I (A)* curves for the CP**1** composite and **(c)** *dV/dlnI vs. I (A)* , **(d)** *H (I) vs. I (A)* curves for the [CP**1**+Pd^{2+}] composite based device under dark and photo illumination condition.

In this regard, we estimated the transit time and mobility to achieve a comprehensive view of the charge transfer kinetics. The distinctive I-V curves of CP**1** on logarithmic scale under dark and light conditions revealed that it can be divided into two slope regions (**Figure 4.30a** and **4.30b**).

However, the I-V properties of [CP**1**+Pd^{2+}] have three regions. The various regions of these I-V characteristics represent various charge transfer methods. Region-I has slope ~1, implying the Ohmic region, and it follows the I∝V relation. In Region-II, the current is
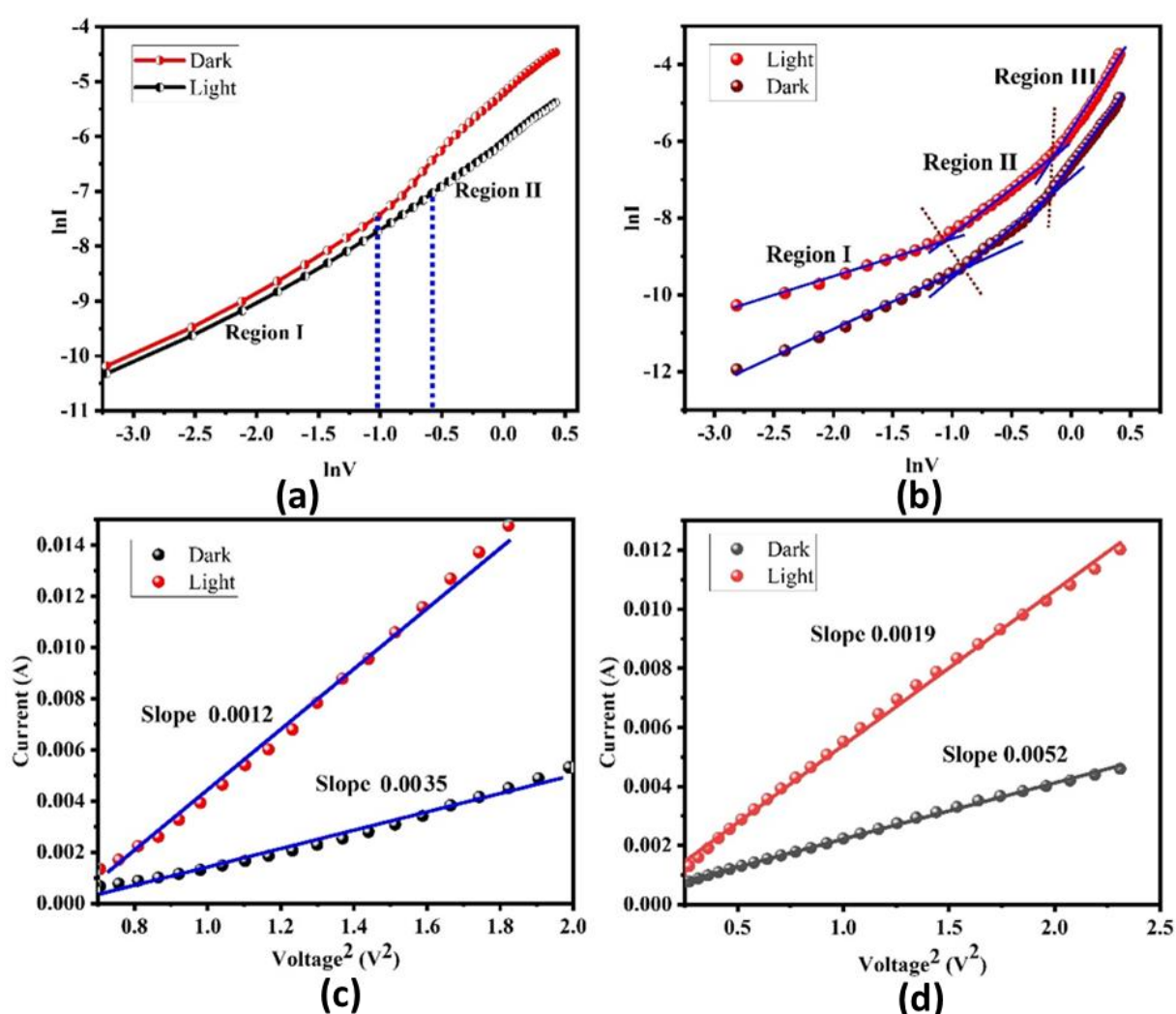
Figure 4.30. (a) and **(b)** *lnI vs. lnV* plots, **(c)** and **(d)** *I vs. V²* curves for CP**1** and [CP**1**+Pd^{2+}] composite based devices under dark and illumination conditions.

roughly proportional to V^2, indicating a space charge limited current (SCLC) regime. The trapped-charge-limited-current (TCLC) exists in Region III (**Figure 4.30d**) which has a slope greater than 2. This means that as the voltage goes over a certain threshold, electrons are trapped by Pd(II) defect-induced traps of the sample that are distributed exponentially within the forbidden gap. As a result, the electrical current will rapidly increase until it approaches the ON state. If the injected charge carriers are higher than background charge carriers, then injected charge carriers spread and create a space-charge field. Guided by this model, the effective charge carrier mobility has been evaluated from the higher voltage region of the plot I *vs.* V^2 (**Figure 4.30c** and **4.30d**) following Mott-Gurney equation: [51]

$$I = \frac{9\mu_{eff}\varepsilon_0\varepsilon_r A}{8}\left(\frac{V^2}{d^3}\right) \tag{4.12}$$

where, I, μ_{eff}, ε_0 and ε_r, is the current, effective mobility, permittivity of free space and relative dielectric constant of the synthesized materials respectively.

Diffusion length (L_D) and transit time (τ) are some of the important parameters, for analyzing charge transport across the junction. For such purpose, the value of τ has been calculated (**Eq. 4.13**) from the slope of the logarithmic plot of the forward biased I-V characteristics in SCLC region (Region-II, **Figure 4.30a** and **4.30b**).

$$\tau = \frac{9\varepsilon_0\varepsilon_r A}{8d}\left(\frac{V}{I}\right) \tag{4.13}$$

$$\mu_{eff} = \frac{qD}{kT} \tag{4.14}$$

$$L_D = \sqrt{2D\tau} \tag{4.15}$$

where, D is the diffusion coefficient and estimated using Einstein–Smoluchowski equation (**Eq.4.14**).[52] As MS junction gets developed, the diffusion length (L_D, **Eq. 4.15**) of the charge carrier has a prominent role in the performance of the device.
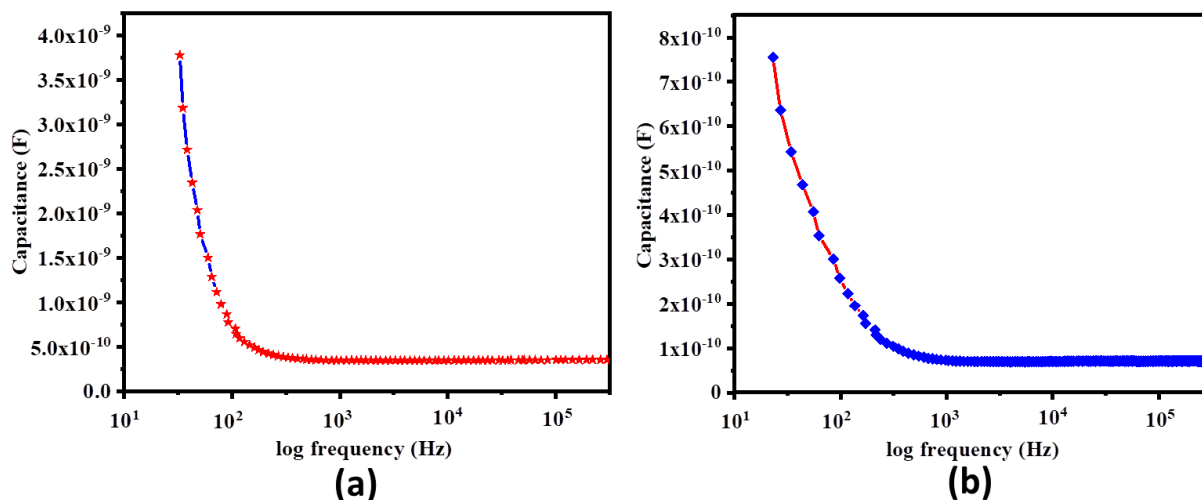
Figure 4.31. (a) and **(b)** represent capacitance vs log frequency of CP**1** and [CP**1**+Pd^{2+}] based MS device respectively.

The dielectric permittivity (ε_r) of the composite has been derived (**Eq. 4.16**) from the saturated value of capacitance at the higher frequency region (**Figure 4.31**):

$$\varepsilon_r = \frac{1}{\epsilon_0} \cdot \frac{C.d}{A} \tag{4.16}$$

Where, C gives the capacitance (at saturation), A defines the effective area and d is the thickness of the film considered to be ~1 μm. From the relation (**Eq. 16**) above, the relative dielectric constant of the CP**1** and [CP**1**+Pd^{2+}] composite have been found to be 0.83 and 1.30.

Almost all characteristics in the SCLC regions demonstrated that the charge transport properties of CP**1** is enhanced after Pd^{2+} incorporation as well as under light conditions (**Table 4.11**). The increased diffusion lengths (L$_D$) under light demonstrates that charge carriers travel a long distance before recombination, resulting in an increment in the current shown by the device under illumination. The [CP**1**+Pd^{2+}] composite-based diode exhibits enhanced charge transfer kinetics than CP**1**. Results have concluded that such material emerges as pathway for bright future in device applications.

Table 4.11. Charge conduction parameters of the CP**1** and [CP**1**+Pd^{2+}] Composite Based MS Thin Film Devices

Device	Condition	ε_r	Effective mobility μ_{eff}	Transit time τ (S)	$\mu_{eff}\tau$ (m^{2}V^{-1})	Diffusion coefficient D ($\times 10^{-7}$)	Diffusion length, L_D ($\times 10^{-10}$) (nm)
CP**1**	Dark	0.83	4.15×10^{-6}	1.01×10^{-12}	1.44×10^{-18}	1.07	2.73
	Light		1.21×10^{-5}	3.47×10^{-13}	1.23×10^{-17}	3.11	7.96
[CP**1**+Pd^{2+}]	Dark	1.30	4.27×10^{-6}	2.36×10^{-12}	3.68×10^{-18}	1.10	4.36
	Light		1.22×10^{-5}	8.61×10^{-13}	2.88×10^{-17}	3.18	1.22

The electrical Schottky contact may be employed by lattice matching with the molecular system and deformation potential. Usually, deformation refers to the energy gap between HOMO and LUMO. Normally, absolute deformation potential (ADPs) has been used for evaluation of the band gap[53] in CPs. The calculated energy difference between HOMO and LUMO in CP**1** is 2.64 eV, which corresponds to the experimental band gap 3.61 eV. The calculated energy difference of HOMO and LUMO of [CP**1**+Pd^{2+}] is 1.09 eV where the experimental gap is 3.05 eV. Difference of energy gap is dependent on the electronic nature of structural components including the geometrical strain of network[54] of CP. Therefore, the energy gap of CP**1** and [CP**1**+Pd^{2+}] reveals the lowering of gap upon inclusion of Pd^{2+} and has resulted the better charge transportation as well as electrical conductivity.

4.4. Conclusion

A 2D coordination polymer (2D-CP), {[Cd(HAIPA)(tppz)(OH)].3H$_2$O}$_n$, (CP**1**) is self-assembled to 3D supramolecule and is highly blue emissive in aqueous-acetonitrile (40:1, v/v) suspension. The CP**1** selectively absorbs Pd^{2+} only out of sixteen cations and quenches the

emission (LOD, 0.08 μM). Besides, the material, CP**1** and [CP**1**+Pd^{2+}], lies in semiconducting region (band gap : 3.61 and 3.05 eV) and exhibits better electrical conductivity at light irradiation (Λ_{CP1} : 7.42×10^{-5} S m^{-1} (dark) and 2.45×10^{-4} S m^{-1} (light) and ($\Lambda_{[CP1+Pd^{2+}]}$: 1.20×10^{-4} S m^{-1} (dark) and 3.81×10^{-4} S m^{-1} (light)). Hence, the material is accommodating Pd^{2+} within it followed by severe quenching of blue emission and detection limit is also quite low. Upon inclusion of this metal ion there is an enhancement of electrical conductivity taken place. It may be stated that Palladium included compound may be employable to resolve the energy crisis issue. With this we believe that the single material having multifunctional applicability will be acted as an ornament for the material researchers.

4.5. Reference

1. Negishi, E. Ed. Handbook of Organopalladium Chemistry for Organic Synthesis; Wiley-Interscience: New York, **2002**.

2. Tsuji, J. Palladium Reagents and Catalysts: New Perspectives for the 21st Century; Wiley and Sons: New York, **2003**.

3. Tsuji, J. Ed. Palladium in Organic Synthesis; Springer: Berlin, **2005**.

4. Heck, R. F. Palladium Reagents in Organic Synthesis; Academic Press: New York, **1985**.

5. Li, J. J.; Gribble, G. W. Palladium in Heterocyclic Chemistry; Pergamon: New York, **2000**.

6. Punniyamurthy, T.; Velusamy, S.; Iqbal, J. Recent Advances in Transition Metal Catalyzed Oxidation of Organic Substrates with Molecular Oxygen. *Chem. Rev.* **2005**, *105*, 2329–2365.

7.   Environmental Health Criteria 226, PALLADIUM, World Health Organization Geneva, **2002**.

8.   Rodríguez, J.; Martínez-Calvo, M. Transition-Metal-Mediated Modification of Biomolecules. *Chem. Eur. J*., **2020**, *26*, 9792-9813.

9.   Bhanja, A. K.; Mishra, S.; Kar, K.; Naskar, K.; Maity, S.; Saha, K.D.; Sinha, C. Use of rhodamine-allyl Schiff base in chemodosimetric processes for total palladium estimation and application in live cell imaging. *New J. Chem*., **2018**, *42*, 17351-17358.

10. Bhanja, A. K.; Mishra, S.; Saha, K. D.; Sinha, C. A fluorescence 'turn-on' chemodosimeter for the specific detection of Pd^{2+} by a rhodamine appended Schiff base and its application in live cell imaging. *Dalton Trans*., **2017**, *46*, 9245-9252.

11. Adak, K. A.; Dutta, B.; Manna, K. S.; Sinha, C. Rhodamine-Appended Benzophenone Probe for Trace Quantity Detection of Pd^{2+} in Living Cells. *ACS Omega.*, **2019**, *4*, 18987-18995.

12. Adak, K. A.; Purkait, R.; Manna, K. S.; Ghosh, C. B.; Pathak, S.; Sinha, C. Fluorescence sensing and intracellular imaging of Pd^{2+} ions by a novel coumarinyl-rhodamine Schiff base. *New J. Chem*., **2019**, *43*, 3899-3906.

13. Liu, Q.; Liu, C.; Cai, S.; He, S.; Zhao, L.; Zeng, X.; Gong, J. A highly sensitive sensor for colorimetric detection of palladium(II) in lysosomes and its applications. *Dalton Trans*., **2022**, *51*, 3116-3121.

14. Song, F.; Garner, L. A.; Koide, K. A. Highly Sensitive Fluorescent Sensor for Palladium Based on the Allylic Oxidative Insertion Mechanism. *J. Am. Chem. Soc.,* **2007**, *129*, 12354–12355.

15. Zhang, P. X.; Yuan, Q.; Qi, L. Y.; Zheng, J. D.; Liu, X. Q.; Wang, Z. B.; Yang, S. Y.; Zhu, L. H. An umbelliferone-derivated fluorescent sensor for selective detection of

palladium(II) from palladium(0) in living cells. *Spectrochim. Acta, Part A.*, **2019**, *220*, 117134.

16. V. Pekarik, M. Peskova, J. Duben, M. Remes and Z. Heger, Direct fuorogenic detection of palladium and platinum organometallic complexes with proteins and nucleic acids in polyacrylamide. gels. *Sci. Rep.*, **2020**, *10*,12344.

17. Bhunia, S.; Dutta, B.; Pal, K.; Chandra, A.; Jana, K.; Sinha, C. Ultra-trace level detection of Cu^{2+} in an aqueous medium by novel Zn (II)-dicarboxylato–pyridyl coordination polymers and cell imaging with HepG2 cells. *New J. Chem.*, **2021**, *45,* 13941-13948

18. Dutta, B.; Jana, R.; Bhanja, K. A.; Ray, P. P.; Sinha, C.; Mir, MH. Supramolecular aggregate of Cadmium (II)-based one-dimensional coordination polymer for device fabrication and sensor application. *Inorg. Chem.*, **2019**, *58*, 2686-2694.

19. Dutta, B., Purkait, R., Bhunia, S., Khan, S., Sinha, C.; Mir, M.H., Selective detection of trinitrophenol by a Cd (II)-based coordination compound. *RSC Adv.,* **2019**, *9*, 38718-38723.

20. Nirala, N. R.; Tiwari, M.; Prakash, R. A nanoporous palladium (II) bridged coordination polymer acting as a peroxidase mimic in a method for visual detection of glucose in tear and saliva. *Microchim. Acta.,* **2018**, *185*, 1-10.

21. Xu, T. Y.; Wang, H.; Li, J. M.; Zhao, Y. L.; Han, Y. H.; Wang, X. L.; He, K. H.; Wang, A. R.; Shi, Z. F. A water-stable luminescent Zn (II) coordination polymer based on 5-sulfosalicylic acid and 1, 4-bis (1H-imidazol-1-yl) benzene for highly sensitive and selective sensing of Fe^{3+} ion. *Inorg. Chim. Acta.*, **2019**, *493*, 72-80.

22. He, J.; Zha, M.; Cui, J.; Zeller, M.; Hunter, A. D.; Yiu, S. M.; Lee, S. T.; Xu, Z. Convenient detection of Pd (II) by a metal–organic framework with sulfur and olefin functions. *J. Am. Chem. Soc.*, **2013**, *135*, 7807-7810.

23. Sanda, S.; Parshamoni, S.; Biswas, S.; Konar, S. Highly selective detection of palladium and picric acid by a luminescent MOF: a dual functional fluorescent sensor. *Chem. Commun.*, **2015**, *51*, 6576-6579.

24. Mir, M.H.; Bera, S.; Khan, S.; Maity, S.; Sinha, C.; Dutta, B. Sunlight assisted SCSC dimerization of a 1D coordination polymer impacts the selectivity of Pd (II) sensing in water. *Chem. Commun.*, **2021**, *57*, 6197-6200.

25. Dutta, B.; Bera, S.; Bairy, G.; Shit, M.; Sinha, C.; Mir, M. H. Exploitation of a Series of Zn (II)-Coordination Polymers for Pd (II)-Detection in Aqueous Medium. *ES Energy & Environ.*, **2022**.

26. Sheldrick, G. M. A short history of SHELX. *Acta Crystallogr., Sect. A: Found. Crystallogr*. **2008**, *64*, 112-122.

27. SMART.; SAINT. Bruker AXS Inc.: Madison, WI, **1998**.

28. SADABS. Bruker AXS area detector scaling and absorption correction; Bruker AXS Inc.: Madison, WI, **2014**.

29. Goher, M. A.; Mautner, F. A.; Abu-Youssef, M. A.; Hafez, A. K.; Badr, A. M. A. Synthesis and crystal structure of three new 2D polymeric cadmium (II) complexes of some pyridine derivatives with different cadmium (II)–azide topologies. *J. Chem. Soc., Dalton Trans.*, **2002**, 3309–3312.

30. Zhang, Y. M.; Wang, L. Y.; Li, B. L.; Yang, J. H.; Zhang, Y. Structural diversity of four novel cadmium coordination polymers constructed by 1, 4-bis (imidazol-1-yl) butane and anion ligands. *J. Mol. Struct*., **2008**, *875*, 527–539.

31. Ray, S.; Konar, S.; Jana, A.; Jana, S.; Patra, A.; Chatterjee, S.; Golen, J. A.; Rheingold, A.L.; Mandal, S. S.; Kar, S. K. Three new pseudohalide bridged dinuclear Zn (II), Cd (II) complexes of pyrimidine derived Schiff base ligands: Synthesis, crystal structures and fluorescence studies. *Polyhedron*, **2012**, *33*, 82–89.

32. He, X.; Lu, C. Z. Synthesis and crystal structures of two cadmium coordination chain polymers. *Z. Anorg. Allg. Chem.*, **2004**, *630*, 2583-2586.

33. Gou, L.; Wu, Q. R.; Hu, H. M.; Qin, T.; Xue, G. L.; Yang, M. L.; Tang, Z. X.; An investigation of the positional isomeric effect of terpyridine derivatives: Self-assembly of novel cadmium coordination architectures driven by N-donor covalence and $\pi\cdots\pi$ non-covalent interactions. *Polyhedron*, **2008**, *27*, 1517-1526.

34. Nawrot, I.; Machura, B.; Kruszynski, R. Coordination assemblies of Cd(II) with 2, 2′: 6′, 2″-terpyridine (terpy), 2, 3, 5, 6-tetra-(2-pyridyl) pyrazine (tppz) and pseudohalide ions–structural diversification and luminescence properties. *CrystEngComm*, **2015**, *17*, 830-845.

35. Seyed Sadjadi, M.; Ebadi, A.; Zare, K.; Amani, V.; Khavasi, H. R.; μ-2, 3, 5, 6-Tetra-2-pyridylpyrazine-κ3N1, N2, N6: κ3N3, N4, N5-bis [(methanol-κO)(nitrato-κ2O, O′)(nitrato-κO) cadmium (II)]. *Acta Crystallogr., Sect. E: Struct. Rep. Online.*, **2008**, *64*, 1050–1051.

36. Hadadzadeh, H.; Hosseinian, S. R.; Fatemi, S. J. A Rhodium (III) and cadmium (II) complexes based on the polypyridyl ligand 2, 3, 5, 6-tetrakis (2-pyridyl) pyrazine (tppz). *Polyhedron*, **2009**, *28*, 2776-2784.

37. Bondi, A. V. van der Waals volumes and radii. *J. Phys. Chem.*, **1964**, *68*, 441-451.

38. Hambley, T. W. van der Waals Radii of Pt (II) and Pd (II) in Molecular Mechanics Models and an Analysis of Their Relevance to the Description of Axial M⊙⊙⊙ H (−

C), M⊙⊙⊙ H (− N), M⊙⊙⊙ S, and M⊙⊙⊙ M (M= Pd (II) or Pt (II)) Interactions. *Inorg. Chem.*, **1998**, *37*, 3767-3774.

39. Zhang, M.; Yin, Q.; Ji, X.; Wang, F.; Gao, X.; Zhao, M.. High and fast adsorption of Cd (II) and Pb (II) ions from aqueous solutions by a waste biomass based hydrogel. *Sci. Rep.*, **2020**, *10*, 1-13.

40. Yoshida, T.; Yamasaki, K.; Sawada, S. An X-ray photoelectron spectroscopic study of biuret metal complexes. *Bull. Chem. Soc. Jpn.,* **1978**, *51*, 1561-1562.

41. Ding, Z. D.; Zhu, W.; Li, T.; Shen, R.; Li, Y.; Li, Z.; Ren, X.; Gu, Z. G. A metalloporphyrin-based porous organic polymer as an efficient catalyst for the catalytic oxidation of olefins and arylalkanes. *Dalton Trans.,* **2017**, *46*, 11372-11379.

42. Wu, N.; Li, Z. Synthesis and characterization of poly (HEA/MALA) hydrogel and its application in removal of heavy metal ions from water. *J. Chem. Eng.,* **2013**, *215*, 894-902.

43. Wood, L. D.; Tauc, J. Weak Absorption Tails in Amorphous Semiconductors. *Phys. Rev. B: Solid State*, **1972**, *5*, 3144–3151.

44. Sun, L.; Campbell, MG.; Dincă, M. Electrically Conductive Porous Metal-Organic Frameworks. *Angew. Chem., Int. Ed. Engl.*, **2016**, *55*, 3566–3579.

45. Dutta, B.; Jana, R. Synthesis of a Cd(ɪɪ) based 1D coordination polymer by *in situ* ligand generation and fabrication of a photosensitive electronic device. *Inorg. Chem. Front.,* **2018**, *5*, 1998–2005.

46. Sen, S.; Manik, B. N.; Effect of Zinc Oxide (ZnO) Nanoparticles on Interfacial Barrier Height and Band Bending of Phenosafranin (PSF) Dye-Based Organic Device. *J. Electron. Mater.,* **2020**, *49*, 4647-4652.

47. Ahmed, Faruk.; Halder, Soumi.; Synthesis and structural characterization of a Cu(II)-based 1D coordination polymer and its application in Schottky devices. *New J. Chem.,* **2017**, *41*, 11317-11323.

48. Sharma, Mamta.; Tripathi, K. S.; Study of barrier inhomogeneities in I–V-T and C-V-T characteristics of Al/Al$_2$O$_3$/PVA:n-ZnSe metal–oxide–semiconductor diode. *J. Appl. Phys.*, **2012**, *112*, 024521-024531.

49. Sullivan, P. J.; Tung, T. R.; Pinto, R. M. Electron transport of inhomogeneous Schottky barriers: A numerical study. *J. Appl. Phys.,* **1991**, *70*, 7403-7424.

50. Mahato, Somnath.; Biswas, Debaleen.; Gerling, G. Luis.; Analysis of temperature dependent current-voltage and capacitance-voltage characteristics of an Au/V2O5/*n*-Si Schottky diode. *AIP Adv.*, **2017**, *7*, 085313-085325.

51. Soylu, M.; Abay, B. Analysing space charge-limited conduction in Au/n-InP Schottky diodes, Low-dimensional Systems and Nanostructures. *Phys. E.*, **2010**, *43*, 534–538.

52. Ahmed, Faruk.; Datta, J. Cation dependent charge transport in linear dicarboxylate based isotypical 1D coordination polymers. *RSC Adv.,* **2017**, *7*, 10369–10375.

53. Li, Y.-H.; Gong, X. G.; Wei, S.-H. Ab initio calculation of hydrostatic absolute deformation potential of semiconductors. *Appl. Phys. Lett.*, **2006**, *88*, 042104−042106.

54. Kato, R.; Kobayashi, H.; Kobayashi, A.; Mori, T.; Inokuchi, H. Preparation and structure of highly conductive anion radical salts, M (2, 5-R1, R2-DCNQI2)(DCNQI= N, N′-dicyanoquinonediimine; R1, R2= Me, MeO, halogen; M= Ag, Li, Na, K, NH4). *Synth. Met.,* **1988**, *27*, 263−268.

55. Li, Z.; Zhan, Z.; Hu, M. A luminescent terbium coordination polymer as a multifunctional water-stable sensor for detection of Pb^{2+} ions, PO$_4$$^{3−}$ ions, Cr$_2$ O$_7$$^{2−}$ ions, and some amino acids. *CrystEngComm*, **2020**, *22*,6727-6737.

56. Mir, M.H.; Bera, S.; Khan, S.; Maity, S.; Sinha, C.; Dutta, B. Sunlight assisted SCSC dimerization of a 1D coordination polymer impacts the selectivity of Pd (II) sensing in water. Chem. Commun., **2021**, *57*, 6197-6200.

57. Dutta, B.; Bera, S.; Bairy, G.; Shit, M.; Sinha, C.; Mir, M. H. Exploitation of a Series of Zn (II)-Coordination Polymers for Pd (II)-Detection in Aqueous Medium. *ES Energy & Environ.*, **2022**.

58. Sanda, S.; Parshamoni, S.; Biswas, S.; Konar, S. Highly selective detection of palladium and picric acid by a luminescent MOF: a dual functional fluorescent sensor. *Chem. Commun.*, **2015**, *51*, 6576-6579.

Chapter 5

Correlation in Structural Architecture towards Fabrication of Schottky Device with a Series of Pyrazine Appended Coordination Polymers
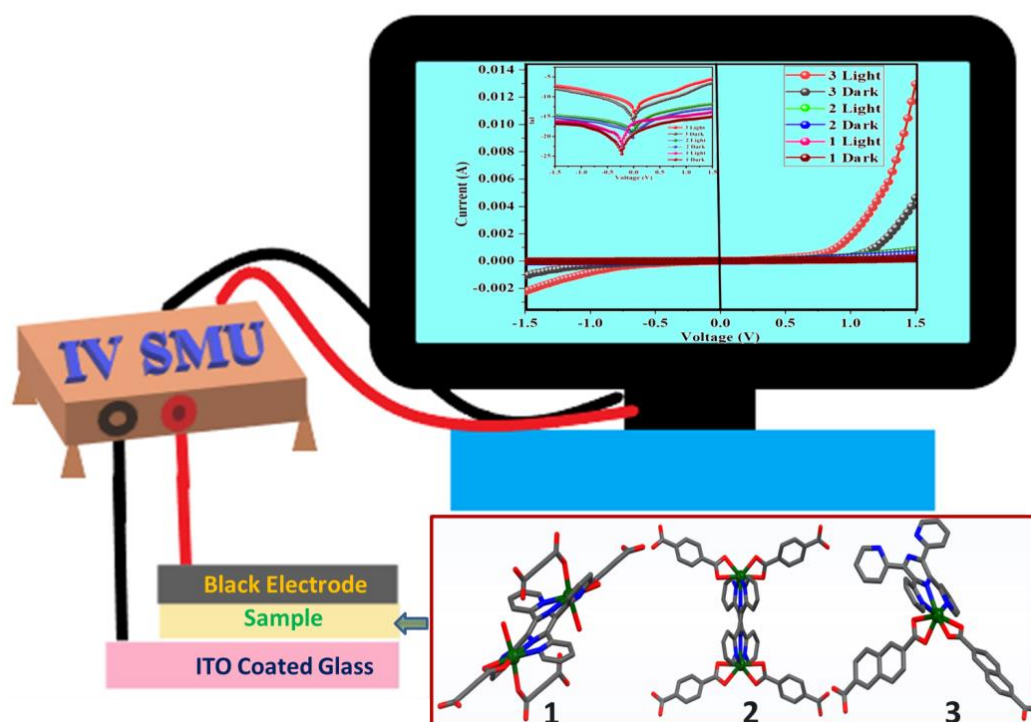
Chapter 5

Abstract

Energy is the centre of importance for the sustenance of the civilization. Use of fossil fuel is going to be suspended and renewable energy is technologically costlier. In quest of new energy sources and to minimise fuel expenditure, the design of energy efficient devices is of current solution. Towards this objective, a highly delocalised π-acidic N-hetreocycle pyrazine bridged CPs of Cd(II)-carboxylato derivatives, [Cd(tppz)(adc)(MeOH)] (**1**), [Cd(tppz)(trep)] (**2**) and [Cd(tppz)(2,6-ndc)] (**3**) (tppz = 2,3,5,6-Tetrakis(2-pyridyl)pyrazine) are synthesized in combination with dicarboxylato linkers (acetylene dicarboxylic acid (H_2adc), terephthalic acid (H_2trep) and 2,6 naphthalene dicarboxylic acid (2,6 H_2ndc)). The structures of the compounds, **1**-**3**, have been confirmed by the single crystal X-ray diffraction measurements. The 'CdN_3O_4' core is distorted pentagonal bipyramidal geometry and is self-assembled *via* $\pi\cdots\pi$ stacking, H-bonding and constructed supramolecular networks. Analysis of electrical property demonstrates that the conductivity follows the order **3** > **2** > **1**; the compound **3** shows the highest conductivity (1.93×10^{-3} (light), 1.12×10^{-4} S.m^{-1} (dark)) than **2** (1.10×10^{-4} (light), 1.80×10^{-4} S.m^{-1}(dark)) and **1** (5.06×10^{-5} (light), 4.72×10^{-5} S.m^{-1} (dark)). The trends of conductivities follow the order of the charge mobility through the coordination networks. Theoretical study (HOMO-LUMO energy gap) supports the experimental band gap (**3<2<1**) of CPs which guide the variation of conductivity.

5.1. Introduction

Coordination polymers (CPs) are unveiling outstanding deliverable properties (**Chapters 1-4**). A continuous effort has been entrusted to fabricate diverse materials of higher chemical, optical, magnetic and thermal stability to make them attractive for the researcher with valuable application potential. The coordination polymers (CPs)[1-14] have been attracted much for the multifunctional property and are potential for sustainable applications. These materials have been exploited in the field of gas storage and mixture separation,[15,16] electrical conductivity,[17-19] sensing,[20-23] water splitting,[24] variable temperature magnetism,[25] catalysis[26], ion exchange[27] etc. It is surprising that a diamagnetic metal knot bridged *via* non-conducting O-donor (Carboxylato) centres also exhibit conducting properties.[17,18] Many of the CP frameworks are showing great conductivity and fine-tunability through self-assembly and become a challenging material for the next generation electronic devices. The advancement of this research is very important issue regarding the increasing energy demand and environmental pollution towards sustainable development[28] and needs condensed holistic effort for developing energy harvesting supercapacitor and superconductor. The tuning of the structure and electrical conductivity with the choice of metal knot, bridge building groups and experimental program (solvents, reaction condition etc.) to extensive application in environmental responsive technologies, such as batteries, molecular wires, sensors and photovoltaics is of utmost important.

Mainly 'N' (pyridyl or other N-heterocycles), 'O' (Dicarboxylates), halides/ pseudohalides donor ligands are used to fabricate the bridging ligands to architect the CPs.[29-31] Naphthalene dicarboxylate is more conjugated than the alkyne/alkene/phenyl dicarboxylates and has been used to design the CPs those respond smartly to external stimuli.[32] The properties of CPs depend on the electronic and steric effect of organic/inorganic nature of linkers and electronic

configuration, periodic position of the metal knot.[33] Most of the CP's act as insulator or low conducting due to insulating nature of carbon atom enriched linker and weak interaction between linker π–orbitals and metal dπ-symmetric functions. The CPs constituted by metal ions with d^{10} electronic configuration (Zn^{2+}, Cd^{2+}) and carboxylate-O linkers exhibit semiconducting property[34-36] and have smart application in the electronic devices. Cd^{2+} (4d series) is more delocalisable than Zn^{2+} (3d series) and demonstrates better conducting CPs.[32,33] The semiconductivity of the CPs has been capitalized to design Schottky barrier diodes (SBD) by depositing on conducting surface for fast switching speed and low forward voltage drop.

In this situation, suitably constructed crystalline CPs in presence of electrically conducting surface are playing beneficial role for the material science. Our group has reported few Zn[37-39]/Cd-based[40-42] CPs with electrical conductivity. Herein, we focus attention on the synthesis of three pyrazine based Cd(II)-CPs (**1-3**) with organic bridging ligands from three different dicarboxylates such as, acetylene dicarboxylic acid (H_2adc, **1**), terephthalic acid (H_2trep, **2**) and 2,6 naphthalene dicarboxylic acid (2,6 H_2ndc, **3**). The structural motifs are assembled via $\pi\cdots\pi$ and H-bondings and exhibit appreciably high electrical conductivity. Out of three CPs, **3** has been shown highest electrical conductivity (1.93×10^{-3} (light), 1.12×10^{-4} S.m^{-1} (dark)) than **2** (1.10×10^{-4} (light), 1.80×10^{-4} S.m^{-1}(dark)) and **1** (5.06×10^{-5} (light), 4.72×10^{-5} S.m^{-1} (dark)) which may be due to better π conjugation in ndc^{2-}. For higher conjugation, the band gap decreases and has been calculated from the DFT computation. Experimental band gap (Tauc's plot) is nearly matched with the theoretically calculated energy difference of HOMO and LUMO levels which has been supported by the electrical conductivity measured from the optical devices fabricated using the compounds (**1**, **2** and **3**).

5.2. Experimental Section

5.2.1. Synthesis and formulation
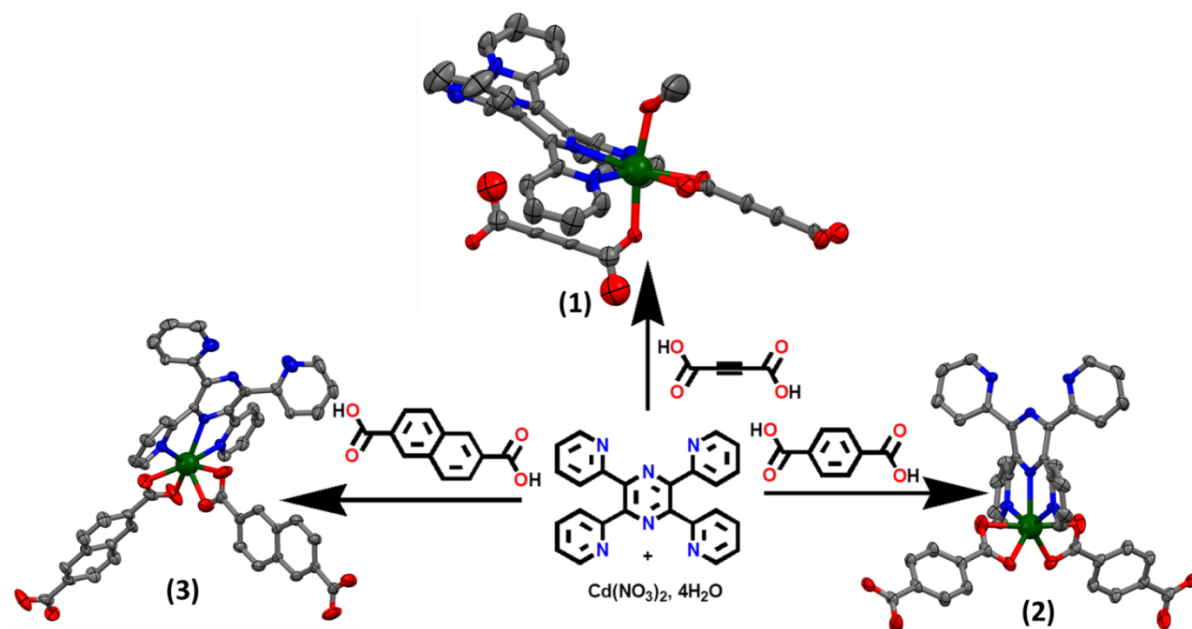
Scheme 5.1. Synthesis of **1**,**2** and **3** using $Cd(NO_3)_2.4H_2O$, tppz and corresponding acid.

A model synthesis is detailed below (**Scheme 5.1**) for the compound **1**. To aqueous solution (2 mL) of $Cd(NO_3)_2.4H_2O$ (0.06 g, 0.2 mmol) water-methanol solution (1:1 v/v; 2 mL) was added slowly to make a buffer layer followed by the slow covering with methanol solution (2 mL) of tppz (0.0194 g, 0.05 mmol) carefully. To this unstirred solution, H_2adc (0.023 g, 0.2 mmol) in ethanol solution (2 mL) neutralized by Et_3N (0.042 g, 0.4 mmol) was added gradually. Finally, colourless block shaped crystals were obtained within 5 days (Yield: 0.76 mg, 68%). Elemental analysis (%): calculated for **1**: C, 43.91; H, 2.53; N, 9.60. Found: C, 43.83; H, 2.45; N, 9.54. IR, $\overline{\nu}$ (cm^{-1}): 3209, ν(-OH); 2918, ν(-CH); 1583, ν_{asy}(-COOH); 1536, ν_{sys}(COO); 1370, ν (-OH bending). (**Figure 5.1a**). Other two compounds **2** and **3** were also followed same synthesized route using H_2trep and 2,6 H_2ndc, respectively. Colourless crystal **2** (yield: 0.78 mg, 57%) and **3** (yield: 1.16 mg, 63%) were obtained within a week. Elemental analysis (%): calculated for **2**: C, 47.16; H, 2.96; N, 7.86. Found: C, 47.08; H, 3.01; N, 7.79. IR $\overline{\nu}$(cm^{-1}) : 3441, ν(-OH);

1660, ν_{asy}(-COO); 1546, ν_{sys}(COO); 1370, ν(-OH bending). (**Figure 5.1b**). Elemental analysis (%): calculated for **3**: C, 60.47; H, 3.10; N, 11.75. Found: C, 60.34; H, 3.04; N, 11.67. IR $\bar{\nu}$ (cm^{-1}) : 3242, ν(-OH); 1659, ν_{asy}(-COO); 1597, ν_{sys}(COO); 1387, ν(-OH bending). (**Figure 5.1c**).
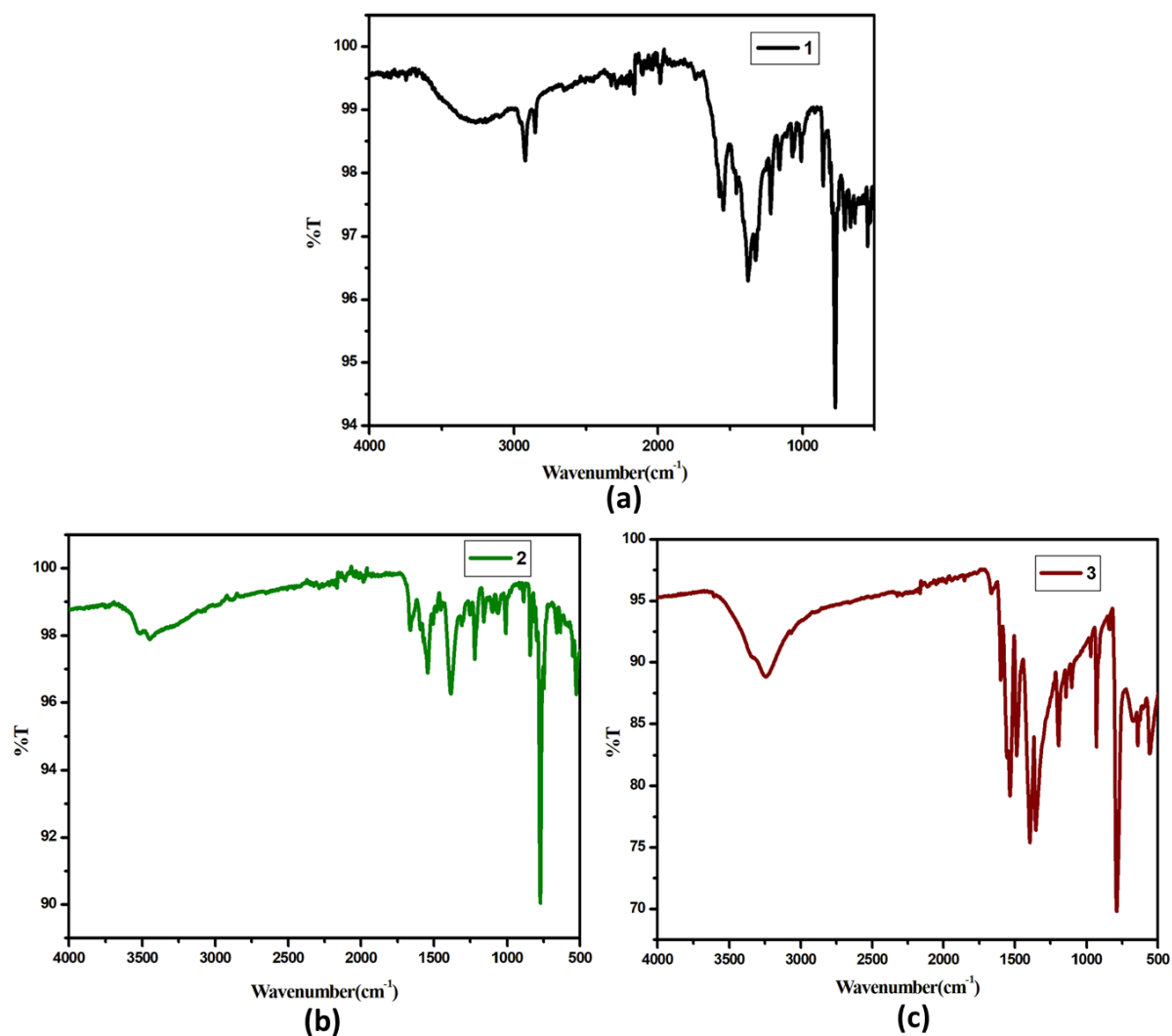
Figure 5.1. IR spectra of compounds **1(a)**, **2(b)** and **3(c)**.

Phase purity of the compounds was examined by comparing the Powder X-Ray Diffraction (PXRD) profile with the as-synthesized simulated pattern of the compounds (**1**, **2** and **3**). The spectra are well matched with the simulated pattern (**Figure 5.2**). Thermal stability of the compounds was observed by the Thermogravimetric analysis (TGA). The
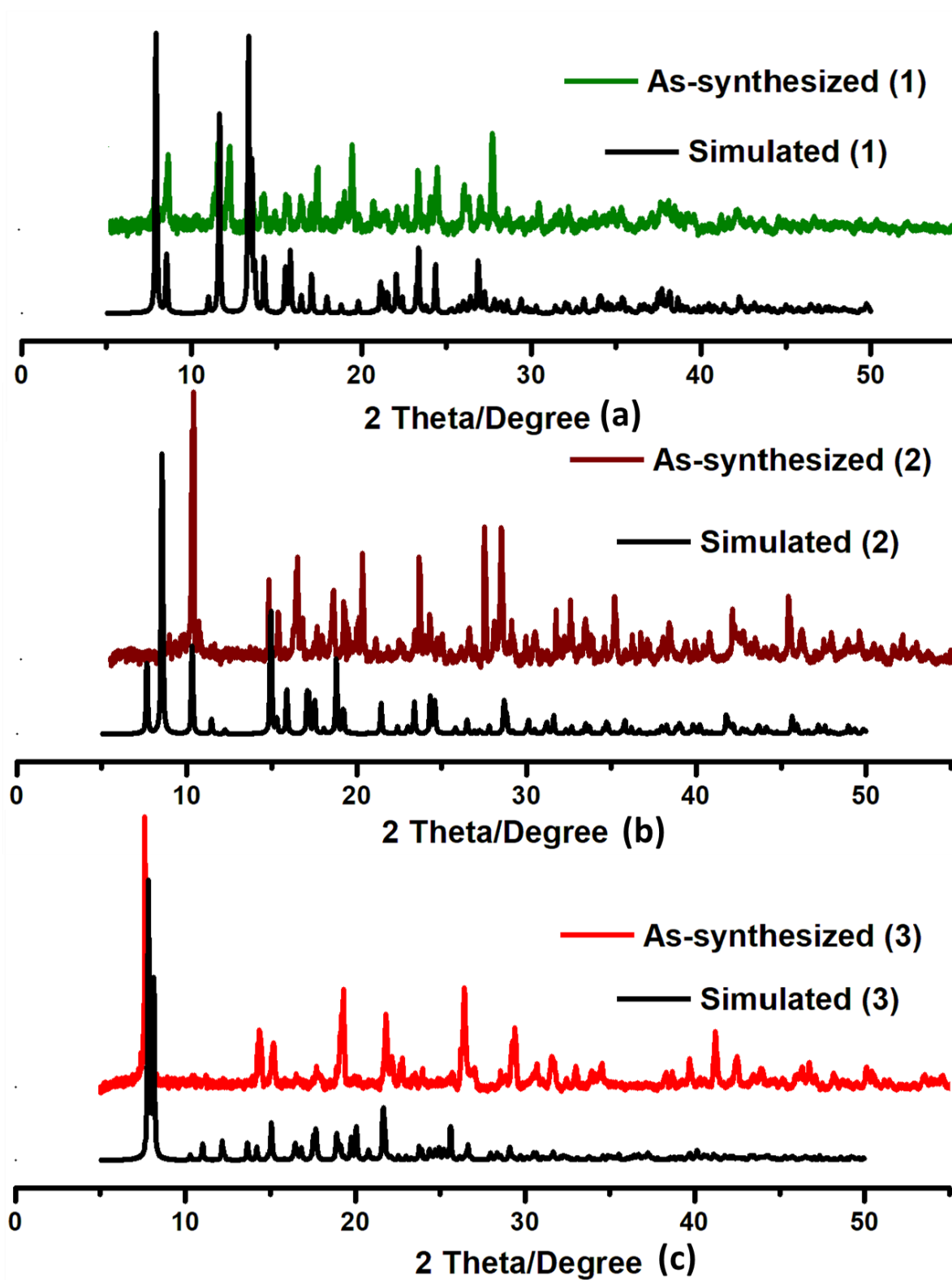
Figure 5.2. Powder X-ray diffraction pattern of **1**, **2** and **3**.

results of the TGA exhibited that compounds **1**, **2** and **3** stable upto nearly 267°, 391° and 423° C, respectively, *i.e* stability order of the CPs is **3**>**2**>**1** (**Figure 5.3**).
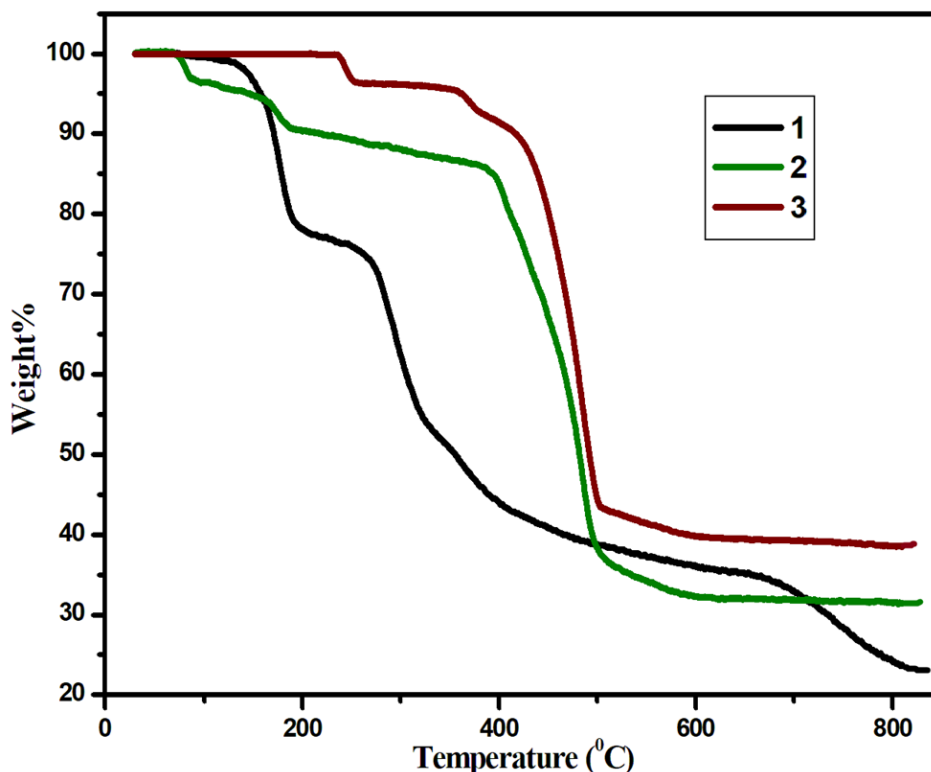
Figure 5.3. Thermogravimetric Analyses Curves of compounds **1**, **2** and **3**.

5.2.2. Materials and Physical Measurements

All the chemicals (H_2adc, H_2trep, 2,6 H_2NDC, tppz, and $Cd(NO_3)_2$, $4H_2O$) and solvent were purchased from commercial sources (Sigma, TCI, Merck) and used for experiments without further purification. Elemental analyser Perkin-Elmer 240C was used for the microelement analyses (C, H, N). Infrared (IR) spectrum was recorded using a Perkin Elmer SPECTRUM II LITA FT-IR spectrometer. Bruker D8 Advance X-ray diffractometer was used to collect the powder X-ray diffraction (PXRD) data, using Cu Kα radiation source having wavelength of 1.548 Å at the room temperature. Thermogravimetric analysis at the temperature range 30-850 °C were done using the PerkinElmer TGA 4000 System with heating rate 10°C/min under the N_2 atmosphere. Lambda 25 spectrophotometer was used for UV−vis spectra. Gaussian 09

software used to optimize the CPs motif and determined the band gap. B3LYP strategy and LAN2DZ basis set was applied for optimization. Herein, GAUSSSUM used to calculate the fractional distribution of metal and different ligands. Crystal explorer 3.1 version software was used to evaluate the Hirshfeld surface and 2D fingerprint plots using the CIF as an input file. Presence of different interaction in compounds was evaluated using this software.

5.2.3. Structure determination by X-Ray

Cd-coordination polymers **1**, **2** and **3** ware characterised using singe crystal X-Ray diffraction with suitable dimension. Bruker APEX-II CCD diffractometer equipped with graphite-monochromatized Mo-Kα radiation (λ = 0.71073 Å) was used. Single crystal structure was evaluated with the helped of SHELX-97.[43] Crystal orientation matrices and unit cell parameter were evaluated for the CPs by least square refinements of all reflection within the hkl range -10 $\leq$ h $\leq$ 10, -13 $\leq$ k $\leq$ 12, -14 $\leq$ l $\leq$ 13 (**1**); -13 $\leq$ h $\leq$ 13, -26 $\leq$ k $\leq$ 26, -29 $\leq$ l $\leq$ 29 (**2**); -14 $\leq$ h $\leq$ 14, -16 $\leq$ k $\leq$ 16, -16 $\leq$ l $\leq$ 16 (**3**). For cell refinement, indexing and scaling of data set were done by the Bruker Smart Apex and Bruker Saint packages.[44,45] Crystal structure was solved with the help of direct method and subsequent Fourier analyses. Non hydrogen atoms were refined using anisotropic thermal parameters. All the hydrogen atoms were located in their exact geometrical position. All the data and molecular pictures are evaluated using the WinGX System, Mercury 3.10.3 and Discovery Studio 2017R2. Crystallographic data of **1, 2** and **3** is concise in **Table 5.1**, respectively. Selected bond lengths and bond angle are prescribed in **Table 5.2** (**1**), **Table 5.3** (**2**) and **Table 5.4** (**3**).

Table 5.1. Crystal data of **1**, **2** and **3**

Compound	1	2	3
Formula	$C_{17}H_{11}CdN_3O_5$	$C_{20}H_{12}CdN_3O_4$	$C_{74}H_{47}Cd_2N_{12}O_9$
Formula Weight	449.69	470.73	1473.06
Crystal System	Triclinic	Orthorhombic	Triclinic
Space group	P-1	Ccca	P-1
a[Å]	8.0423(18)	10.3257(8)	11.4086(9)
b[Å]	10.441(2)	20.751(2)	12.7091(10)
c [Å]	11.159(3)	23.1700(17)	12.9609(11)
Alpha [°]	89.872(6)	90.00,	60.921(2)
beta [°]	88.659(6)	90.00	83.658(2)
gamma [°]	86.687(6)	90.00	78.909(2)
V[Å³]	935.1(4)	4964.6(7)	1611.4(2)
Z	2	8	1
D(calc) [g/cm³]	1.597	1.260	1.518
Mu(MoKa) [/mm]	1.198	0.903	0.730
F(000)	444	1864.0	743
Temperature (K)	273(2)	273	273(2)
Radiation [Å]	0.71073	0.71073	0.71073
Observed data [I > 2.0 sigma(I)]	3229	2368	5145
R	0.1390	0.0356	0.0446
wR2	0.3469	0.1006	0.1229
S	1.104	1.102	1.127

Table 5.2. Selected bond length (Å) and bond angels (°) of **1**.

Bond length (Å)			
Cd1 - O3	2.301(13)	Cd1 - N2	2.405(12)
Cd1 - O5	2.336(14)	Cd1 - N1	2.408(15)
Cd1 - O2	2.373(12)	Cd1 - O1	2.440(14)
Cd1 - N3	2.391(17)		

Bond angels (°)			
O3 - Cd1 - O5	170.1(5)	N2 - Cd1 - N1	68.4(4)
O3 - Cd1 - O2	81.4(5)	O3 - Cd1 - O1	83.1(5)
O5 - Cd1 - O2	89.7(5)	O5 - Cd1 - O1	88.1(5)
O3 - Cd1 - N3	93.1(7)	O2 - Cd1 - O1	54.1(5)
O5 - Cd1 - N3	90.6(6)	N3 - Cd1 - O1	139.5(5)
O2 - Cd1 - N3	85.5(5)	N2 - Cd1 - O1	150.8(5)
O3 - Cd1 - N2	105.6(4)	N1 - Cd1 - O1	84.6(5)
O5 - Cd1 - N2	84.3(4)	O3 - Cd1 - C16	81.2(5)
O2 - Cd1 - N2	153.6(4)	O5 - Cd1 - C16	88.9(5)
N3 - Cd1 - N2	68.9(5)	O2 - Cd1 - C16	27.1(5)
O3 - Cd1 - N1	86.8(6)	N3 - Cd1 - C16	112.6(6)
O5 - Cd1 - N1	97.0(7)	N2 - Cd1 - C16	173.1(5)
O2 - Cd1 - N1	138.0(5)	N1 - Cd1 - C16	111.3(5)
N3 - Cd1 - N1	135.5(6)	O1 - Cd1 - C16	26.9(5)

Table 5.3. Selected bond length (Å) and bond angels (°) of **2**.

Bond length (Å)			
Cd(1) - N(7)	2.396(2)	Cd(1) - O(2)	2.376(3)
Cd(1) - N(8)	2.397(3)	Cd(1) - O(1)	2.335(2)
Cd(1) - O(1)a	2.335(2)	Cd(1) - O(2)a	2.376(3)
Cd(1) - N(7)a	2.396(2)		

Bond angels (°)			
O(1) - Cd(1) - O(2)	55.00(10)	O(1) - Cd(1) - N(7)	125.41(10)
O(1) - Cd(1) - N(8)	134.72(6)	O(1) - Cd(1) - C(1)	27.38(9)
O(1) - Cd(1) - O(1)a	90.56(8)	O(1) - Cd(1) - O(2)a	128.62(10)
O(1) - Cd(1) - N(7)a	86.53(9)	O(1) - Cd(1) - C(1)a	110.90(10)
O(2) - Cd(1) - N(7)	85.96(11)	O(2) - Cd(1) - N(8)	87.94(7)
O(2) - Cd(1) - C(1)	27.62(11)	O(2) - Cd(1) - O(1)a	128.62(10)
O(2) - Cd(1) - O(2)a	175.89(11)	O(2) - Cd(1) - N(7)a	92.52(11)
O(2) - Cd(1) - C(1)a	155.94(11)	N(7) - Cd(1) - N(8)	68.36(6)
N(7) - Cd(1) - C(1)	106.82(9)	N(7) - Cd(1) - O(1)a	86.53(9)
N(7) - Cd(1) - O(2)a	92.52(11)	N(7) - Cd(1) - N(7)a	136.73(8)
N(7) - Cd(1) - C(1)a	89.37(9)	N(8) - Cd(1) - C(1)	112.18(8)
N(8) - Cd(1) - O(1)a	134.72(6)	N(8) - Cd(1) - O(2)a	87.94(7)
N(8) - Cd(1) - N(7)a	68.36(6)	N(8) - Cd(1) - C(1)a	112.18(8)
C(1) - Cd(1) - O(1)a	110.90(10)	C(1) - Cd(1) - O(2)a	155.94(11)
C(1) - Cd(1) - N(7)a	89.37(9)	C(1) - Cd(1) - C(1)a	135.65(11)
O(1)a - Cd(1) - O(2)a	55.00(10)	O(1)a - Cd(1) - N(7)a	125.41(10)
O(1)a - Cd(1) - C(1)a	27.38(9)	O(2)a - Cd(1) - N(7)a	85.96(11)
O(2)a - Cd(1) - C(1)a	27.62(11)	N(7)a - Cd(1) - C(1)a	106.82(9)

Table 5.4. bond length and bond angel of **3**.

Bond length (Å)			
Cd(1) - O(3)	2.667(7)	Cd(1) - O(4)	2.241(4)
Cd(1) - O(5)	2.561(4)	Cd(1) - O(6)	2.254(3)
Cd(1) - N(7)	2.393(4)	Cd(1) - N(8)	2.405(3)
Cd(1) - N(9)	2.346(4)	Cd(1) - C(37)	2.757(4)

Bond angels (°)			
O(3) - Cd(1) - O(4)	51.2(2)	O(3) - Cd(1) - N(7)	134.74(19)
O(3) - Cd(1) - C(37)	106.6(2)	O(4) - Cd(1) - N(7)	83.51(19)
O(4) - Cd(1) - C(37)	118.4(2)	O(5) - Cd(1) - N(8)	72.00(18)
O(6) - Cd(1) - N(7)	106.36(18)	O(6) - Cd(1) - C(37)	26.4(2)
N(7) - Cd(1) - C(37)	92.99(17)	N(9) - Cd(1) - C(37)	101.00(17)
Cd(1) - O(5) - C(37)	85.7(5)	Cd(1) - N(7) - C(30)	117.7(4)
Cd(1) - N(8) - C(25)	120.1(3)	O(3) - Cd(1) - O(5)	131.5(2)
O(3) - Cd(1) - N(8)	144.32(17)	O(4) - Cd(1) - O(5)	137.3(2)
O(4) - Cd(1) - N(8)	134.59(18)	O(5) - Cd(1) - O(6)	52.7(2)
O(5) - Cd(1) - N(9)	95.04(18)	O(6) - Cd(1) - N(8)	123.96(19)
N(7) - Cd(1) - N(8)	67.38(16)	N(8) - Cd(1) - N(9)	68.49(17)
Cd(1) - O(3) - C(12)	82.1(5)	Cd(1) - O(6) - C(37)	99.9(4)
O(3) - Cd(1) - O(6)	81.2(2)	O(3) - Cd(1) - N(9)	81.47(19)
O(4) - Cd(1) - O(6)	96.7(2)	O(4) - Cd(1) - N(9)	123.9(2)
O(5) - Cd(1) - N(7)	79.23(18)	O(5) - Cd(1) - C(37)	26.3(2)
O(6) - Cd(1) - N(9)	104.74(18)	N(7) - Cd(1) - N(9)	135.06(17)
N(8) - Cd(1) - C(37)	97.94(18)	Cd(1) - O(4) - C(12)	102.8(5)

5.2.4. Device Fabrication

The Schottky devices of the compounds were developed in a sandwich-like ITO/**1**, **2**, and/or **3**/Al arrangement. In an ultrasonic bath, acetone, soap solution, distilled water and ethanol were used to clean indium tin oxide (ITO) covered glass substrates. To create a stable dispersion, the substance was disseminated in DMSO medium and ultrasonicated. The material was then created as a thin film on the ITO coated glass using the spin-coating process at 1000 rpm for 60 seconds and then dried. Surface profiler was used to determine the thicknesses of the developed films (5 μm). Metal semiconductor (MS) junction was architected using Al as a

rectifier metal contact and located on the films using a thermal evaporation process. A shadow mask kept the effective diode area constant at 3×3 mm^2. The current was recorded at the corresponding applied bias voltage progressively within the range of ± 1.5 V to investigate the electrical attributes.

5.3. Results and Discussion

5.3.1. Structure determination

The compound **1** is crystallized in the triclinic system with space group P-1 and Z=2. The molecular unit consists of distorted pentagonal bipyramid about the Cd(II) centre having CdN$_3$O$_4$ sphere (**Figure 5.4**). The coordination zone is constituted by three pyridyl-Ns from tppz, chelation of carboxylate-O, O of one adc^{2-} and monodentate carboxylate-O of another adc^{2-} linker and a coordinated MeOH. The bond lengths Cd1 - O3, 2.301(13); Cd1 - O5, 2.336(14); Cd1 - O2, 2.373(12); Cd1 - N3, 2.391(17) Å. Cd1 - N2, 2.405(12); Cd1 - N1, 2.408(15); Cd1 - O1, 2.440(14) Å, and chelate angle O2 - Cd1 - O1, 54.1(5) and other angles (°)O3 - Cd1 - O5, 170.1(5); N2 - Cd1 - N1, 68.4(4); N3 - Cd1 - N2, 68.9(5) (**Table 5.2**) lie within reported limit.[46-48] Two bridging ligands (tppz and adc^{2-}) are mutually orthogonal to form
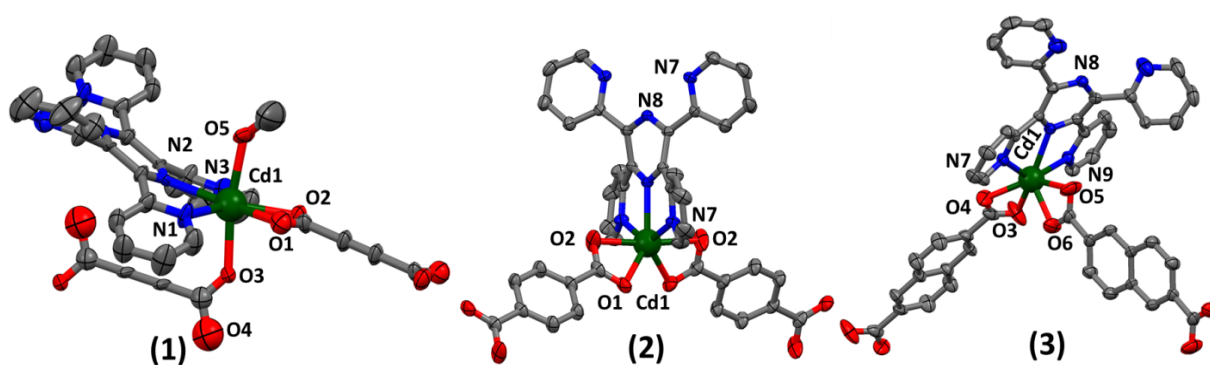

Figure 5.4. Coordination unit of CdN$_3$O$_4$ sphere of [Cd(tppz)(adc)(MeOH)] (**1**), [Cd(tppz)(trep)] (**2**) and [Cd(tppz)(2,6-ndc)] (**3**)

2D network (**Figure 5.5a**) and constitute 3-nodal net and the point symbol is {0}2{12^3}2{12}3 (**Figure 5.5b**). The noncovalent interactions ($\pi\cdots\pi$ interaction, 5.126 Å) in **1** makes supramolecular assemble (**Figure 5.6**) to form 3D network (**Figure 5.7**).

The compound **2** crystallizes in orthorhombic system with Ccca space group and Z=8 and **3** is crystallized in triclinic system and the space group is $\overline{P}1$ and Z=2. These two compounds are isostructural with **1** and bear CdN_3O_4 coordination environment having pentagonal bipyramidal geometry about Cd(II). The coordination is satisfied by the three tppz-Ns and four carboxylate-'O' of two different $trep^{2-}/ndc^{2-}$ moiety. The bond parameters are comparable with **1**. The bond lengths about coordination zone are Cd(1) - O(2), 2.376(3); Cd(1) - N(7), 2.396(2); Cd(1) - N(8), 2.397(3); Cd(1) - N(7)a, 2.396(2); Cd(1) - O(1), 2.335(2); Cd(1) - O(1)a, 2.335(2); Cd(1) - O(2)a, 2.376(3) Å, and bond angles (°) are O(1) - Cd(1) - O(2), 55.00(10); O(1)a - Cd(1) - O(2)a, 55.00(10); N(7) - Cd(1) - N(8), 68.36(6); N(8) - Cd(1) - N(7)a, 68.36(6) for compound **2** (**Table 5.3**). In compound **3** the bond lengths are Cd(1) - O(3), 2.667(7); Cd(1) - N(7), 2.393(5); Cd(1) - N(8), 2.404(5); Cd(1) - N(9), 2.344(5); Cd(1) - O(4), 2.243(6); Cd(1) - O(5), 2.560(7); Cd(1) - O(6) 2.251(5) Å and bond angles are O(3) - Cd(1) - O(4), 51.2(2); O(3) - Cd(1) - O(4), 51.2(2); O(5) - Cd(1) - O(6), 52.7(2); N(7) - Cd(1) - N(8), 67.38(16); N(8) - Cd(1) - N(9), 68.49(17)° (**Table 5.4**). The 2D network of **2** is extended to 3D supramolecule *via* $\pi\cdots\pi$ interaction (4.317 Å**, Figure 5.5c,** (**Figure 5.6, Table 5.5**) with 2-nodal net and point symbol for net is {12^3}2{12}3 (**Figure 5.5d**). Similarly, the compound **3** (**Figure 5.5e**) with 3-nodal net constitutes the point symbol {0}(**Figure 5.5f**). This 1D chain of **3** has been assembled by the $\pi\cdots\pi$ stacking (4.142 Å**, Figure 5.6, Figure 5.7**).
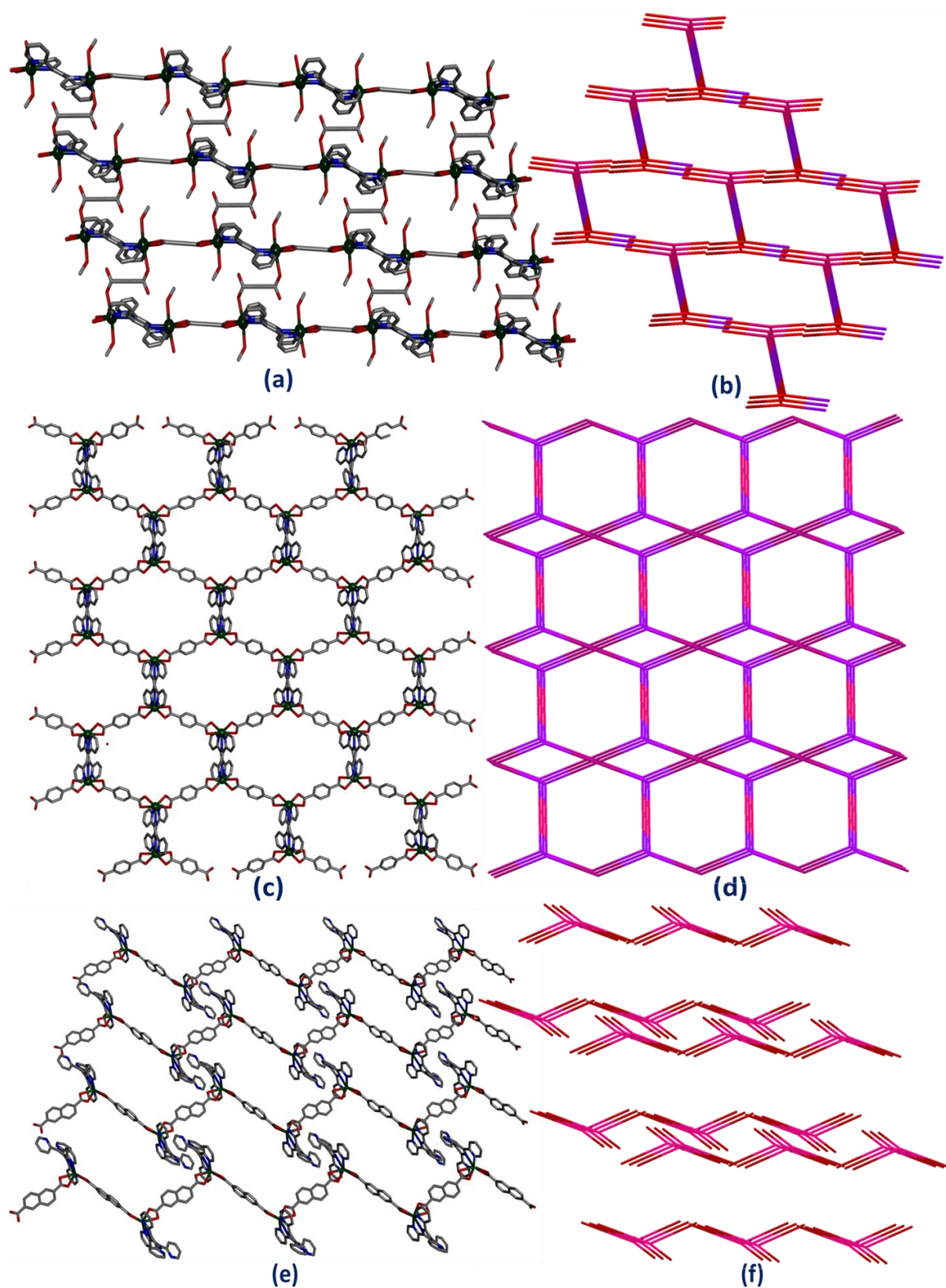
Figure 5.5. View of 2D network with a tropology of (a, b) **1**, (c, d) **2** and (e, f) **3**.

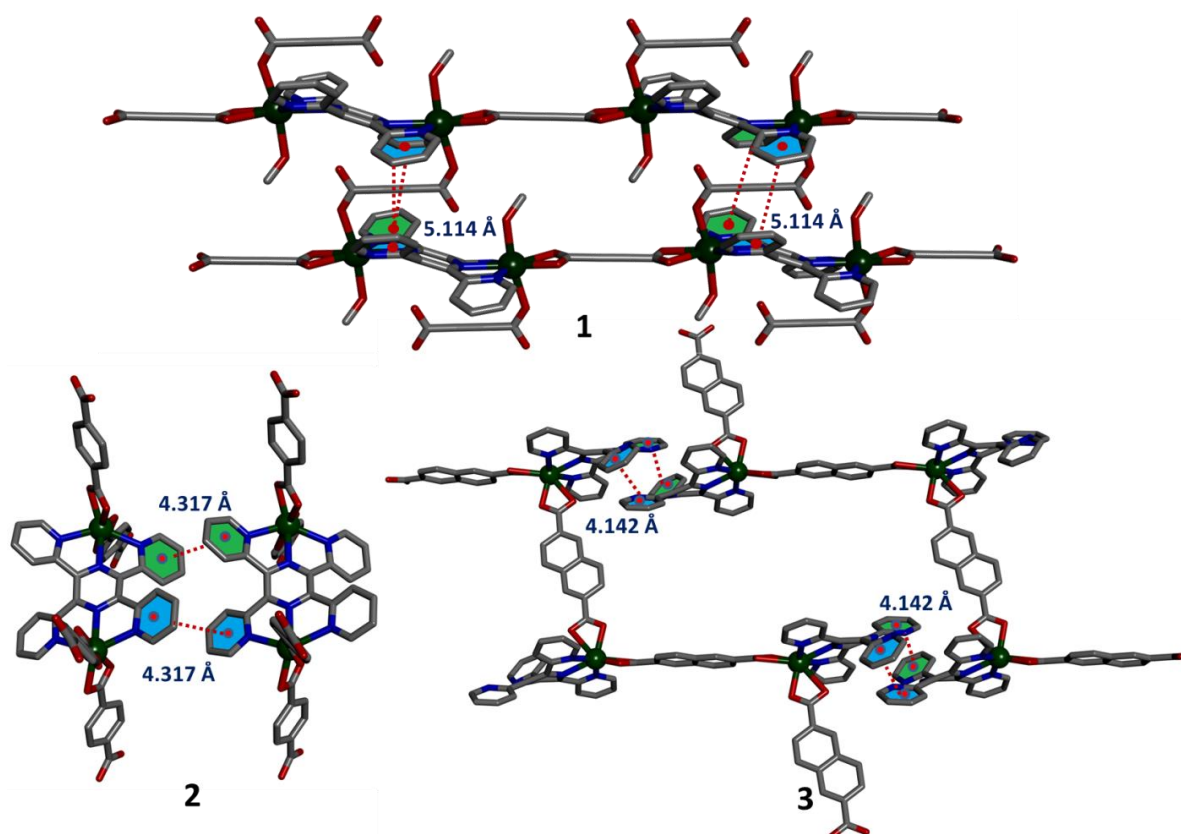**Figure 5.6.** π···π interaction of **1** (5.126 Å), **2** (4.317 Å) and **3** (4.142 Å).
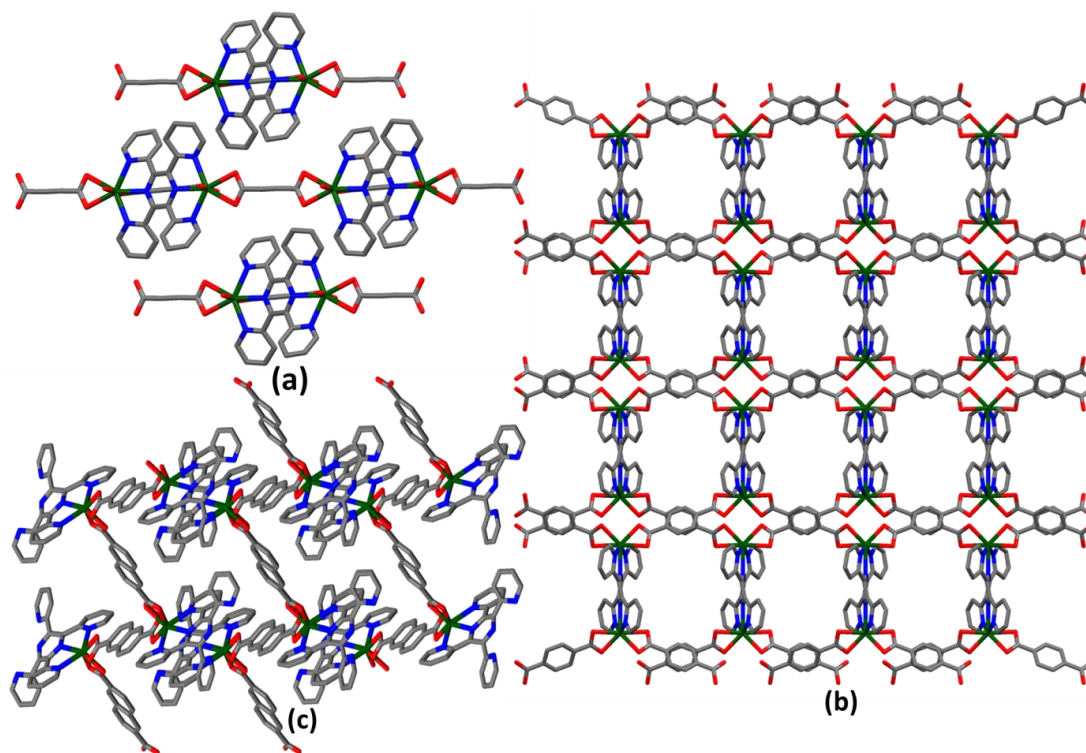

Figure 5.7. (a) Supramolecular assemble of **1** along a axis, **(b) 2** along the b axis and **(c)** along the a axis **3**.

Table 5.5. Presence of π…π interaction in the **1**, **2** and **3**.

π…π interaction (**1**)		
Ring(i) → Ring(j)	Distance between the (i, j) ring centroids (Å) in the crystal	[ARU(j)]
R(1) → R(3)	5.114(14)	[2666.01]
R(3) → R(1)	5.035(14)	[2566.01]
R(3) → R(3)	5.141(15)	[2556.01]
π…π interaction (**2**)		
R(1) → R(1)	4.31(18)	[2555.01]
R(2) → R(2)	5.16(19)	[10565.01]
R(1) → R(2)	5.71(2)	[9445.01]
π…π interaction (**3**)		
R(1) → R(3)	4.14(3)	[2666.01]
R(4) → R(5)	4.15(3)	[2676.01]
R(4) → R(8)	4.23(3)	[2675.01]
R(6) → R(1)	4.48(3)	[1545.01]

5.3.2. Hirshfeld surface analysis

In the Hirshfeld isosurface two different type of distance d_i and d_e are present, where d_i has denoted the distance between the surface and the nearest nucleus internal to the surface, whereas d_e define as a just opposite to the d_i, i.e the distance between the surface and nearest nucleus external to the surface. The normalized contact distance (d_{norm}) following the equation

$$d_{norm} = \{(d_i - r_i^{vdW})/r_i^{vdW}\} + \{(d_e - r_e^{vdW})/r_e^{vdW}\}$$

r_i^{vdW} and r_e^{vdW} denoted as the van der waal radii[49] of the atoms. Hirshfeld surface of the compound mapped completed with the d_{norm}, shape index and curvedness. Intermolecular
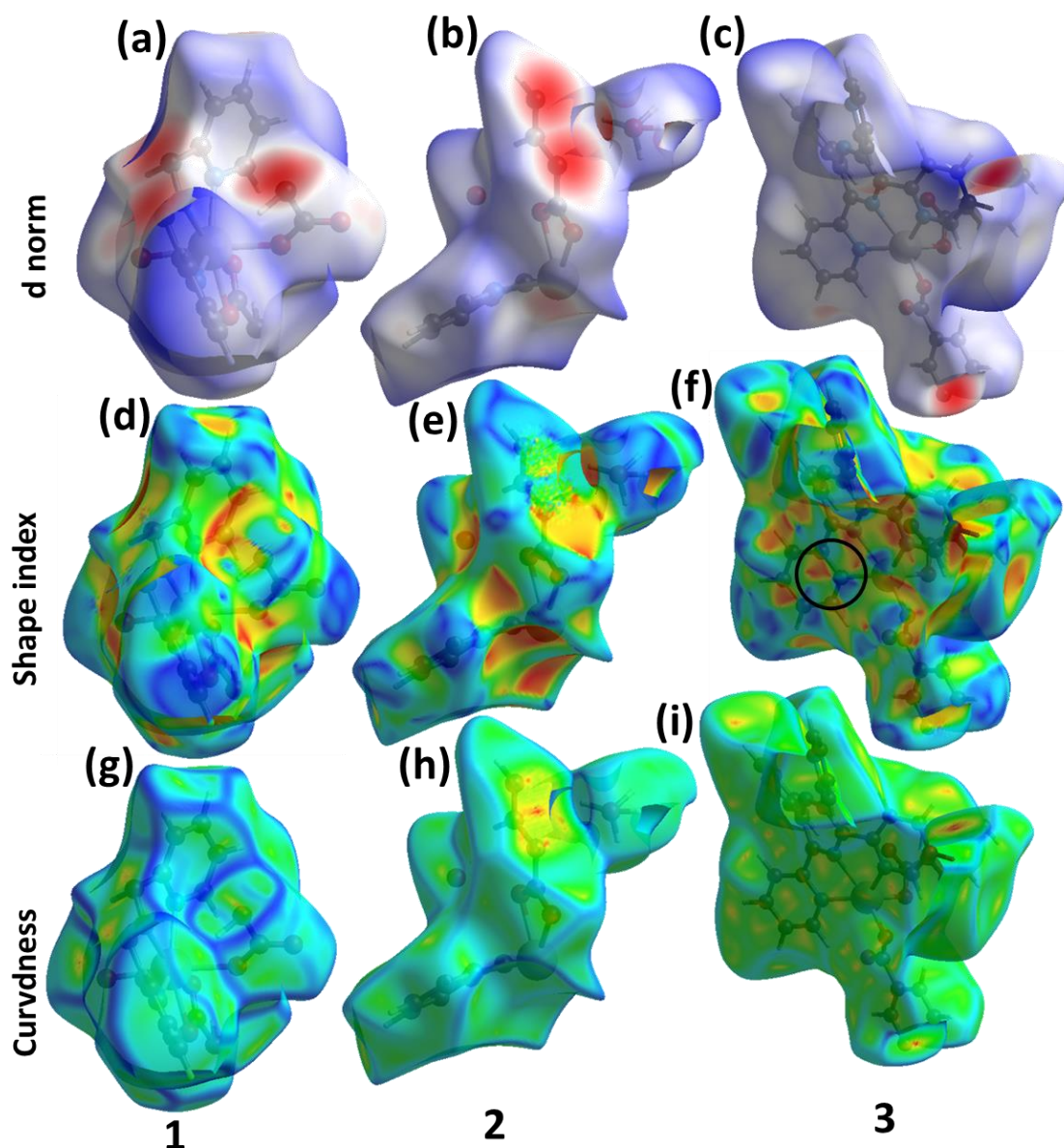
Figure 5.8. Hirshfeld surface mapped with **(a-c)** d norm **(d-f)** shape index **(g-i)** curvedness of **1**, **2** and **3**.

contact are longer than, shorter than or equal to van der waals separations depends on the d_{norm} values, may be positive, negative and equal, respectively. The value of d_{norm} at the different point is variant which denote by the different colour (red, blue and white). Herein, red colour spot assigned the shorter contact, blue was lacking of short contact and white spot region denoted the contact equivalent to the van der waal separation (**Figure 5.8**). Shape index of the

hirshfeld surface used to identify complementary hollow (red) and bumps (blue) and two molecular surfaces touch one another. The shape index has formed combination of two shape and the properties depends on the two shape. If the change in the sign its changes to the complementary pairs. Hirshfeld surface gives the information about the possibility of the different intermolecular interaction in crystal system. Herein, local morphology of the surface was represented by the shape Index using the different colours (red and blue). Hirshfeld surface (HS) analyses of the compounds were mapped by calculating the d_{norm}, shape index and curvedness to support noncovalent interactions. Colour code defines the intermolecular contacts relative to Van der Waals separation, such as, red spot is assigned to the shorter contact, blue color corresponds to the short contact and white spot region denotes the contact equivalent to the Van der Waal's separation (**Figure 5.8**). The interactions involve C-H/H-C, N-H/H-N, O-H/H-O and H-H/H-H combination pattern in the 2D finger print region (**Figure 5.9**). Local morphology determines the shape indices using red and blue colours. Symmetrically presence of blue and red triangle in the compound **3** indicates the presence of $\pi\cdot\cdot\pi$ interaction which is denoted by black circle (**Figure 5.8f**).
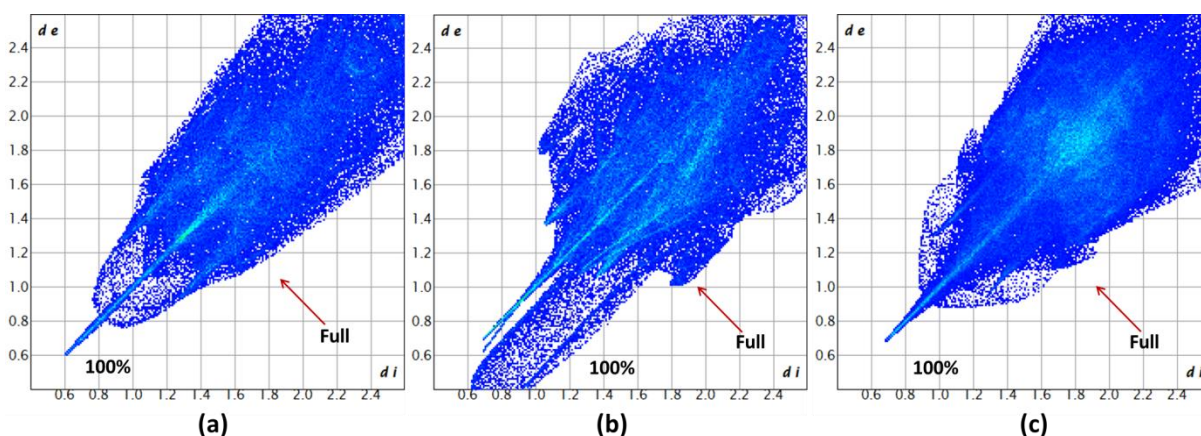

Figure 5.9. 2D fingerprint plot full of compounds **1(a)**, **2(b)** and **3(c)**.

Blue triangle interprets the convex region due to the C-atoms in the naphthalene ring of the molecule inside the surface and red triangle represents the concave region due to the π-stacked

outside it. Root means square curvature of the surface was evaluated from the curvedness. Relatively flat green region of the map was separated by the dark blue edges.

Presence of π··π interaction in the molecules was characterised by the flat region of the curvedeness.[50] Compound **3** has the greater number of red and blue spots in Shape index and flatter green region in curvedness than the others (**2**, **3**) which may be the region of the highest conjugation of π electron density and therefore, the cause of high electrical conductivity.

The surface morphology of the compounds has been investigated by FESEM micrographs (**Figure 5.10**). These types of microstructures of the polymeric CPs are very much helpful to exhibit shape and sizes; in this case, the characterization of MS junction is carried out to fabricate the Schottky diodes. The images revealed that the particles of **1** and **2** are block shaped and for compound **3** is square shaped. These shapes normally offer higher surface area and conveyed to higher contact area and resulted efficient charge transportation as well as higher electrical conduction. This has motivated us to undertake fabrication of devices for the electrical conductivity measurement of these compounds.
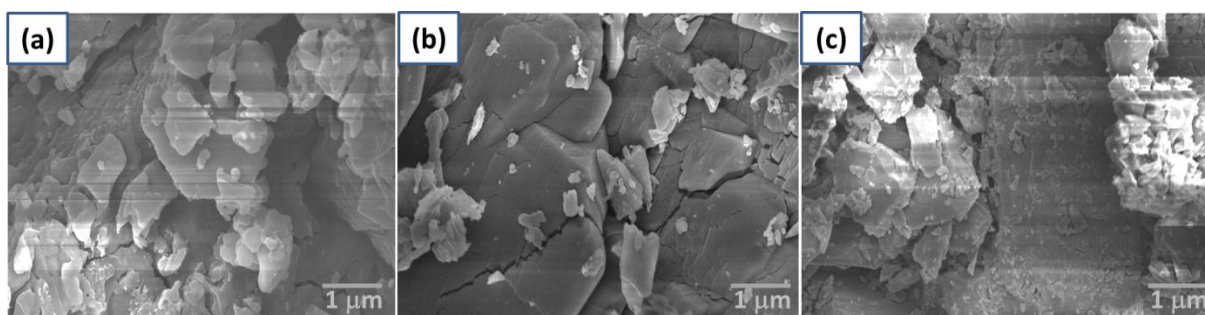

Figure 5.10. FESEM image of compounds (a) **1**, (b) **2** and (c) **3** at range 1μm.

5.3.3. Electrical characterisation

The absorption spectra (200-600 nm) of thin films deposited on the ITO plates of compounds (**1**, **2**, and **3**) by spin coating of the dispersed solution in DMSO (insets, **Figure 5.11**) were used

to calculate optical band gap (3.35 eV (**1**), 3.34 eV (**2**), 3.22 eV (**3**)) by using Tauc's plot following the equation (**Eq. 5.1**).[51]

$$(\boldsymbol{\alpha h\nu})^k = K(\boldsymbol{h\nu} - \boldsymbol{E_g}) \qquad\qquad (5.1)$$

Where, absorption coefficient, band gap, Planck's constant are denoted by α, E_g and h, respectively with frequency of light is ν and exponent k is dependent constant of electron transition processes and value is 0.5 in the process.

Theoretical calculations (DFT) have been done by using crystallographic parameters of the compounds **1-3** and the energy difference of CPs (ΔE = E_{LUMO} – E_{HOMO}, in eV) are 3.43 (**1**), 3.29 (**2**), 2.90 (**3**) eV. The experimental results differ slightly because of selection of the parameters in the DFT computation; only coordinative monomeric motif is selected for computation. However, both experimental and calculated results support the fabrication of effective semiconducting device using these materials.

The substantial absorption of the compounds, **1-3**, in the UV and visible region has suggested that the charge transport mechanism may generate substantial current with small change in potential, *i.e.,* non-Ohmic current. Furthermore, the lowest optical band gap in the compound **3** is observed compared to the other two compounds (**1** and **2**) that has implied that metal semiconductor barrier of [Cd(tppz)(2,6-ndc)] (**3**) is lowest.
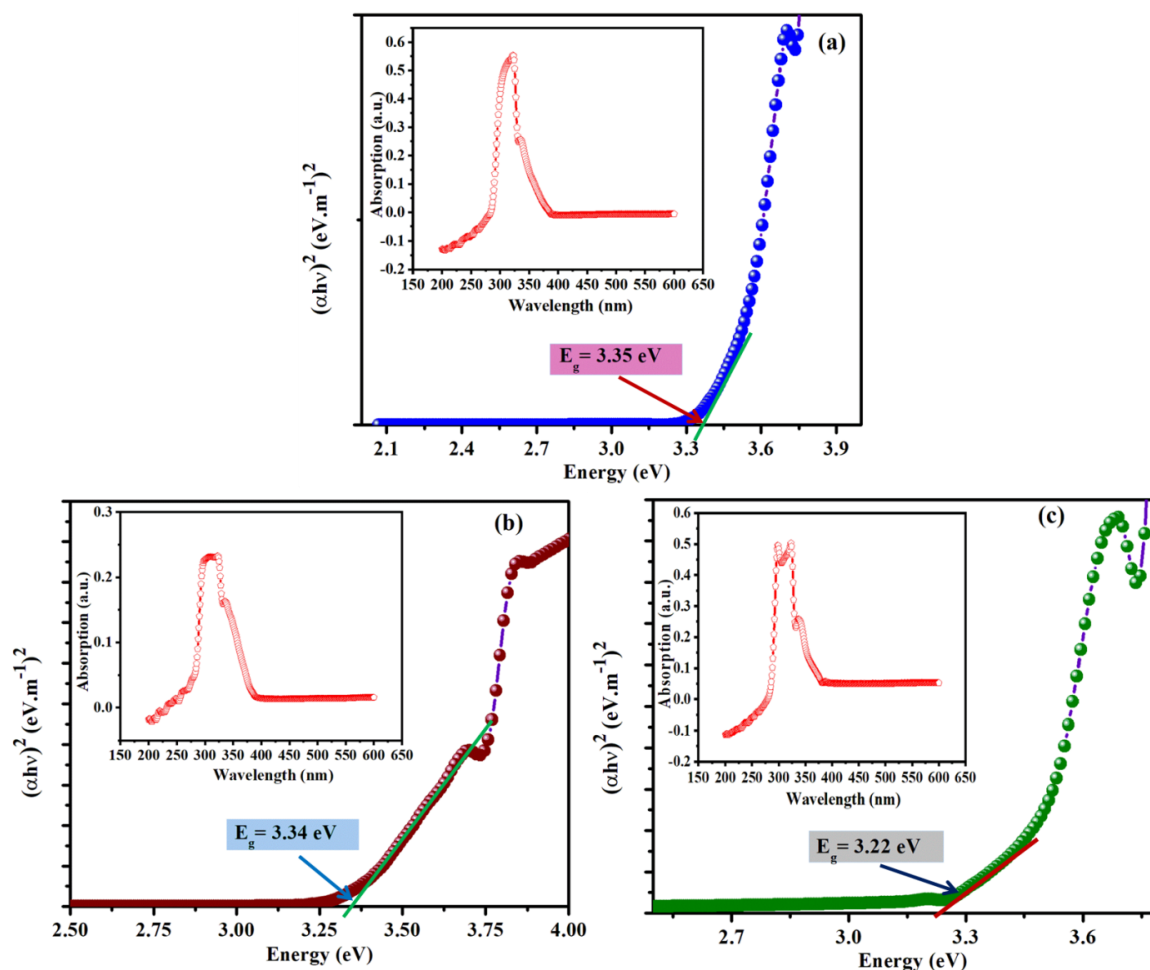
Figure 5.11. Absorption spectra (inset) and corresponding Tauc's plots of thin film devices formed by the compounds: (a) **1**; (b) **2**; (c) **3**.

The thin films on the top of ITO coated glass substrates were formed with addition of well-dispersed solution of CPs. Under dark and light conditions, the current(I)-voltage(V) characteristic plots for **1**, **2**, and **3** based thin film devices are recorded (**Figure 5.12**). It is clear that the I-V characteristic curves display extremely nonlinear rectifying behaviour. The non-Ohmic nature of the dominant conduction mechanism is indicated by the logarithmic I-V characteristic's nonlinearity. Under dark condition, the rectification ratios of **1** is 8; for **2** and **3** the values are 8.99 and 13.5, respectively.
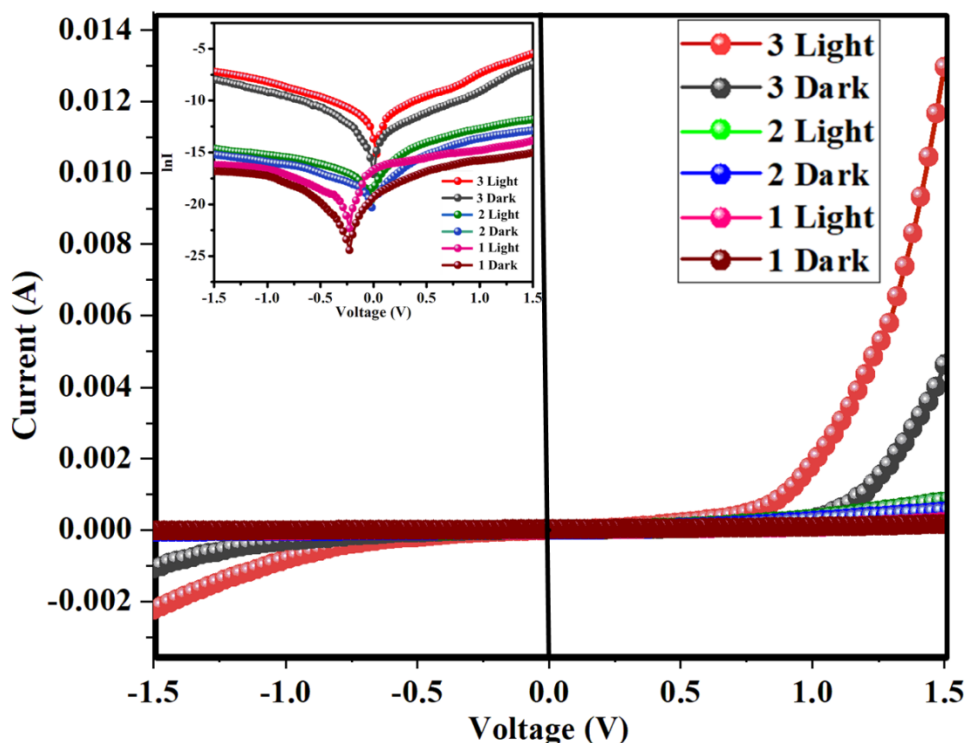
Figure 5.12. *I−V* characteristics curve for ITO/compounds (**1**–**3**)/Al structured thin film devices under dark and light condition.

The I-V representative of the composite-based device has been investigated using thermionic emission (TE) theory (**Eq. 5.2**).[52]

$$I = I_0 \left[exp\left(\frac{qV}{rkT}\right) - 1 \right] \tag{5.2}$$

Where, applied bias voltage, electronic charge, ideality factor, Boltzmann constant and operating temperature (K) are denoted by the V, q, r, k, and T respectively. Reverse saturation current, I_0, of TE theory was revealed in the **Eq. 5.3**.

$$I_0 = AA^*T^2 exp\left(-\frac{q\phi_b}{kT}\right) \tag{5.3}$$

Where, Effective area of Schottky diodes was denoted by A and the value is 9×10^{-6} m^2, effective Richardson constant was signified by A^*, which is expected as 1.20×10^6 AK^{-2} m^{-2}, barrier height (BH) is denote ϕ_b at the junction. From the intercept of lnI at V = 0, the reverse

saturation current was extracted. Temperature dependence ideality factor (r) is expressed in **Eq. 5.4**.

$$r = \frac{q}{kT}\left[\frac{dV}{d(lnI)}\right] \tag{5.4}$$

Eq. 5 is used to obtain the temperature-dependent BH (ϕ_b) at zero bias and can be articulated as **Eq. 5.5**.

$$\phi_b = \frac{kT}{q} ln\left(\frac{AA^*T^2}{I_0}\right) \tag{5.5}$$

Slope and intercept of lnI *vs.* V plots are helped to evaluate the ideality factor and ϕ_b of the Schottky device, respectively (**Table 5.6**). Forward biased dV/dlnI *vs.* I plot (**Figure 5.13**) is aided to evaluate series resistance (R_s) which is an important Schottky parameters and the plot is employing by Cheung's method [18] (**Eq. 5.6**).

$$\frac{dV}{d(lnI)} = IR_S + \frac{rkT}{q} \tag{5.6}$$

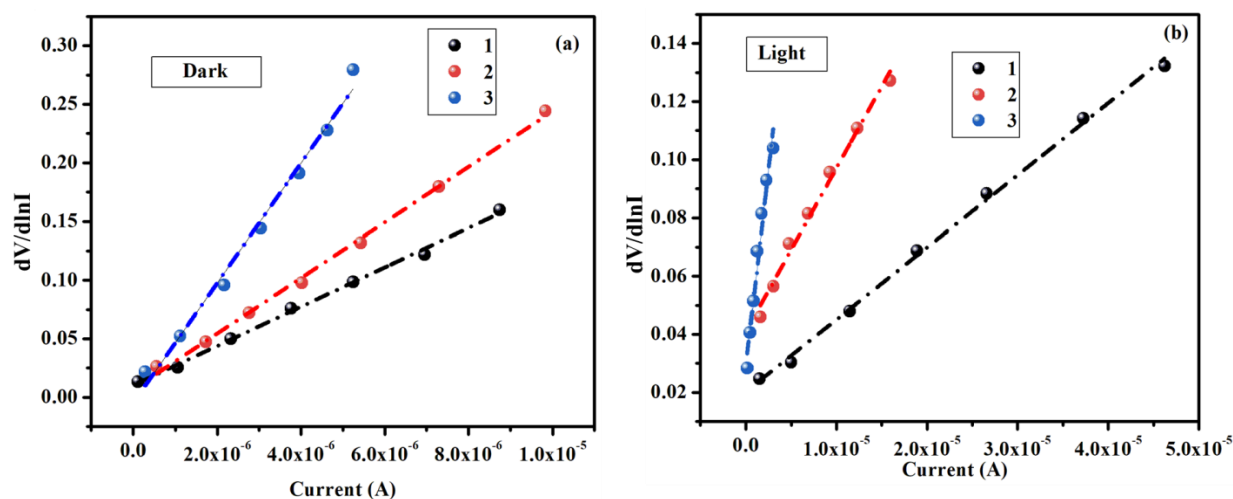**Figure 5.13.** d*V*/dln*I* vs. *I* curve of CPs (**1–3**) based on thin film devices under dark, and photo-illumination condition.

Inhomogeneity in the Schottky barrier junction is the reason for the deviation of the 'r' factor from the ideal behaviour in the dark and is the reason for recombination of hole and electron in the depletion zone.[53] Under dark and light conditions, the **r**s values of the device based on **1**

are 2.00 (dark) and 1.84 (light), respectively; for other devices the **r**s are 1.53 (dark) and 1.33 (light) for **2** and 1.36 (dark) and 1.29 (light) for **3**. These values are deviated from the ideal value (~1). This could be owing to the presence of inhomogeneities at the Schottky barrier junction and series resistance of the junction of Schottky device.[53,54] The decrement in ideality factor from the ideal value in presence of light suggests that the composite-based device has less carrier recombination at the junction and the barrier potential height is decreased under photo-illumination condition (**Table 5.6**). The better photosensitivity of **3** makes it good rectifier (17.60, light) than **1** and **2**.

Table 5.6. Some electrical parameters of **1**–**3** based Schottky device.

Sample	Condition	Rectification ratio	Conductivity (S.m^{-1})	Photo sensitivity	Ideality Factor (r)	Barrier Height (eV)	R_S From dV/dln I (Ω)
1	**Dark**	8.05	4.72×10^{-5}	1.12	2.00	0.74	51031
	Light	10.20	5.06×10^{-5}		1.84	0.72	27235
2	**Dark**	8.99	1.80×10^{-4}	1.35	1.53	0.74	23677
	Light	16.70	1.10×10^{-4}		1.33	0.71	5608
3	**Dark**	13.5	1.12×10^{-4}	5.79	1.36	0.75	16757
	Light	17.60	1.93×10^{-3}		1.29	0.70	2477

Investigation of the current-voltage (I-V) curves following the space charge limited current (SCLC) theory has facilitated to interpret the Schottky diode property of the device. The parameters of charge transport phenomena like transient response time (τ), effective carrier mobility (μ_{eff}), threshold voltage (V_{th}) and trap energy (E_t) have been evaluated from the analysis of forward bias steady state I-V characteristics. Effective carrier mobility has been

estimated from the slope of I *vs.* V^2 graph (**Figure 5.14a**) at higher voltage region using the Mott−Gurney equation (**Eq. 5.7**)[55]:

$$I = \frac{9\mu_{eff}\varepsilon_0\varepsilon_r A}{8}\left(\frac{V^2}{d^3}\right) \tag{5.7}$$

Where, d = thickness of the film which was ~5 μm for the device. The plot of capacitance (C) vs. frequency of the device fabricated from the synthesised materials in the form of film at constant bias potential has been used to determine the relative dielectric constant (**Figure 5.14b**). Saturated capacitance values at the higher frequency regime and the dielectric permittivity of the CPs were assessed from the equation (**Eq. 5.8**).[56,57]

$$\varepsilon_r = \frac{1}{\varepsilon_0}\frac{C.D}{A} \tag{5.8}$$

Where, capacitance denoted as *C* at the saturation and thickness of the film denoted by the *D* which was considered as ~5 μm with an effective area *A*. Relative dielectric constant of the compounds were determined using the above formula and the values are 0.338 (**1**), 0.506 (**2**) and 1.48 (**3**).
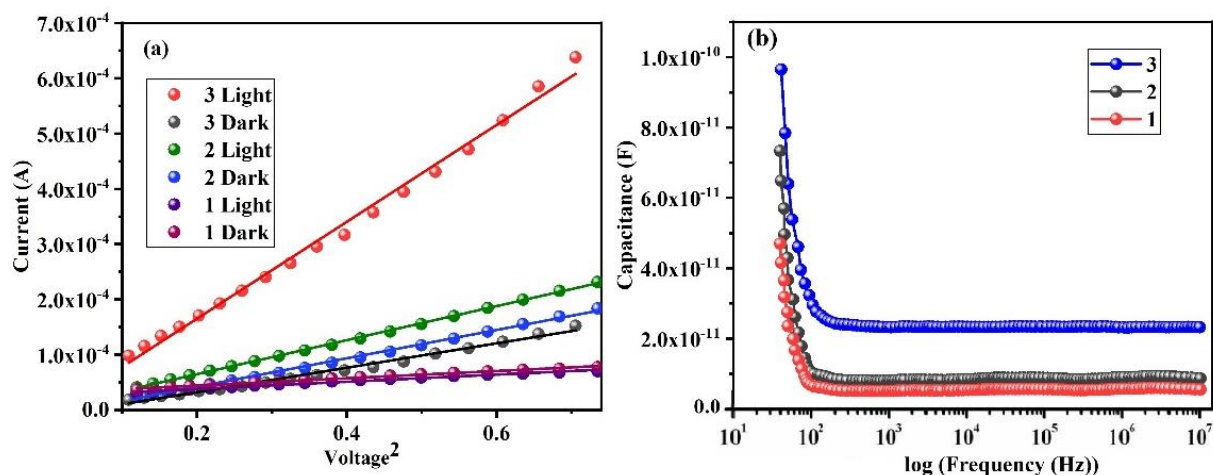

Figure 5.14. (**a**) I *vs.* V^2 plot **1**-**3**; (**b**) Capacitance *vs.* frequency curve of three compounds-based devices.

Transit time (τ) is one of the important parameters of the charge carriers which represents the average time of a carrier before they got collected at electrode or recombine. Hence, τ was estimated from **Eq. 5.9**, by using the slope of lnI-lnV characteristics in the SCLC region (Region-II) of **Figure 5.15**.[57,58]

$$\tau = \frac{9\varepsilon_0\varepsilon_r A}{8d}\left(\frac{V}{I}\right) \tag{5.9}$$

$$\mu_{eff} = \frac{qD}{kT} \tag{5.10}$$

$$L_D = \sqrt{2D\tau} \tag{5.11}$$

Estimated values of effective carrier mobility, transit time, diffusion constant (D) and diffusion length (L_D) (**Eqs. 5.9-5.11**) of the devices are presented in **Table 5.7**. The results exhibited that the compound **3** has far better charge transport properties than the that of **1** and **2**. The higher mobility implies the higher transport through the MS junction of **3**, and the transit time in the device represents totality of carrier lifetime and carrier trapping time. The device based on **3** has four times faster carrier transit rate than **1** and 3.5 times faster than **2**. Therefore, to explain the carrier transit through the device, consideration of trapping of charge carrier gives the complete understanding of charge transport mechanism.

Table 5.7. Charge conducting parameters of compounds, **1–3**, based on thin film devices.

Device	Condition	ε_r	μ_{eff} (m^{2}V^{-1}s^{-1})	τ (ns)	$\mu_{eff}.\tau$	D	L_D (μm)
1	Dark	0.338	2.67×10^{-4}	5.53	1.48×10^{-12}	6.91×10^{-6}	0.27
	Light		2.72×10^{-4}	4.36	1.19×10^{-12}	7.04×10^{-6}	0.25
2	Dark	0.506	5.01×10^{-4}	5.12	2.57×10^{-12}	1.30×10^{-5}	0.37
	Light		6.62×10^{-4}	3.97	2.63×10^{-12}	1.71×10^{-5}	0.36
3	Dark	1.48	5.03×10^{-4}	2.26	1.14×10^{-12}	1.30×10^{-5}	0.25
	Light		8.24×10^{-4}	1.37	1.13×10^{-12}	2.13×10^{-5}	0.24

The trapping of charge carriers plays an important character in the transport mechanism of the thin film-based system. It gives the information about smoothness of charge transfer pathway. To find out what extend and how charge carriers being controlled by traps in the device before collection at the electrode, the trap energy has been measured. The lnI vs. lnV graphs (**Figure 5.15**) have been analysed for the three discrete regions with different slopes. The Region-I follows ohmic nature (I α V) as the slopes are ~1 (**Table 5.8**) and the current is mostly contributed by the bulk generated thermionic electrons of the film, as an alternative of the inserted free carriers.[59] After a threshold voltage ($V_{1\,th}$), the Region-II maintains I α V^2 relation and is dominated by space charge limited current (SCLC). In this region, injected carriers are accumulated near the electrode and create a space charge region which limits the current flow in the device. At higher voltages i.e., after second threshold voltage ($V_{2\,th}$), the accumulated space charges rush to occupy the traps in the film, considerably enhancing the current such that the slope is greater than 2. General form of this Region III is represented by I α V^m, where m > 2. This region is known as trap assisted SCLC region.[60] Therefore, trapped charges are said to play a significant role within the region III for power law conduction mechanism. The HOMO and LUMO[61] energy gap of the CPs is coupled in these traps. In presence of this trap levels, a large number of the transporters inserted from the electrode are trapped and is mentioned as trap charge limiting conduction (TCLC) process.
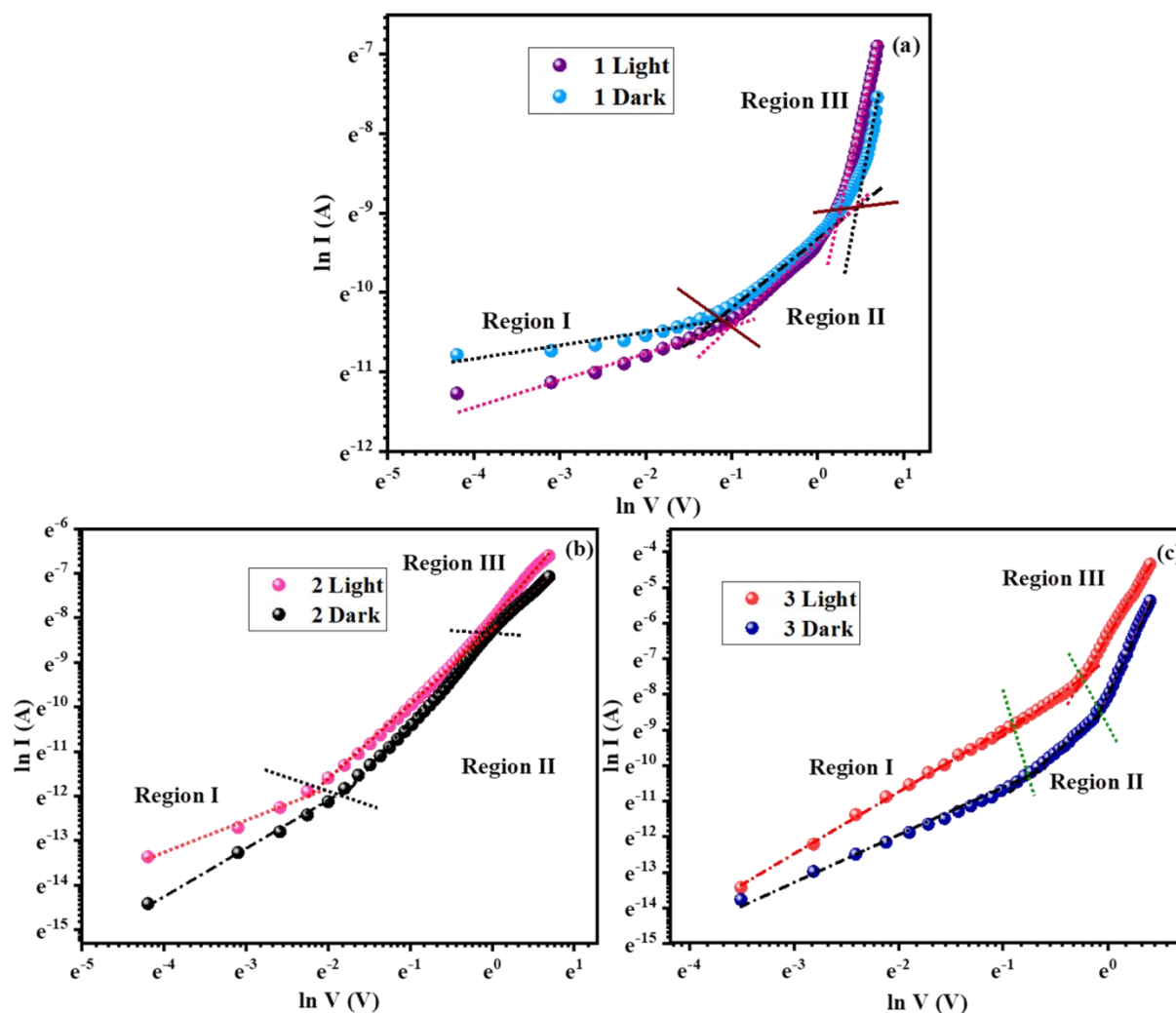
Figure 5.15. lnI vs. lnV curves of CPs **1-3** based Schottky devices respectively.

The trap centres are expected to be exponentially spread, according to **Eq. 5.12**.[62]

$$g(E) = \frac{N_T}{k_B T_T} \exp(\frac{-E_n}{k T_T})$$ **(5.12)**

Where, the total trap concentration (N_T), Fermi energy (E_n), Boltzmann constant (k) and characteristic temperature (T_T) are determined. The I-V characteristic was evaluated using **Eq. 5.12** to obtain the power law, $I \sim V^{m+1}$; where V = applied voltage and m = T_T/T. The linear fitting of lnI vs lnV provided two threshold voltages and three slopes for separate regions. The trap energies in Region-III have been demonstrated in **Table 5.8**. It shows that the trap energies for all three devices are quite high, which could be attributed to the existence of impurity,

vacancy state, and poor material-electrode interface. As a result, device conduction is ohmic at low biased regions ($<<V_{1\,th}$). However, at higher applied voltages ($\geq V_{2\,th}$), exponentially distributed trap states regulate the device's injected carriers. In this region, traps are filled by injected carriers. Since device made up of **3** has a high mobility, the trap states fill at low applied voltages (Dark; 0.93 V, Light; 0.80 V) in comparison to the others, hence it requires less transit time (τ) to cover a diffusion length (L_D). The density of free charge carriers is increased that causes high conductivity. The second threshold voltage for **1** and **2** is substantially high (**Table 5.8**) which may be linked to the low mobility of the samples. As a result, **3** is a potential and attractive material for the use of thin-film optoelectronic Schottky devices.

Table 5.8 Threshold voltages and different parameters linked to estimation of trap energy.

Sample	Condition	Region I	Region II		Region III		
		Value of slope (m_1)	Threshold voltage $V_{1\,th}$ (V)	Value of slope (m_2)	Threshold voltage $V_{2\,th}$ (V)	Value of slope (m_3)	Trap energy, E_T (meV)
1	**Dark**	0.71	0.37	1.92	1.23	3.25	84.17
	Light	0.94	0.33	2.01	1.62	4.71	121.98
2	**Dark**	0.69	0.16	1.82	0.99	2.30	59.57
	Light	1.03	0.12	2.03	0.82	2.50	64.75
3	**Dark**	1.20	0.45	1.86	0.93	4.79	124.06
	Light	1.30	0.40	2.31	0.80	6.67	172.75

Schottky electrical contact was generated to use the lattice matching and deformation potential. The deformation commonly refers the band gap between the HOMO and LUMO with corresponding energy ΔE (eV) ($E_{LUMO} - E_{HOMO}$).[63] Band gap of CPs were determined using

the absolute deformation potentials (ADPs).[64] Coordination polymers are formed using organic and inorganic hybrids, so band gap as well as electrical contact of CPs depends upon the electronic nature of both. The CPs are formed with the Cd(II), a d^{10}, metal centre, with greatly delocalised 4d-orbitals. The band gap was related with the electronic feature of ligand and geometrical strain of CPs framework. Theoretical band gaps between HOMO and LUMO were determined using the DFT computation (3.43 (**1**), 3.29 (**2**) and 2.90 (**3**) eV) which were nearly matched with the band gap of Tauc's plot (3.35 (**1**); 3.34 (**2**); 3.22 eV (**3**)) (**Figure 5.11**).

Table 5.9. DFT table of [Cd(tppz)(ADC)] (**1**)

Excitation Energy (eV)	Wavelength Exp.(nm)	Wavelength Thro.(nm)	Oscillation frequency (f)	Key Transitions	Nature of Transitions
3.9983	311	310.09	0.008	(20%) HOMO-5 →LUMO+1	ILCT
3.9217	316	316.15	0.0091	(39%) HOMO-7 →LUMO+1	ILCT

ILCT: Intra ligand charge transfer transition.

Table 5.10. Composition of MOs and their energy in **1**.

MO	Energy(eV)	Cd	Ligand
LUMO+10	-1.06	1	99
LUMO+9	-1.15	0	100
LUMO+8	-1.32	0	100
LUMO+7	-1.39	0	100
LUMO+6	-1.43	0	100
LUMO+5	-1.45	0	100
LUMO+4	-1.74	0	100
LUMO+3	-1.78	0	100

MO	Energy(eV)	Cd	Ligand
LUMO+2	-2.04	0	100
LUMO+1	-2.96	1	99
LUMO	-3.21	0	100
HOMO	-6.64	1	99
HOMO-1	-6.95	0	100
HOMO-2	-7.00	0	100
HOMO-3	-7.04	0	100
HOMO-4	-7.30	1	99
HOMO-5	-7.48	2	98
HOMO-6	-7.54	1	99
HOMO-7	-7.57	0	100
HOMO-8	-7.60	0	100
HOMO-9	-7.62	1	99
HOMO-10	-7.72	2	98

Table 5.11. DFT table of [Cd(tppz)(trep)] **(2)**

Excitation Energy (eV)	Wavelength Exp.(nm)	Wavelength Thro.(nm)	Oscillation frequency (f)	Key Transitions	Nature of Transitions
4.0652	304	304.99	0.0015	(40%) HOMO-17 →LUMO	ILCT
3.9279	314	315.65	0.0152	(44%) HOMO-12 →LUMO+1	ILCT

ILCT: Intra-ligand charge transfer transition.

Table 5.12. Composition of MOs and their energy in **2**.

MO	Energy(eV)	Cd	Ligand
LUMO+10	-0.76	0	100
LUMO+9	-1.06	0	100

LUMO+8	-1.22	0	100
LUMO+7	-1.34	0	100
LUMO+6	-1.68	0	100
LUMO+5	-1.69	0	100
LUMO+4	-1.77	0	100
LUMO+3	-1.79	0	100
LUMO+2	-1.94	0	100
LUMO+1	-2.86	1	99
LUMO	-3.10	0	100
HOMO	-6.39	2	98
HOMO-1	-6.49	1	99
HOMO-2	-6.68	0	100
HOMO-3	-6.77	0	100
HOMO-4	-6.91	0	100
HOMO-5	-6.96	0	100
HOMO-6	-6.96	0	100
HOMO-7	-7.03	0	100
HOMO-8	-7.17	4	96
HOMO-9	-7.20	0	100
HOMO-10	-7.35	4	96

Table 5.13. DFT table of [Cd(tppz)(2,6-NDC)] **(3)**

Excitation Energy (eV)	Wavelength Exp.(nm)	Wavelength Thro.(nm)	Oscillation frequency (f)	Key Transitions	Nature of Transitions
4.1186	301	301.04	0.0043	(40%) HOMO-3 →LUMO+4	ILCT

ILCT: Intra ligand charge transfer transition.

Table 5.14. Composition of MOs and their energy in **3**.

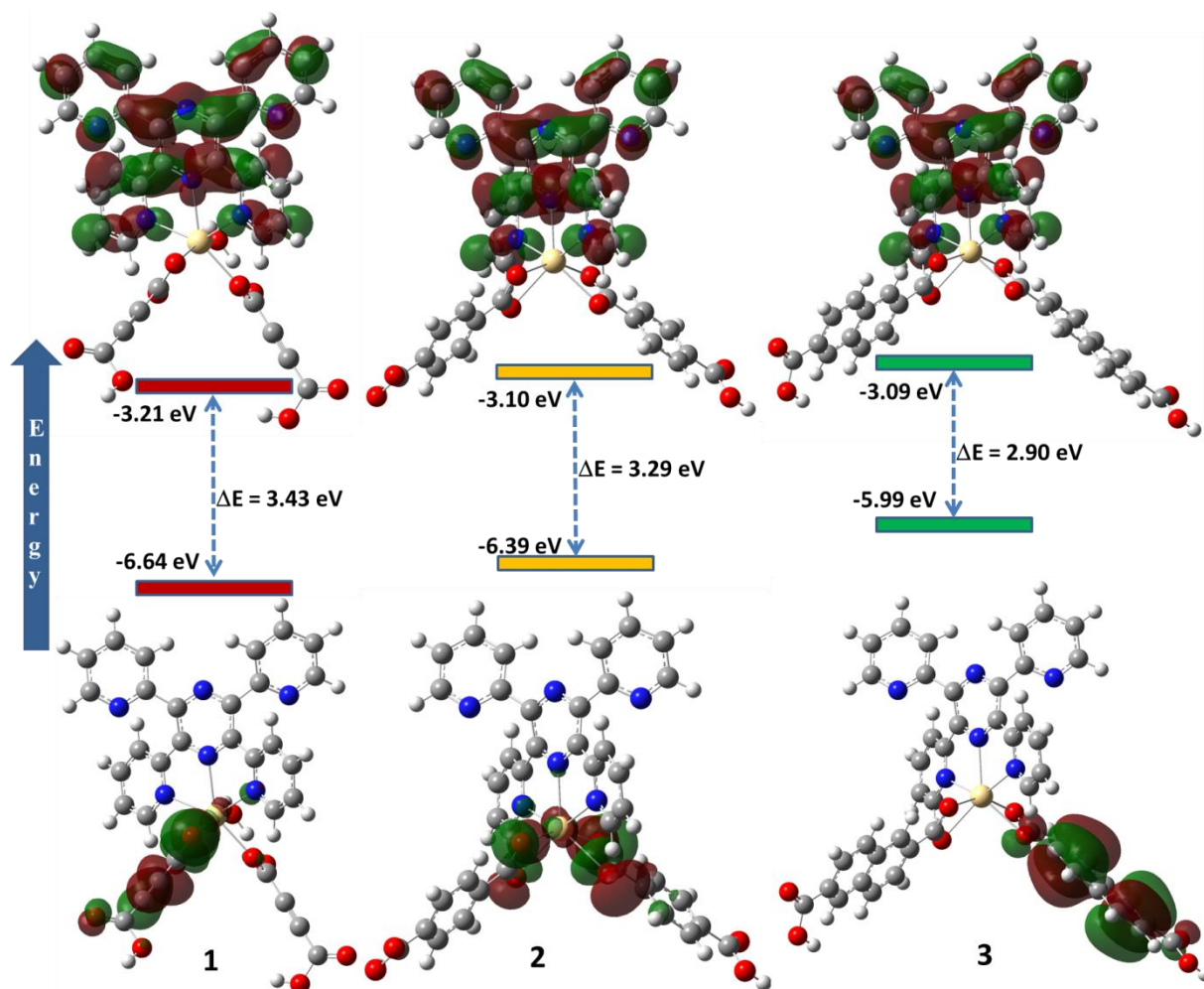| MO	Energy(eV)	Cd	Ligand
LUMO+10	-0.99	0	100
LUMO+9	-1.05	0	100
LUMO+8	-1.21	0	100
LUMO+7	-1.32	0	100
LUMO+6	-1.67	0	100
LUMO+5	-1.67	0	100
LUMO+4	-1.91	0	100
LUMO+3	-1.92	0	100
LUMO+2	-1.99	0	100
LUMO+1	-2.84	1	99
LUMO	-3.09	0	100
HOMO	-5.99	0	100
HOMO-1	-6.21	0	100
HOMO-2	-6.34	2	98
HOMO-3	-6.43	1	99
HOMO-4	-6.68	0	100
HOMO-5	-6.72	0	100
HOMO-6	-6.77	0	100
HOMO-7	-6.89	0	100
HOMO-8	-6.94	0	100
HOMO-9	-7.12	4	96
HOMO-10	-7.31	4	96

Figure 5.16. DFT computational energy of **1**, **2** and **3** and energy gap between HOMO and LUMO.

A small change of calculated band gap may be assigned to the geometry factor which has not being considered during the DFT calculation; herein, only single motif of CPs has been used for computation studies by electronic transition [HOMO-5→LUMO+1 (20%, **1**), HOMO-17→LUMO (40%, **2**) and HOMO-3→ LUMO+4 (40%, **3**) (**Table 5.9-5.14**)] of CPs were determined from the TD-SCF nearly matched with wavelength of UV-Visible experiments. The results of observation (calculated band gap, **Figure 5.16**) on lowest band gap of **3** (2.90 eV) than the others **2** (3.29 eV), **1** (3.43 eV) were described by the higher conjugation and structurally flexibility of 1D chain of **3**, over **2** and **1**. In the compounds **1** and **2** both 2D coordination polymers attributed lower flexibility with lower conjugation. Among **1** and **2**, the compound **2** has shown higher conjugation with short metal-metal distance and has exhibited

lower band gap with higher conductivity than **1**. In addition to this, electrical property of the molecular systems has been corresponded to the charge transportation through it. The charge carrier delocalization is also manifested with the structural architecture. In case of these materials, to the close proximity of adjacent polymeric chains and networks, are able to form supramolecular assembly with different secondary interactions. The charge might transfer through covalent or coordination bonds and following noncovalent contacts by means of so-called "hopping transport" (**Scheme 5.2**).
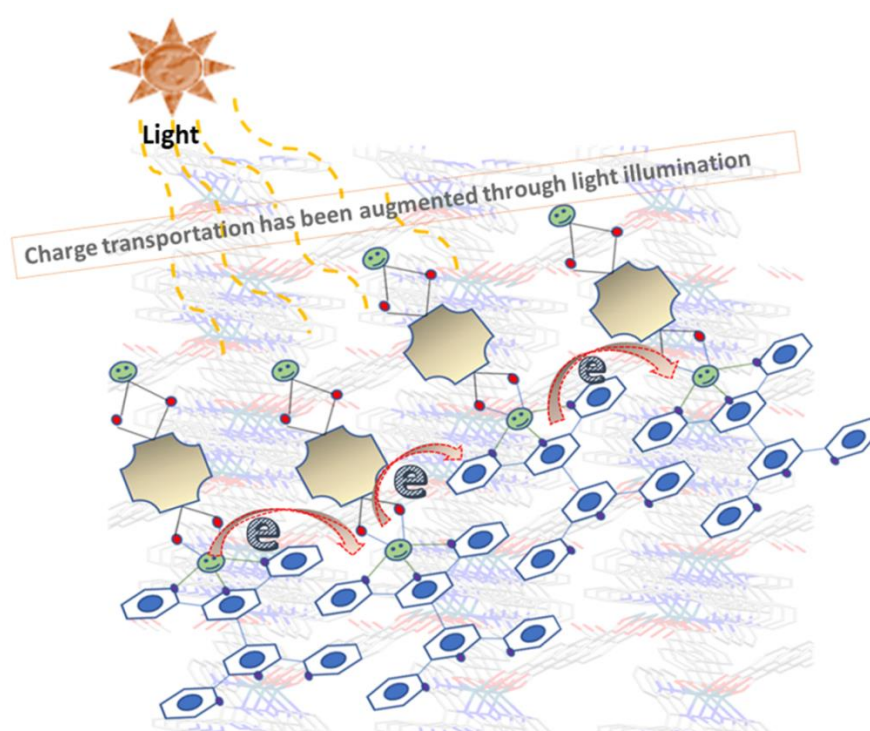
Scheme 5.2. Schematic representation of charge transportation for photo-responsive electrical conductivity.

Actually, the highly -organized structural components are well oriented in crystalline solid state to construct a unitary cell-like arrangement, even while, illumination of light, these cells-like system are do collected photons through the high surface area.[65] The organic ligands are acted as antenna of the polymeric chains to collect light energy. Therefore, during the illumination, these ligands absorb light and boost the charge carriers, ensuing in the upsurge in mobility and

improvement of electrical conductivity. As a consequence of this naphthalene-based system has been acted as a highly efficient in the above activity and exhibited higher conductivity. In addition to this, distance within polymeric layers and secondary interactions plays pivotal role in the exhibition of electrical property. The electrical conductivity of lower-dimensional coordination polymers has been well-established with different controlling factors[32,67,68] and hence, our synthesized material following the similar trend.

5.4. Conclusion

In this report, a series of three Cd(II)-mixed ligand coordination polymers are utilized to explore structure-property relationship towards fabrication of smart electronic materials. Structural characterization has been well established regarding role of ligand moieties and secondary interactions in the molecular properties of the materials. Highly conjugated fused aromatic ring decorated **3** (corresponds to ndc^{2-} acid) exhibited highest electrical conductivity revealing better charge mobility. Interestingly, the CPs presented augmentation of electrical conductivity upon illumination of light in a similar trend. However, considering the energy crisis and environmental pollution**,** these types of light responsive materials are highly desire for sustainable development. In addition to this, findings of this case study, may be helpful for future researchers in this field for flagged the way of energy materials.

5.5. Reference

1. Fletcher, A. J.; Cussen, E. J.; Prior, T. J.; Rosseinsky, M. J.; Kepert, C. J.; Thomas, K. M. Adsorption dynamics of gases and vapors on the nanoporous metal organicframework material $Ni_2(4, 4'\text{-bipyridine})_3(NO_3)_4$: guest modification of host sorptionbehavior. *J. Am. Chem. Soc.,* **2001**, *123*, 10001-10011.

2. Desiraju, R. G.; Gavezzotti, A. From molecular to crystal tructure; polynuclear aromatic hydrocarbons. *J. Chem. Soc., Chem. Commun.*, **1989**, 621–623

3. Rao, C. N. R.; Natarajan, S.; Vaidhyanathan, R. Metal carboxylates with open architectures. *Angew. Chem.Int.Ed.,* **2004**, *43*, 1466−1496.

4. Kondo, A.; Noguchi, H.; Ohnishi, S.; Kajiro, H.; Tohdoh, A.; Hattori, Y.; Xu, W. C.; Tanaka, H.; Kanoh, H.; Kaneko, K. Novel expansion/shrinkage modulation of 2D layered MOF triggered by clathrate formation with CO_2 molecules. *Nano Lett.,* **2006**, *6*, 2581−2584.

5. Schoedel, A.; Li, M.; Li, D.; O'Keeffe, M.; Yaghi, O. M. Structures of metal–organic frameworks with rod secondary building units. *Chem. Rev.*, **2016**, *116*, 12466–12535.

6. Duan, J.; Jin, W.; Kitagawa, S. Water-resistant porous coordination polymes for gas separation. *Chem. Soc. Rev.*, **2017**, *332*, 48–74.

7. Kreno, L. E.; Leong, K.; Farha, O. K.; Allendorf, M.; Van Duyne, R. P.; Hupp, J. T. Metal–organic framework materials as chemical sensors. *Chem. Rev.*, **2012**, *112*, 1105–1125.

8. Kumar, B.; Kaushik, B. K.; Negi, Y. S. Organic thin film transistors: structures, models, materials, fabrication, and applications: a review. *Polym. Rev.*, **2014**, *54*, 33.

9. Hulvey, Z.; Furman, J. D.; Turner, S. A.; Tang, M.; Cheetham, A. K. Dimensionality trends in metal-organic frameworks containing perfluorinated or nonfluorinated benzenedicarboxylates. *Cryst. Growth Des.,* **2010**, *10*, 2041−2043.

10. Heremans, P.; Gelinck, G. H.; Muller, R.; Baeg, K. J.; Kim, D. Y.; Noh, Y. Y. Polymer and organic nonvolatile memory devices. *Chem. Mater.*, **2011**, *23*, 341.

11.   Rosi, N. L.; Eckert, J.; Eddaoudi, M.; Vodak, D. T.; Kim, J.; O'Keeffe, M.; Yaghi, O. M. Hydrogen storage in microporous metal-organic frameworks. *Science*, **2003**, *300*, 1127–1129.

12.   Carlucci, L.; Ciani, G.; Proserpio, D. M.; Spadacini, L. Supramolecular isomers in the same crystal: a new case involving two different types of layers polycatenated in the 3D architecture of [Cu (bix)$_2$ (SO$_4$)]· 7.5 H$_2$O [bix= 1, 4-bis (imidazol-1-ylmethyl) benzene]. *CrystEngComm.*, **2004**, *6*, 96−101.

13.   Biradha, K.; Su, C.-Y.; Vittal, J. J.; Recent developments in crystal engineering. *Cryst. Growth Des.*, **2011**, *11*, 875–886.

14.   Shit, M.; Sahoo, D.; Dutta, B.; El Fallah, S.; Kundu, A.; Manik, N. B.; Sinha, C. Exploration of Variable Temperature Magnetism and Electrical Properties of a Pyridyl-isonicotinoyl Hydrazone Bridged Three-Dimensional Mn-Metal–Organic Framework with a Thiophene Dicarboxylato Link. *Cryst. Growth Des.*, **2022**, *22*, 7143-7152.

15.   Murray, J. L.; Dincă, M.; Long, R. J.; Hydrogen storage in metal–organic frameworks. *Chem. Soc. Rev.*, **2009**, *38*, 1294−1314.

16.   Hazra, A.; Kanoo, P.; Maji, T. K. High heat of hydrogen adsorption and guest-responsive magnetic modulation in a 3D porous pillared-layer coordination framework. *Chem. Commun*. **2011**, *47*, 538−540.

17.   Naskar, K.; Dey, A.; Dutta, B.; Ahmed, F.; Sen, C.; Mir, M. H.; Roy, P. P.; Sinha, C. Intercatenated coordination polymers (ICPs) of carboxylato bridged Zn (II)-isoniazid and their electrical conductivity. *Cryst. Growth Des.,* **2017**, *17*, 3267-3276.

18.   Dutta, B.; Dey, A.; Sinha, C.; Ray, P. P.; Mir, M. H. Tuning of the para-position of pyridyl ligands impacts the electrical properties of a series of Cd (II) ladder polymers. *Dalton Trans.*, **2019**, *48*, 11259-11267.

19. Bairy, G.; Dey, A.; Dutta, B.; Ray, P. P.; Sinha, C. Rational synthesis of a pyridyl-imidazoquinazoline based multifunctional 3D Zn (II)-MOF: structure, luminescence, selective and sensitive detection of Al^{3+} and TNP, and its semiconducting device application. *Dalton Trans.,* **2022**, *22*, 3138-3147.

20. Gole, B.; Bar, A. K.; Mukherjee, P. S. Fluorescent metal–organic framework for selective sensing of nitroaromatic explosives. *Chem. Commun.*, **2011**, *47*, 12137−12139.

21. Allendorf, M. D.; Bauer, C. A.; Bhakta, R. K.; Houk, R. J. T. Luminescent metal–organic frameworks. *Chem. Soc. Rev.*, **2009**, *38*, 1330−1352.

22. Li, G. B.; Fang, H. C.; Cai, Y. P.; Zhou, Z. Y.; Thallapally, P. K.; Tian, J. Construction of a novel Zn-Ni trinuclear Schiff base and a Ni^{2+} chemosensor. *Inorg. Chem.*, **2010**, *49*, 7241−7243.

23. Bhunia, S.; Dutta, B.; Pal, K.; Chandra, A.; Jana, K.; Sinha, C. Ultra-trace level detection of Cu^{2+} in an aqueous medium by novel Zn (II)-dicarboxylato–pyridyl coordination polymers and cell imaging with HepG2 cells. *New J. Chem.*, **2021**, *45*, 13941-13948.

24. Biradha, K.; Das, S. K.; Bu, X. H. "Coordination Polymers as Heterogeneous Catalysts for Water Splitting and CO_2 Fixation."*Cryst. Growth Des.,* **2022**, *22*, 2043-2045.

25. Mu, Y.; Ran, Y.; Zhang, B.; Du, J.; Jiang, C.; Du, J. Dicarboxylate ligands modulated structural diversity in the construction of Cd (II) coordination polymers built from N-heterocyclic ligand: synthesis, structures, and luminescent sensing. *Cryst. Growth Des.,* **2020**, *20*, 6030-6043.

26. Biradha, K.; Goswami, A.; Moi, R. Coordination polymers as heterogeneous catalysts in hydrogen evolution and oxygen evolution reactions. *Chem. Comm.,* **2020**, *56*, 10824-10842.

27. Pan, J.; Zhang, D.; Shang, M. M.; Mu, Y.; Han, D. S.; Wang, M. G. An anionic Cd-based coordination polymer exhibiting ion-exchange behavior for photoluminescence and selective dye adsorption. *J. Lumin.,* **2019**, *210*, 70-74.

28. Givaja, G.; Amo-Ochoa, P.; Gómez-García, C. J.; Zamora, F. Electrical conductive coordination polymers. *Chem. Soc. Rev.,* **2012**, *41*, 115-147.

29. Dutta, B.; Debsharma, K.; Dey, S.; Sinha, C. Advancement and future challenges of metal–organic coordination polymers: A case study of optical sensor for the detection of the environmental contaminants, *Appl. Organomet. Chem.,* **2022**, 6919.

30. Englert, U. Halide-bridged polymers of divalent metals with donor ligands-structures and properties, *Coord. Chem. Rev.,* **2010**, *254*, 537-554.

31. Khan, S.; Roy, S.; Bhar, K.; Ghosh, R.; Lin, C. -H.; Ribas, J.; Ghosh, B. K. Syntheses, structures and magnetic properties of two neutral coordination polymers of cobalt(II) containing a tailored aromatic diamine and pseudohalides as bridging units: Control of dimensionality by varying pseudohalide, *Inorg. Chim. Acta.,* **2013**, *398*, 40-45.

32. Ahmed, F.; Dutta, B.; Mir, M. H. Electrically conductive 1D coordination polymers: design strategies and controlling factors, ***Dalton Trans.*,** **2021**, *50*, 29-38.

33. Naskar, K.; Dey, A.; Maity, S.; Ray, P. P.; Sinha, C. Charge Transportation in Zn (II)/Cd (II)-Based 2D MOFs of 5-Nitro-isophthalate with Isonicotinic Hydrazide, *Cryst. Growth Des.,* **2021**, *21*, 4847-4856.

34. Li, W. J.; Liu, J.; Sun, Z. H.; Liu, T. F.; Lü, J.; Gao, S. Y.; He, C.; Cao, R.; Luo, J. H.; Integration of metal-organic frameworks into an electrochemical dielectric thin film for electronic applications. *Nat. Commun.* **2016**, *7*, 11830−11837.

35. Maji, T. K.; Matsuda, R.; Kitagawa, S. A flexible interpenetrating coordination framework with a bimodal porous functionality. *Nat. Mater.,* **2007**, *6*, 142−148.

36. Xia, W.; Mahmood, A.; Zou, R.; Xu, Q. Metal-organic frameworks and their derived nanostructures for electrochemical energy storage and conversion. *Energy Environ. Sci.,* **2015**, *8*, 1837−1866.

37. Bairy, G.; Dey, A.; Dutta, B.; Maity, S.; Sinha, C. Rational synthesis of a pyridyl-imidazoquinazoline based multifunctional 3D Zn (II)-MOF: structure, luminescence, selective and sensitive detection of Al^{3+} and TNP, and its semiconducting device application, *Dalton Trans.,* **2022**, *51*, 13749-13761.

38. Dutta, B.; Sinha, C.; Mir, M. H. The sunlight-driven photosalient effect of a 1D coordination polymer and the release of an elusive cyclobutane derivative. *Chem. Comm.,* **2019**, *55*, 11049-11051.

39. Dutta, B.; Jana, R.; Sinha, C.; Ray, P. P.; Mir, M. H. Synthesis of a Cd (II) based 1D coordination polymer by in situ ligand generation and fabrication of a photosensitive electronic device, *Inorg. Chem. Front.,* **2018**, *5*, 1998-2005.

40. Chandra, A.; Das, D.; Castro, J. O.; Naskar, K.; Jana, S.; Frontera, A.; Ray, P. P.; Sinha, C. Cd (II) coordination polymer of fumaric acid and pyridyl-hydrazide schiff base: Structure, photoconductivity and theoretical interpretation. *Inorg. Chim Acta.,* **2021**, *518*, 120253.

41. Naskar, K.; Dey, A.; Maity, S.; Ray, P. P.; Ghosh, P.; Sinha, C. Biporous Cd (II) Coordination Polymer via in Situ Disulfide Bond Formation: Self-Healing and

Application to Photosensitive Optoelectronic Device. *Inorg. Chem.,* **2020**, *59*, 5518-5528.

42. Shit, M.; Paul, S.; Chatterjee, T.; Dutta, B.; Sinha, C. Towards Design of Energy Efficient Semiconducting Material: An Example of 1D Cd (II)-2, 5-thiophene dicarboxylato Co-ordination Polymer. *ES Energy & Environment.*, **2022**, *16*, 40-46.

43. G. M. Sheldrick, A short history of SHELX. *Acta Crystallogr., Sect. A: Found. Crystallogr.* 2008, **64**, 112-122.

44. SMART.; SAINT. Bruker AXS Inc.: Madison, WI, 1998.

45. SADABS. Bruker AXS area detector scaling and absorption correction; Bruker AXS Inc.: Madison, WI, 2014.

46. Nawrot, I.; Machura, B.; Kruszynski, R. Coordination assemblies of Cd II with 2, 2′: 6′, 2″-terpyridine (terpy), 2, 3, 5, 6-tetra-(2-pyridyl) pyrazine (tppz) and pseudohalide ions–structural diversification and luminescence properties. *CrystEngComm.*, **2015**, *17*, 830-845.

47. Sadjadi, M. S.; Ebadi, A.; Zare, K.; Amani, V.; Khavasi, H. R. μ-2, 3, 5, 6-Tetra-2-pyridylpyrazine-κ3 N 1, N 2, N 6: κ3 N 3, N 4, N 5-bis [(methanol-κO)(nitrato-κ2 O, O′)(nitrato-κO) cadmium (II)]. *Acta Crystallogr., Sect. E: Struct. Rep. Online.,* **2008**, *64*, 1050.

48. Hadadzadeh, H.; Hosseinian, S. R.; Fatemi, S. J. Rhodium (III) and cadmium (II) complexes based on the polypyridyl ligand 2, 3, 5, 6-tetrakis (2-pyridyl) pyrazine (tppz). *Polyhedron*, **2009**, *28*, 2776-2784.

49. R.S. Sarkar, T. Basak, R. M. Gomila, A. Frontera, S. Chattopadhyay, *Polyhedron*, 2022, **225**, 116039.

50. Dutta, B.; Purkait, R.; Bhunia, S.; Khan, S.; Sinha, C.; Mir, M. H. Selective detection of trinitrophenol by a Cd (II)-based coordination compound. *RSC adv.,* **2019**, *9*, 38718-38723.

51. Wood, L. D.; Tauc, J. Weak absorption tails in amorphous semiconductors. *Phys. Rev. B: Solid State*, **1972**, *5***,** 3144–3151.

52. Sahoo, D.; Manik, N. B. Study on the effect of temperature on electrical and photovoltaic parameters of lead-free tin-based Perovskite solar cell. *Indian J Phys.,* **2022**, 1-9.

53. Sharma, M.; Tripathi, K. S. Analysis of interface states and series resistance for Al/PVA: n-CdS nanocomposite metal–semiconductor and metal–insulator–semiconductor diode structures. *J. Appl. Phys.*, **2013**, *113*, 491-499.

54. Sullivan, P. J.; Tung, T. R.; Pinto, R. M. Electron transport of inhomogeneous Schottky barriers: A numerical study. *J. Appl. Phys.,* **1991**, *70*, 7403-7424.

55. Shit, M.; Dey, A.; Mahapatra, A.; Dutta, B.; Naskar, K.; Ray, P. P.; Sinha, C. Supramolecular assembly of an Au (III) complex of 2-(3-phenyl-1H-1, 2, 4-triazol-5-yl) pyridine: Structure, biological studies and charge transportation. *Appl. Organomet. Chem.,* **2022**, *36*, 6754.

56. Dey, A.; Middya, S.; Jana, R.; Das, M.; Datta, J.; Layek, A.; Ray, P. P. Light induced charge transport property analysis of nanostructured ZnS based Schottky diode. *J. Mater. Sci. Mater. Electron.,* **2016**, *27*, 6325–6335.

57. Kao, K. C. Dielectric phenomena in solids. Elsevier Inc., San Diego, California, **2004**.

58. Rhoderick, E. H.; Williams, R. H.; Metal–Semiconductor Contacts; Clarendon Press,Oxford, 2nd edn., **1988**.

59. Gupta, R. K.; Yakuphanoglu, F. Photoconductive Schottky diode based on Al/p-Si/SnS2/Ag for optical sensor applications. *Sol. Energy.,* **2012**, *86*, 1539-1545.

60. Blom, P. W. M.; de Jong, M. J. M.; van Munster, G. M. Electric-field and temperature dependence of the hole mobility in poly (p-phenylene vinylene). *Phys. Rev. B* **1997**, *55*, R656-R659.

61. Jain, A.; Kumar, P.; Jain, S. C.; Kumar, V.; Kaur, R.; Mehra, R. M. Trap filled limit voltage (V_{TFL}) and V^2 law in space charge limited currents, *Appl. Phys.* **2007**, *102*, 94505-94509.

62. Chakraborty, S.; Manik, N. Improvement of electrical and photovoltaic properties of methyl red dye based photoelectrochemical cells in presence of single walled carbon nanotubes. *Front. Optoelectron.,* **2015**, *8*, 289–297.

63. Butler, K. T.; Hendon, C. H.; Walsh, A. Electronic structure modulation of metal–organic frameworks for hybrid devices. *ACS Appl. Mater.Interfaces.,* **2014**, *6*, 22044−22050.

64. Li, Y. H.; Gong, X. G.; Wei, S.-H. Ab initio calculation of hydrostatic absolute deformation potential of semiconductors, *Appl. Phys. Lett.,* **2006**, *88*, 042104−042106.

65. Dutta, B.; Jana, R.; Bhanja, A. K.; Ray, P. P.; Sinha, C.; Mir, M. H. Supramolecular aggregate of Cadmium (II)-based one-dimensional coordination polymer for device fabrication and sensor application. *Inorg. Chem.,* **2019**, *58*, 2686-2694.

66. Naskar, K.; Sil, S.; Sahu, N.; Dutta, B.; Slawin, A. M. Z.; Ray, P. P.; Sinha, C. Enhancement of electrical conductivity due to structural distortion from linear to nonlinear dicarboxylato-bridged Zn (II) 1D-coordination polymers. *Cryst. Growth Des.,* **2019**, *19*, 2632-2641.

67. Jana, S.; Jana, R.; Sil, S.; Dutta, B.; Sato, H.; Ray, P. P.; Datta, A.; Akitsu, T.; Sinha, C. Influence of axial linkers on polymerization in paddle-wheel Cu (II) coordination polymers for the application of optoelectronics devices. *Cryst. Growth Des.,* **2019**, *19*, 6283-6290.

Chapter 6

Selective detection of trinitrophenol by a Cd(ɪɪ)-based coordination compound
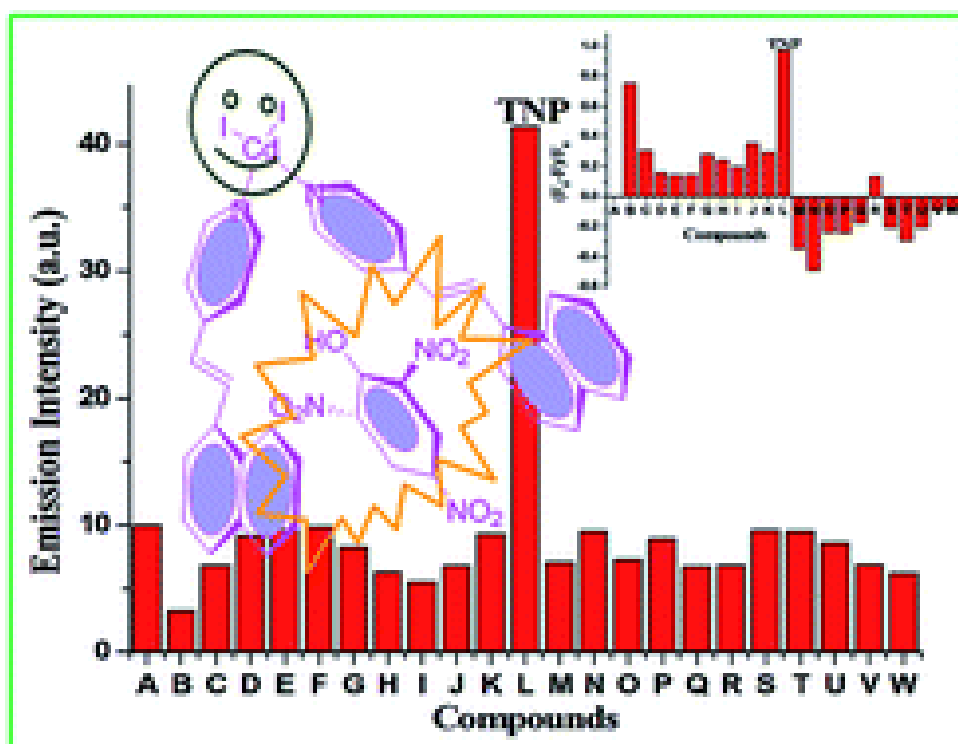
Chapter 6

Abstract

A Cd(II)-based coordination compound, [CdI$_2$(4-nvp)$_2$] (**1**), has been synthesized using CdI$_2$ and monodentate N-donor ligand, 4-(1-naphthylvinyl)pyridine (4-nvp). The solid-state supramolecular architecture has been characterized by X-ray crystallography and shows supramolecular geometry assembled through C-H---I and π---π interactions. Admirable thermal stability and excellent level of phase purity tempted us to use it for material applications. Interestingly, compound **1** exhibits a high selectivity towards trinitrophenol (TNP) in the presence of other nitroaromatics. Therefore, this material may be used for combating terrorist activities in the detection of explosive materials as well as in the recognition of TNP in analytical laboratories.

6.1. Introduction

Synthetic inorganic chemistry is being enriched every day through the generation of various types of coordination compounds (**Chapter 1**).[1–3] In the past, it was a really difficult task to authenticate and/or characterize coordination moieties. However, after the historic invention of Alfred Werner in the year 1913, the chemistry of these compounds attracted the attention of the research community. Metal ions and organic ligands are combined to form coordination compounds due to their inherent electronic properties. The desired structural architectures have been achieved *via* judicious selection of metal ions and ligands. The chemistry of such materials is of great interest to synthetic chemists because of their intriguing structural motifs as well as potential applications in the areas such as catalysis, magnetism, ion exchange, drug delivery, conductance, photoluminescence and chemical sensing.[4–15] In addition to the direct role of the metal ions and organic ligands, there are many more essential conditions, including counter anions, reaction temperatures, solvent media, external stimuli, and pH of the reaction medium, which play crucial roles during compound formation. In addition, there is an eternal relationship among the structure, property and application of the compounds. Therefore, one can easily design the compound according to the desired application.[16–19]

In recent years, the design of chemical sensors and their applications in the detection of ions/molecules have received active interest from chemistry, chemical engineering, physics, electrical and electronic engineering, and many other branches of science and technology. Usually, a molecular sensor is a chemical compound (organic or inorganic complex) that is used for sensing an analyte to crop a detectable change or signal. The action of a chemosensor typically involves the continuous monitoring of the activity of a chemical species in a given matrix such as solution, air, blood, tissue, waste effluents, and drinking water.[20,21] All chemosensors are intended to comprise a signalling moiety and a recognition moiety and they are connected either directly or through a connector or a spacer.[21,22]

Nitroaromatics[22–29] are normally explosive in nature and have been used in terroristic activities. They have become an area of concern for the Crime Bureau of Intelligence (CBI), Ministry of Home Affairs (MHA), and Ministry of Defense (MOD) of the government.[16,17] Many methods of detecting explosive materials such as energy-dispersive X-ray diffraction, police dog detection, ion migration spectroscopy, plasma desorption mass spectrometry, surface-enhanced Raman spectroscopy, and additional imaging techniques are known. However, none of them are economically viable. Therefore, it is very important to develop a special type of chemosensor that is efficient, commercially realistic, rapidly responsive, inexpensive and portable. In addition, there is a possibility of mixing aromatic compounds in the laboratory or in industry. Therefore, it is necessary to easily detect them at a glance and quantify. Keeping the above mentioned points in mind, we have designed and synthesized a Cd(II)-based discrete coordination compound $[CdI_2(4\text{-nvp})_2]$ (**1**), (4-nvp = 4-(1-naphthylvinyl)pyridine), which is highly selective towards trinitrophenol (TNP).

6.2. Experimental section

6.2.1. Materials and physical method

All chemicals were obtained in reagent grade and were used without any additional purification. For the analysis of elements, *i.e.* C, H, N, a PerkinElmer 240C elemental analyzer was used. Thermo-gravimetric analysis (TGA) was performed using a PerkinElmer Pyris Diamond TG/DTA instrument in a temperature range between 30 °C and 800 °C under an inert nitrogen atmosphere at a heating rate of 10 °C min^{-1}. The powder XRD data of the finely powdered sample was collected on a Bruker D8 Advance X-ray diffractometer using Cu Kα radiation ($\lambda = 1.548$ Å) produced at 40 kV and 40 mA. To verify the phase purity of the sample, the PXRD spectrum was recorded in a 2θ range of 5–50°. The fluorescence spectra were recorded using a PerkinElmer spectrofluorimeter model LS55. The UV-vis spectra were

obtained from a PerkinElmer Lambda 25 spectrophotometer. The time-resolved single-photon

counting measurements were performed using a time-correlated single-photon counting setup

from HORIBA Jobin-Yvon. ^{1}H NMR spectra were collected in DMSO-d_6 using a Bruker 300

MHz FT-NMR spectrometer with TMS as the internal standard.

6.2.2. Synthesis of compound 1
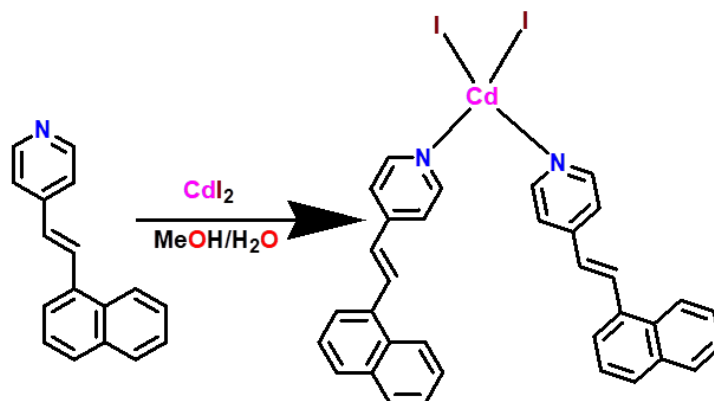
Scheme 6.1. Synthesis of **1** using CdI$_2$ and 4-(1-naphthylvinyl)pyridine (4-nvp) ligand.

A solution of 4-nvp (0.046 g, 0.2 mmol) in MeOH (2 mL) was slowly and carefully layered

into a solution of CdI$_2$ (0.073 g, 0.2 mmol) in H$_2$O (2 mL) using 2 mL of a 1 : 1 (v/v) buffer

solution of MeOH and H$_2$O. It was then allowed to diffuse for a few days. The colorless needle-

shaped crystals of [CdI$_2$(4-nvp)$_2$] (**1**) were obtained (**Scheme 6.1.**) after three days (0.107 g,

yield 65%). Elemental analysis (%) calcd for C$_{34}$H$_{26}$CdI$_2$N$_2$: C 49.27, H 3.16, N 3.18; found:

C 49.31, H 3.13, N 3.41.

6.2.3. Single Crystal X-ray Crystallography

A suitable single crystal of compound **1** with the proper dimensions (0.124 × 0.105 × 0.099

mm^3) was used for data collection using a Bruker SMART APEX II diffractometer equipped

with graphite-monochromated MoKα radiation ($\lambda = 0.71073$ Å). The molecular structure of the

single crystal was solved using the SHELX-97 package.[30] Non-hydrogen atoms of the

compound were refined with anisotropic thermal parameters. All the hydrogen atoms were

located in their geometrically perfect positions and constrained to ride on their parent atoms. The crystallographic data for compound **1** is summarized in **Table 6.1.** The selected bond lengths and bond angles are also given in **Table 6.2.**

Table 6.1. Crystal data and refinement parameters for compound **1**

Formula	$C_{34}H_{26}CdI_2N_2$ (**1**)
fw	828.78
Crystal system	monoclinic
space group	*C2/c*
a (Å)	28.4498(19)
b **(Å)**	7.4390(5)
c (Å)	17.7851(12)
α(deg)	90
β(**deg)**	125.191(2)
γ(deg)	90
V **(Å³)**	3076.1(4)
Z	4
D_{calcd} **(g/cm³)**	1.790
μ(**mm⁻¹)**	2.742
λ(Å)	0.71073
data[$I > 2\sigma(I)$]/params	2703/177
GOF on F_2	1.088
Final *R* indices[$I > 2\sigma(I)$]*a,b*	R1 = 0.0329 wR2 = 0.0887

Table 6.2. Selected bond lengths and bond angles in **1**

I(1) - Cd(1)	2.6915(4)	Cd(1)-N(1)-C(5)-C(4)	166.6(5)
Cd(1) - N(1)	2.306(4)	C(3)-C(4)-C(5)-N(1)	1.0(10)
Cd(1) - N(1)a	2.306(4)	Cd(1)-N(1)-C(1)-H(1)	12
I(1) - Cd(1) - N(1)	105.24(11)	C(1)-N(1)-C(5)-H(5)	179
N(1) - Cd(1) - I(1)a	110.10(11)	N(1)a-Cd(1)-N(1)-C(1)	63.7(4)
Cd(1) - N(1) - C(1)	1 1 8.4(3)	I(1)-Cd(1)-N(1)-C(5)	5.5(5)
I(1) - Cd(1) - I(1)a	131.34(2)	I(1)a-Cd(1)-N(1)-C(5)	151.4(4)
N(1)- Cd(1) - N(1)a	85.22(16)	I(1)-Cd(1)-N(1)-C(1)	173.3(4)
Cd(1) - N(1) - C(5)	123.3(4)	I(1)a - Cd(1) - N(1)a	105.24(11)
I(1) - Cd(1) - N(1)a	110.10(11)	C(15)-C(16)-C(17)-H(17)	178

6.2.4. Hirshfeld surfaces analysis

Hirshfeld surfaces[31–33] and the associated two-dimensional (2D) fingerprint[34–36] plots were calculated using Crystal Explorer,[37] with the bond lengths to the hydrogen atoms being set to standard values.[38] For each point on the Hirshfeld isosurface, two distances, d_e (the distance from the point to the nearest nucleus external to the surface) and d_i (the distance to the nearest nucleus internal to the surface), were defined. The normalized contact distance (d_{norm}) based on d_e and d_i is given by

$$d_{norm} = \frac{\left(d_i - r_i^{vdW}\right)}{r_i^{vdW}} + \frac{\left(d_e - r_e^{vdW}\right)}{r_e^{vdW}}$$

Where, r_i^{vdW} and r_e^{vdW} are the van der Waals radii of the atoms. The value of d_{norm} is negative or positive depending on the intermolecular contacts being shorter or longer than the van der Waals separations. The parameter d_{norm} displays a surface with a red-white-blue color scheme, where the bright red spots highlight shorter contacts, the white areas represent contacts around the van der Waals separation, and the blue regions are devoid of close contacts. For a given crystal structure and set of spherical atomic electron densities, the Hirshfeld surface is

unique,[39] and thus suggests the possibility of gaining additional insight into the intermolecular interaction of molecular crystals.

6.2.5. Theoretical calculations

By utilizing the GAUSSIAN-09 [40] program package, the optimized geometries and molecular functions of the compound were attained. The hybrid DFT-B3LYP[41] theoretical functional was used throughout the process. The LanL2DZ basis set was allotted for the compound. The single crystal X-ray coordinates were taken for **1**. To entrust the low lying electronic transitions in the spectra, the time-dependent density functional theory (TDDFT)[42–44] formalism of the compound was developed. To calculate the fractional involvement of the metal molecular orbitals and organic ligand molecular orbitals, Gauss sum[45] was operated.

6.3. Results and discussion

6.3.1. Structural descriptions of [CdI$_2$(4-nvp)$_2$] (1)
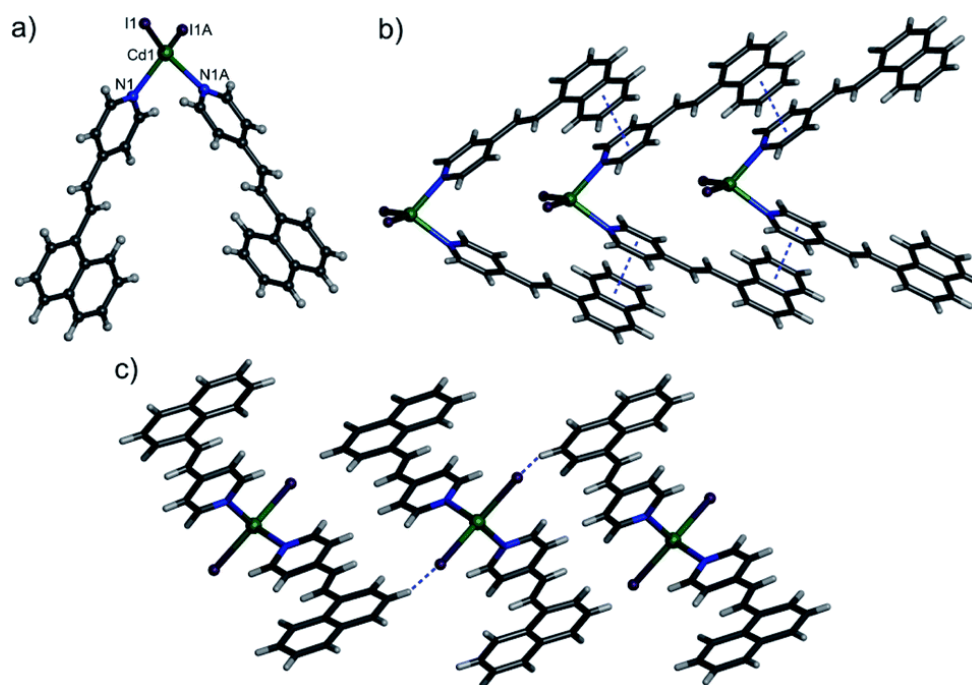
Figure 6.1. (a) A representation of **1** showing the coordination environment of the Cd(II) centre. (b) The 1D chain formed by π···π stacking interactions. (c) C–H···I interactions in **1**.

Single Crystal X-ray crystallography analysis revealed that **1** crystallizes in the $P\bar{1}$ space group with $Z = 4$. The asymmetric unit contains a 4-nvp ligand, a Cd(II) ion, and an iodide ion. The coordination geometry around the Cd(II) ion is tetrahedral and bonded to two 4-nvp ligands through pyridine N atoms and two iodide ions (**Figure 6.1a**). In **1**, the Cd–N and Cd–I bond distances are 2.306(4) and 2.6915(4), respectively. However, the 4-nvp ligands are not exactly planar. The dihedral angle between the planes of pyridine and the aryl rings is 5.54°. In the crystal structure, the discrete neutral $[CdI_2(4\text{-nvp})_2]$ units stacked together by the combination of π···π stacking (**Figure 6.1b**) and C–H···I (**Figure 6.1c**) interactions to generate a supramolecular assembly (**Figure 6.2**).
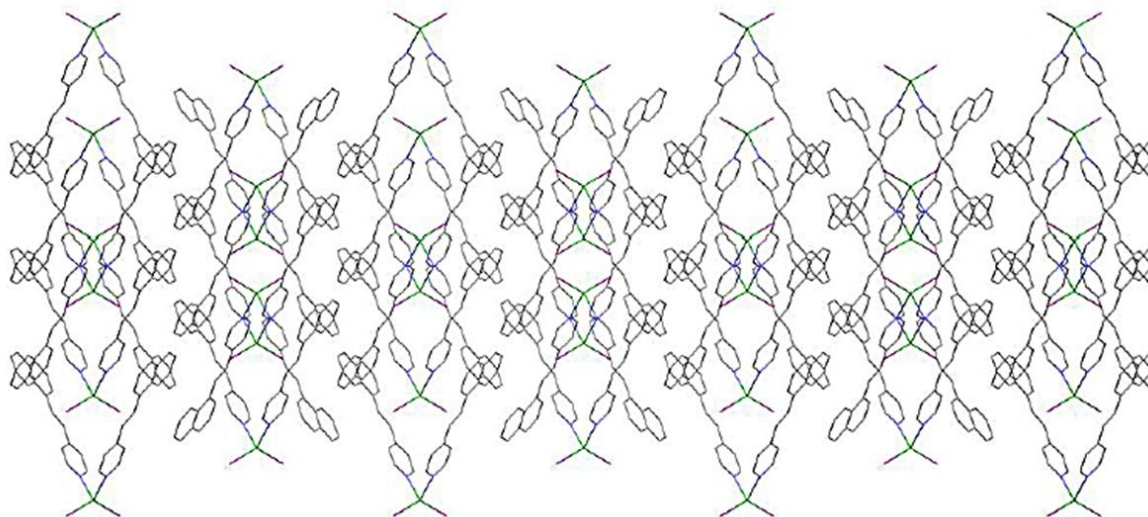
Figure 6.2. 3D supramolecular assembly of compound **1** viewed along *c*-axis.

As-synthesized pattern of PXRD was well matched with the simulated pattern (**Figure 6.3**). Thermogravimetric analysis (TGA) curve shown that compound **1** stable upto 260 °C and after that decomposition was started. Decomposition of compound 1 completed ~490 °C (**Figure 6.4**).
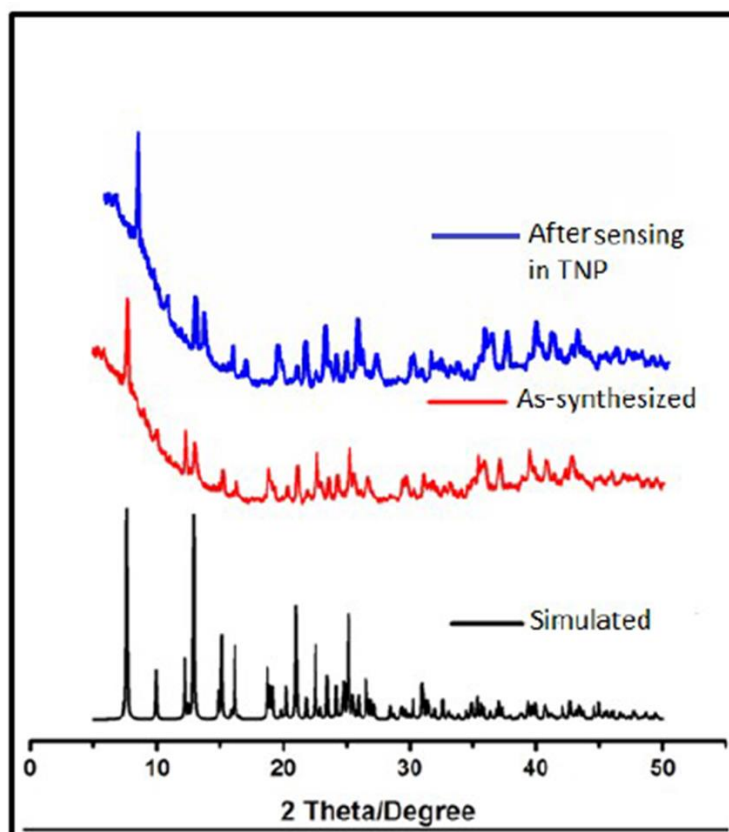
Figure 6.3. PXRD patterns of simulated **1** (black), as-synthesized **1** (red) and after sensing of **1** in TNP (blue).
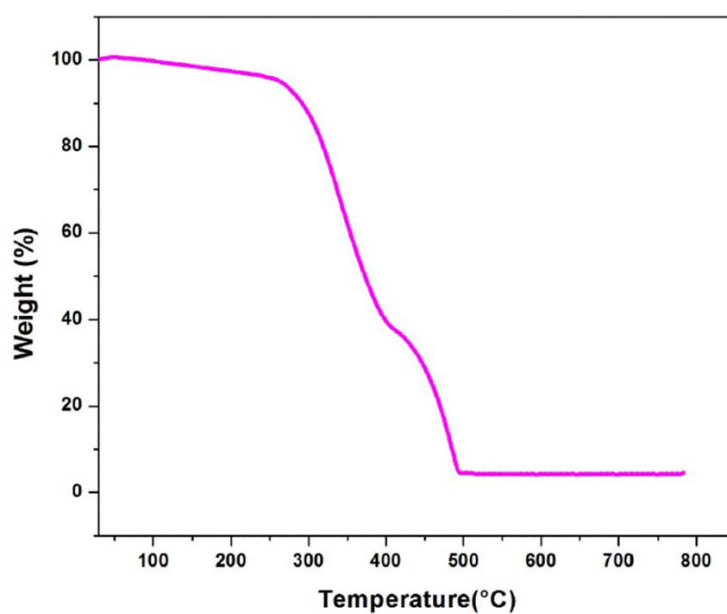
Figure 6.4. Thermogravimetric Analysis Curve of **1**.

6.3.2. Hirshfeld surface analysis of 1

The Hirshfeld surfaces for **1** are mapped over the d_{norm}, shape index and curvedness (**Figure 6.5**). The surfaces are shown as transparent to allow the visualization of the molecular moiety, around which they were calculated. The dominant interactions are between the C and H atoms for **1**. Other visible spots in the Hirshfeld surfaces correspond to the H···H contacts. The small extent of the area and light color on the surface indicates a weaker and longer
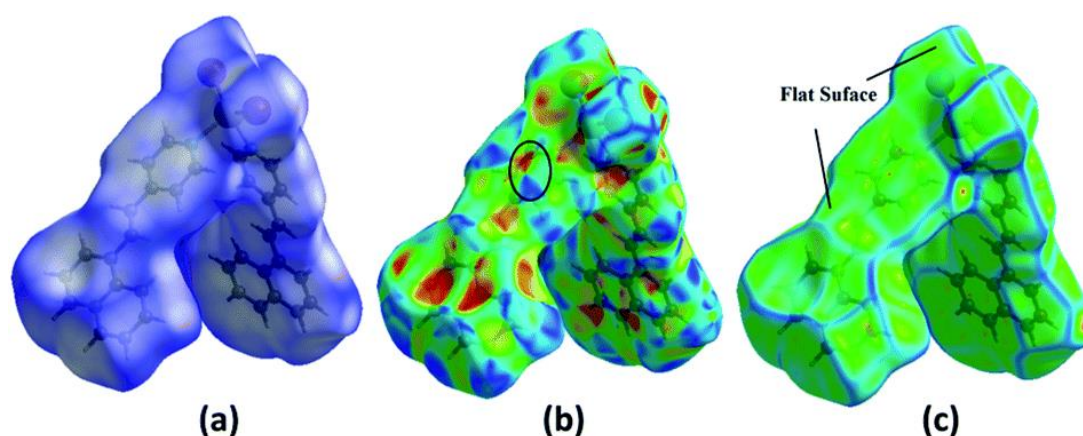
Figure 6.5. Hirshfeld surfaces mapped with (a) d_{norm} and (b) shape index (the presence of red and blue triangles is shown in the black ellipse, in which the red and blue color represent the bumps and hollow regions on the shape index surfaces, respectively). (c) Curvedness of compound **1** for identifying the planar (green) and curved (blue edge) regions for planar stacking interactions.

contact other than hydrogen bonds. The C···H/H···C interactions appear as distinct spikes in the 2D fingerprint plot (**Figure 6.6**). The complementary regions are visible in the fingerprint plots, where one molecule acts as a donor ($d_e > d_i$) and the other as an acceptor ($d_e < d_i$). The fingerprint plots can be decomposed to highlight the contributions from different interaction types, which overlap in the full fingerprint.[34]
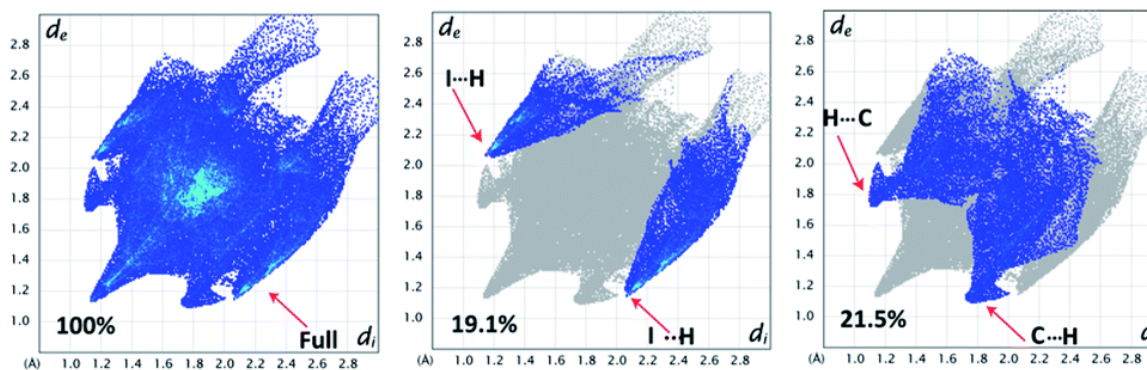
233

Figure 6.6. 2D fingerprint plots: full (left), I···H/H···I (middle), and C···H/H···C (right) interactions that contributed to the total Hirshfeld surface area for compound **1**.

The proportion of C···H/H···C interactions comprise 21.5% of the interactions in **1**. The C···H interaction is represented by a lower spike ($d_i = 1.74$, $d_e = 1.16$ Å) and the H···C interaction is also represented by a lower spike ($d_i = 1.16$, $d_e = 1.74$ Å) (**Figure 6.6**) and can be viewed as bright red spots on the d_{norm} surface (**Figure 6.5**). The proportions of the I···H/H···I interactions comprise 19.1% of the Hirshfeld surfaces for each molecule of the complex. The I···H interaction is represented by a lower spike ($d_i = 2.06$, $d_e = 1.14$ Å) and the H···I interaction is represented by another upper spike ($d_i = 1.14$, $d_e = 2.06$ Å) spike (**Figure 6.6**) and can be viewed as bright red spots on the d_{norm} surface (**Figure 6.5**). The shape index represents the local morphology of any given surface in terms of colour coded information, *i.e.*, hollow (red) and bumps (blue). **Figure 6.5b-c** show how the shape index and curvedness surfaces are used to identify planar π···π stacking interactions. The presence of red and blue triangles in the same region of the shape index surface shown by the black ellipse in **Figure 6.5b** indicates that the π···π interaction is almost identically present in the crystal structure. Blue triangles represent the convex region, which is formed due to the carbon atoms present in the naphthalene ring of the molecule inside the surface, while red triangles represent concave regions due to the carbon atoms of the π-stacked molecule above it. The mapping of the curvedness on the Hirshfeld surface (**Figure 6.5c**) shows a flat green region separated by blue edges. These clearly visible

flat regions on the curvedness surface are another characteristic of the $\pi \cdots \pi$ stacking interaction. Compound **1** has delocalized π-electrons in the C = C bonds, due to which all C = C bonds can have different energy spacings between the ground and excited states, which are responsible for radiative recombination, leading to a luminescence spectrum for the grown crystal. Therefore, compound **1** can be a good candidate for sensing applications.

6.3.3. Sensor application

Compound **1** in acetonitrile shows two absorption bands at 222 and 318 nm (**Figure 6.7a**). On fixing the excitation wavelength at 320 nm, the compound exhibits strong fluorescence at 417 nm (**Figure 6.7b**). Fluorescence spectra of compound **1** in acetonitrile after mixing with 23 different aromatic compounds exhibit that the highest quenching is observed in the presence of TNP (**Figure 6.8a**). It is very astonishing to see a new emission band centered at $\lambda_{em} = 524$, developed in the presence of a higher concentration of TNP exclusively, which shifted in the red region by 107 nm compared to that for the free compound **1** (λ_{em}, 417 nm) (**Figure 6.8b**). Thus, compound **1** is very selective towards TNP, as confirmed by the fluorescence spectroscopy results in terms of both quenching at 417 nm (**Figure 6.9a**) as well as the turn-on at 524 nm (**Figure 6.9b**). Nitroaromatics are oxidants because of the presence of low-lying unoccupied π^*-orbitals, which can accept an electron from the excited state fluorophore, thus efficiently turning off the fluorescence emission of this compound.[35] For the fruitful fluorescence quenching of small toxic compounds such as nitroaromatic explosive compounds (NACs), it is necessary for them to be closer to the sensor molecule and interact with the sensor.

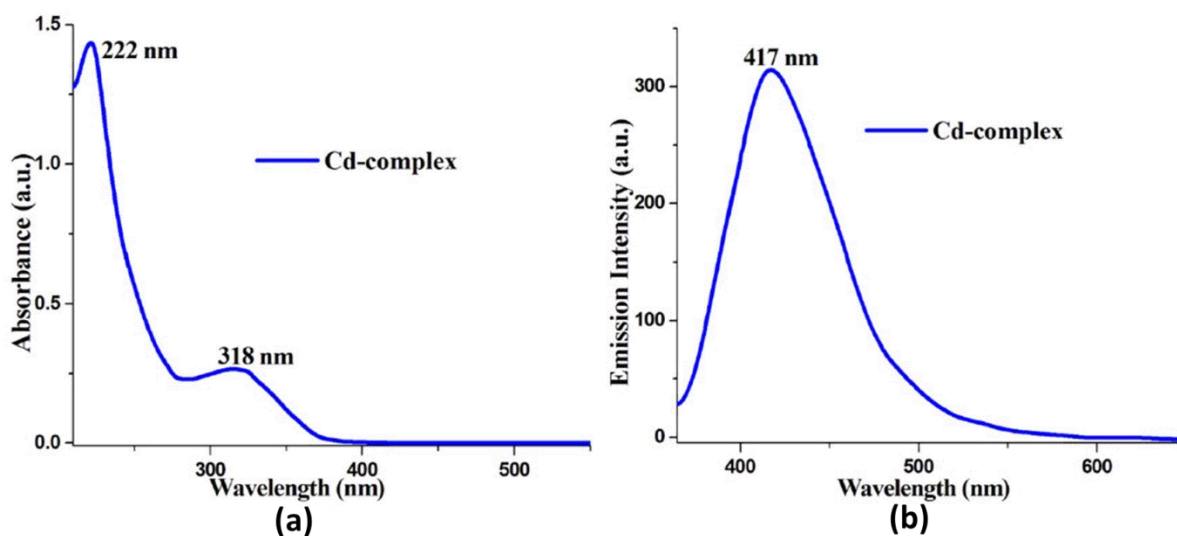The interactions are mainly based on π-interactions, namely, C–H···π and

Figure 6.7 (a) UV-vis spectra of **1** in acetonitrile, **(b)** Fluorescence spectra of **1** in acetonitrile (λex 320).
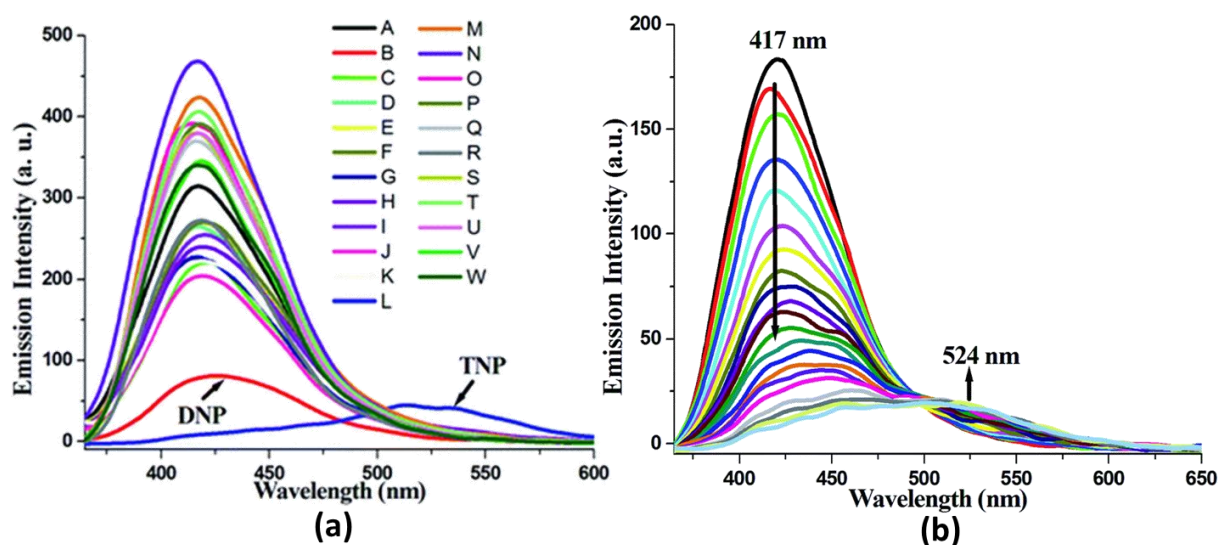

Figure 6.8. (a) Fluorescence spectra of **1** in the presence of various nitroaromatics (A: **1**, B: DNP, C: nitrophenol, D: nitrobenzoic acid, E: dinitrobenzene, F: nitrotoluene, G: dinitrophenol, H: nitrosalisylic acid, I: chloronitro benzene, J: 4-nitrophenol, K: nitrocoumarine, L: TNP, M: *p*-cresol, N: 2,4-dichloro phenol, O: 4-chloro-3-methyl phenol, P: 2-iodo benzoic acid, Q: 4-chlorophenol, R: *o*-vaniline, S: 4-chloroaniline, T: 4-methoxyphenol,

U: *p*-xylene, V: diphenylamine, and W: 2,6-ditertyarybutyl*p*-cresol) in acetonitrile. (λ_{ex}: 320 nm; excitation slit: 15; emission slit: 10), **(b)** Changes in the fluorescence emission spectra of the Cd-complex on the gradual addition of TNP in acetonitrile medium.
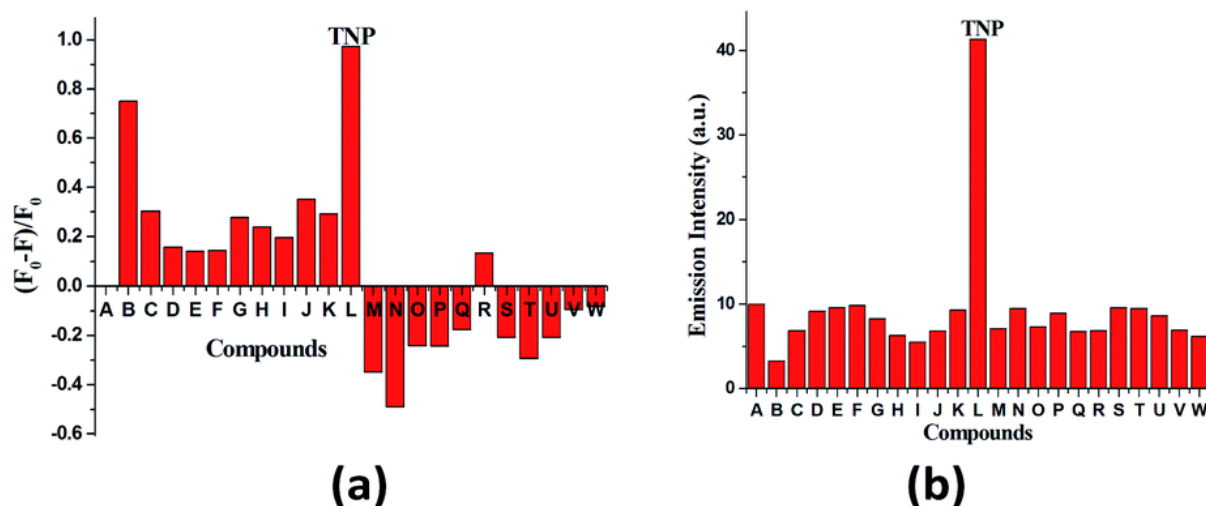

Figure 6.9. (a) Fluorescence quenching efficiency of the mentioned aromatic compound monitored at 417 nm (A to W as **Figure 6.8a**). **(b)** Fluorescence emission intensities at 524 nm of **1** in the presence of the mentioned aromatics (A to W as **Figure 6.8a**).

$\pi\cdots\pi$ stacking interactions.[36] Herein, the presence of polyaromatic rings in emissive compound **1** makes it electron rich and the structure shows the possibility to form a good $\pi\cdots\pi$ stacked charged transfer complex (**Figure 6.10**). The DFT computation using the B3LYP/LanL2DZ method for compound **1** resulted in LUMO ($LUMO_{Cd}$) and HOMO ($HOMO_{Cd}$) energy of -2.72 and -4.93 eV, respectively. However, the LUMO of TNP ($LUMO_{TNP}$) was -4.21 eV, which was lower than $LUMO_{Cd}$, but higher than $HOMO_{Cd}$. On excitation, the electrons went from the $HOMO_{Cd}$ to the $LUMO_{Cd}$ and were unable to revert back due to the presence of the low-lying $LUMO_{TNP}$. Thus, the electron jumps from the $LUMO_{Cd}$ to the $LUMO_{TNP}$ and then comes to the ground state (**Figure 6.11**). Therefore, the quenching of the emission (λ_{em}, 417 nm) for **1** has been observed for TNP and the structure of
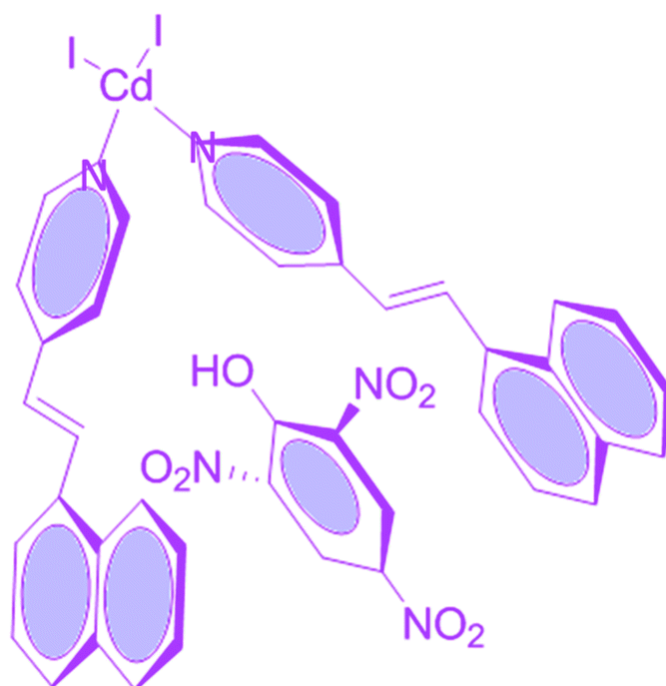
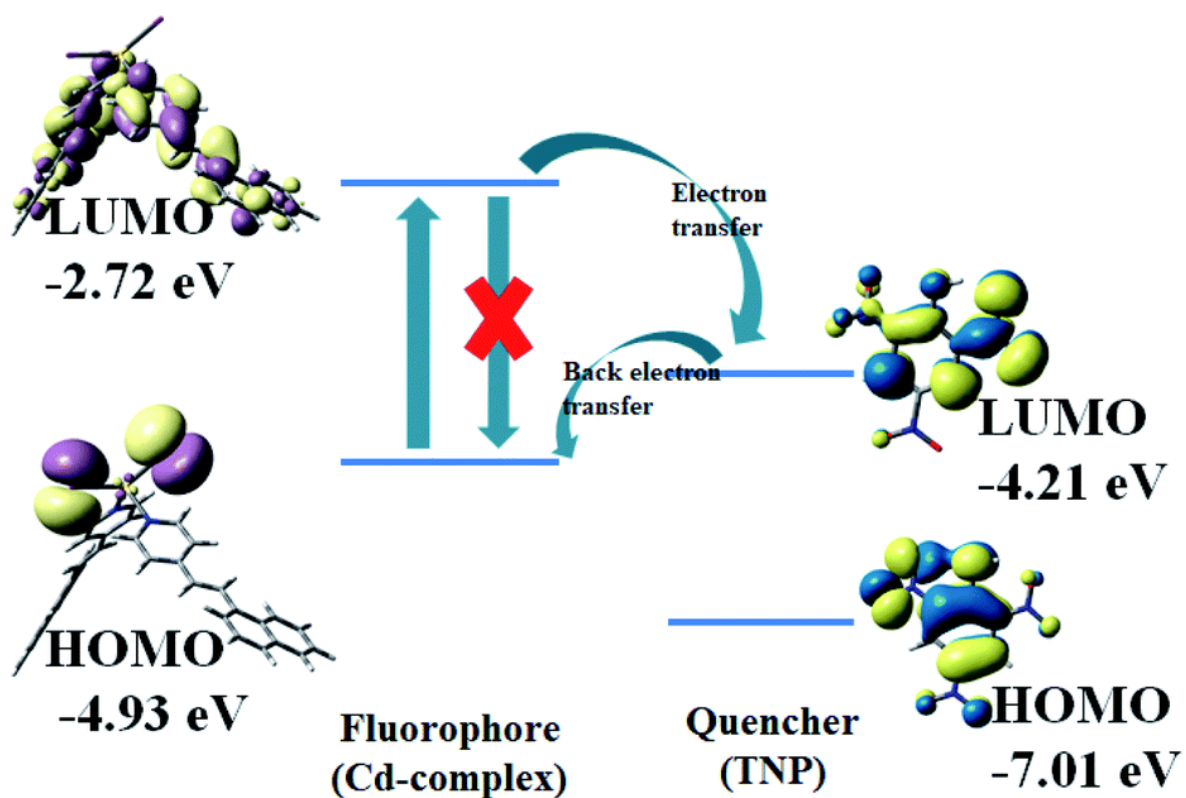**Figure 6.10.** Possibilities for the π-interaction of TNP with the Cd-complex.

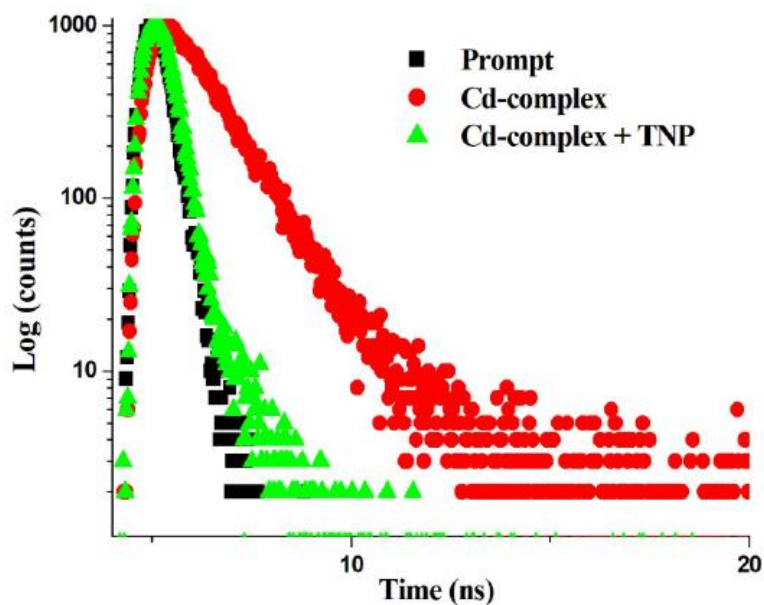**Figure 6.11.** Frontier orbital energy correlation diagram *via* electron transfer fluorescence quenching.

Figure 6.12. Fluorescence decay profile of compound **1** and compound **1** with TNP.

the compound encourages TNP to come closer to **1** through $\pi\cdots\pi$ interactions (**Figure 6.10**). The fluorescence decay profiles of both **1** and **1** with TNP exhibit bi-exponential nature. The fluorescence lifetime of **1** is 1.06 ns, which decreased to 0.11 ns in the presence of TNP (**Figure 6.12**). A red-shifted turn-on band observed at a higher concentration of TNP may have been observed due to the formation of a co-complex between TNP and **1**, which resulted in a new band gap corresponding to the emission at 524 nm.
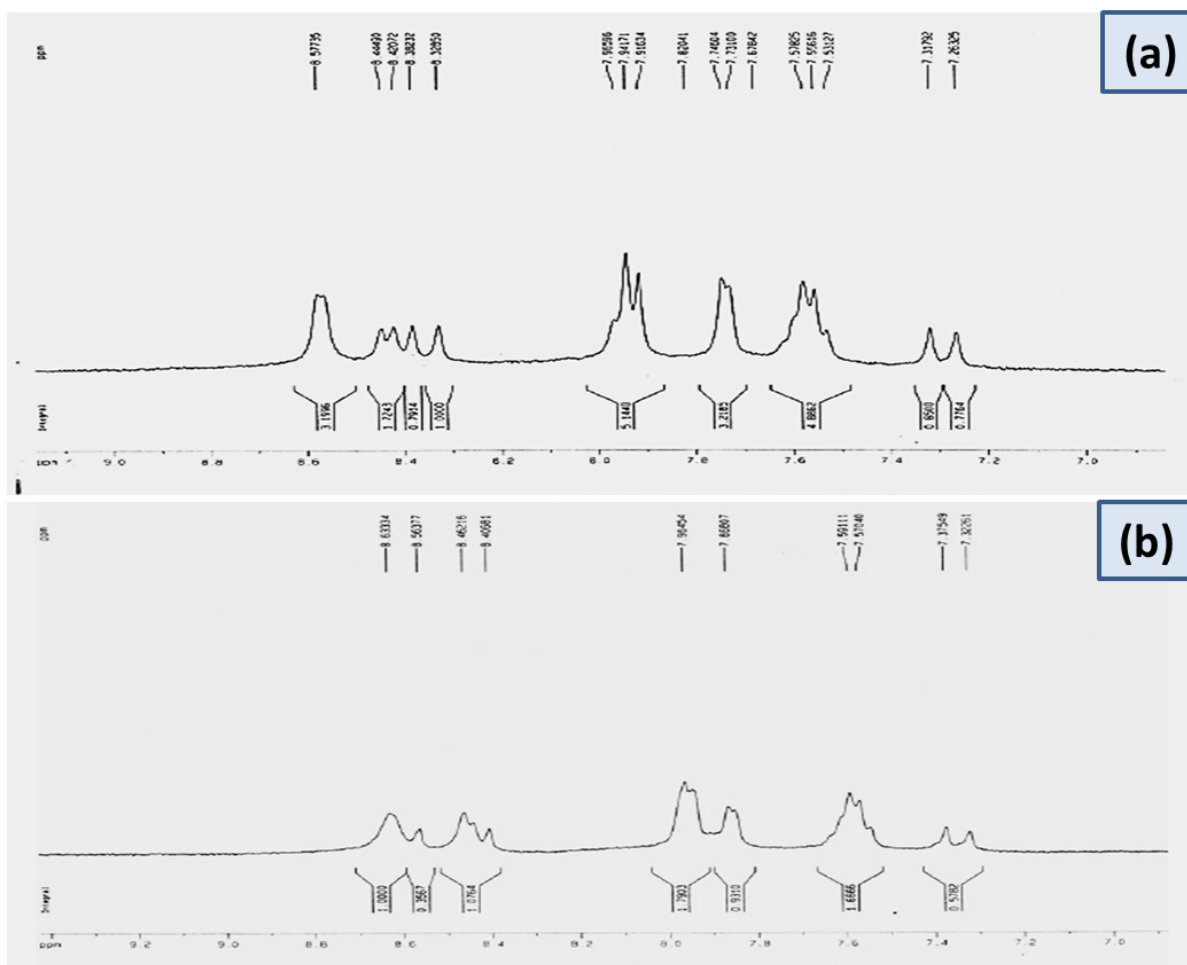
Figure 6.13. (a) ^{1}H NMR spectra of **1** in DMSO-d[6] solvent, **(b)** ^{1}H NMR spectra of **1** with trinitrophenol (TNP) in DMSO-d[6].

In order to conclude the sensing and interaction mechanism of the nitroaromatics with the complex in solution, ^{1}H NMR spectra have been recorded for varying amounts of TNP in DMSO-d$_6$ (**Figure 6.13a-b**). It was detected that the protons of the aromatic region gradually shifted to the downfield area with an increase in the concentration of the nitroaromatic compound. As we know, nitroaromatics are electron deficient and hence, during the formation of the pi-complex with these components (compound and nitroaromatics), the nitrocompounds withdraw the electron density from the complex and shift the protons toward the deshielded region. The other peaks remain practically at the same position in each step of this NMR titration. It was also confirmed that compound **1** was not decomposed during the interaction

with the nitroaromatics. To understand the mechanism, fluorescence lifetime measurements for

the sensor in the presence and absence of the quencher were performed.
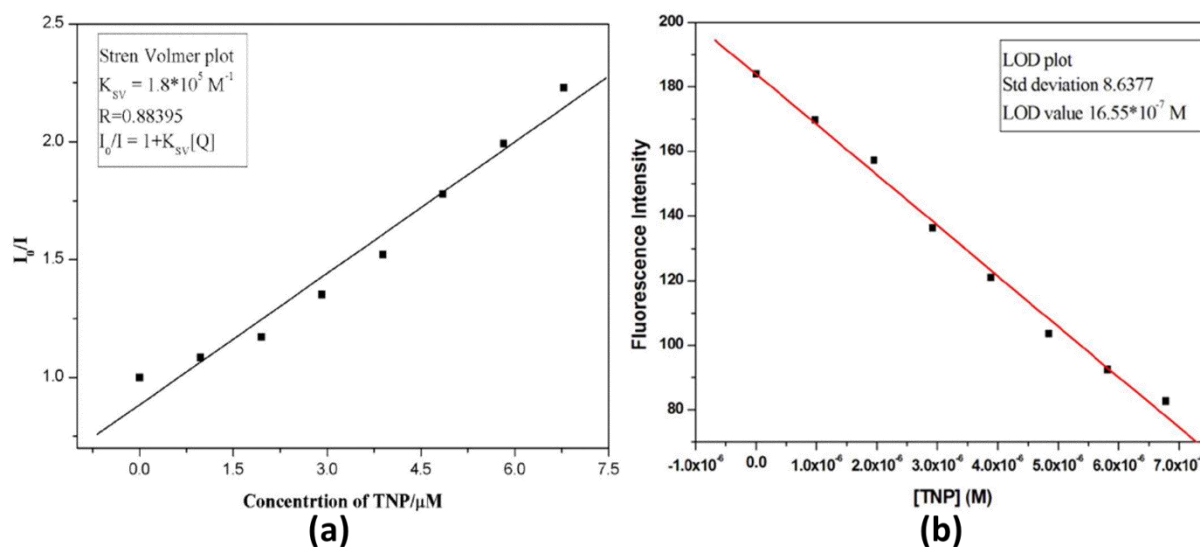

Figure 6.14 (a) Plot of I^0/I against the concentration of TNP, **(b)** Limit of detection (LOD) plot

for TNP using 3σ method.

The fluorescence intensity ratio (I_0/I) was plotted against the concentration of TNP and a Stern–

Volmer (SV) plot was obtained (**Figure 6.14a**). The SV coefficient, K_{sv}, value was determined

as 1.8×10^5 M^{-1}, which was due to the quenching of the fluorescence intensity. To quantify

the sensing efficiency, the limit of detection (LOD) was calculated as 16.55×10^{-7} M from the

3σ method (**Figure 6.14b**).[46]

6.4. Conclusion

In conclusion, the 4-NVP coordinated Cd(II)-based coordination compound was synthesized,

and the molecular arrangement was assigned from a single crystal X-ray study. Phase purity

and excellent thermal stability were also realized *via* corresponding PXRD and TGA study.

The exceptional emission of compound **1** tempted us to perform the sensing experiment for the

explosive TNP. Interestingly, in the presence of different aromatic compounds, **1** can easily

detect TNP. Thus, compound **1** can be an outstanding material for detecting TNP during security checking.

6.5. References

1. Earnshaw, A. and Greenwood, N.N. Oxford: Butterworth-Heinemann., *Chemistry of the Elements* , Butterworth-Heinemann, **1997**.

2. Cotton, F.A., Wilkinson, G., Murillo, C.A. and Bochmann, M. John Wiley and Sons, Inc. *Adv. Inorg. Chem.*, Wiley-Interscience, New York, **1999**.

3. Moroz, Y.S., Kulon, K., Haukka, M., Gumienna-Kontecka, E., Kozłowski, H., Meyer, F. and Fritsky, I.O. Synthesis and structure of [2× 2] molecular grid copper (II) and nickel (II) complexes with a new polydentate oxime-containing Schiff base ligand. *Inorg. Chem.*, **2008**, *47*, 5656-5665.

4. Chaudhuri, P. Homo-and hetero-polymetallic exchange coupled metal-oximates. *Coord. Chem. Rev.*, **2003**, *243*, 143-190.

5. Papatriantafyllopoulou, C., Stamatatos, T.C., Efthymiou, C.G., Cunha-Silva, L., Paz, F.A.A., Perlepes, S.P. and Christou, G. A High-Nuclearity 3d/4f Metal Oxime Cluster: An Unusual Ni8Dy8 "Core− Shell" Complex from the Use of 2-Pyridinealdoxime. *Inorg. Chem.*, **2010**, *49*, 9743-9745.

6. Ruben, M., Rojo, J., Romero-Salguero, F.J., Uppadine, L.H. and Lehn, J.M., Grid-type metal ion architectures: functional metallosupramolecular arrays*. Angew. Chem., Int. Ed. Engl., **2004**, *43*,* 3644-3662.

7. Middya, S., Layek, A., Dey, A., Datta, J., Das, M., Banerjee, C. and Ray. Role of zinc oxide nanomorphology on Schottky diode properties. *Chem. Phys. Lett.;* **2014**, *610*, 39-44.

8. Mitra, M., Hossain, A., Manna, P., Choudhury, S.R., Kaenket, S., Helliwell, M., Bauzá, A., Frontera, A. and Mukhopadhyay, S. Melamine-mediated self-assembly of a Cu (II)–methylmalonate complex assisted by π^+–π^+ and anti-electrostatic H-bonding interactions. *Coord. Chem. Rev.*, **2017**, *70*, 463-474.

9. Addison, A.W., TN Rao, J. Reedijk, J. Rijin, and GC Verschoor. *J. Chem. Soc., Dalton Trans.*, **1984**, *1349*.

10. Wang, S., Cao, T., Yan, H., Li, Y., Lu, J., Ma, R., Li, D., Dou, J. and Bai, J., Functionalization of microporous lanthanide-based metal–organic frameworks by dicarboxylate ligands with methyl-substituted thieno [2, 3-b] thiophene groups: sensing activities and magnetic properties. *Inorg. Chem.*, **2016**, *55*, 5139-5151.

11. Mi, X., Sheng, D., Yu, Y.E., Wang, Y., Zhao, L., Lu, J., Li, Y., Li, D., Dou, J., Duan, J. and Wang, S. Tunable light emission and multiresponsive luminescent sensitivities in aqueous solutions of two series of lanthanide metal–organic frameworks based on structurally related ligands. *ACS Appl. Mater. Interfaces.*, **2019**, *11*, 7914-7926.

12. Chen, Z., Mi, X., Lu, J., Wang, S., Li, Y., Dou, J. and Li, D.,. From 2D→ 3D interpenetration to packing: N coligand-driven structural assembly and tuning of luminescent sensing activities towards Fe^{3+} and $Cr_2O_7^{2-}$ ions. *Dalton Trans.,* **2018**, *47,* 6240-6249.

13. Mi, X., Sheng, D., Yu, Y.E., Wang, Y., Zhao, L., Lu, J., Li, Y., Li, D., Dou, J., Duan, J. and Wang, S.,. Tunable light emission and multiresponsive luminescent sensitivities in aqueous solutions of two series of lanthanide metal–organic frameworks based on structurally related ligands. *ACS Appl. Mater. Interfaces.*, **2019***, 11*, 7914-7926.

14. Guo, L.Y., Su, H.F., Kurmoo, M., Wang, X.P., Zhao, Q.Q., Lin, S.C., Tung, C.H., Sun, D. and Zheng, L.S. Multifunctional triple-decker inverse 12-metallacrown-4 sandwiching halides. *ACS Appl. Mater. Interfaces.*, **2017**, *9* ,19980-19987.

15. Chen, W.M., Meng, X.L., Zhuang, G.L., Wang, Z., Kurmoo, M., Zhao, Q.Q., Wang, X.P., Shan, B., Tung, C.H. and Sun, D.,. A superior fluorescent sensor for Al^{3+} and UO_2^{2+} based on a Co (II) metal–organic framework with exposed pyrimidyl Lewis base sites. *J. Mater. Chem.*, **2017**, *5*, 13079-13085.

16. Wang, X.P., Han, L.L., Wang, Z., Guo, L.Y. and Sun, D. Microporous Cd (II) metal-organic framework as fluorescent sensor for nitroaromatic explosives at the sub-ppm level , *J. Mol. Struct.*, **2016**, 1107.

17. Espallargas, G.M. and Coronado, E., 2018. Magnetic functionalities in MOFs: from the framework to the pore. *Chem. Soc. Rev.*, **2018**, *47*, 533-557.

18. Sheikh, J.A., Jena, H.S., Clearfield, A. and Konar, S. Phosphonate based high nuclearity magnetic cages. *Acc. Chem. Res.*, **2016**, *49*, 1093-1103.

19. Suh, M.P., Park, H.J., Prasad, T.K. and Lim, D.W., Hydrogen storage in metal–organic frameworks. *Chem. Rev.*, **2012**, *112*, 782-835.

20. Sengupta, K., Chatterjee, S. and Dey, A., Catalytic H_2O_2 disproportionation and electrocatalytic O2 reduction by a functional mimic of heme catalase: direct observation of compound 0 and compound I in situ. *ACS Catal.,* **2016**, *6*, 1382-1388.

21. Yao, P.S., Liu, Z., Ge, J.Z., Chen, Y. and Cao, Q.Y. A novel polynorbornene-based chemosensor for the fluorescence sensing of Zn^{2+} and Cd^{2+} and subsequent detection of pyrophosphate in aqueous solutions. *Dalton Trans.*, **2015,** *44*, 7470-7476.

22. Sengupta, K., Chatterjee, S. and Dey, A. Catalytic H_2O_2 disproportionation and electrocatalytic O2 reduction by a functional mimic of heme catalase: direct observation of compound 0 and compound I in situ. *ACS Catal.,* **2016**, *6*, 1382-1388.

23. McQuade, D.T., Pullen, A.E. and Swager, T.M. Conjugated polymer-based chemical sensors. *Chem. Rev.*, **2000**, *100*, 2537-2574.

24. Eiceman, G.A. and Stone, J.A. Peer reviewed: ion mobility spectrometers in national defense, **2004**.

25. Kou, M., Zhai, X., Duan, W.L., Zhang, P., Martí-Rujas, J. and Guo, F. Exploring the sensing behavior in the detection of nitroaromatics using coordination complexes based on 4, 4′-(1, 3-phenylenedioxy)-dianiline ligand. *Inorg. Chim. Acta.*, **2019,** *494*, 154-159.

26. Tang, Z., Chen, H., Zhang, Y., Zheng, B., Zhang, S. and Cheng, P. Functional two-dimensional coordination polymer exhibiting luminescence detection of nitroaromatics. *Cryst. Growth Des.*, **2019,** *19*, 1172-1182.

27. Zhang, X.D., Zhao, Y., Chen, K., Guo, J.H., Wang, P., Wu, H. and Sun, W.Y. Cucurbit [6] uril-based supramolecular assemblies incorporating metal complexes with multiaromatic ligands as structure-directing agent for detection of aromatic amines and nitroaromatic compounds. *Sens. Actuators B Chem.*, **2019**, *282*, 844-853.

28. Huang, W.H., Ren, J., Yang, Y.H., Li, X.M., Wang, Q., Jiang, N., Yu, J.Q., Wang, F. and Zhang, J., Water-stable metal–organic frameworks with selective sensing on Fe3+ and nitroaromatic explosives, and stimuli-responsive luminescence on lanthanide encapsulation, *Inorg. Chem.*, **2019**, *58*, 1481-1491.

29. Liu, Y., Zhang, Q., Jing, D., He, X., Cui, S. and Liu, Y. Rapid visual identification of nitroaromatics compounds by aggregation-induced enhanced emission fluorescent assays with a Cd (II)-H_3BTT complex. *Sens. Actuators B* Chem*: chemical.,* **2019**, *296*, 126623

30. Ren, L.L., Cui, Y.Y., Cheng, A.L. and Gao, E.Q. Water-stable lanthanide-based metal-organic frameworks for rapid and sensitive detection of nitrobenzene derivatives. *J. Solid State Chem.*, **2019**, *270*, 463-469.

31. Sheldrick, G.M. A short history of SHELX. *Acta Crystallogr., Sect. A: Found. Crystallogr.*, **2008**, *64* , 112-122.

32. Spackman, M.A. and Jayatilaka, D. Hirshfeld surface analysis. *CrystEngComm.*, **2009**, *11*, 19-32.

33. Hirshfeld, F.L. Bonded-atom fragments for describing molecular charge densities. *Theor. Chim. Acta.*, **1977**, *44* , 129-138.

34. Clausen, H.F., Chevallier, M.S., Spackman, M.A. and Iversen, B.B. Three new co-crystals of hydroquinone: crystal structures and Hirshfeld surface analysis of intermolecular interactions. *New J. Chem.*, **2010**, *34*, 193-199.

35. Rohl, A.L., Moret, M., Kaminsky, W., Claborn, K., McKinnon, J.J. and Kahr, B. Hirshfeld surfaces identify inadequacies in computations of intermolecular interactions in crystals: pentamorphic 1, 8-dihydroxyanthraquinone. *Cryst. Growth Des.*, **2008**, *8* , 4517-4525.

36. Parkin, A., Barr, G., Dong, W., Gilmore, C.J., Jayatilaka, D., McKinnon, J.J., Spackman, M.A. and Wilson, C.C. Comparing entire crystal structures: structural genetic fingerprinting. *CrystEngComm.*, **2007**, *9*, 648-652.

37. Spackman, M.A. and McKinnon, J.J. Fingerprinting intermolecular interactions in molecular crystals. *CrystEngComm.*, **2002**, *4*, 378-392.

38. Wolff, S.K., Grimwood, D.J., McKinnon, J.J., Jayatilaka, D. and Spackman, M.A., University of Western Australia, Perth, Australia, *Crystal Explorer 2.0.*, **2007**.

39. Allen, F.H., Kennard, DG Watson, L. Brammer, AG Orpen and R. Taylor. *J. Chem. Soc., Perkin Trans.*, **1987**, *2*, S1-S19.

40. Kinnon, J. J., Spackman, M. A. and Mitchell, A. S. Crystal Packing Studies, Thermal Properties and Hirshfeld Surface Analysis in the Zn(II) Complex of 3-Aminopyridine with Thiocyanate as Co-Ligand, *Acta Crystallogr., Sect. B: Struct. Sci.*, **2004**, *60*, 627-668.

41. Frisch, M. J., Trucks, G. W., Schlegel, H. B., Scuseria, G. E., Robb, M. A., Cheeseman, J. R., Scalmani, G. Barone, V., Mennucci, B., Petersson, G. A., Nakatsuji, H., Caricato, M., Li, X., Hratchian, H. P., Izmaylov, A. F., Bloino, J., Zheng, G., Sonnenberg, J. L., Hada, M., Ehara, M., Toyota, K., Fukuda, R., Hasegawa, J., Ishida, M., Nakajima, T., Honda, Y., Kitao, O., Nakai, H., Vreven Jr, T., Montgomery, J. A., Peralta, J. E., Ogliaro, F. M., Bearpark, J., Heyd, J., Brothers, E., Kudin, K. N., Staroverov, V. N., Kobayashi, R., Normand, J., Raghavachari, K., Rendell, A., Burant, J. C., Iyengar, S. S., Tomasi, J., Cossi, M., Rega, N., Millam, J. M., Klene, M., Yazyev, O., Austin, A. J., Cammi, R., Pomelli, C., Ochterski, J. W., Martin, R. L., Morokuma, K., Zakrzewski, V. G., Salvador, G. A. P., Dannenberg, J. J., Dapprich, S., Daniels, A. D., Farkas, Ö., Foresman, J. B., Ortiz, J. V., Cioslowski, J. and Fox, D. J. Gaussian, Inc., Wallingford, CT, **2009**.

42. Becke, A. D. The Effects of Oxidation States, Spin States and Solvents on Molecular Structure, Stability and Spectroscopic Properties of Fe-Catechol Complexes: A Theoretical Study. *J. Chem. Phys.*, **1993**, *98*, 5648 —5652.

43. Bauernschmitt, R. and Ahlrichs, R. Treatment of electronic excitations within the adiabatic approximation of time dependent density functional theory. *Chem. Phys. Lett.*, **1996**, *256*, 454-464.

44. Stratmann, R.E., Scuseria, G.E. and Frisch, M.J. An efficient implementation of time-dependent density-functional theory for the calculation of excitation energies of large molecules. *J. Chem. Phys.*, **1998**, *109*, 8218-8224.

45. Casida, M.E., Jamorski, C., Casida, K.C. and Salahub, D.R. Molecular excitation energies to high-lying bound states from time-dependent density-functional response theory: Characterization and correction of the time-dependent local density approximation ionization threshold. *J. Chem. Phys.*, **1998**, *108*, 4439-4449.

46. O'boyle, N. M., Tenderholt, A. L. and Langner, K. M., Cclib: a library for package-independent computational chemistry algorithms. *J. Comput. Chem.*, **2008**, *29*, 839-845.

47. Dutta, B., Jana, R., Bhanja, A.K., Ray, P.P., Sinha, C. and Mir, M.H. Supramolecular aggregate of Cadmium (II)-based one-dimensional coordination polymer for device fabrication and sensor application. *Inorg. Chem.*, **2019**, *58*, 2686-2694.

Chapter 7

Conclusions of Research Work

7.1. Conclusions

In this work, 1D (one-dimensional) and 2D (two-dimensional) coordination polymers (CPs) have been designed and synthesized using terpyridine/pyrazine based ligand and aromatic/unsaturated dicarboxylate linker. Herein, Zn(II) and Cd(II) metal ions coordinate with ligands and bridging dicarboxylates to construct the polymeric network (1D and 2D).

Being a part of chemistry, material chemistry connects the area of physics, chemistry and biology. Only in the field of chemistry can materials be designed and synthesised for valuable applications in physics or biology. Design and synthesis of new 1D or 2D coordination polymers based on this concept. Metal ions with various dicarboxylates and 'N' donating ligands were used to synthesize the specified materials. In presence of secondary interactions, coordination networks (1D or 2D) are assembling to form supramolecular 3D network. In extension of π-conjugation within the structural architecture are capable to bind with specific metal ions and molecules exhibiting selective sensing, biology and electrical conductivity.

The **chapter 2,** describe about the design and synthesis of two 1D coordination polymers using $Zn(NO_3)_2$, 4-Cltpy and followed by addition of corresponding acid (H_2ADC and trans H_2muca). These 1D chain polymers are assemble in presence of different secondary interaction. This Zn(II) metal centre containing two coordination polymers exhibit higher emission intensity in presence of secondary interaction and structural network and exhibits selectivel Cu^{2+} quenching with biological cell imaging.

The **chapter 3** discuss about the synthesis of one Zn(II) based coordination polymer using the end capping ligand 4-Cltpy and 2,6 NDC^{2-} linker. This 1D CP is extended in zig-zag way and supramolecular assemble occurs in presence of secondary interaction and specifically detectes $Fe^{2+/3+}$ in presence of other metal ions. Color of the compound is changing from colorless to pink with addition of $Fe^{2+/3+}$. The Zn^{2+} is substituted by the Fe, from the coordination moiety.

Also biological cell imaging has been performed in presence of $Fe^{2+/3+}$ using the MDA-MB 231 cells.

Synthesis of a Cd(II) based pyrazine appended 2D coordination polymer and characterise with using different spectroscopic technique in **chapter 4**. This 2D coordination polymer forms 3D assembly in presence of different supramolecular interactions. This CP exhibits selective quenching in presence of Pd^{2+} and shows potential electrical conductivity due to this type of structural architecture within CP and the substantial enhancement of electrical conductivity has been observed with addition of Pd^{2+} to the coordination polymer.

The **chapter 5**, discuss design and synthesis three Cd(II) based coordination polymers Cd(tppz)(adc)(MeOH)] (**1**), [Cd(tppz)(trep)] (**2**) and [Cd(tppz)(2,6-ndc)] (**3**) using the 2,3,5,6-Tetrakis(2-pyridyl)pyrazine (tppz) ligand with corresponding dicarboxylic acid (acetylene dicarboxylic acid (H_2adc), terephthalic acid (H_2trep) and 2,6 naphthalene dicarboxylic acid (2,6 H_2ndc)). Here, two compounds exhibits 2D network (**1**, **2**) and other one (**3**) is 1D chain. This three compound exhibits electrical conductivity but compound **3** shows highest conductivity than the others due to the structural framework and high π-conjugation within the networks. The DFT computational study correlates the semiconducting nature of this materils.

Synthesis a coordination compound [CdI$_2$(4-nvp)$_2$] using CdI$_2$ and 4-(1-naphthylvinyl)pyridine (4-nvp) in **chapter 6**. In presence of different secondary interactions ($\pi\cdots\pi$, C-H$\cdots$I) the single block unit has been assembled. This compound is highly selective to detect TNP in presence of other nitroaromatics. The mechanisim of the TNP sesing is supported by the DFT computational study.

Rights and Permission

Chapter 1:

Figure reprinted with permission from *Chem. Commun*., **2009***, 30,* 4539-4541.

Copyright: Royal Society of Chemistry.

Figure reprinted with permission from *Cryst. Growth Des., 2016, 16, 5514-5519*

Copyright 2016: American Chemical Society

Figure reprinted with permission from *Coord. Chem. Rev*., **2007**, *251*, 2490-2509

Copyright: Elsevier.

Chapter 2:

Reprinted (adapted) with permission from *New J. Chem.*, **2021**, *45*, 13941-13948.

Copyright: Royal Society of Chemistry

Chapter 3:

Reprinted (adapted) with permission from *Inorg. Chem.*, **2022**, *61*, 19790-19799.

Copyright 2022: American Chemical Society

CCC **Marketplace**

Order Confirmation

Thank you, your order has been placed. An email confirmation has been sent to you. Your order license details and printable licenses will be available within 24 hours. Please access Manage Account for final order details.

This is not an invoice. Please go to manage account to access your order history and invoices.

CUSTOMER INFORMATION

Payment by invoice: You can cancel your order until the invoice is generated by contacting customer service.

📇 Billing Address

SUPRAVA BHUNIA
JADAVPUR UNIVERSITY
JADAVPUR UNIVERSITY
KOLKATA
WEST BENGAL
Kolkata, 700032
India

+91 8637393562
bhuniasuprava1994@gmail.com

📍 Customer Location

SUPRAVA BHUNIA
JADAVPUR UNIVERSITY
JADAVPUR UNIVERSITY
KOLKATA
WEST BENGAL
Kolkata, 700032
India

📄 PO Number (optional)

N/A

💳 Payment options

Invoice

PENDING ORDER CONFIRMATION

Confirmation Number: Pending

Order Date: 20-Jan-2023

1. New journal of chemistry   0.00 USD

Article: Ultratrace level detection of Cu2+ in aqueous medium by novel Zn(II)-dicarboxylato – pyridyl coordination polymers and cell imaging with HepG2 cells

Order License ID	Pending	Publisher	ROYAL SOCIETY OF CHEMISTRY
ISSN	1369-9261		
Type of Use	Republish in a thesis/dissertation	Portion	Page

LICENSED CONTENT

Publication Title	New journal of chemistry	Publication Type	e-Journal

CCC
RightsLink

🏠 Home ❓ Help ✓ 🗨 Live Chat 👤 SUPRAVA BHUNIA ✓

ACS Publications

Spectrophotometric Determination of Trace Amount of Total FeII/FeIII and Live Cell Imaging of a Carboxylato Zn(II) Coordination Polymer

Author: Suprava Bhunia, Satyajit Halder, Kaushik Naskar, et al
Publication: Inorganic Chemistry
Publisher: American Chemical Society
Date: Dec 1, 2022

Copyright © 2022, American Chemical Society

PERMISSION/LICENSE IS GRANTED FOR YOUR ORDER AT NO CHARGE

BACK CLOSE WINDOW

CCC
RightsLink

🏠 Home ❓ Help ✓ 🗨 Live Chat 👤 SUPRAVA BHUNIA ✓

ACS Publications

Halogen···Halogen Interactions in the Supramolecular Assembly of 2D Coordination Polymers and the CO2 Sorption Behavior

Author: Faruk Ahmed, Syamantak Roy, Kaushik Naskar, et al
Publication: Crystal Growth and Design
Publisher: American Chemical Society
Date: Sep 1, 2016

Copyright © 2016, American Chemical Society

PERMISSION/LICENSE IS GRANTED FOR YOUR ORDER AT NO CHARGE

BACK CLOSE WINDOW

CCC Marketplace

< Return to search

SHOPPING CART   Empty this cart

	Currency	USD ▼

1. Chemical communications 📝   0.00 USD

Article: Water helicate (H(2)O)(7), hosted by a diamondoid metal-organic framework.

ISSN	1364-548X	**Publisher**	ROYAL SOCIETY OF CHEMISTRY
Type of Use	Republish in a thesis/dissertation	**Portion**	Chart/graph/table/figure

LICENSED CONTENT

Publication Title	Chemical communications	**Rightsholder**	Royal Society of Chemistry
Article Title	Water helicate (H(2)O)(7), hosted by a diamondoid metal-organic framework.	**Publication Type**	e-Journal
		Start Page	4539
		End Page	4541
Author/Editor	Royal Society of Chemistry (Great Britain)	**Issue**	30
		Volume	0
Date	01/01/1996		
Language	English		
Country	United Kingdom of Great Britain and Northern Ireland		

REQUEST DETAILS

Portion Type	Chart/graph/table/figure	**Distribution**	Worldwide
Number of Charts / Graphs / Tables / Figures Requested	1	**Translation**	Original language of publication
		Copies for the Disabled?	No
Format (select all that apply)	Print, Electronic	**Minor Editing Privileges?**	No
Who Will Republish the Content?	Academic institution	**Incidental Promotional Use?**	No
Duration of Use	Life of current edition		
Lifetime Unit Quantity	Up to 499	**Currency**	USD
Rights Requested	Main product		

NEW WORK DETAILS

Rightslink® by Copyright Clearance Center

CCC
RightsLink

Home | Help ∨ | Email Support | SUPRAVA BHUNIA ∨

Chemistry of coordination space of porous coordination polymers

Author: Susumu Kitagawa, Ryotaro Matsuda

Publication: Coordination Chemistry Reviews

Publisher: Elsevier

Date: November 2007

Order Completed

Thank you for your order.

This Agreement between JADAVPUR UNIVERSITY – SUPRAVA BHUNIA ("You") and Elsevier ("Elsevier") consists of your license details and the terms and conditions provided by Elsevier and Copyright Clearance Center.

Your confirmation email will contain your order number for future reference.

License Number	5485951392597	🖶 Printable Details
License date	Feb 11, 2023	

🗎 Licensed Content

Licensed Content Publisher	Elsevier
Licensed Content Publication	Coordination Chemistry Reviews
Licensed Content Title	Chemistry of coordination space of porous coordination polymers
Licensed Content Author	Susumu Kitagawa, Ryotaro Matsuda
Licensed Content Date	Nov 1, 2007
Licensed Content Volume	251
Licensed Content Issue	21-24
Licensed Content Pages	20

🗎 Order Details

Type of Use	reuse in a thesis/dissertation
Portion	figures/tables/illustrations
Number of figures/tables/illustrations	2
Format	both print and electronic
Are you the author of this Elsevier article?	No
Will you be translating?	No

🗎 About Your Work

Title	Coordination Polymer: Synthesis, Characterization and Structure-Property Correlation for Sensing and Electrical Conductivity
Institution name	Jadavpur University
Expected presentation date	Aug 2023

🗎 Additional Data

Portions	Fig. 18 and Fig. 19

<u>Appendix</u>

List of Publications, Presentations and Awards

List of Publications:

1. **<u>Bhunia, S.</u>**, Halder, S., Naskar, K., Dutta, B., Sahoo, D., Jana, K and Sinha, C. Spectrophotometric Determination of Trace Amount of Total Fe^{II}/Fe^{III} and Live Cell Imaging of a Carboxylato Zn(II) Coordination Polymer. *Inorg. Chem.,* **2022**, *61*, 19790-19799.

2. **<u>Bhunia, S</u>**., Dutta, B., Pal, K., Chandra, A., Jana, K. and Sinha, C. Ultra-trace level detection of Cu^{2+} in an aqueous medium by novel Zn (II)-dicarboxylato–pyridyl coordination polymers and cell imaging with HepG2 cells. *New J. Chem.,* **2021**, *45*, 13941-13948.

3. Dutta, B., Purkait, R., **<u>Bhunia, S</u>**., Khan, S., Sinha, C. and Mir, M.H. Selective detection of trinitrophenol by a Cd (II)-based coordination compound. *RSC Adv.,* **2019**, *9*, 38718-38723.

4. Chandra, A., Halder, S., **<u>Bhunia, S.</u>**, Pal, S., Jana, K. and Sinha, C. Zn (II)-dicarboxylato-terpyridyl Coordination Polymer-a 'Turn on'fluorogenic platform for Al^{3+} sensing in aqueous medium and life cell imaging. *J. Mol. Struct.,* **2022**, 134559.

Article

Spectrophotometric Determination of Trace Amount of Total Fe^{II}/Fe^{III} and Live Cell Imaging of a Carboxylato Zn(II) Coordination Polymer

Suprava Bhunia, Satyajit Halder, Kaushik Naskar, Basudeb Dutta, Dipankar Sahoo, Kuladip Jana, and Chittaranjan Sinha*

Cite This: *Inorg. Chem.* 2022, 61, 19790−19799

Read Online

ACCESS | 📊 Metrics & More | 📑 Article Recommendations | 🆂🅸 Supporting Information

ABSTRACT: The coordination polymer, (Zn(II)-CP, **1**), {[Zn(2,6-NDC)(4-Cltpy)](H$_2$O)$_4$} (**1**) (2,6-H$_2$NDC = 2,6-naphthalene dicarboxylic acid and 4-Cltpy = 4′-chloro-[2,2′;6′,2″]terpyridine) is structurally characterized by single crystal X-ray diffraction measurement and other physicochemical studies (PXRD, FTIR, thermal analysis, microanalytical data). 4-Cltpy acts as end-capping ligand, and NDC$^{2−}$ is a carboxylato bridging motif to constitute ZnN$_3$O$_2$ distorted trigonal bipyramid core that propagates to construct 1D chain. The coordination polymer, **1**, detects total iron (Fe^{3+} and Fe^{2+}) in aqueous solution by visual color change, colorless to pink. Absorption spectrophotometric technique in aqueous medium measures the limit of detection (LOD) 0.11 μM (Fe^{2+}) and 0.15 μM (Fe^{3+}), and binding constants (K$_d$) are 6.7 × 10^4 M$^{−1}$ (Fe^{3+}) and 3.33 × 10^4 M$^{−1}$ (Fe^{2+}). Biocompatibility of **1** is examined in live cells, and intracellular Fe^{2+} and Fe^{3+} are detected in MDA-MB 231 cells. Zn(II) substitution is assumed upon addition of Fe^{III}/Fe^{II} solution to the suspension of the coordination polymer, **1**, in water−acetonitrile (41:1) (LZn^{II} + Fe$^{III/II}$ → LFe^{III} + Zn^{II}, where L is defined as coordinated ligands), which is accompanied by changing from colorless to pink at room temperature. The color of the mixture may be assumed to the charge transfer transition from carboxylate-O to Cltpy via Fe(II/III) bridging center (carboxylate−O−Fe-CltPy). The product isolated from the reaction is finally characterized as **Fe(III)@1-CP**. It is presumed that product **Fe(II)@1-CP** may undergo fast aerial oxidation to transform **Fe(III)@1-CP**. The Fe^{III} exchanged framework (**Fe(III)@1-CP**) has been characterized by PXRD, IR, TGA and energy dispersive X-ray analysis (EDX)-SEM. The MTT assay calculates the cell viability (%), and the tolerance limit is 100 μM to total Fe^{2+} and Fe^{3+}.
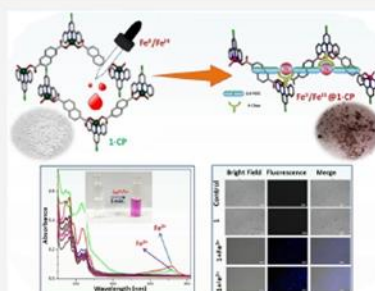
■ INTRODUCTION

In the field of material chemistry, coordination polymers (CPs)[1−13] are receiving great attention due to their novel applications like gas absorption, catalysis, electrical conductivity, magnetism, photocatalytic reduction and oxidation, chromatographic separation, water splitting, electrochemistry, drug delivery, energy saving device fabrication, sensing and dye degradation, etc.[14−34] Use of CPs as sensors[35−40] for the detection of a trace quantity of ions, various pollutants, explosive materials, or volatile organic compounds[41−43] is currently focused in chemical, environmental, engineering, and biomedical research. The sensing property of CPs in aqueous medium is a challenging because biologically important ions are sorbed in living cells mainly from food, drinks, beverages, etc. In comparison to molecular sensors, CPs are beneficial and sustainable because of stability, flexibility, and reusability. However, the sensing of paramagnetic ions/molecules is troublesome by fluorescence process because of paramagnetic quenching; an absorption spectrophotometric process is more useful in this respect.

The stable CPs/metal organic frameworks (MOFs) may be formulated following the selection of metal ion(s) and ligand centers using the hard and soft acid base (HSAB) principle.[44−47] The −COO and pyridyl-N donor ligands are considered as a hard base and bind with a hard acid like Fe^{3+}, Cr^{3+}, Ti^{4+}, Zr^{4+}, etc. to form stable CPs. Sometimes the post synthetic metathesis (PSM) and red-ox reactions[48−50] may be used to transform more stable and useful CPs. The metal exchange reaction by the postsynthetic method is one common tool for the synthesis of new CPs.[49−55]

Iron (Fe) is an essential element in the growth of civilization and life. Iron oxides form the outer layer and inner core of the earth. Iron is widely used in equipment manufacturing,

PAPER

Check for updates
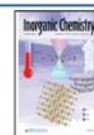
Ultra-trace level detection of Cu²⁺ in an aqueous medium by novel Zn(II)-dicarboxylato–pyridyl coordination polymers and cell imaging with HepG2 cells†

Suprava Bhunia,[a] Basudeb Dutta, [ID][a] Kunal Pal,[b] Angeera Chandra,[a] Kuladip Jana[b] and Chittaranjan Sinha [ID] *[a]

Two newly designed coordination polymers (CPs), [Zn(adc)(4-Cltpy)(H₂O)] (**CP1**) and [Zn(*trans*-muca) (4-Cltpy)] (**CP2**) (4-Cltpy = 4′-Chloro-2,2′:6′,2″-terpyridine, H₂adc = Acetylene-dicarboxylic acid, *trans*-H₂muca = *trans, trans*-muconic acid), are synthesized and structurally characterized by single crystal X-ray crystallography, PXRD, TGA, IR and elemental analysis. The coordination unit gets polymerized through the bridging of dicarboxylic acids and a 1D chain has been constructed. The 1D chain undergoes self-assembly *via* H-bonding, C−H···π and π···π interactions. Interestingly, the 4′-chloro-2,2′:6′,2″-terpyridine appended CPs are highly emissive in aqueous media and exhibit selective quenching by Cu²⁺ ions; the calculated (3σ method) limits of detection (LODs) are 0.14 μM (**CP1**) and 0.06 μM (**CP2**), respectively. Microscopic cell imaging determines the internalization of CPs within HepG2 cells. An MTT assay displays a tolerance limit of 100 μM.

Introduction

In the history of inorganic chemistry (after the winning of the Nobel prize by Alfred Werner in 1913), the coordination polymers (CPs)[1–11] have been most stimulating in the field of materials science. CPs are the polymeric form of a coordination moiety, and are composed of inorganic and organic components. On judicious selection of the metal and ligands, a variety of CPs can be designed that could exhibit different properties. The properties of a material are the key factor for its application. Thus, there is a vital relationship among the structure, properties and applications. CPs are employed for numerous applications, like gas absorption, electrical conductivity, catalysis, water splitting, electrochemistry, magnetism, dye degradation, drug delivery, device fabrication and sensing, *etc.*[12–19] The sensing properties of CPs are utilized as a powerful tool for fluorescence chemosensors[20–28] because of their high sensitivity, selectivity, rapid response, reusability and low cost. Recently, fluorescent materials have been used intensively for the

detection of toxic or useful cations, anions and small organic molecules, explosive materials, *etc.* by achieving perceivable changes *via* quenching or enhancement of the luminescence. Fluorescence sensing of CPs has also been applied to detect volatile organic compounds[29,30] (styrene *etc.*), heavily toxic metal ions, chemical sensing and temperature sensing[31] *etc.* However, the fluorescence properties of CPs have been recognised in few cases.[32,33]

Copper is the 3rd most abundant element[34] among the heavy metals (next to Fe, Zn) in biological systems and is a naturally occurring element in the soil, rocks, air, sediment and water. It has played a major role in the growth of civilization by contributing to building construction, electrical equipment, industrial machinery and so forth. It also plays a pivotal role in several physiological processes and is a co-factor of numerous enzymes. But excess uptake of copper is injurious to health as it causes Menkes disease, Wilson's disease, Alzheimer's disease, hypoglycaemia, gastrointestinal disease, dyslexia, infant liver damage, *etc.*[35] Therefore, it is important to measure Cu²⁺ in food stuffs, drinks, beverages *etc.* as well as in living systems for public health management. Due to its essentiality and toxic nature, intracellular copper absorption and distribution is strictly controlled by cells. One of the methods is to utilise fluorophoric chemosensors for copper detection. There are a few reports[36–38] where CPs are used for Cu²⁺ detection in aqueous solution. Sensor applications in aqueous media are scarce, which may be mainly due to poor solubility and complicated synthetic strategies.

[a] Department of Chemistry, Jadavpur University, Kolkata 700032, West Bengal, India. E-mail: crsjuchem@gmail.com

[b] Department of Life Science and Biotechnology, Jadavpur University, Kolkata 700032, West Bengal, India

† Electronic supplementary information (ESI) available: Crystallographic data for the structural analysis of the two complexes have been submitted to the Cambridge Crystallographic Data Centre, CCDC 2044205 (**CP1**) and 2044203 (**CP2**). For ESI and crystallographic data in CIF or other electronic format see DOI: 10.1039/d1nj00917f

Conference Attended

1. Poster Presentation: Suprava Bhunia, and Chittaranjan Sinha.

Poster title: Designing of Some Fluorogenic Molecules and Their Sensing Application

"CONTEMPORARY RESEARCH IN CHEMICAL SCIENCE" organised by Department of Chemistry ULUBERIA COLLEGE, In Collaboration with Department of Chemistry JADAVPUR UNIVERSITY.

2. Poster Presentation: Suprava Bhunia, and Chittaranjan Sinha.

Poster title: "Detection of trace amount Pd^{2+} by newly designed Cd(II) Pyrazine Coordination Polymer in aqueous Medium".

"Recent Trends in Chemical Science (RTCS-2021)" organized by the Indian Chemical Society, Kolkata, December 2021.

Awards and Recognitions

1. NET JRF, University Grant Commission, India (Roll No. 127894, Ref. No. 19/06/2016(i)EU-V).

2. NET JRF, University Grant Commission, India (Roll No. 133716, F. No. 16-9(June 2018)/2019(NET/CSIR).